
Influence of Surface Roughness and Shape on the Hydraulic Forces on a Submerged Floating Tunnel

Master thesis submitted to Delft University of Technology in partial
fulfilment of the requirements for the degree of

MASTER OF SCIENCE in Civil Engineering

Faculty of Civil Engineering and Geosciences

by

Niels Ruiter

Student number: 4156846

TO BE DEFENDED IN PUBLIC ON JANUARY 11TH 2023

Graduation committee:

Chairperson: Prof.Dr.Ir. W.S.J. Uijtewaal, TU Delft, Section EFM

Committee: Dr.Ir. D.J. Peters, Royal HaskoningDHV/TU Delft, Section HSFR

Dr.Ir. P. Zou, TU Delft, Section HSFR

Dr.Ir. X. Chen, Royal HaskoningDHV

Dr.Ir. J.D. Bricker, TU Delft, Section HSFR/University of Michigan

Acknowledgements

Now that I'm coming up on the final week of my time as a student, there are several people that helped me throughout this period and I would like to express my thanks to them. First of all, I would like to thank my committee members for all their help and support during my thesis. Thank you all for making the time for our many bi-weekly meetings, and offering insights and solutions to all my problems and questions. I would like to thank Pengxu Zou for the unlimited amount of help you offered by literally being a daily supervisor. Whether it was being available on a Sunday night to answer questions, finding solutions to the problems we faced, helping me write the data analysis codes, or helping me analyze the results. You've put much more work into helping me than I could have ever expected, so thank you for that.

I would like to thank my committee chair, Wim Uijttewaal, for your leading our meetings and for your guidance throughout my thesis. You helped me understand what it means to do research, pushed me to continue when I got hung up on details and offered all your practical and theoretical knowledge. I also would like to extend my thanks to Dirk-Jan Peters for helping me with finding a graduation topic and for granting me the opportunity to join this very interesting study. Your help behind the scenes made this thesis possible. I would like to thank Xuexue Chen for introducing me to the colleagues at RHDHV, and for your help with the programming side of the research. You also helped me with the finance side of the research and made the transition to working at a company easier for me. I would also like to thank Jeremy Bricker for stepping in at the last minute to complete our committee and therefore allowing me to graduate. Thank you all.

Furthermore, I would like to thank Arie, Pieter, Chantal, Arno, and Frank, without whom I would not have been able to complete my experiments, and have a lot of fun while doing them. They were always available to help me solve my many problems and offered a lot of guidance on the practical side of the experiments. Without all of you, it would not have been possible to finish the experiments in time.

Finally, I would like to thank my family for their support throughout the entirety of my studies. You've all helped me in more ways than I can name.

Niels Ruiter, January 2023

Abstract

Submerged floating tunnels (SFTs) are always exposed to water, therefore, they will be subjected to marine fouling. This thesis aims to investigate the influence that marine fouling and the associated increased roughness have on the hydrodynamic response of an SFT when subjected to a steady current, regular waves, and a combination of a steady current and regular waves. This is achieved by performing small-scale experiments in the wave-current flume at the Water Lab of the Delft University of Technology. Pyramid-shaped surface roughness with varying roughness heights and coverage percentages is added to the tunnels, and the forces they experience are measured. The corresponding force coefficients are determined with the use of the Morison equation. Furthermore, a new parametric SFT shape is designed by (Zou et al., 2020), and the implications of this shape are investigated by making the comparison between the circular-shaped and parametric-shaped tunnels in the conducted flume tests.

SFTs with various roughness designs are constructed from 3D-printed slices of the desired tunnel. The assembled model is suspended to a load cell and installed inside the flume. Multiple combinations of current velocities, wavelengths, and wave heights are tested. The orbital velocities at the tunnel are determined using Stokes' second-order wave theory in combination with the measured wavelengths and wave heights. The tested range of Reynolds numbers is 16.000 - 48.000 for the current tests. The tested range of Keulegan-Carpenter (KC) numbers is $0 < KC < 3$ for the wave tests and $0 < KC < 6$ for the combined tests.

It is found that in comparison to the circular shape, the parametric shape can reduce the drag coefficient in the current-only conditions by decreasing the wake width. In the wave and combined conditions, the parametric shape lowers the inertia coefficients. However, the total force experienced by the parametric-shaped tunnel is larger than the force on a circular-shaped tunnel with an equal height and surface roughness. One of the benefits of the new shape, however, is that a smaller diameter is required to achieve equal tunnel clearance, meaning that a smaller diameter is required which will lower the forces on the parametric-shaped tunnel compared to a circular-shaped tunnel with equal clearance. In general, an increase in roughness height or coverage percentage leads to increasing drag coefficients and decreasing inertia coefficients.

The force coefficients found in this research, are used to define fitted coefficients in the investigated range of KC numbers. These coefficients can be used to predict the forces on circular-shaped and parametric-shaped tunnels more accurately than coefficients from engineering codes can for the tested range of non-dimensional numbers. This shows the need for more research to cover a larger range of KC numbers and to assess the effect of an SFT's high blockage ratio and the influence of marine fouling on the hydraulic forces on a submerged floating tunnel.

Contents

1	Introduction	1
1.1	Research Context	1
1.2	Problem Statement	3
1.3	Research Objective	3
1.3.1	Research Questions and Methods	3
1.4	Scope/Assumptions/Limitations	4
1.5	Report Structure	4
2	Literature Review	5
2.1	Flow Around Circular Cylinders: Steady Current	5
2.1.1	Flow Regimes	5
2.1.2	Vortex Shedding	6
2.1.3	Influence of Surface Roughness on Flow in Current Conditions	8
2.2	Forces on a Circular Cylinder: Steady Current	8
2.2.1	Drag Force	9
2.2.2	Lift Force	10
2.2.3	Influence of Surface Roughness on Forces in Current Conditions	11
2.3	Flow Around Circular Cylinders: Regular Waves	12
2.3.1	Wave Theory	12
2.3.2	Keulegan-Carpenter Number	13
2.4	Forces On Circular Cylinders: Regular Waves	13
2.4.1	In-line Force	13
2.4.2	Lift Force	15
2.4.3	Influence of Surface Roughness on Forces in Wave Conditions	15
2.5	Flow and Forces Around Circular Cylinders: Current and Waves	15
2.6	Shape Influence	16
2.7	Previous Research on Roughness Effects	16
2.7.1	Shipping Fouling	17
2.7.2	Cylinders	17
2.7.3	Knowledge Gaps in Previous Research	19
3	Methodology	20
3.1	Set-Up	20
3.1.1	Flume	20
3.1.2	Model Design	21
3.2	Scope	24
3.3	Measurement Techniques	25
3.3.1	Force Measurements	25
3.3.2	Wave Measurements	26
3.3.3	Velocity Measurements	27
3.3.4	Boundary Layer and Wake	27
3.3.5	Instrument Set-Up	27
3.4	Data Analysis	28
3.4.1	General Processing and Filtering	28

3.4.2	Wave Signals	30
3.4.3	Velocity Signals	31
3.4.4	Force Coefficients	35
3.4.5	Vortex-Shedding Frequency	35
3.4.6	Keulegan-Carpenter Number	36
4	Results and Analysis	37
4.1	Current Tests	37
4.1.1	Experiment Observations	37
4.1.2	Validation of the Experiment Results	38
4.1.3	Drag Coefficient Results	40
4.1.4	Lift Coefficient	44
4.1.5	Strouhal Number	45
4.2	Wave Tests	47
4.2.1	Experiment Observations	48
4.2.2	Influence of the Tunnel Shape	51
4.2.3	Influence of the Roughness Height	55
4.2.4	Influence of the Coverage Percentage	58
4.3	Combined Tests	61
4.3.1	Experiment Observations	61
4.3.2	Influence of Tunnel Shape	63
4.3.3	Influence of Roughness Height	66
4.3.4	Influence of Coverage Percentage	68
4.4	Force Prediction	71
4.4.1	Force Coefficients from Engineering Codes	71
4.4.2	Fitted Force Coefficients	73
4.4.3	Force Prediction Results	74
5	Discussion	80
5.1	Definitions	80
5.1.1	Equivalent Diameter	80
5.1.2	Cross-Sectional Area	80
5.1.3	Non-Dimensional Numbers	80
5.2	Errors in the Velocity Signals	81
5.3	Time Shift Calculation Errors	81
5.4	Influence of the High Blockage Ratio	82
5.4.1	Current Conditions	82
5.4.2	Wave and Combined Conditions	82
5.5	Measurement Inaccuracies	82
5.5.1	Equipment	82
5.5.2	Signal Filtering	83
5.5.3	Tunnels	83
5.6	Conclusion	83
6	Conclusions and Recommendations	84
6.1	Answers to the Research Questions	84
6.2	Recommendations	87
6.2.1	Improving the Experiments	87
6.2.2	Future Research	88
	Bibliography	90
A	Linear Wave Theory	93
B	Calibration Results	95
B.1	Wave Gauges	95
B.2	Load Cell	96

C	Results of Wave Heights and Periods per test	99
C.1	Wave Tests	99
C.2	Combined Tests	100
D	Load Cell Test	102
E	Strouhal Results	105
F	Video Images of the Wake Structure	108
G	Difference between Max/Min Method and Least Squares Method	111
G.1	Waves	111
G.1.1	Horizontal Drag	112
G.1.2	Vertical Drag	114
G.1.3	Horizontal Inertia	116
G.1.4	Vertical Inertia	117
G.2	Combined	117
G.2.1	Horizontal Drag	118
G.2.2	Vertical Drag	119
G.2.3	Horizontal Inertia	120
G.2.4	Vertical Inertia	121
H	Combined Conditions Results	122
H.1	Influence of Tunnel Shape	122
H.1.1	Vertical Drag Coefficient	122
H.2	Influence of Roughness Height	123
H.2.1	Vertical Drag Coefficient	123
H.3	Influence of Coverage Percentage	123
H.3.1	Vertical Drag Coefficient	123
I	Fitted Coefficients	124
I.1	Wave Results	124
I.1.1	Horizontal Inertia Coefficient	124
I.1.2	Vertical Inertia Coefficient	126
I.1.3	Horizontal Drag Coefficient	128
I.1.4	Vertical Drag Coefficient	129
I.1.5	Summary of all Coefficients	131
I.2	Combined Results	131
I.2.1	Horizontal Inertia Coefficient	131
I.2.2	Vertical Inertia Coefficient	132
I.2.3	Horizontal Drag Coefficient	133
I.2.4	Vertical Drag Coefficient	134
I.2.5	Summary of all Coefficients	135
J	Force Prediction Accuracy and Comparison	137
J.1	Current Results	137
J.2	Wave Results	138
J.3	Combined Results	139

List of Symbols

The next list describes several symbols that will later be used within the body of the document.

$\bar{\tau}_0$	Time-averaged wall shear stress [N/m ²]
\bar{F}_D	Mean drag force per unit length [N/m]
\bar{F}_f	Friction force per unit length [N/m]
\bar{F}_p	Pressure force per unit length [N/m]
\bar{p}	Time-averaged pressure [N/m ²]
ω	Radial frequency [rad/s]
ϕ	Separation angle [°]
ψ	Wake amplification factor [-]
Uw/Ut	Ratio of orbital velocity over total velocity [-]
C	Wave celerity [m/s]
C_D	Drag coefficient [-]
C_L	Lift coefficient [-]
C_M	Inertia coefficient [-]
C_m	Hydrodynamic-mass coefficient [-]
$C_{DS,API}$	Steady flow drag coefficient from (API, 2014) [-]
$C_{DS,DNV}$	Steady flow drag coefficient from (DNV, 2010) [-]
D_{hor}	Horizontal tunnel diameter [m]
D_{ver}	Vertical tunnel diameter [m]
F_m	Hydrodynamic-mass force [N]
F_p	Froude-Krylov force [N]
f_v	Vortex shedding frequency [1/s]
F_L	Lift force per unit length [N/m]
H	Wave height [m]
k	Wavenumber [rad/m]
KC	Keulegan-Carpenter number [-]
L	Wavelength [m]

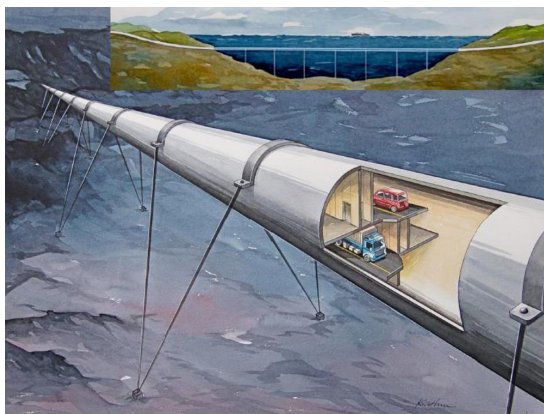
r_0	Cylinder radius [m]
St	Strouhal number [-]
T	Wave period [s]
t_1	Time of maximum orbital velocity [s]
t_2	Time of maximum orbital acceleration [s]
U_c	Current velocity [m/s]
U_m	Maximum orbital velocity [m/s]
μ	Dynamic viscosity [kg/m·s]
ν	Kinematic viscosity [m ² /s]
ρ	Density [kg/m ³]
D_{eq}	Equivalent cylinder diameter [m]
D	Cylinder diameter [m]
Re	Reynolds number [-]

Chapter 1

Introduction

1.1 Research Context

A submerged floating tunnel (SFT) is an innovative solution for crossing large bodies of water; it is a tunnel that floats underwater by balancing the buoyancy force and the support force to achieve structural stability. There are various methods to provide support to a submerged floating tunnel, through connection to the bed via columns or tethers, through anchoring at the coast, or through connecting it to pontoons that are floating at the surface. Two examples of support methods for an SFT are given in figure 1.1, a cable-supported and a pontoon-supported SFT.



(a) Cable supported SFT (Indridason et al., 2014)



(b) Pontoon supported SFT (Won et al., 2019)

Figure 1.1: Support methods for a submerged floating tunnel

The submerged floating tunnel is an alternative to traditional bridges and tunnels and offers many advantages. They are economically more viable than a suspension bridge when the length of the bridge increases, because the cost of a suspension bridge increases exponentially with its length, and the cost of an SFT per unit length remains almost constant, according to (Faggiano et al., 2005). Another advantage is that due to their submergence depth, surface waves will have less effect on the tunnel. Additionally, they do not interfere with the traffic at the water surface and visually they do not impose on the landscape, which can be a restriction in certain areas. Since the tunnel parts can be pre-fabricated, the installation can be completed quickly. Furthermore, since the SFTs are installed at a lesser depth than bored or immersed tunnels, their slope is lower which is advantageous when it comes to the energy consumption of the vehicles using the tunnel, as well as providing more comfort while driving.

An SFT has never been constructed to this day, even though the idea has been around for a long time. This is partly due to a psychological safety factor described by (Ostlid, 2010), as it is a new concept without any practical experience. Being underwater combined with the fact that the tunnel relies on

buoyancy are psychological factors for the general public, the tunnel is floating and seems to be able to move much more than conventional tunnels (Faggiano et al., 2005). The perceived risk of motion makes research on the SFT's response in flow all the more relevant. The psychological factor can also be improved by gaining experience with a larger prototype, and by presenting the design in a clear and concise manner and linking it to structures similar to SFTs where much more experience has been gained.

Besides the psychological factor, there are other possible disadvantages to SFTs. Some of these are about SFTs in general, and some are specific to a support method such as the exposure of the support pontoons to currents, waves, and wind. The pontoon-supported tunnel's stability depends on these pontoons and it can cause significant problems if the pontoon's stability is compromised. A more general disadvantage is the foundation, it has to abide by very strict rules and demands where it can't allow much motion, it needs to provide stability when the tunnel is full of vehicles, and the structure needs to be designed in a way where the failure of a single foundation unit does not lead to the failure of the entire structure. From the mechanical standpoint, the pontoons are exposed directly to free-surface motions related to waves, tides, and tsunamis, and are therefore more vulnerable. The pontoons specifically take away one of the advantages mentioned above, namely the imposing on the landscape. The pontoons float at the water surface, where they can hinder passing vessels and they can have a negative impact on the view of the surroundings.

Since the exterior of an SFT is always exposed to water, it is subjected to marine fouling. Marine fouling is defined in (Sarakinis and Busse, 2019) as the accumulation of organisms on man-made structures such as pipelines, ship hulls, and possibly in the future, submerged floating tunnels. This accumulation is often unwanted because it can have a negative effect on the structure or vessel it is attached to. For ships, it can increase the hull roughness, which leads to higher frictional resistance and increases fuel consumption. For structures such as pipelines and tunnels, marine fouling can influence the hydrodynamics of the structure by increasing the effective diameter and surface roughness. An increase in effective diameter and in surface roughness influences the drag and inertia forces on the structure where drag forces are often larger due to these changes. However, inertia forces can be lowered by the presence of surface roughness, therefore not all marine fouling is per definition unwanted. In (Henry et al., 2016) it is explained that marine fouling increases the mass of the structure and an increase in mass influences the natural frequency of the structure and its buoyancy-weight ratio, which is an important parameter for submerged floating tunnels. Marine fouling can also have an environmental impact, but this is mainly the case for ships as they carry different organisms around the world.

There are two main ways to categorize marine fouling, as microfouling and macrofouling, or as hard fouling, soft fouling, and long-flapping fouling. The latter definitions are more often used in engineering research and are therefore used in this thesis. Soft fouling contains organisms like anemones, soft corals, and seaweeds. Long-flapping fouling contains longer seaweeds such as kelp. Hard fouling contains hard marine growth such as oysters, mussels, and barnacles. In figure 1.2, an example of all three types of fouling can be seen. According to (Schoefs et al., 2021), it is well known that the roughness created by hard fouling is one of the main drivers for hydrodynamic changes and that long flapping kelp increases the vortex-induced vibrations which have a significant influence on the dynamic behavior of a structure.



Figure 1.2: Examples of hard, soft, and long flapping fouling

It is possible to prevent fouling by using anti-fouling measures such as anti-fouling paint, this is a method often used in the shipping industry. However, besides the possible negative effects on the environment as found by (Karlsson et al., 2009), this is also not a viable solution for SFTs due to their size and submergence depth. Covering an entire tunnel is expensive and the anti-fouling paints need to be replaced every 5 years (Salta et al., 2009), which makes it more expensive and unpractical because of the submergence depth. Anti-fouling paints could be a last resort solution if the fouling turns out to have too many negative effects on the tunnel's hydrodynamics.

1.2 Problem Statement

Submerged floating tunnels have never been constructed, so there are no real-life examples of the effect that marine fouling has on them. The uncertainties in the hydrodynamics of SFTs are of significant importance to their assessment. The research that has been done on the effect of marine fouling in the field of hydrodynamics, is mainly focused on structures of a smaller scale, like pipelines or jacket-type structures. Furthermore, the combination of current and waves has received little attention when researching the effect that marine fouling has on hydrodynamics. Research on the influence of various roughness parameters can be used to determine whether marine fouling on SFTs must be prevented, if it needs to be addressed during the design phase, or if it can be accepted up to a certain point.

Previous research conducted by (Drost, 2019) and (Hemel, 2019) focused on a rectangular-shaped SFT, this is not an optimal shape for economic and practical reasons. It costs much more material to construct and experiences larger hydrodynamic loads due to its non-streamlined shape. In a study by (Zou et al., 2020), an optimized parametric tunnel shape is found which decreases the drag force experienced by an SFT. Because this shape has never been physically modeled, there is no engineering knowledge of how a tunnel with this shape performs in practice. Results from the experiments conducted for this thesis can be used to validate and improve the numerical models used in designing this improved tunnel shape. Additionally, the results can be used to find force coefficients under various circumstances that can be used to predict the loads that such a tunnel experiences and can be used in designing the parametric-shaped tunnel itself and its foundation.

1.3 Research Objective

The objective of this thesis is to develop a better understanding of the effect of hydrodynamics from waves and currents, on a submerged floating tunnel with different types of marine fouling, and to investigate the parametric tunnel shape's implications compared to a circular tunnel.

1.3.1 Research Questions and Methods

Based on the research objective, the following research questions were formulated:

1. What is the influence of an optimized tunnel shape and multiple roughness parameters on the hydrodynamic properties of a submerged floating tunnel, when exposed to different environmental parameters? For the envisaged scaled experiments in a flume where waves and currents can be generated simultaneously, this implies the following:
 - The roughness parameters that are studied are the roughness height and the roughness density, described by the percentage of the tunnel's surface area that is covered.
 - The investigated tunnel shapes are a circular-shaped tunnel and the optimized parametric-shaped tunnel as described by (Zou et al., 2020).
 - The hydrodynamic properties are the vertical and horizontal drag, lift and inertia forces, and the vortex shedding frequency.

- The environmental parameters that are investigated are the wave height, the wave period, and the current velocity.
2. How accurately can the hydraulic forces on parametric and circular-shaped tunnels be predicted using the Morison equation, and how does the prediction accuracy of standard coefficients found in engineering codes compare to the coefficients found in this research?

1.4 Scope/Assumptions/Limitations

- In this thesis, the focus lies on a fixed SFT, the motion response is not within the scope of this research
- Only parametric- and circular-shaped tunnels are investigated
- The wave and current direction is perpendicular to the tunnel in all tests
- Only regular waves are used in the tests
- Buoyancy-weight ratio is kept close to one to allow only loads from the environment on the tunnel
- The parametric shape of the tunnel follows the findings in (Zou et al., 2020)

1.5 Report Structure

This thesis is structured in the following manner, in Chapter 1, an introduction to the thesis subject is given. In Chapter 2, a summary of the literature study is shown along with an overview of the theory used in this thesis. Chapter 3 consists of a detailed description of the experimental method and how the data from the experiments is acquired and processed. In Chapter 4, the results of processing and analyzing the data from the experiments are shown. In Chapter 5, these results are discussed and finally, in Chapter 6, conclusions concerning the research questions are given together with a reflection on the research itself and the chapter ends with recommendations for further studies.

Chapter 2

Literature Review

In this chapter, an overview of the theory used in this thesis is given along with some previous studies on the subject of marine fouling and hydrodynamics, which might be used as reference. The theory presented in this chapter is used in later chapters to explain the results and observations.

2.1 Flow Around Circular Cylinders: Steady Current

In order to describe the flow around a circular cylinder, the Reynolds number is needed. The Reynolds number is a dimensionless number that expresses the ratio of inertial forces to viscous forces in a fluid that is flowing. In fluid mechanics, inertial forces are the resistance to a fluid's change in velocity, and viscous forces are the resistance to the flowing of a fluid due to its cohesion. The Reynolds number is used to determine if a fluid is in turbulent flow, where inertial forces are dominant and the Reynolds number is high, or in laminar flow, where viscous forces are dominant and the Reynolds number is low. The formula for calculating the Reynolds number is shown in 2.1.

$$Re = \frac{\rho U D}{\mu} = \frac{U D}{\nu} \quad (2.1)$$

Where:

Re =	Reynolds number [-]
ρ =	Fluid density [kg/m ³]
U =	Fluid velocity [m/s]
D =	Cylinder diameter [m]
ν =	Kinematic viscosity [m ² /s]
μ =	Dynamic viscosity [kg/m·s]

2.1.1 Flow Regimes

The Reynolds number is also used to describe the different flow regimes that can be experienced. First, two different flow regions need to be mentioned, the boundary layer and the wake, as shown in figure 2.1. The boundary layer is the part of the fluid that flows along the cylinder before it separates and it has a thickness δ , which is usually small compared to the cylinder diameter. The wake is the part of the flow after the separation and extends over a distance approximately equal to the cylinder diameter.

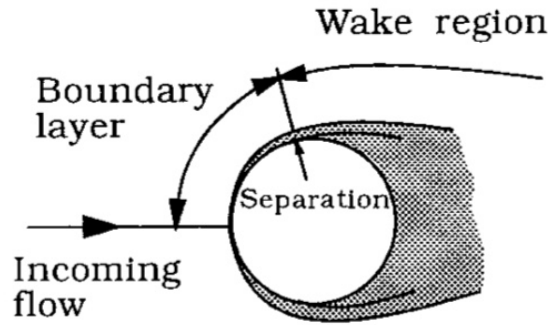


Figure 2.1: Definition of the different flow regions (Sumer and Fredsoe, 2006)

For very small Re values, as described in (Sumer and Fredsoe, 2006), no separation occurs, only when $Re = 5$, the boundary layer starts separating. In the range $5 < Re < 40$, a fixed pair of symmetric vortices form in the wake, and in $40 < Re < 200$ the wake will become unstable and vortex shedding will start, where the vortices will shed from alternating sides of the cylinder and form a vortex street, at this point the vortex street is laminar. When the Reynolds number increases, the vortices start to transition to being turbulent, and this transition moves closer to the cylinder with an increasing Reynolds number. When $Re = 400$, the vortices are turbulent directly when they are formed and the entire wake is turbulent. At this point, the boundary layer is still laminar and will remain so in the range $300 < Re < 3 \times 10^5$, this is called the subcritical flow regime.

An even higher Reynolds number leads to a transition in the boundary layer towards turbulent flow, this starts at the separation point and moves upstream towards the front of the cylinder. At this point the flow moves into the next regime, called the critical or lower-transition flow regime, the transition occurs in the range $3 \times 10^5 < Re < 3.5 \times 10^5$. Here, the boundary layer becomes turbulent alternately on one side of the cylinder, leading to a non-zero mean lift force caused by the asymmetry of the flow.

When the boundary layer becomes turbulent on both sides of the cylinder, we have entered the supercritical flow regime, this occurs in the range $3.5 \times 10^5 < Re < 1.5 \times 10^6$. However, the boundary layer is not yet entirely turbulent, the transition point between laminar and turbulent flow is located between the front of the cylinder and the separation point. When the Reynolds number reaches $1.5 \times 10^6 < Re < 4.5 \times 10^6$, the boundary layer becomes fully turbulent alternately on one side of the cylinder in what is called the upper-transition flow regime. When the Reynolds number finally increases above $Re = 4.5 \times 10^6$, the flow regime transitions into the transcritical flow regime where the boundary layers on both sides of the cylinder are fully turbulent.

2.1.2 Vortex Shedding

Vortex shedding was mentioned as a feature of flow regimes, this is a phenomenon that occurs in all flow regimes where $Re > 40$, it happens when the boundary layer separates, due to an adverse pressure gradient, and forms a shear layer behind the cylinder, as shown in figure 2.2. There is a substantial amount of vorticity present in the boundary layer, this is transferred into the shear layer and causes it to roll up and create a vortex on both sides of the cylinder. The instability of this vortex pair causes one vortex to grow larger than the other, the larger vortex then becomes strong enough to pull the smaller vortex across the wake. The vortices are rotating in opposite directions and the vorticity of the smaller vortex will cut off the supply of vorticity to the larger vortex. At this point, the larger vortex is shed and transported downstream. This process will repeat itself, only now the smaller vortex becomes the large vortex that pulls a new, smaller vortex from the opposite side across the wake, this process keeps continuing and vortices are shed from alternating sides of the cylinder.

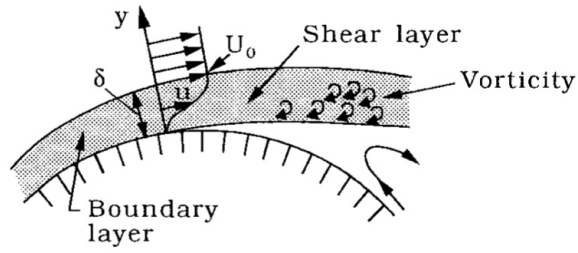


Figure 2.2: Illustration of the boundary layer separation (Sumer and Fredsoe, 2006)

The vortices are shed with a certain frequency, called the vortex-shedding frequency. This frequency can be normalized using the current velocity and the diameter of the cylinder, the normalized vortex-shedding frequency is called the Strouhal number and can be seen as a function of the Reynolds number, its formula is shown in equation 2.2. In figure 2.3, the relation between the Strouhal number and the Reynolds number can be seen.

$$St = \frac{f_v D}{U_c} \quad (2.2)$$

Where:

- $St =$ Strouhal number [-]
- $f_v =$ Vortex-shedding frequency [1/s]
- $D =$ Cylinder diameter [m]
- $U_c =$ Current velocity [m/s]

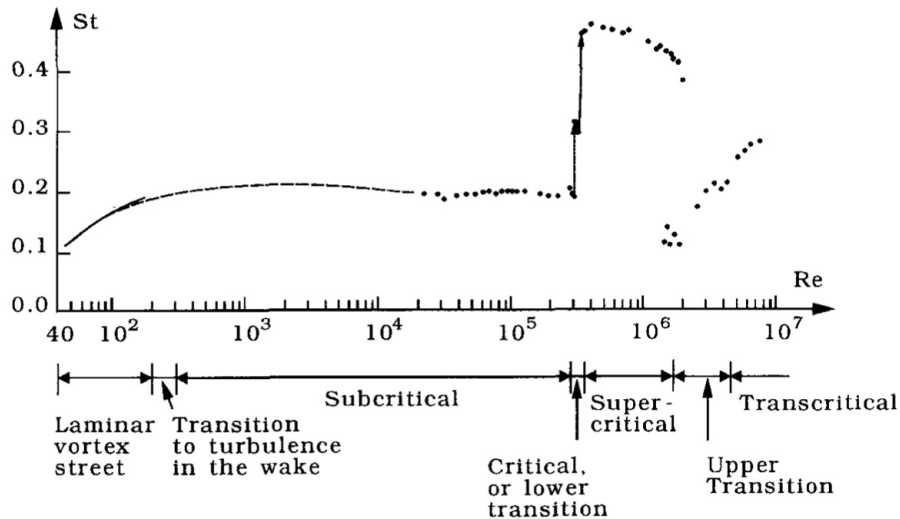


Figure 2.3: Strouhal number for a smooth circular cylinder, in different flow regimes (Sumer and Fredsoe, 2006)

Two significant jumps in the Strouhal number can be seen in figure 2.3, the first jump is found at the transition from a subcritical to a supercritical flow regime, around $Re = 3 \times 10^5$. At this point, the boundary layers on both sides of the cylinder become turbulent at the separation point. This delays the

boundary layer separation and the separation point moves downstream. Now the separation points of both sides are closer together, allowing the vortices to interact with each other faster, thus increasing the vortex-shedding frequency and the Strouhal number. The second jump is found at a Reynolds number of approximately $Re = 1.5 * 10^6$. Here, one of the boundary layers is now completely turbulent, and the other one is still transitioning. This gives an asymmetric situation that hinders the interaction between vortices partially, leading to irregular vortex shedding with a lower Strouhal number. When the transcritical flow regime is reached, regular vortex shedding is restored.

2.1.3 Influence of Surface Roughness on Flow in Current Conditions

The surface roughness of the cylinder has a significant influence on vortex-shedding and the Strouhal number, which is not only a function of the Reynolds number now, but also of the relative roughness (k/D), which is the roughness height divided by the cylinder diameter. When the relative surface roughness reaches a value of $k/D > 3 * 10^{-3}$, the critical, supercritical, and upper transition flow regimes are skipped and the flow regime changes to transcritical immediately, and this happens at much lower Reynolds numbers than for smooth cylinders, this is shown in figure 2.4. The reason for this is that transition to turbulence in the boundary layer occurs at much lower Reynolds numbers when the surface gets a higher relative roughness.

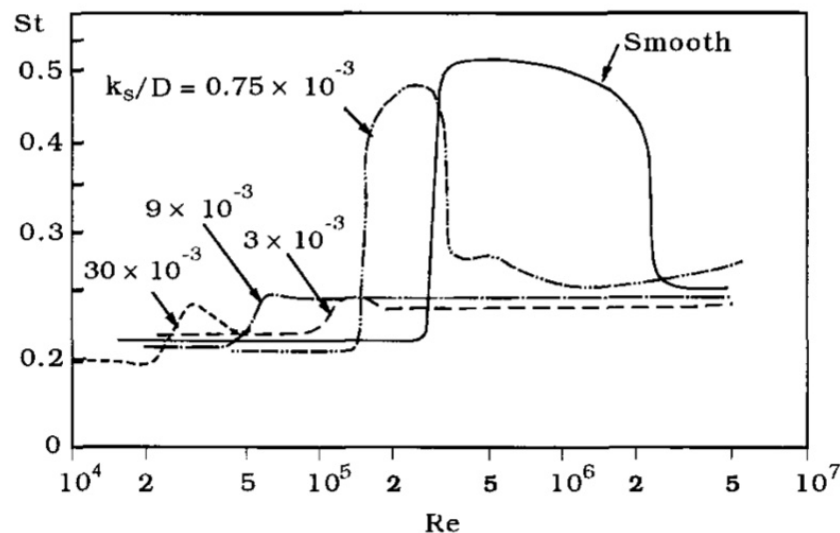


Figure 2.4: Influence of surface roughness on the Strouhal number (Sumer and Fredsoe, 2006)

2.2 Forces on a Circular Cylinder: Steady Current

The forces that act on a cylinder due to a flowing fluid can be divided into two contributions, a pressure force, or form drag, and a friction force originating from skin friction. The pressure force works perpendicular to the cylinder's surface and the friction force works in line with the cylinder's surface. The total in-line force, called the mean drag force, is the sum of the in-line contributions of these two forces. The formulas for the in-line contributions of the pressure force, friction force, and total force can be seen in equations 2.3, 2.4, and 2.5, respectively.

$$\bar{F}_p = \int_0^{2\pi} \bar{p} \cos(\phi) r_0 d\phi \quad (2.3)$$

$$\bar{F}_f = \int_0^{2\pi} \bar{\tau}_0 \sin(\phi) r_0 d\phi \quad (2.4)$$

$$\bar{F}_D = \bar{F}_p + \bar{F}_f \quad (2.5)$$

Where:

$\bar{F}_p =$	Pressure force [N/m]
$\bar{F}_f =$	Friction force [N/m]
$\bar{F}_D =$	Mean drag force [N/m]
$\bar{p} =$	Time-averaged pressure [N/m ²]
$\bar{\tau}_0 =$	Time-averaged wall shear stress [N/m ²]
$\phi =$	Separation angle [°]
$r_0 =$	Cylinder radius [m]

There is also a cross-flow component of the total force on the cylinder, this cross-flow directed force is called the lift force. The mean lift force is zero due to the symmetry of the flow, but there are instantaneous non-zero lift forces that stem from the growth of the vortex at one side of the cylinder. A growing vortex on the lower side gives an upwards-directed lift force and a growing vortex on the upper side gives a downwards-directed lift force.

Unless the Reynolds number is under 40, vortex shedding is present in each flow regime. The shedding of the vortices leads to periodic changes in the pressure distribution around the cylinders, which results in periodic variations in the drag and lift forces. The in-line drag force oscillates around the mean drag force, and the cross-flow lift force oscillates around zero. The drag force oscillates at a frequency of twice the vortex-shedding frequency and the lift force oscillates at the vortex-shedding frequency. The force amplitudes are not constant and can only be described by statistical properties.

Equation 2.5 can be rewritten in the form seen in equation 2.6, where the right-hand side terms are all functions of the Reynolds number and can be written as \bar{C}_D , the drag coefficient which is also a function of the Reynolds number. The formula for the lift coefficient, equation 2.7, can be written in the same form as the drag coefficient. The relation between the drag coefficient and the Reynolds number can be seen in figure 2.5.

$$\frac{\bar{F}_D}{\frac{1}{2}\rho DU^2} = \bar{C}_D \quad (2.6)$$

$$\frac{F_L}{\frac{1}{2}\rho DU^2} = C_L \quad (2.7)$$

Where:

$\bar{F}_D =$	Mean drag force [N/m]
$\bar{F}_L =$	Lift force [N/m]
$C_D =$	Drag coefficient [-]
$C_L =$	Lift coefficient [-]
$\rho =$	Fluid density [kg/m ³]
$U =$	Fluid velocity [m/s]
$D =$	Cylinder diameter [m]

2.2.1 Drag Force

The relation between the drag force, and therefore the drag coefficient, and the Reynolds number can be seen in figure 2.5. From this figure, it shows that the drag coefficient decreases with an increasing

Reynolds number until $Re \approx 1000$, from there it maintains a fairly constant value of 1.2. At the point where $Re = 3 \times 10^5$, the drag crisis occurs. This is a sudden decrease in the drag coefficient to a value of 0.25 which maintains throughout the supercritical flow regime, the cause of this sudden drop is the fact that the separation angle increases and the separation point moves downstream along the cylinder. This results in a narrower wake with smaller pressure differences acting on the cylinder, causing a reduction in the mean drag. When the flow enters the upper-transitional flow regime, the separation angle decreases again and the drag coefficient reaches a fairly constant value of 0.5.

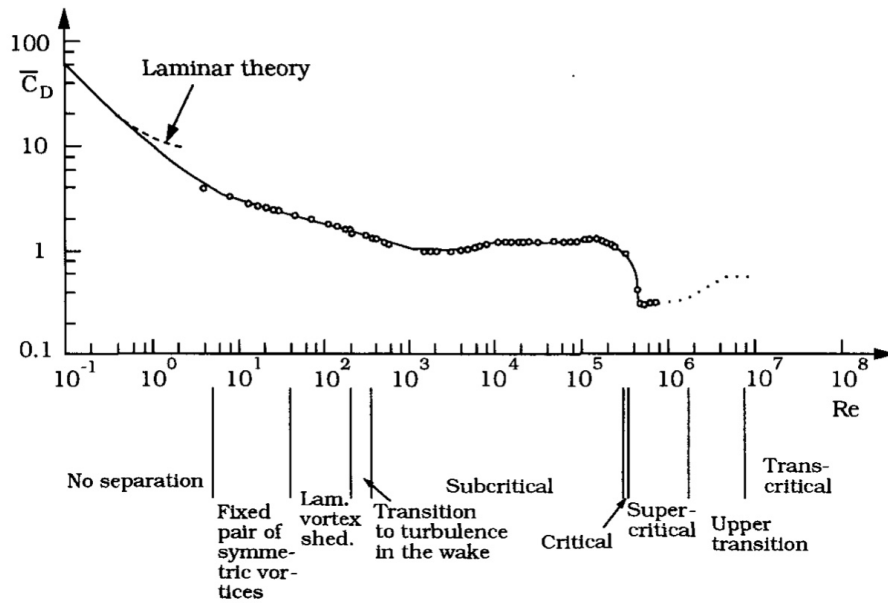


Figure 2.5: Relation between drag coefficient and Reynolds number (Sumer and Fredsoe, 2006)

2.2.2 Lift Force

In (Sumer and Fredsoe, 2006), two ways to describe the lift force are mentioned, through its maximum value (eq. 2.8), or through its root-mean-square value (eq. 2.9). The root-mean-square value considers the magnitude of the lift force instead of its maximum value and is used most in literature, and therefore in this thesis as well. Figure 2.6 shows the range of root-mean-square values of the lift coefficients of a circular cylinder.

$$F_{L \max} = \frac{1}{2} \rho C_{L \max} D U^2 \quad (2.8)$$

$$F_{L rms} = \frac{1}{2} \rho C_{L rms} D U^2 \quad (2.9)$$

Where:

- $F_{L \max}$ = Maximum lift force [N]
- $F_{L rms}$ = Root-mean-square lift force [N]
- $C_{L \max}$ = Maximum lift force coefficient [-]
- $C_{L rms}$ = Root-mean-square lift force coefficient [-]

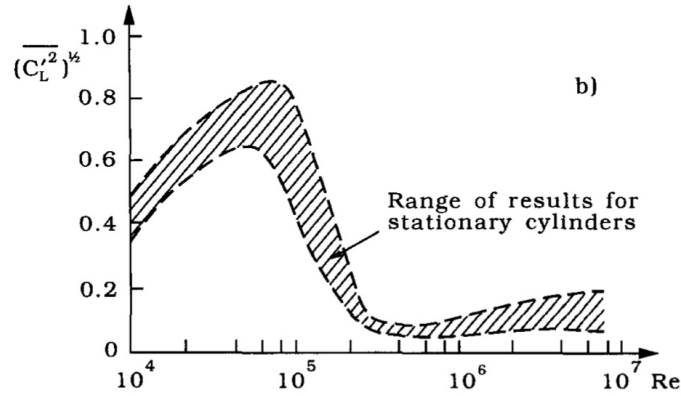


Figure 2.6: RMS values of the lift coefficient of a cylinder (Sumer and Fredsoe, 2006)

2.2.3 Influence of Surface Roughness on Forces in Current Conditions

In general, surface roughness has a significant influence on the flow around a cylinder. The influence of surface roughness was already mentioned in paragraph 2.1.2, where its influence on the Strouhal number was explained. The surface roughness also has an impact on the mean drag force, as the drag coefficient now becomes a function of the Reynolds number and the relative roughness, k/D . In the subcritical flow regime and for even lower Reynolds numbers, there is no difference between a rough and a smooth cylinder. However, when the relative roughness increases, the boundary layer transitions into turbulence at lower Reynolds numbers and shifts the curve in the drag coefficient versus Reynolds number graph to the left, as can be seen in figure 2.7.

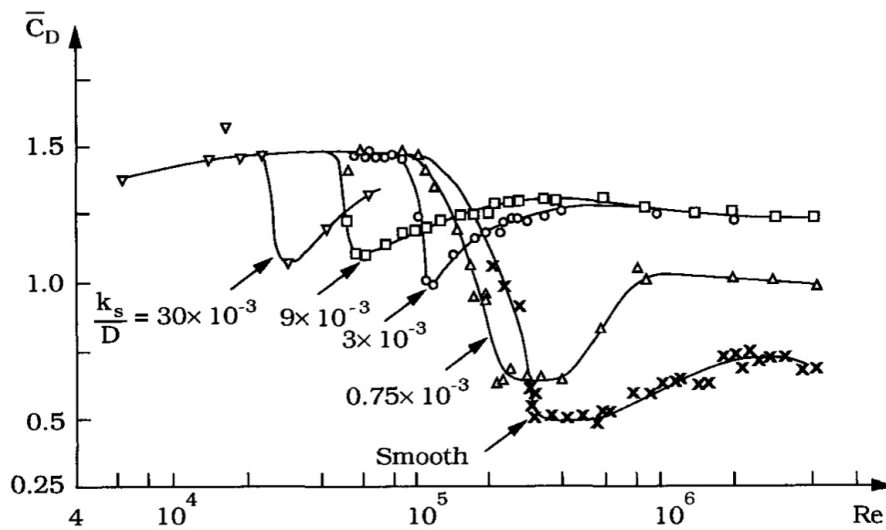


Figure 2.7: Drag coefficient for different values of relative roughness (Sumer and Fredsoe, 2006)

The drag crisis decreases in severity with increasing relative roughness; the reason for this is that the boundary layer increases in thickness due to the roughness, which in turn causes a weaker momentum exchange near the cylinder. A weaker momentum exchange leads to a lower separation angle increase during the drag crisis, compared to a smooth cylinder. The lesser increase in separation angle means a lesser decrease in wake width, which in turn leads to a lesser drop in mean drag force for rough cylinders. Another possible effect of surface roughness is that the flow can separate at a prescribed point, at the tip of sharp roughness elements for example. When this happens on both sides of a cylinder for roughness

with a large height, the width of the wake is increased. A larger wake leads to larger pressure differences and thus a larger mean drag force.

2.3 Flow Around Circular Cylinders: Regular Waves

2.3.1 Wave Theory

When surface gravity waves are present, the water particles below the surface start moving in an orbital motion. This orbital motion consists of horizontal and vertical particle velocities and can be described using various wave theories, the simplest being linear wave theory which was first described by (Airy, 1845). The horizontal and vertical particle velocities are necessary for determining the force coefficients, as will be explained in paragraph 2.4.

When the waves become too steep or the water depth becomes too shallow, linear wave theory might not be applicable anymore. If this is the case, a non-linear wave theory needs to be applied. An example of a non-linear wave theory is the theory by (Stokes, 1847). In Stokes' theory, a second harmonic wave is introduced which flattens the troughs of the waves and makes the peak higher and sharper. This second wave allows the non-linear parts of the governing equations to be solved. In figure 2.8, a graph with the applicability of each wave theory is shown. All the applied waves in this experiment fall within the range of Stokes 2nd order wave theory and are intermediate water waves.

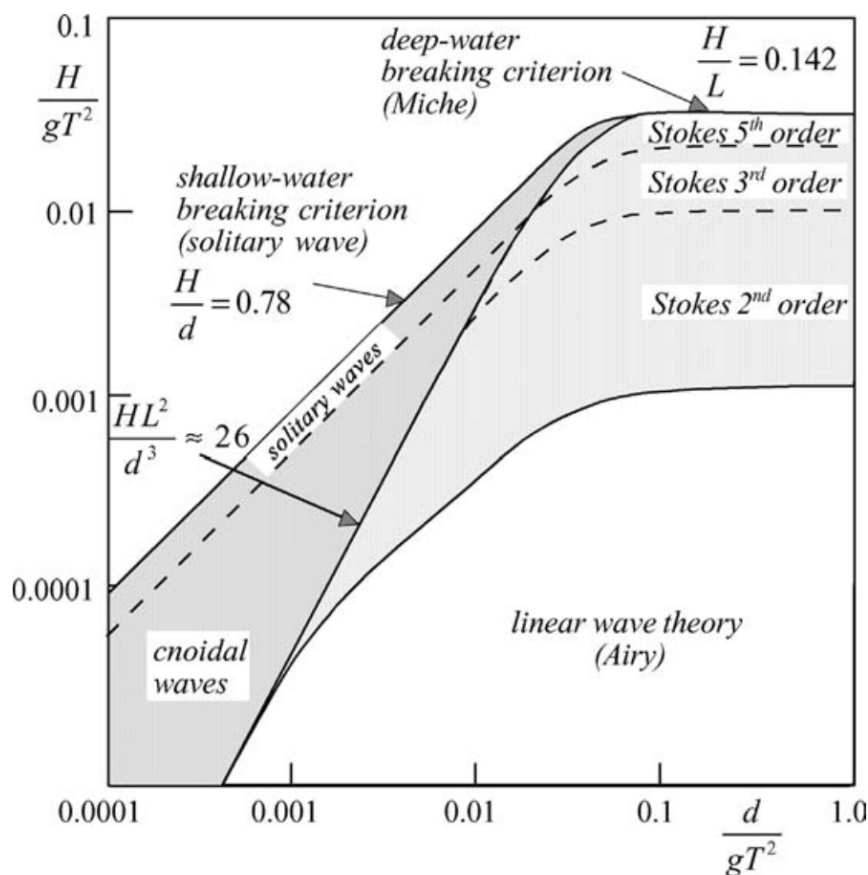


Figure 2.8: Validity of different wave theories (LeMehaute, 1976)

The equations for calculating the horizontal and vertical orbital velocities of a 2nd order Stokes wave can be found in equations 2.10 and 2.11 respectively (Sundar, 2016). The formulas to calculate the other necessary wave parameters can be found in Appendix A.

$$u_{hor} = \frac{HgT}{2L} \frac{\cosh[k(z+d)]}{\cosh kd} \cos(kx - \omega t) + \frac{3}{4} \left(\frac{\pi H}{L} \right)^2 C \frac{\cosh[2k(z+d)]}{\sinh^4 kd} \cdot \cos 2(kx - \omega t) \quad (2.10)$$

$$u_{ver} = \frac{\pi H}{L} C \frac{\sinh[k(z+d)]}{\sinh kd} \sin(kx - \omega t) + \frac{3}{4} \left(\frac{\pi H}{L} \right)^2 C \frac{\sinh[2k(z+d)]}{\sinh^4 kd} \cdot \sin 2(kx - \omega t) \quad (2.11)$$

2.3.2 Keulegan-Carpenter Number

When describing the flow around a cylinder due to oscillatory flow, the Keulegan-Carpenter number, KC, is an important dimensionless parameter along with the Reynolds number. When KC is small it says that the orbital motion of the water is small compared to the cylinder diameter, and the flow is unlikely to separate. When KC is large, the orbital motion of the water is much larger than the tunnel diameter, the flow will separate and there is vortex shedding, and the flow acts like a steady current for each half period of the motion if KC gets even larger.

$$KC = \frac{U_m T}{D} \quad (2.12)$$

Where:

KC	=	Keulegan-Carpenter number [-]
U_m	=	Maximum velocity [m/s]
D	=	Cylinder diameter [m]
T	=	Period of oscillatory flow [s]

2.4 Forces On Circular Cylinders: Regular Waves

The forces on a cylinder from the oscillatory flow caused by waves are similar to the forces from a steady current, they contain an in-line force and a lift force. In this section, both forces are covered.

2.4.1 In-line Force

The drag coefficient equation 2.6 is first rewritten in the form of equation 2.13. To describe the in-line force on a cylinder in oscillatory flow, two extra contributions are added to the drag force in the form of the hydrodynamic-mass force and the Froude-Krylov force, which together are called the inertia force. The hydrodynamic-mass force comes from the fluid mass around the cylinder that accelerates with the movement of the cylinder and is calculated with equation 2.14. The Froude-Krylov force is caused by a pressure gradient that is present due to the acceleration of the fluid in the outer-flow region and is calculated using equation 2.15. The Froude-Krylov force is only present when the cylinder is held in place and the fluid accelerates.

$$F_D = \frac{1}{2} \rho C_D D U |U| \quad (2.13)$$

$$F_m = \rho C_m A \dot{U} \quad (2.14)$$

$$F_p = \rho A \dot{U} \quad (2.15)$$

Where:

$F_m =$	Hydrodynamic-mass force [N]
$F_p =$	Froude-Krylov force [N]
$A =$	Cross-sectional area [m ²]
$C_m =$	Hydrodynamic-mass coefficient [-]
$\dot{U} =$	Fluid acceleration [m/s ²]

Combining equations 2.13, 2.14 and 2.15, and using $C_M = C_m + 1$, gives the Morison equation for the total in-line force on a cylinder, shown in equation 2.16 and was first formulated by (Morison et al., 1950). The first term is the drag force known from steady currents, and the second term is called the inertia force, with C_M being the inertia coefficient. The drag force and the inertia force are 90 degrees out of phase, which is important for determining the maximum value of the in-line force. To determine which of the two forces is dominant, the Keulegan-Carpenter number (KC) is used. A high KC number says that the drag force term is dominant, and a low KC number says that the inertia force term is dominant.

$$F = \frac{1}{2}\rho C_D D U |U| + \rho C_M A \dot{U} \quad (2.16)$$

The Morison equation was formulated for vertical cylinders and needs to be modified to be valid for horizontal cylinders. In the modified Morison equation, the horizontal and vertical directions are assigned separate force coefficients. The modified Morison equation can be seen in equations 2.17 and 2.18. This method has been used in the papers by (Bai et al., 2017) and (Venugopal et al., 2008). In the paper by (Chaplin, 1988), this was reported to give accurate results.

$$F_x = \frac{1}{2}\rho C_{Dx} D_x U_x \sqrt{U_x^2 + U_z^2} + \rho C_{Mx} A \dot{U}_x \quad (2.17)$$

$$F_z = \frac{1}{2}\rho C_{Dz} D_z U_z \sqrt{U_x^2 + U_z^2} + \rho C_{Mz} A \dot{U}_z \quad (2.18)$$

The drag and inertia coefficients are approximated using the method of least squares, which was first published by (Legendre, 1805). In this method, the coefficients take the value where they cause the smallest mean-squared difference between the measured force in the experiments and the force predicted using the Morison equation. Both coefficients depend on the KC number and on the Reynolds number. The method of least squares uses the following formulas to calculate the drag and inertia coefficients, where $i = x, z$. Solving equations 2.20 and 2.21 simultaneously leads to the drag and inertia coefficients.

$$\varepsilon^2 = \sum \left[f_{Di} U_i \sqrt{U_x^2 + U_z^2} + f_{Mi} a_i - F_{mi} \right]^2 \quad (2.19)$$

$$\frac{\partial \varepsilon^2}{\partial f_{Di}} = 0 \rightarrow f_{Di} \left(\sum U_i^2 (U_x^2 + U_z^2) \right) + f_{Mi} \left(\sum U_i \sqrt{U_x^2 + U_z^2} a_i \right) = \sum U_i \sqrt{U_x^2 + U_z^2} F_{mi} \quad (2.20)$$

$$\frac{\partial \varepsilon^2}{\partial f_{Mi}} = 0 \rightarrow f_{Di} \left(\sum U_i \sqrt{U_x^2 + U_z^2} a_i \right) + f_{Mi} \left(\sum a_i^2 \right) = \sum a_i F_{mi} \quad (2.21)$$

With:

$$f_{Di} = \frac{1}{2}\rho C_{Di} D_i \quad f_{Mi} = \rho C_{Mi} A$$

Where:

ϵ = Error between the measured and predicted force
 A = Area of the circular cylinder
 D_i = Vertical diameter for $i = x$, Horizontal diameter for $i = z$
 a_i = Fluid particle acceleration in i -direction
 U_i = Fluid particle velocity in i -direction
 C_{Di} = Drag coefficient i -direction
 C_{Mi} = Inertia coefficient in i -direction

2.4.2 Lift Force

Lift forces start emerging when KC reaches a value of about 6, since that is when vortex shedding starts which is the cause of the lift forces. In the experiments for this thesis, the KC number is much lower than 6, and lift forces are not present during the wave tests.

2.4.3 Influence of Surface Roughness on Forces in Wave Conditions

Surface roughness has an influence on the drag and inertia coefficients, as the drag and lift coefficients increase with increasing relative roughness, and the inertia coefficient decreases under the same circumstances. The increase in drag force can be explained using the same reasoning as used in paragraph 2.2.3, where increasing relative roughness leads to a further increase in drag coefficient by increasing the cylinder diameter. For the decrease in inertia, (Sumer and Fredsoe, 2006) offers no clear explanation besides noting that the mechanism that reduces the hydrodynamic mass occurs more strongly with rough cylinders. In figure 2.9, results are shown from experiments where the influence of relative roughness on inertia coefficients was investigated. For a KC lower than 3, there was no difference found in the inertia coefficient between the smooth and rough cylinders.

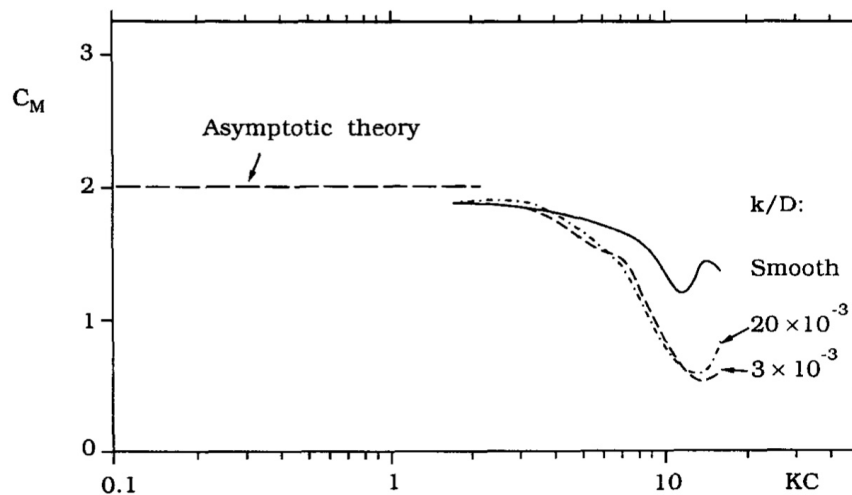


Figure 2.9: Relative roughness height influence on inertia coefficient (Sumer and Fredsoe, 2006)

2.5 Flow and Forces Around Circular Cylinders: Current and Waves

In this thesis, it is assumed that the current velocity and the oscillating velocity are not interacting, and together they compose the total velocity. This changes the horizontal component of the modified Morison equation, equation 2.17, by changing the definition of the total velocity to:

$$U_x = U_c + U_m \sin(\omega t) \quad (2.22)$$

The Reynolds number and the Keulegan-Carpenter number use the definitions as if it were a case with pure oscillatory flow, the Strouhal number changes to the following equation:

$$St = \frac{f_v D}{(U_c + U_m)} \quad (2.23)$$

An important parameter in the case of combined current and waves is the ratio of current velocity to the maximum velocity of the oscillatory flow, U_c/U_m . In figure 2.10, the effect of this ratio on the forces is shown.

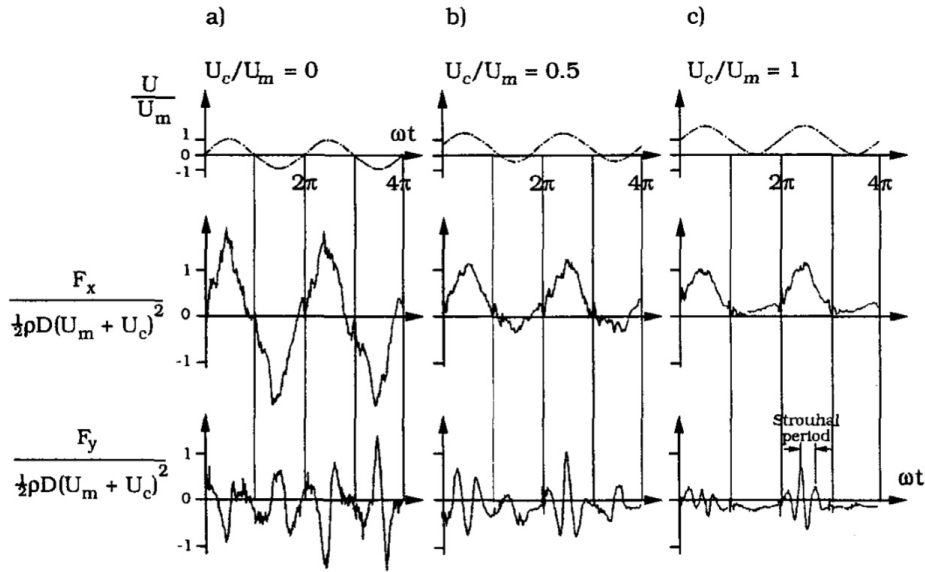


Figure 2.10: Forces for different ratios of U_c/U_m (Sumer and Fredsoe, 2006)

As can be seen in figure 2.10, the addition of a current generally leads to lower force coefficients, and when the ratio of current velocity to the oscillatory flow velocity increases, the coefficients approach the values of a current-only case.

2.6 Shape Influence

The shape of the cylinder can have a large influence on its hydrodynamics. A rectangular shape, for example, has a fixed separation point at the corners and will not be subject to the changes caused by a changing separation angle. This is not the case for circular and more streamlined tunnels where the change in separation angle is a cause for decreasing or increasing mean drag force, lift force, and vortex shedding frequency. A more streamlined tunnel makes it easier for the boundary layer to stay attached to the tunnel, this leads to a downstream shift in separation point. As a result, the tunnel's wake has a smaller width, and this leads to a lower mean drag force and a higher Strouhal number. In the research by (Zou et al., 2020), a new tunnel shape has been proposed. The cross-section of an SFT was optimized using parametric Bézier curves to increase hydrodynamic performance.

2.7 Previous Research on Roughness Effects

In this section, an overview of previous research on the subject of the influence of marine fouling on hydrodynamics is given.

2.7.1 Shipping Fouling

In the marine industry, marine fouling is an important subject. Ship hulls get covered in fouling and increase the resistance of the ship, which in turn increases the fuel consumption of the ship. In this paragraph, a summary of the experiments in several research papers is given along with their relevant conclusions.

Demirel et al. and Uzun et al.

(Demirel et al., 2017) conducted a series of towing tests to predict the added resistance of ship hulls that were covered in barnacles. They tested flat plates that were covered with 3D-printed barnacles with varying heights and coverage percentages. These plates were towed through a tank using a towing carriage and the total resistance was measured. It was found that both a higher roughness height and a higher coverage percentage lead to an increase in frictional resistance. However, it was mainly the roughness height that was important, as a plate with large-sized roughness and 20% coverage leads to a higher resistance than a plate with medium-sized roughness with a 50% coverage.

Using the same set-up, another set of experiments was held by (Uzun et al., 2017). Again, flat plates were covered with 3D printed barnacles but this time the roughness consisted of barnacles with varying roughness height. It was found that a plate covered in a combination of three different barnacle sizes results in almost the same frictional increase as a plate covered with only the largest-sized barnacles present. This led to the conclusion that the influence of the largest-sized barnacle outweighs the presence of the smaller barnacles and will increase the frictional resistance just as much as a plate with only large-sized barnacles.

Song et al.

(Song et al., 2021) studied the influence of the heterogeneity of marine fouling by using the model of a Wigley hull and covering in various roughness conditions. Sand grit was used to create the roughness on various parts of the hull, a fully rough and fully smooth hull was tested, but also hulls where only the aft or only the bow of the hull was roughened. The tests were conducted in a tank with a towing carriage. It was found that when using the same amount of roughness on the bow or on the aft side, the bow side roughness leads to a larger total resistance coefficient. This was the case when a quarter of the hull was covered in roughness as well. Roughness on the front side of a ship hull leads to a larger resistance than roughness on the back side of a ship hull.

2.7.2 Cylinders

The influence of surface roughness on circular cylinders has been extensively researched in the past. In this paragraph, a summary of the experiments in several research papers is given along with their relevant conclusions.

Sun et al.

In the paper by (Sun et al., 2020), a smooth cylinder and four cylinders with hemispherical surface roughness with different roughness heights were tested to investigate the wake characteristics using PIV. The experiment was held in a closed-loop water flume at a Reynolds number of 2520. The Strouhal number was found to decrease with increasing roughness height, as was expected, since the increase in roughness moves the separation points upstream, and thereby moving the vortices away from each other. This results in a drop in vortex-shedding frequency. However, in this experiment, they used the smooth cylinder diameter for all their calculations, including the Strouhal number. When accounting for the increase in diameter and recalculating the Strouhal numbers for each cylinder, there were no significant differences in Strouhal numbers between the different roughness heights.

Marty et al.

In a study by (Marty et al., 2021), the hydrodynamic behavior of a submarine cable was investigated. Realistic mussel roughness designs with different patterns and shapes were applied to horizontal cylinders and exposed to currents, oscillating motions, and a combination of currents and oscillating motions. The oscillating motions were meant to simulate the effect of wave-induced motions on the cylinder. Seven different roughness designs were tested, a smooth cylinder, two partially smooth and partially rough cylinders, two fully homogeneously rough cylinders, and two fully homogeneously rough cylinders.

In this paper a different definition of the relative roughness was used, here they choose to include the dense bottom layer of the mussels in the diameter of the cylinder itself, calling this the equivalent diameter D_{eq} . The roughness height k is defined as the length of the mussels sticking out from the dense bottom layer and the relative roughness formula is the ratio of the roughness height over the equivalent diameter.

One of the conclusions of this paper is that the higher the coverage percentage is, the higher the drag coefficient becomes. Furthermore, there were no significant differences found between the homogeneous and heterogeneous roughness designs, leading to the conclusion that the equivalent diameter is the parameter with the most influence. The drag coefficient can be up to four times higher when comparing the smooth and the rough cylinders. The surface roughness also decreases the vortex-shedding frequency, as expected. When oscillating flow was simulated, there was no significant influence of roughness parameters found for the inertia coefficient, roughness increases the inertia coefficient but this increase did not change between different roughness patterns and shapes.

Zeinoddini et al.

In a study by (Zeinoddini et al., 2016), smooth horizontal cylinders and cylinders covered in pyramid-shaped roughness with a uniform distribution are towed through the water, and the drag and lift forces were measured. In their experiments, the drag and lift forces were lower for the rough cylinders than for the smooth ones. This can be explained by noting that for smooth cylinders the drag crisis occurs at higher Reynolds numbers than for rough cylinders. The Reynolds numbers in this experiment caused the drag crisis to occur for the roughen cylinders, but not for the smooth cylinder, which explains the lower hydrodynamic forces on the rough cylinders.

Theophanatos and Wolfram.

In a study by (Theophanatos and Wolfram, 1989), a set of experiments with 30 PVC cylinders was conducted in a deep tank where the cylinders accelerated upwards through the water due to the buoyancy force, the range of Reynolds numbers was $10^5 < Re < 10^6$. Diameters ranging from 160 mm to 400 mm were used, and various surface roughness designs and distributions were tested. The roughness designs include different coverage percentages, soft and hard roughness, and different methods of modeling the roughness. Hard roughness was modeled using real mussels, gravel, sand, and artificial pyramids.

For fully roughened cylinders, an increase in drag coefficient was found when the relative roughness increased. They also found that the drag coefficients of pyramid-shaped roughness showed a good correlation with the drag coefficients of barnacle-covered cylinders from previous studies. This suggests that modeling realistic roughness as pyramids leads to similar values of the drag coefficient. This is the same conclusion that was drawn from the tests where similar random distributions of partially covered cylinders were tested, one with real mussels and one with gravel. The tested mussel height was 29.5 mm and the tested gravel height was 8 mm. The drag coefficients were quite similar, which suggests that marine growth can be artificially modeled and still provide realistic results, but this also infers that the height of the roughness has little effect on the drag coefficient for these values of relative roughness.

Henry et al.

In a study by (Henry et al., 2016), sand-roughened vertical cylinders were tested to investigate the wake structure in low Reynolds flows in the range of $2.16 * 10^3 < Re < 1.94 * 10^4$, and the effect of fouling on the mean drag force. A circulating water tunnel was used and the flow was visualized by inserting dye into the water and making video records. It was found that an increase in relative roughness leads to an increase in drag coefficient, in a subcritical flow regime, the Strouhal number was again found to decrease with increasing relative roughness. Besides the change in vortex-shedding frequency, it was also found that the medium-sized roughness ($k/D = 0.01 - 0.02$), increases the width of the vortex street. However, when the roughness increased in size ($k/D = 0.07$), the width decreases again.

2.7.3 Knowledge Gaps in Previous Research

When it comes to submerged floating tunnels, there are multiple facets that have not received much attention, and the research for this thesis was conducted in an attempt to fill some of these gaps. One of the main points of interest was the influence of the tunnel shape on its hydrodynamics. Most research focused on horizontal or vertical cylinders, such as cables and pipelines, where the size of the cylinder is much smaller and only the circular shape is used. For an SFT, it is much more relevant to change its shape to reduce hydrodynamic forces in order to lower the necessary strength of the tunnel itself and its foundations. In the research for this thesis, the influence of the tunnel shape is investigated by modeling the parametric tunnel shape as devised by (Zou et al., 2020).

The effect of a combination of waves and currents is not often studied when it comes to cylinders, and when it is studied, the waves are simulated in most studies by moving the cylinder in an oscillating motion. This method has some drawbacks, as explained in (Sumer and Fredsoe, 2006), since the Froude-Krylov force is not present when moving the tunnel through still water. In paragraph 2.4.1, it was explained that this force is generated by a pressure gradient that comes from the acceleration of the fluid in the outer-flow region. This acceleration is missing when moving the tunnel itself through still water and thus missing an additional force on the tunnel. By generating actual waves, reality is more accurately simulated and the results are closer to the real-world results.

The definition of the cylinder diameter that is used varies between studies, some use the smooth diameter, some use the full diameter that includes the full roughness height, and in papers such as (Marty et al., 2021), an equivalent diameter that lies between the smooth and rough definitions is used. It is unknown what the correct definition is, but using the smooth or rough dimensions seems like an under- or overestimation. Therefore, in this thesis an equivalent diameter is defined based on the blockage area of the tunnel including the surface roughness; a more detailed explanation of this definition is given in the next chapter. In figure 2.11, the three diameter definitions are visualized.

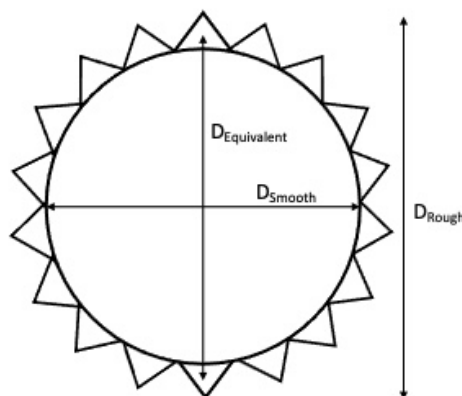


Figure 2.11: Different definitions of the cylinder diameter

Chapter 3

Methodology

In this chapter, the set-up of the experiments that were conducted in the Fluid Mechanics Lab at the Delft University of Technology is described, along with the measuring methods and the data analysis methods.

3.1 Set-Up

Based on the considerations described above, a number of parameters need to be varied in order to characterize the forces on the tunnel. By varying the tunnel shape, roughness height, and roughness density, six tunnels with different shapes and roughness patterns need to be tested in a laboratory flume. In this paragraph, the characteristics and set-up of the flume and the design, characteristics, and set-up of the models are discussed.

3.1.1 Flume

The laboratory flume used for the experiments has a length of 40 m, a width of 0.795 m, and a maximum water depth of 1 m, and the scale of the experiments is 1:50. During the tests, a constant water level of 0.70 m was applied to make sure there is no spillage. Waves are generated by a wave generator combined with an Automatic Reflection Compensation (ARC) function. At the opposite side of the flume, a passive wave absorber is placed inside the flume for tests considering waves. The current is generated by pumping water from the basement water basin into the flume in front of the wave generator. On the other side, a plate is placed to create a weir that assures the correct water level, and an outlet is opened on this side to make sure that the water can flow out. The flume set-ups for both wave tests and current and combined tests can be seen in figure 3.1.

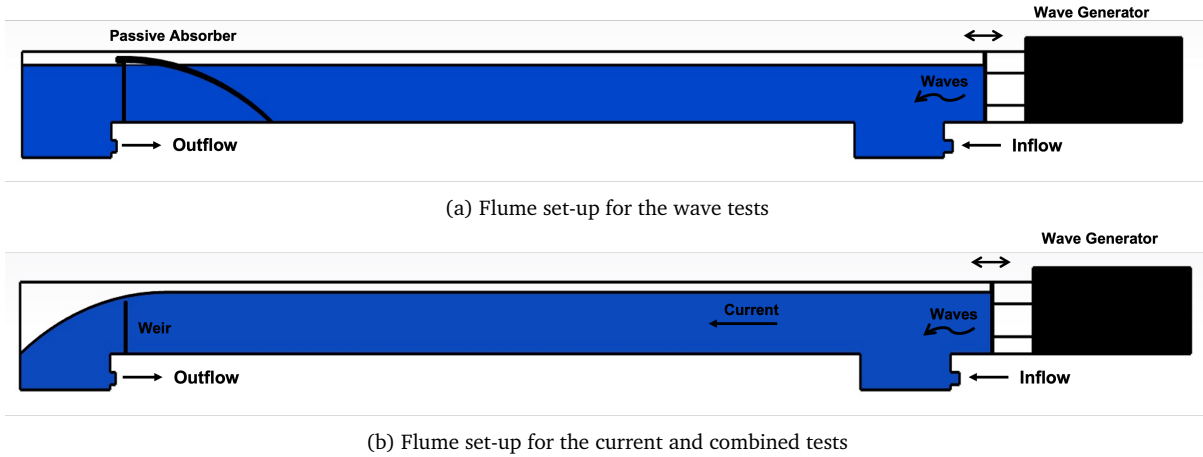


Figure 3.1: Sketches of the different flume set-ups

3.1.2 Model Design

Roughness Design

The difficulty of modeling marine fouling on a structure is very high, due to a large number of uncertainties in the biological processes involved. Both (Ameryoun et al., 2019) and (Schoefs and Ameryoun, 2013) have attempted to model marine fouling accurately, using probabilistic modeling. This would lead to a different research topic and therefore, this will not be attempted in this thesis and simpler roughness designs are adopted. It has been chosen to model the fouling with uniform pyramid-shaped roughness in a staggered arrangement; the pyramids are placed in a staggered manner to prevent sheltering effects. When using a random distribution of the roughness, it represents a single unique case and the hydrodynamic forces are dependent on that specific distribution. In order to reach more general conclusions about the influence of the size and the density of the roughness, a uniform distribution is preferred. As for the pyramid shape, in a paper by (Zeinoddini et al., 2016), it is found that pyramid-shaped roughness gives the least set-up dependent results.

The influence of two roughness parameters is investigated, the roughness height and the roughness density. To test the influence of roughness height, two different roughness heights are chosen, 15 mm and 5 mm. These heights are exaggerated and therefore not to scale, this is done to guarantee significant differences in results between the two roughness heights. The influence of roughness density is tested by having two different coverage percentages, a roughness with 100% coverage and one with 50% coverage.

Tunnel Design

The vertical clearance of the parametric-shaped tunnel and the circular tunnel is kept the same as the vertical clearance used in the experiments conducted by (Drost, 2019), which was 0.16 m. The width of the circular tunnel is 0.16 m as well, and the width of the parametric tunnel is 0.3202 m, calculated using the formula from (Zou et al., 2020). The length of the tunnel is 0.79 m, slightly smaller than the flume width so the tunnel will not touch the side walls. This leads to the prototype dimensions presented in table 3.1

	Experiment	Prototype
Height [m]	0.16	8
Width [m]	0.32	16
Length [m]	0.79	39.5

(a) Parametric tunnel

	Experiment	Prototype
Height [m]	0.16	8
Width [m]	0.16	8
Length [m]	0.79	39.5

(b) Circular tunnel

Table 3.1: Experiment and prototype dimensions of the tunnels

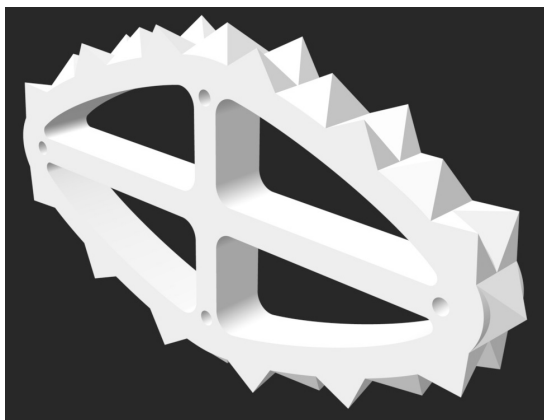
The roughness increases the horizontal and vertical diameter of the rough tunnel. However, there is no clear method of translating roughness height into diameter increase. There are multiple diameter definitions used in literature, the diameter of the smooth tunnel is used, the full roughness height plus the smooth diameter is used, or an equivalent diameter that is in between the two previous options is determined. An example of this is the research by (Marty et al., 2021), as explained in paragraph 2.7.

In this thesis, an equivalent diameter is determined based on the blockage area encountered by the water. The tunnels were designed so that there is a pyramid present on the top and on the sides of the tunnel, as seen in figure 3.2a. Viewed from the side, the pyramid is seen as a triangle. These triangles cover the same area as a rectangular block of half the roughness height. The equivalent diameter is therefore calculated using formula 3.1, as this diameter matches the smooth diameter plus two times the height of the rectangular block that is equivalent in area to the triangular area of the pyramid. The actual roughness height k was determined by measuring the difference between the smooth diameter of the tunnel and the total diameter including roughness. The equivalent diameter of each tunnel is used in all the results that are presented in later chapters.

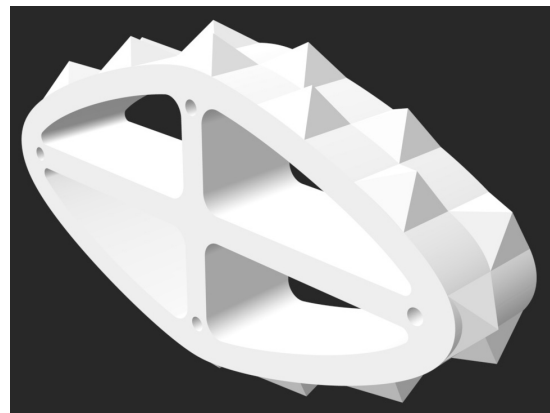
$$D_{eq} = D_{smooth} + 2 \cdot 0.5 \cdot k \quad (3.1)$$

Tunnel Fabrication

All tunnels were produced in the same manner where a 3D printer was used to create a small slice of each tunnel. This slice contains the tunnel's specific roughness pattern and from this slice, a silicon mold was made. The mold was filled with epoxy and this process was repeated several times. When all the slices have hardened, they were combined into two halves of a single tunnel. In figure 3.2, an impression of a slice of two of the tunnel designs can be seen; the four small holes in the slices were used to connect the tunnels using screw threads.



(a) Slice of the parametric tunnel with large roughness



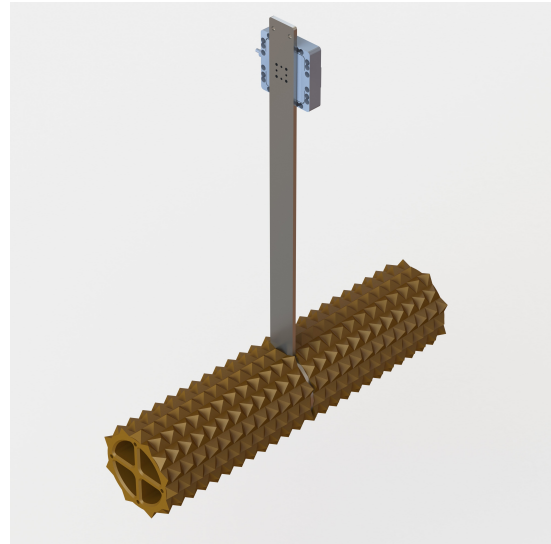
(b) Slice of the parametric 50% coverage tunnel

Figure 3.2: Design of two of the tunnel slices

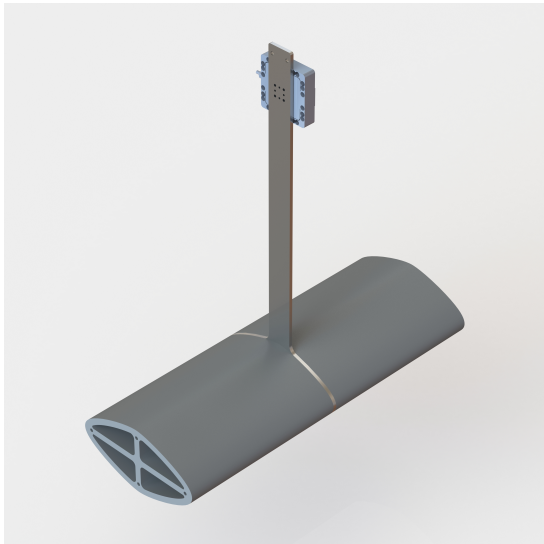
At first, the slices were glued together with an epoxy-chalk mixture. For the smooth tunnels, this method worked fine, although the water-tightness of the tunnel needed more attention. For the rough tunnels, however, the epoxy-chalk mixture spilled out too much and couldn't be sanded away due to the roughness. Silicon sealant was used to combine the slices, and the two halves of the tunnel were then filled with polyurethane foam to make them water-tight. The two tunnel halves are then connected to each other using the four screw threads. In between the two halves sits the metal suspension and two rubber gaskets. In figure 3.3, all six tunnel designs are shown, along with their suspension and the load cell.



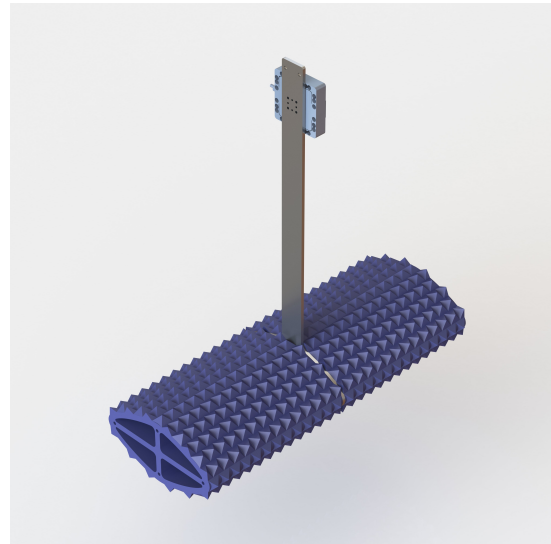
(a) Circular smooth tunnel (CS)



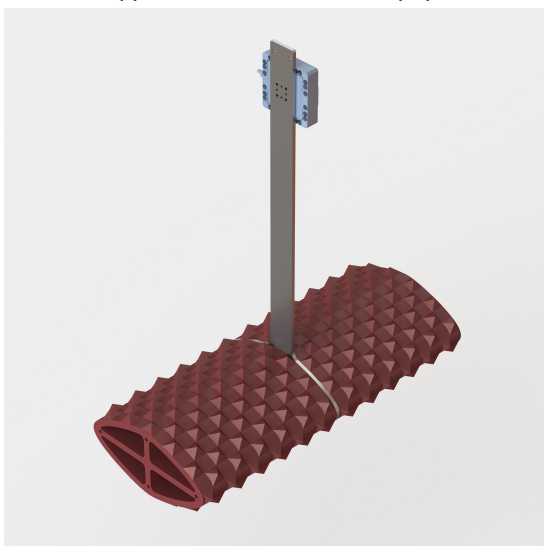
(b) Circular rough tunnel (CR)



(c) Parametric smooth tunnel (PS)



(d) Parametric Rough tunnel (PR)



(e) Parametric rough 50% tunnel (P50)



(f) Parametric rough small tunnel (PRS)

Figure 3.3: All tunnel designs including suspension and load cell

Tunnel Characteristics

Since the tunnels are all handmade, there are some small deviations in size and length, in table 3.2, the actual characteristics of each tunnel can be found. In this table, it can be seen that the calculated roughness height does not agree with the desired 15 and 5 centimeters, the same can be said for the smooth diameters of the tunnel. There are two reasons for this, the first is that there was some unexpected shrinkage of the epoxy. When the epoxy was poured into the mold and left to harden, it came out about a percent smaller than expected. For the circular smooth tunnel it was even larger because during the sanding of the tunnel, a small part of the tunnel was sanded away to make it more smooth.

The second reason concerns only the roughness height. The tunnel has a curvature, and to maintain the shape of the tunnel, it was decided to let the pyramids sink into the tunnel instead of putting them on top of the tunnel and filling out the spaces below. This means that for the circular tunnel, the roughness height is equally smaller for all pyramids due to the constant curvature of the tunnel. For the parametric tunnel, the roughness height on top is decreased less than the roughness height at the sides, since the curvature at the sides is much larger so the pyramids sink in more.

	Code	Length [m]	$D_{smooth,z}$ [m]	k_z [m]	$D_{smooth,x}$ [m]	k_x [m]
Circular Smooth	CS	0.783	0.156	0	0.156	0
Circular Rough	CR	0.778	0.157	0.014	0.157	0.014
Parametric Smooth	PS	0.784	0.158	0	0.315	0
Parametric Rough 50%	P50	0.785	0.158	0.014	0.315	0.010
Parametric Rough	PR	0.775	0.158	0.014	0.315	0.010
Parametric Rough Small	PRS	0.783	0.158	0.005	0.315	0.003

Table 3.2: Tunnel Characteristics

The values shown in table 3.2 lead to a surface area of the tunnel cross-section that is about 5% lower than the surface area of the design tunnel without shrinkage. In the calculations of the force coefficients, this surface area was required. To account for the shrinkage of the epoxy, 95% of the surface area of the design tunnel is used in the calculations.

3.2 Scope

To investigate the response of the tunnel to varying wavelengths, the wave height was kept constant and four different wave periods were chosen. To investigate the response to varying wave heights, the wave period was kept constant and the wave height was varied between three heights. The values of the wave period and height were chosen similarly to those in the research by (Drost, 2019), for possible comparison purposes. For the combined conditions, the same six wave conditions were combined with a current velocity of 0.2 m/s, and the largest and longest wave was also combined with a 0.3 m/s current. In table 3.3, the code names and the environmental parameters of each test are given.

Test	U [m/s]	H [m]	T [s]
C1	0.1	0	0
C2	0.2	0	0
C3	0.3	0	0
W1	0	0.08	0.92
W2	0	0.08	1.12
W3	0	0.08	1.41
W4	0	0.08	1.84
W5	0	0.12	1.84
W6	0	0.16	1.84
CW1	0.2	0.08	0.92
CW2	0.2	0.08	1.12
CW3	0.2	0.08	1.41
CW4	0.2	0.08	1.84
CW5	0.2	0.12	1.84
CW6	0.2	0.16	1.84
CW7	0.3	0.16	1.84

Table 3.3: Code names of the different tests

3.3 Measurement Techniques

In this paragraph, it is discussed how the experiment data was collected and the set-up of the used instruments is shown. Each current test is repeated six times and each wave and combined test is repeated four times.

3.3.1 Force Measurements

To measure the forces on the tunnel, a 3-axis load cell, type K3D60a, with a capacity of 100N was used. This type was chosen because the expected forces for the current tests with the smallest velocity are close to 1N, and this load cell has an accuracy of 0.5%. A larger capacity would lead to inaccuracies larger than the expected force, which makes the measurements less reliable. The load cell was connected to a steel beam that is clamped to the flume. On the front of the load cell, there is a small plate to which the suspension of the tunnel connects. This makes sure that all the forces acting on the tunnel will only be transferred to the load cell. In figure 3.4, the connection of the suspension to the load cell and the load cell to the flume can be seen.

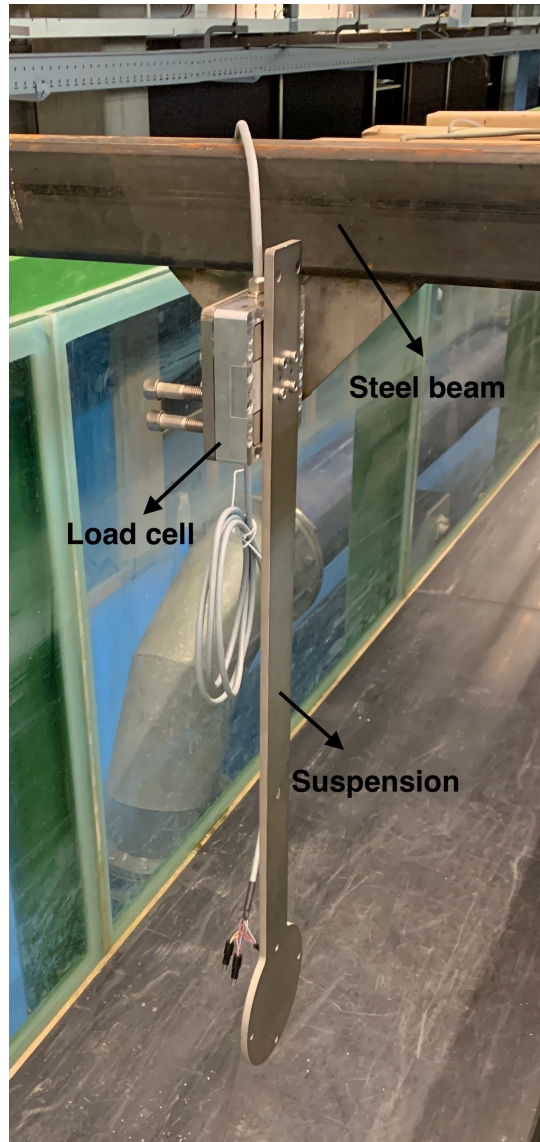


Figure 3.4: Connection of the suspension to the load cell

The small capacity of the load cell did lead to some practical issues because the buoyancy force on the tunnel was larger than the weight of the tunnel and the suspension, so there was a net upwards directed force on the load cell. To stay in the range of the load cell, the buoyancy force combined with the forces on the tunnel due to the current and waves were not allowed to be close to the capacity of the load cell. Therefore, weights were added to the suspension so that the buoyancy-weight ratio of the tunnel was close to 1; this guaranteed that the range of the load sensor was not exceeded. A buoyancy-weight ratio of 1 was achieved by constructing a small container on top of the suspension where weights could be added.

3.3.2 Wave Measurements

Wave gauges are used to measure the wave characteristics, the output of these gauges is in voltage. Before the experiment started, each wave gauge was tested to determine the conversion rate of voltage to centimeters of wave height, this ratio will later be used to convert the voltage measurements. To be able to filter out reflected waves, a certain amount of wave gauges with the proper spacing is necessary. For the reflection of regular waves, two wave gauges on each side of the tunnel are necessary. To separate reflected and incident waves, a method was developed by (Mansard and Funke, 1980) where

three gauges are used along with a least squares method. To separate reflected waves from each end of the flume, three wave gauges on each side of the tunnel are needed. The gauge spacing does not influence the separation unless a critical spacing combination is used. A distance of 0.3 m between the first and second wave gauge from the wave generator and 0.4 m between the second and third gauge is advised and does not lead to the critical spacing combination. The distance between the third wave gauge and the tunnel depends on the wavelength; it should be within the range of $0.2L - 0.25L$. In the end, it was decided to conduct multiple shorter tests that stopped before reflected waves reached the tunnel, instead of a longer test where reflected waves needed to be separated. This means that the wave gauges could be kept in one position, in figure 3.5 the used set-up is shown.

3.3.3 Velocity Measurements

In the thesis by (Drost, 2019), it was mentioned that the velocity should be measured at tunnel depth. This makes depth shift calculations for the velocity unnecessary and allows for the measured horizontal orbital velocities to be used in the Morison equation. Three electromagnetic liquid velocity meters, EMS, are used for the flow velocity measurements, and the type of EMS used is the E30 probe. Two EMS were located at the height of the tunnel, and one was located 15 cm higher. They were placed far enough behind the inlet to ensure a fully developed flow, and far enough in front of the tunnel to avoid influencing the flow at the tunnel. For the calculations, the mean of the two EMS located at tunnel depth is used, and the third EMS can be used to check the uniformity of the current over the water depth.

3.3.4 Boundary Layer and Wake

Two cameras, a Canon EOS 550 and a Nikon D3200, were used to capture video recordings of dye injection at the upstream stagnation point of the tunnel. One was used to capture the wake of the tunnel and one to capture the separation point of the upper half of the tunnel. These images could be analyzed to explain or verify the found results.

3.3.5 Instrument Set-Up

All instruments are located in the center of the flume, at depths that were specified in the paragraphs above. In figure 3.5, the complete set-up of the flume is shown for all tests.

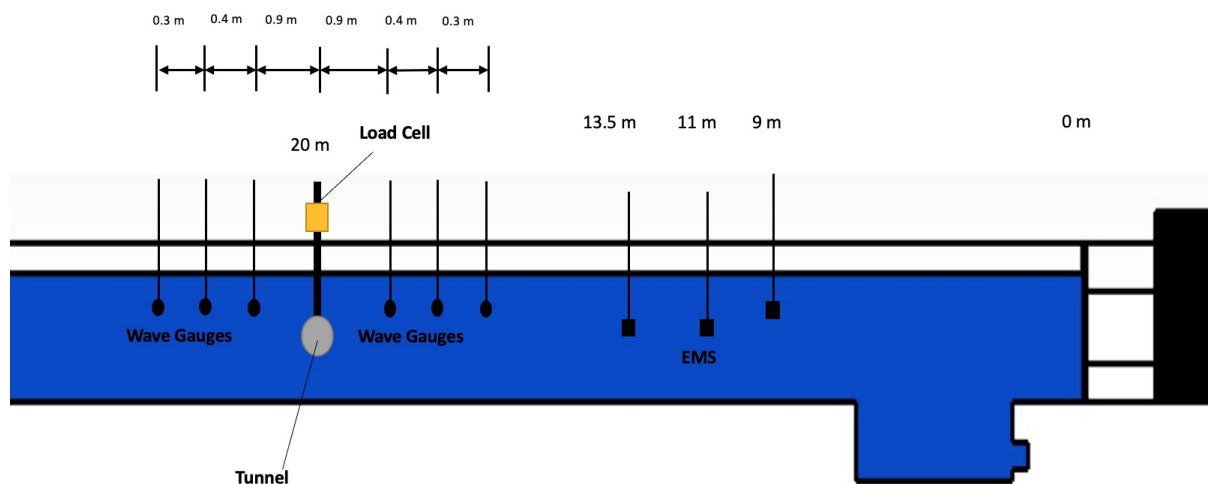


Figure 3.5: Set-up of the instruments used in the experiments

3.4 Data Analysis

In this paragraph, the general data processing and data filtering is described, and the processing and the derivation of each separate signal is explained.

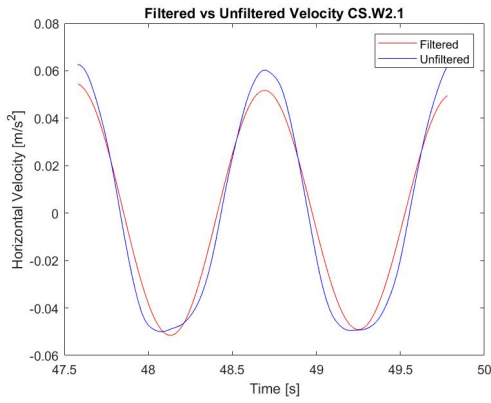
3.4.1 General Processing and Filtering

For the first tests with the circular smooth tunnel, the sampling frequency of the wave height, the force, and the velocity measurements, was set at 50 Hz. After analyzing the results of these tests it was found that this was too low and for the rest of the tests, the sampling frequency was set at 200 Hz with a block size of two. A higher frequency or a smaller block size was not chosen because this led to time delays in the DasyLab program.

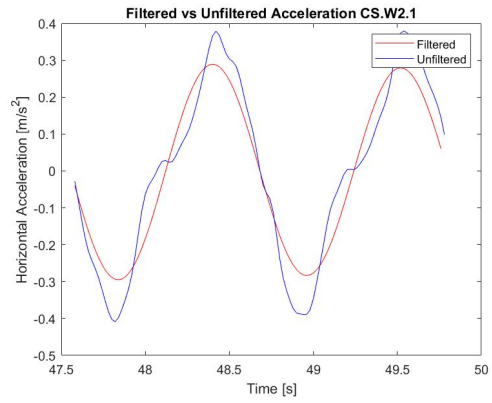
The measured voltage records were converted in DasyLab through conversion formulas, for the EMS this was given by Deltares, and for the load cell and the wave gauges the calibration had to be determined experimentally; the results of this calibration can be seen in Appendix B. The raw and converted data records were stored in separate ASC-files. A Matlab script was written that loads the data from each instrument separately and a low-pass filter was used to filter out frequencies below a specified range.

All the signals were de-noised by applying the low-pass filter, where the filter ranges were determined by analyzing the amplitude spectra of the signals during testing and at rest. The peaks in the amplitude spectra at rest were deemed noise from the lab area and were filtered out. The peaks in the amplitude spectra that only occurred during testing were all put within the range of the filter, except for the frequencies higher than 15Hz, these frequencies could not be attributed to higher harmonics of the investigated processes, so they were filtered out.

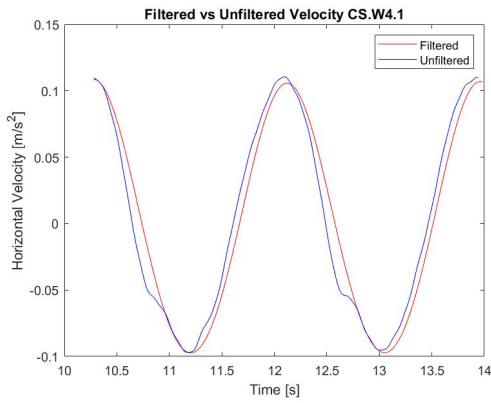
A possible issue with filtering is that there could be a phase shift between the filtered and unfiltered signal. In the figures below it can be seen that there is not much of a phase shift, the small shift that occurs comes from the exact locations of the peaks, the unfiltered signals had some of their peaks one or two data points earlier so the signal had to be cut to make the lengths matching. The main differences between the signals are the amplitude of the signal and the filtered signal becoming more smooth, this is due to the higher frequency phenomena like turbulence being filtered out.



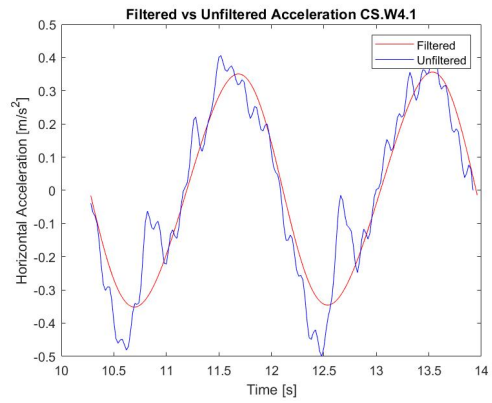
(a) Filtered vs Unfiltered Velocity Signal CS.W2



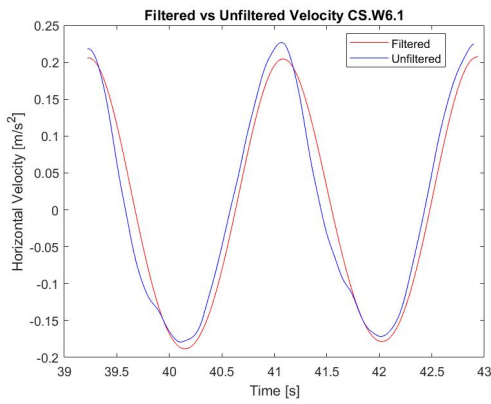
(b) Filtered vs Unfiltered Acceleration Signal CS.W2



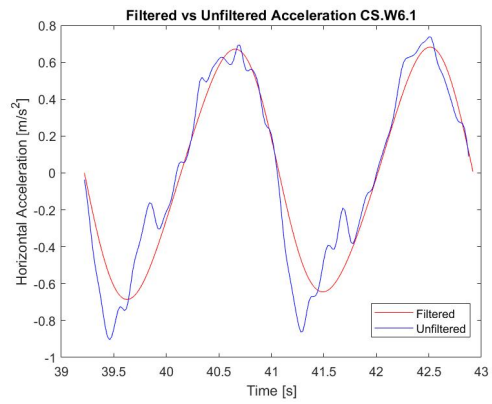
(c) Filtered vs Unfiltered Velocity Signal CS.W4



(d) Filtered vs Unfiltered Acceleration Signal CS.W4



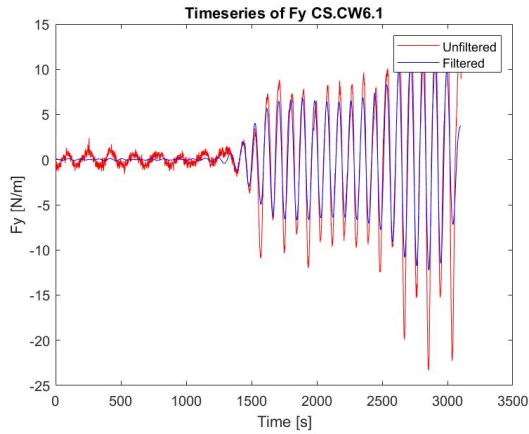
(e) Filtered vs Unfiltered Velocity Signal CS.W6



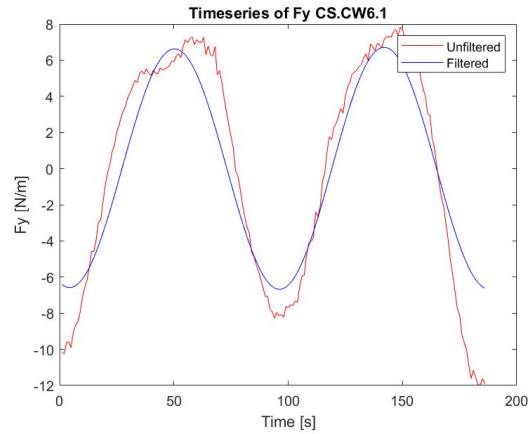
(f) Filtered vs Unfiltered Acceleration Signal CS.W6

Figure 3.6: Filtered vs Unfiltered Velocity and Acceleration Signals

One special case was the vertical force in the combined tests, where there is a lift force present from the vortex shedding, and a vertical drag and inertia force from the waves. To calculate the vertical drag and inertia coefficients, the lift force must be filtered out. Therefore, a very narrow filter range is used to only include the wave frequency. To check whether this had other unwanted effects, the unfiltered and filtered force signals were plotted together; these signals are shown in figure 3.7. The oscillating lift force clearly shows in the first part of the unfiltered signal where only a current is present, unlike the filtered signal where it has been filtered out. The filtering leads to a reduction in amplitude but not to significant phase shifts, so the procedure is acceptable.



(a) Total unfiltered vs filtered signal

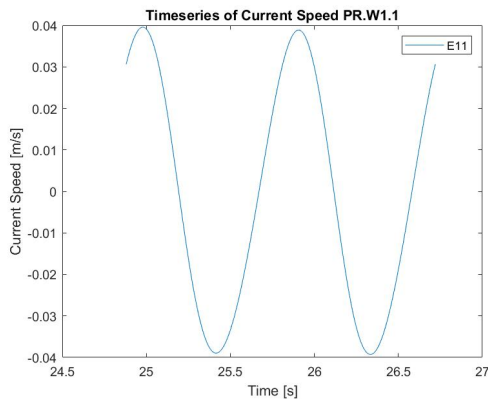


(b) Unfiltered vs filtered signal of the used waves

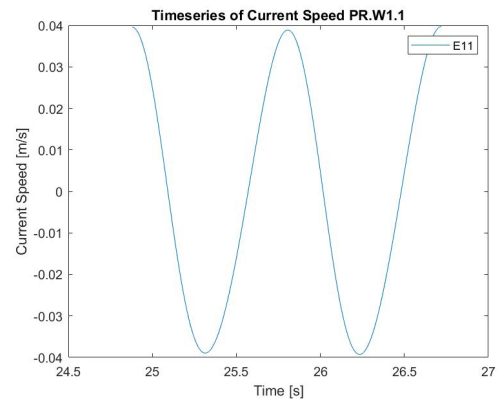
Figure 3.7: Unfiltered vs filtered vertical force signals for the combined tests

3.4.2 Wave Signals

Two full waves that are similar in height are selected from the wave gauge signal, and the corresponding waves from the velocity signal are then determined. There is a time shift between the two signals due to their difference in location, and this was accounted for by using the wave celerity and the distance between the EMS and the tunnel. The wave celerity was calculated by dividing the distance between two wave gauges, by the time it takes a wave to travel between the two gauges. Shifting the velocity signal by using the wave celerity gave incorrect results, as the maximum horizontal orbital velocity should be at the same location as the peak of the wave. This error comes from the small inaccuracies in determining the wave celerity and the large distance between the EMS and the wave gauge, a small error in celerity leads to a significant time shift between the signals. To solve this, the corresponding waves in the velocity signal are manually shifted to the location of the wave gauge to make sure the maximum velocity occurs at the peak of the wave. In figure 3.8, the celerity shifted and manually shifted EMS signals are compared. Here it can be seen that using the wave celerity for the time shift does not result in a signal that starts at its peak, and using the manual shift does.



(a) EMS signal shifted with the wave celerity



(b) Manually shifted EMS signal

Figure 3.8: Results of a theoretically shifted and a manually shifted EMS signal

For the force signal, this was not possible, as there is no such relationship between the force and the wave signal. Therefore, the force signal was shifted in time by using the calculated wave celerity and the distance between the tunnel and the wave gauge, this is possible because this distance is much smaller. It should be noted that there can still be an error in the time shift between the force signals and the velocity

signals. To assess the error of this time shift, a sensitivity analysis was conducted where the time shift was increased and decreased by 6% and the results are used as the positive and negative values in the error bars that are included in the results. The value of 6% represents the possible errors in the distance between the wave gauges, the distance between the wave gauge and the tunnel, and the accuracy of the time measurements.

Especially for the drag coefficients and for the inertia coefficients at the lower KC values, the time shift is assumed to be the main source of inaccuracies. At a low KC value, the force is highly inertia dominated and the drag force only accounts for a small part of the total force. The drag force at low KC values has a large variability and is very unstable, this is also found in the work by (Cook and Simiu, 1989). The inertia coefficients for the larger KC values were much less sensitive to the time shift, for those tests the standard deviation between the separate results is used as a measure for the error bars. These differences in results between the tests could be related to multiple sources of errors, such as measurement errors and differences between the two selected waves and the other waves in the signal, which is mainly an issue with the combined tests. For both the wave tests and the combined tests, the error bars are determined by the procedure described above.

All six wave gauges generate a separate wave signal, the wave signal that is used is from wave gauge G12, which is the gauge closest to the tunnel and the waves reach G12 before they reach the tunnel. From each wave signal, the two selected waves were used to determine the average of the measured wave height and period of the two waves. The wave tests were repeated four times for each tunnel and each of these tests gives a measured wave height and period for that specific test. With the measured wave height and period, the orbital velocities and accelerations were calculated using Stokes' Theory described in paragraph 2.3. These velocities and accelerations were used in the calculations of the force coefficients. For the combined tests, the wave characteristics were determined using the same method. The average wave heights and wave periods for each test can be found in Appendix C.

3.4.3 Velocity Signals

For the current tests, the mean of the two EMS located at tunnel depth is used in the drag coefficient calculations. From analyzing the signals for each test, it followed that both EMS had similar standard deviations and similar mean velocity values, so both signals were used to minimize the possible measurement errors. In figure 3.9 the similarity between the two EMS signals can be seen.

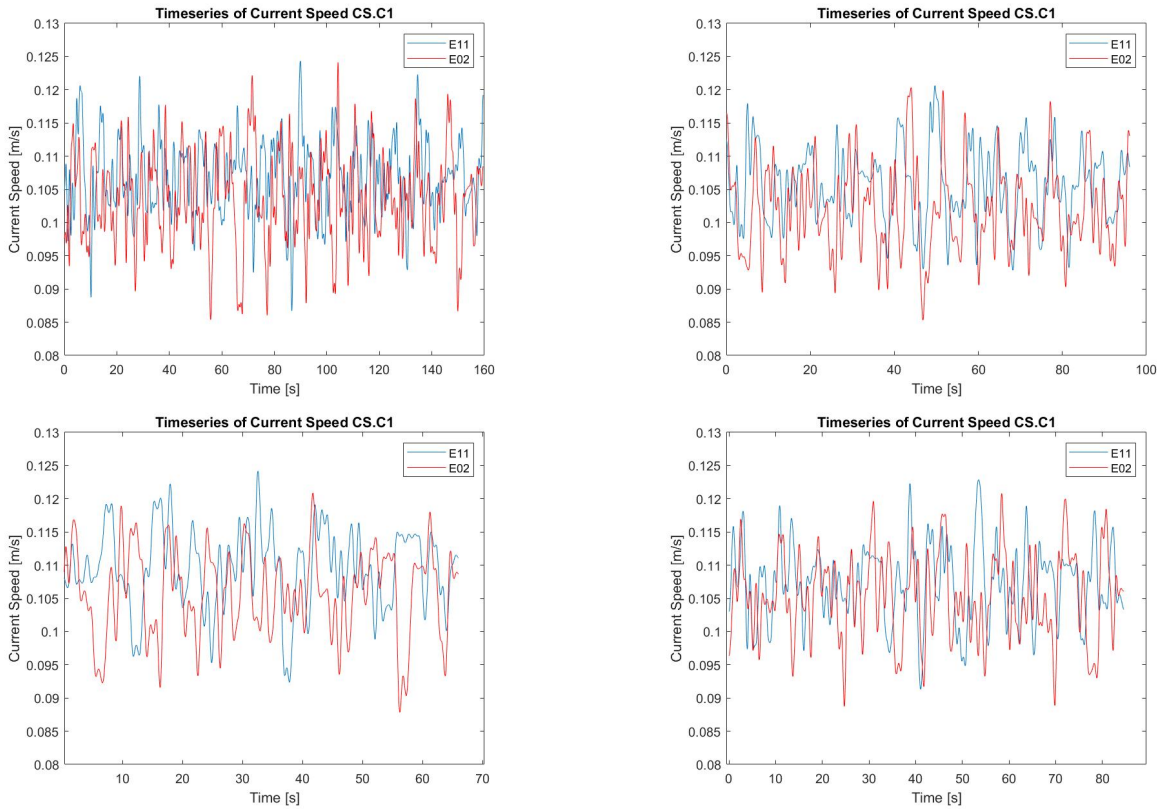


Figure 3.9: Velocity signals of E11 and E02 for different current tests

For the wave tests, the horizontal orbital velocity was measured by the EMS. From there, the horizontal orbital acceleration can be derived by taking the derivative of the velocity signal. Only the EMS closest to the tunnel was used, since taking the derivative of the average signal of both EMS would lead to incorrect accelerations. Furthermore, the EMS signals needed filtering in order to get an accurate acceleration signal. The derived acceleration signal became chaotic when the velocity signal contained too much noise.

When the signal is unfiltered, a large peak shows in the amplitude spectrum at the wave frequency. Much smaller peaks are present at multiples of the wave frequency; these peaks decrease in power with increasing frequency. For filtering the waves, the frequency range is chosen as such that the first two peaks are included in the signal and the rest are filtered out. The higher frequency peaks only disturb the signal and do not add much in terms of amplitude. In figure 3.10, the results of a filtered signal are shown on the left side and an unfiltered signal on the right side. At the bottom, the amplitude spectra of both signals are shown along with their peak values. When including a few more frequency peaks, the acceleration signal becomes completely distorted and unusable in later calculations. Filtering the velocity signal only decreases the amplitude slightly and does not change the phase of the signal. This leads to the conclusion that filtering the signals using this method is correct.

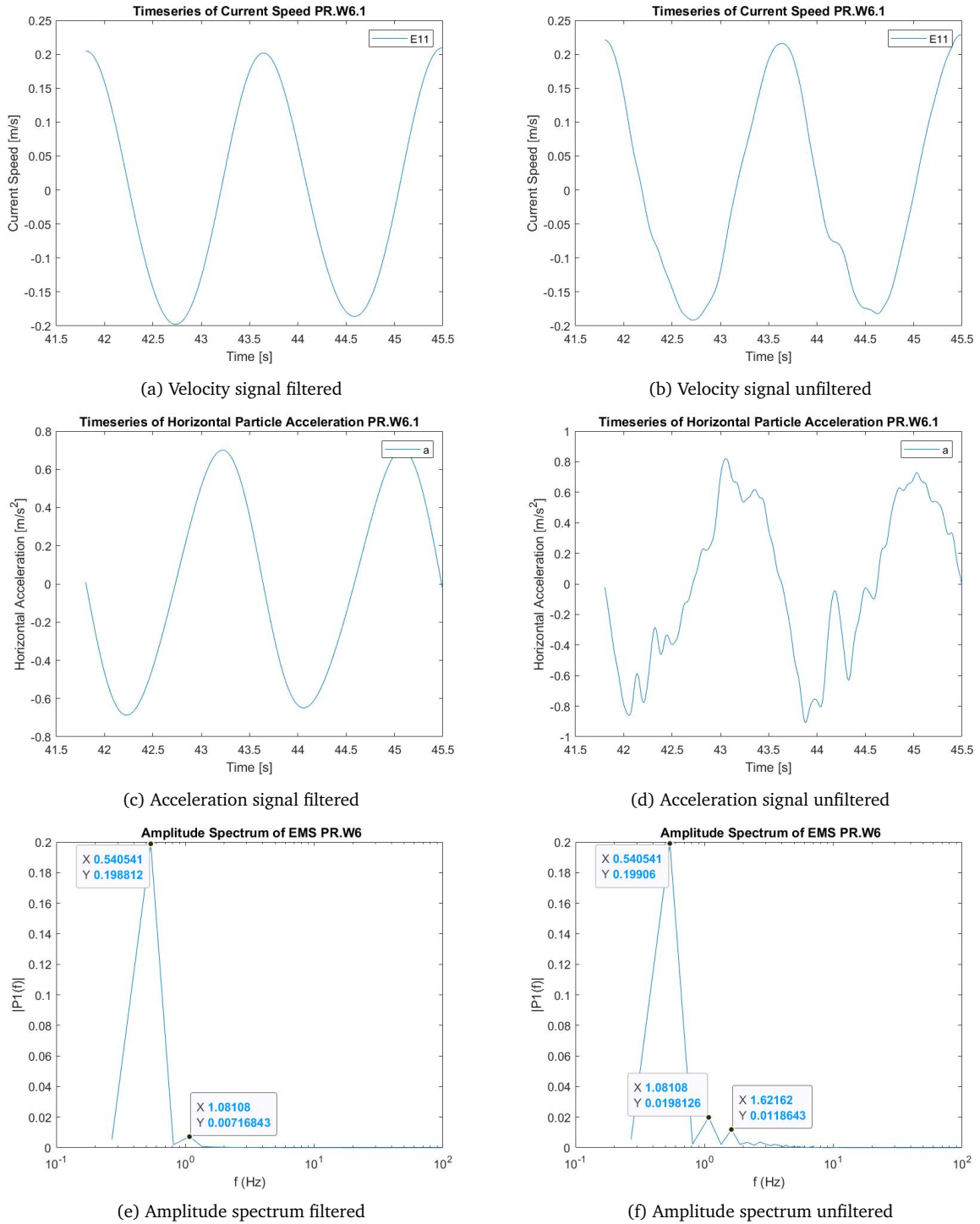
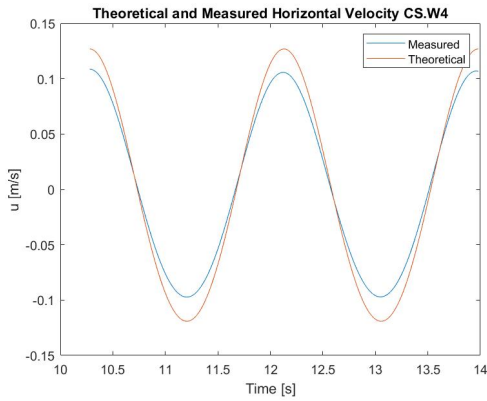
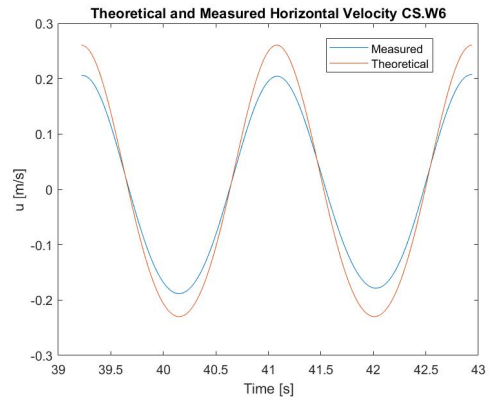


Figure 3.10: Velocity signal, acceleration signal and amplitude spectrum for different filter ranges

The vertical orbital velocity was not measured by the EMS, and to be able to use an accurate approximation in the calculations, the theoretical vertical velocity signal was used. This is expected to give accurate results since the measured horizontal velocity signal looks similar in shape and phase to the theoretical horizontal orbital velocity. The main difference is the amplitude of the signal, which is lower for the measured velocity in every case due to boundary effects from the side walls; two examples can be seen in figure 3.11.



(a) Measured vs Theoretical Horizontal Orbital Velocity CS.W4



(b) Measured vs Theoretical Horizontal Orbital Velocity CS.W6

Figure 3.11: Measured vs Theoretical Horizontal Orbital Velocity

This theoretical vertical orbital velocity signal was scaled with the ratio of the maximum measured horizontal velocity to the maximum theoretical horizontal velocity to account for the fact that the amplitude of the orbital velocity is lower than the expected theoretical amplitude. The vertical orbital acceleration was then determined by taking the derivative of the scaled vertical orbital velocity signal.

For the combined tests, the first part of the signal only contains a current and then the waves were added to the flowing water inside the flume. From this first part, the mean current velocity was determined. The orbital velocity and acceleration determination followed the same procedure as the wave tests, after the mean current velocity was subtracted from the signal. In figure 3.12, a typical combined velocity signal is shown where the first 20 seconds were used to calculate the mean current velocity.

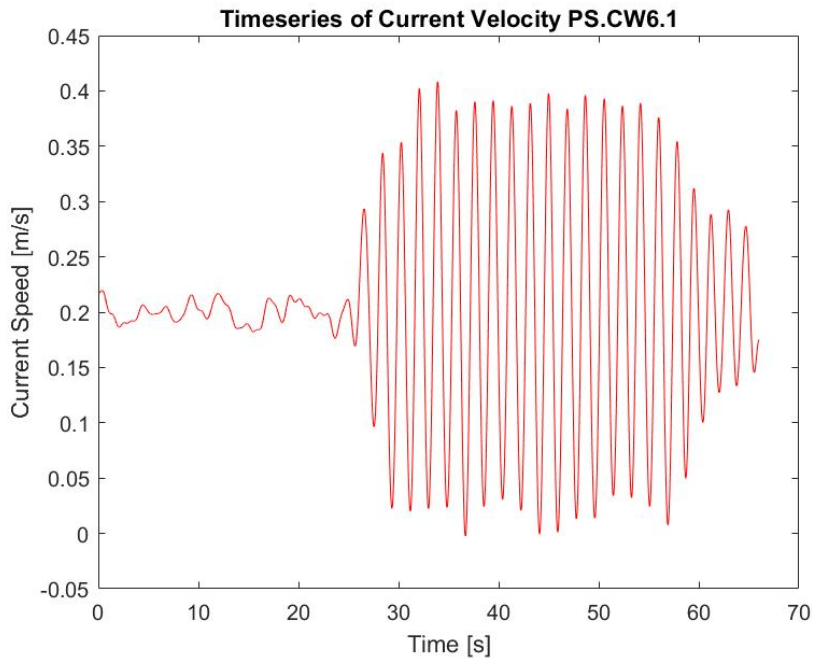


Figure 3.12: Velocity signal of a combined test

3.4.4 Force Coefficients

The drag and lift coefficients for the current tests are calculated using equations 2.6 and 2.9. The velocity is calculated from the mean values of both EMS at tunnel depth. As explained in paragraph 2.4, the drag and inertia coefficients are calculated for the wave tests using the least squares method. However, due to the low KC value in the experiments, the force is highly inertia dominated. This makes the calculations of the drag coefficient very sensitive since the drag force is only a very small part of the total force and a small error in the calculation of the phase difference between the velocity and force signals can lead to large errors. A similar conclusion was reached in the paper from (Mai, 2019). It should be noted that all measured forces are divided by the tunnel length and are of the unit [N/m].

Besides the method of least squares, another method can be used to determine the force coefficients called the Max/Min method. This method was proposed by (Morison et al., 1950) and makes use of the fact that when the orbital velocity is at its maximum, the orbital acceleration must be equal to zero. At this moment, the entire force acting on the tunnel can only contain a drag force component. When the acceleration is at its maximum and the velocity is zero, the force on the tunnel is equal to the inertia force. This leads to equation 3.2 for the drag coefficient and equation 3.3 for the inertia coefficient, where t_1 represents the time where the velocity is at its maximum, and t_2 the time where the acceleration is at its maximum. Both the Max/Min method and the method of least squares are used in this thesis and their results are compared in chapter 6. A general expression for the force coefficients can be obtained by fitting a curve through the found results, these fitted coefficients can be plugged back into the Morison equation to verify whether they give accurate results.

$$C_D = \frac{F_m(t_1)}{\frac{1}{2}\rho D_{eq} |u(t_1)| u(t_1)} \quad (3.2)$$

$$C_M = \frac{F_m(t_2)}{\frac{\pi}{4}\rho D_{eq}^2 a(t_2)} \quad (3.3)$$

Where:

C_D	=	Drag coefficient [-]
C_M	=	Inertia coefficient [-]
F_m	=	Measured force [N/m]
D_{eq}	=	Equivalent diameter [m]
u	=	Fluid velocity [-]
a	=	Fluid acceleration [-]

3.4.5 Vortex-Shedding Frequency

The vortex-shedding frequencies of each test were determined using the amplitude spectra. For the circular smooth tunnel, a clear peak at the same frequency showed in each spectrum. This was reason to believe that an accurate vortex shedding frequency was found for the circular smooth tunnel. For the other tunnels, the amplitude spectra were not as consistent. There are a lot of possible reasons for the different frequencies that showed up in the spectra, such as secondary flow instabilities, distortion of the vortex shedding due to the roughness, and eddy's that are about the size of the tunnel that are present in the water.

The determination of the vortex shedding frequency was dealt with in the following manner. If multiple amplitude spectra showed clear peaks at the same frequency, this was assumed to be the correct vortex shedding frequency, even though one or two spectra showed a different result. If these different results had two peaks around the assumed vortex shedding frequency, then the weighted mean of the two peaks was taken. In some cases, there were two peaks around the assumed vortex shedding frequency, and one slightly lower peak at the assumed frequency, but this peak was exactly in the middle between the larger

peaks. In that case, the assumed frequency was used since the mean of the three peaks would also lead to the same result. If the spectrum differed too much from the assumed vortex shedding frequency, then it was removed from the results.

Because of the uncertainties in determining the correct vortex shedding frequency, it has to be noted that there are possible inaccuracies in the Strouhal number results. Therefore, in Chapter 4, the Strouhal results are shown along with an error bar, where the size of the error bar is an estimation of the size of the error.

3.4.6 Keulegan-Carpenter Number

The difference in horizontal diameter between the circular and the parametric-shaped tunnels needs to be accounted for in the Keulegan-Carpenter numbers, as the KC number relates the stroke of the wave motion to the tunnel diameter. For this thesis, the following horizontal and vertical KC numbers are defined, where the horizontal KC relates the horizontal orbital motion to the horizontal tunnel diameter, and the vertical KC relates the vertical orbital motion to the vertical tunnel diameter.

$$KC_{hor} = \frac{U_{w,hor} \cdot T}{D_{hor}} \quad (3.4)$$

$$KC_{ver} = \frac{U_{w,ver} \cdot T}{D_{ver}} \quad (3.5)$$

Where:

KC_{hor}	=	Horizontal Keulegan-Carpenter number [-]
KC_{ver}	=	Vertical Keulegan-Carpenter number [-]
$U_{w,hor}$	=	Maximum horizontal orbital velocity [m/s]
$U_{w,ver}$	=	Maximum vertical orbital velocity [m/s]
T	=	Wave period [s]
D_{hor}	=	Horizontal tunnel diameter [m]
D_{ver}	=	Vertical tunnel diameter [m]

Chapter 4

Results and Analysis

In this chapter, the results of the laboratory tests are shown and analyzed. The results are divided into three sections, current tests, wave tests, and combined tests.

4.1 Current Tests

In this section, the results of the current tests are covered. First, the observations from the experiment are mentioned, then the experiment results are validated, and then the influence of the roughness parameters and tunnel shape on the drag coefficient is discussed. The lift coefficient and the Strouhal number are discussed separately because the results provided information that did not make sense.

4.1.1 Experiment Observations

Due to the inlet conditions and the high Reynolds number, a turbulent flow is expected. This can be seen in figure 4.1, where a velocity signal of each current case is shown after filtering the signals using a low-pass filter of 10 Hz. The higher the current velocity, the higher the positive and negative velocity fluctuations. The standard deviation of a 0.1 m/s current is 0.0044, of a 0.2 m/s current it is 0.0081 and of a 0.3 m/s current it is 0.0106. However, percentage-wise the standard deviation is around 4% for all current velocities.

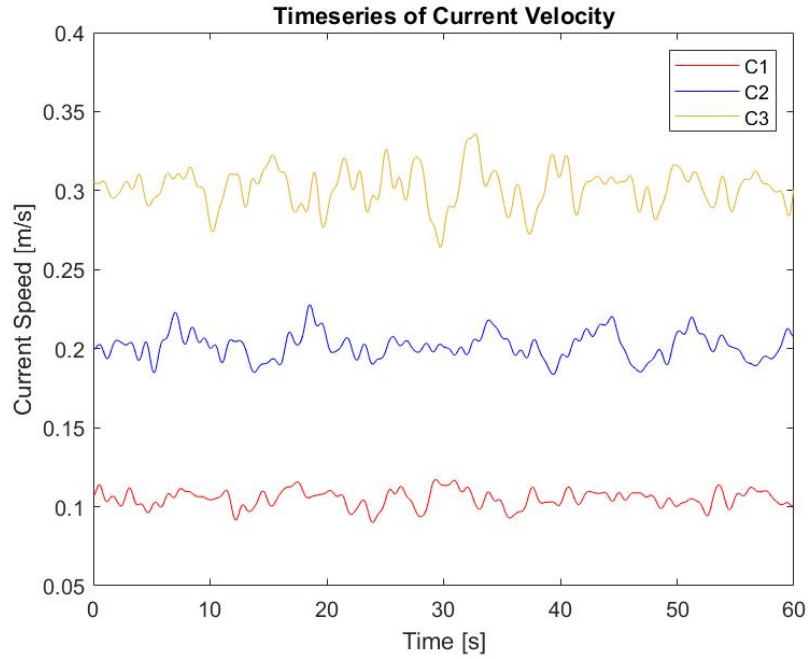
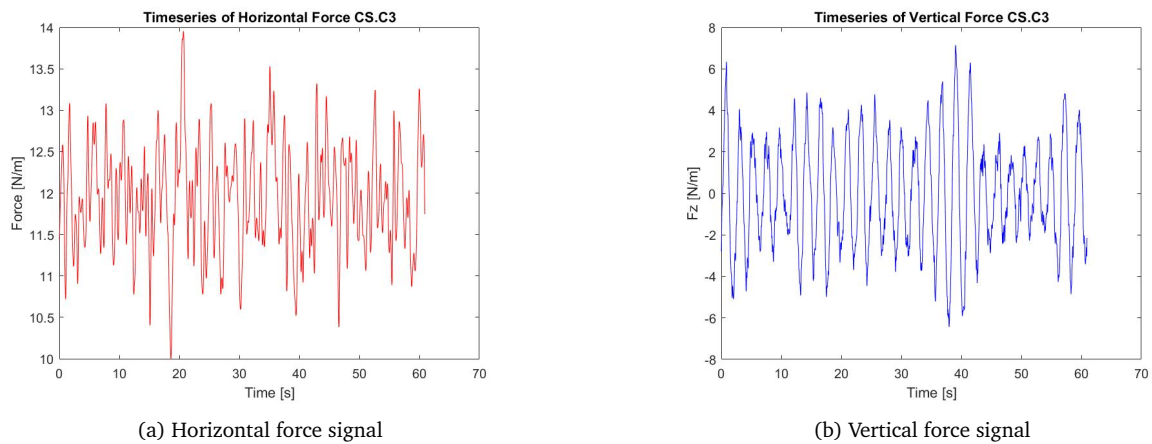


Figure 4.1: Typical EMS signals for the current tests with different velocities

In figure 4.2, the horizontal and vertical force signals of the circular smooth tunnel with a current velocity of 0.3 m/s are shown. The figures show, as expected, a horizontal drag force that has small fluctuations around a mean, and a vertical lift force that oscillates around a zero mean.



(a) Horizontal force signal

(b) Vertical force signal

Figure 4.2: Typical force signals for the current tests

4.1.2 Validation of the Experiment Results

First, the drag coefficient results of the circular smooth tunnel are validated with results from literature to verify that the experiment set-up gives physically realistic results. Afterwards, the rest of the results are discussed. The drag coefficient is calculated using equation 2.6, where the force is the measured horizontal force per unit length and the velocity is the mean of the two EMS signals that are located at tunnel depth.

In figure 4.3, the results of the drag coefficient for the circular smooth tunnel are presented. To check the results and to see if there were no errors in the set-up of the experiment, the load cell was tested.

The load cell test results can be found in Appendix D; there it is shown that the load cell measures the correct force and no force measurement errors occurred. Furthermore, it was found that the EMS has a significant standard deviation, which could lead to errors in the drag coefficient. To show the magnitude of these errors, error bars were added to the drag coefficient graphs. The error magnitude was calculated by using the mean value of the velocity and adding or subtracting the standard deviation of the EMS measurements. This led to maximum and minimum values of the drag coefficient that could reasonably be expected. This resulted in the error bars seen in figure 4.3.

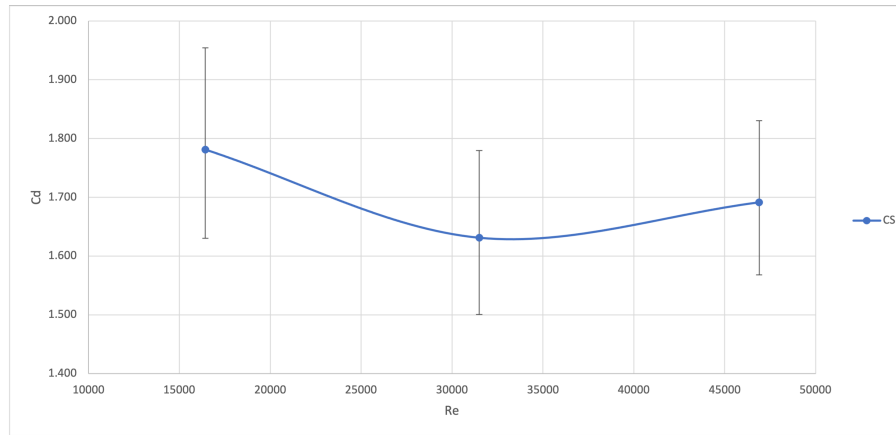


Figure 4.3: Drag coefficient for a circular smooth tunnel in current conditions

The figure shows that the drag coefficients are higher than the values found by (Sumer and Fredsoe, 2006), who found drag coefficients around 1.2 in the investigated range of Reynolds numbers, as shown in figure 2.5. This difference is caused by the large blockage ratio in the experiments conducted for this research, where a high blockage ratio indicates that the vertical diameter of the tunnel combined with its length is large compared to the water depth.

A high blockage ratio influences the flow around the tunnel by increasing the flow velocity, which has a significant influence on the drag coefficient. According to (West and Apelt, 1982), a blockage ratio higher than 6% leads to a distortion of the flow, which could lead to a change in drag coefficient. Therefore, the drag coefficient needs to be corrected since the blockage ratio in these experiments is larger than 20%. In the paper by (Roshko, 1960), equation 4.1 is the used formula that corrects the measured values of C_d by using the blockage ratio of the tunnel. This method is said to be most accurate for regions where the drag coefficient is not highly Reynolds dependent, which is the case for the circular smooth tunnel with a Reynolds number between 16000 and 48000. In figure 4.4, the values of the corrected drag coefficient are presented. The corrected values match the drag coefficients from figure 2.5 by (Sumer and Fredsoe, 2006) quite well, which leads to the conclusion that the set-up of the experiment is providing realistic results.

$$\frac{C_d}{C'_d} = 1 - \frac{1}{2}C'_d \left(\frac{D_{eq}}{h} \right) - 2.5 \left(\frac{D_{eq}}{h} \right)^2 \quad (4.1)$$

Where:

- C_d = Corrected value of the drag coefficient [-]
- C'_d = Measured value of the drag coefficient [-]
- D_{eq} = Equivalent diameter [m]
- h = Water depth [m]

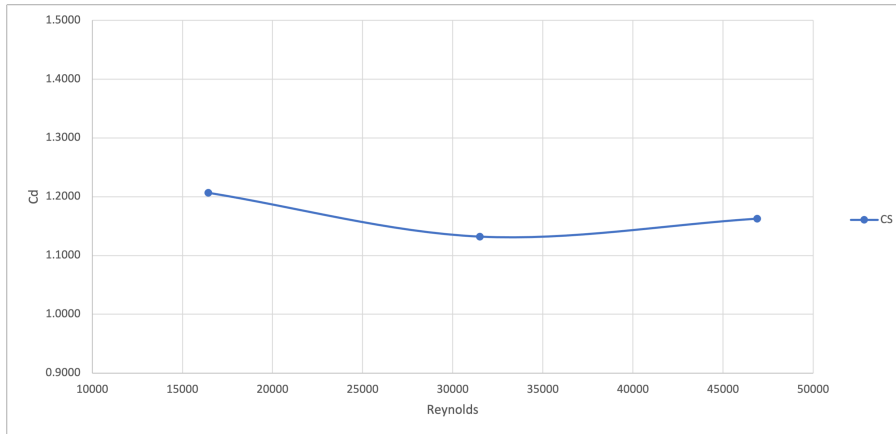


Figure 4.4: Drag coefficients corrected for blockage for the circular smooth tunnel in current conditions

In the following paragraphs, the influence of the current velocity, the tunnel shape, the roughness height, and the coverage percentage on the drag coefficient are presented. The uncorrected drag coefficients are used to analyze the results, since the correction formula is flawed and was determined for a circular cylinder, and it does not include influences of surface roughness. Therefore, all results will be used as they were measured during the tests to make sure the comparisons between the different tests are valid.

4.1.3 Drag Coefficient Results

Influence of the Current Velocity

In figure 4.5, the drag coefficients of each tunnel under different current velocities are shown along with their error bars that were determined in the same manner as described in Chapter 3. Almost all tunnels show a downward slope in their drag coefficient graph for increasing current velocity, except for the parametric smooth tunnel at $Re = 32.000$ and the circular smooth tunnel at $Re = 47.000$. These points differ from the general trend that could be observed for the other tunnels. The possible errors shown with the error bars are one possible explanation for the differences between these points and the general trend.

When taking the size of the error bars into consideration, the downward slope of the graphs for increasing current velocity becomes less clear. According to the theory explained in paragraph 2.2, the drag coefficient remains fairly constant in this range of Reynolds numbers. The reason for the observed downward slope in the graphs is unclear.

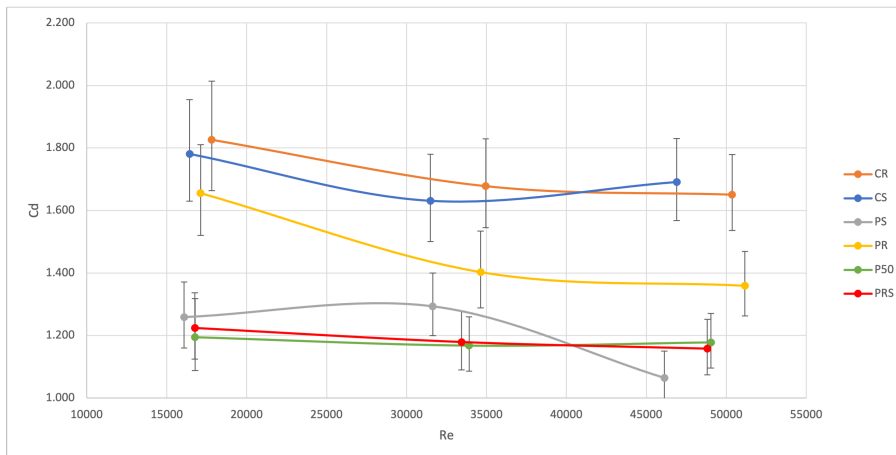


Figure 4.5: Drag coefficient for each velocity in current conditions

Influence of Tunnel Shape

The circular and parametric rough tunnels and the circular and parametric smooth tunnels have equal equivalent diameters. Therefore, the results of these four tunnels are compared to investigate the influence of the tunnel shape. In figure 4.6, the drag coefficients of the four tunnels are shown. This figure shows that both of the parametric-shaped tunnels have lower drag coefficients than the circular ones. The streamlined shape of the parametric-shaped tunnel leads to a lower curvature and the flow can stay attached to the tunnel longer, thus moving the separation point downstream. This in turn decreases the wake width, leading to a smaller pressure gradient and a lower mean drag force, as shown in figure 4.7. The decrease in mean drag force results in a smaller drag coefficient.

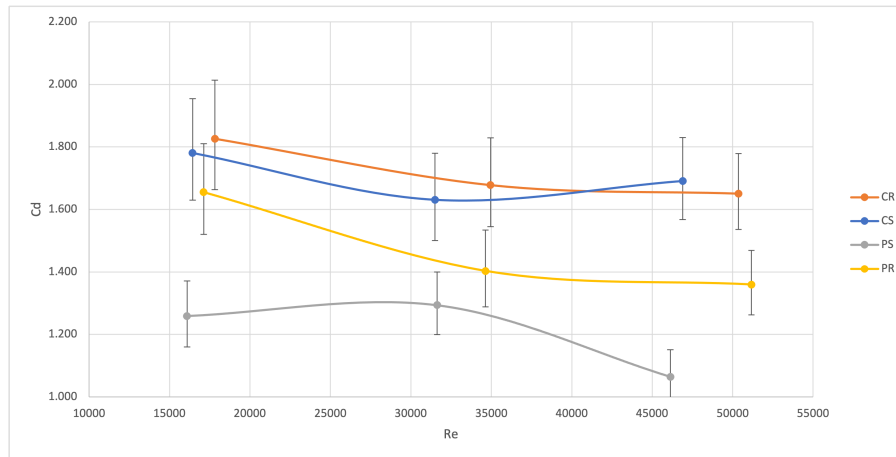


Figure 4.6: Drag coefficient for each tunnel shape in current conditions

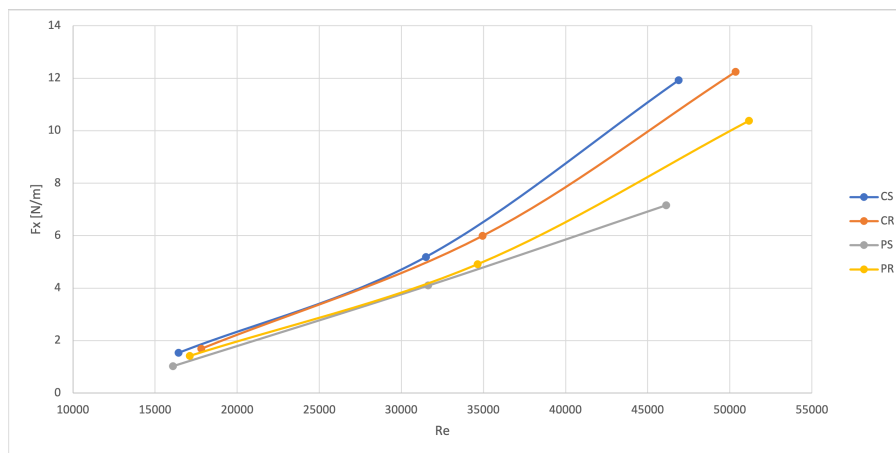


Figure 4.7: Measured horizontal force for varying tunnel shapes in current conditions

The difference between the circular smooth and rough tunnel is smaller than the difference between the parametric smooth and rough tunnel. An explanation for this could be that the larger surface area of the parametric-shaped tunnel includes much more roughness elements, increasing their relative effect compared to their smooth counterpart. The force experienced by the circular smooth tunnel is higher than the force on the circular rough tunnel. This can be attributed to the equivalent diameters used in the Reynolds number calculations, where the larger equivalent diameter of the rough tunnel leads to an increased Reynolds number.

Influence of Roughness Height

The parametric-shaped tunnels with different roughness heights of 15 mm, 5 mm, and 0 mm are compared to investigate the influence of roughness height. In figure 4.8, the results are shown. While a roughness height of 15 mm clearly leads to a higher drag coefficient, the difference between the 5 and 0 mm roughness is much smaller when also looking at the error bars. This does not hold for the parametric smooth tunnel at $Re = 32.000$.

As discussed in paragraph 2.2.3, the presence of surface roughness does not necessarily result in higher drag forces in the tested range of Reynolds numbers. However, the roughness does increase the equivalent diameter of the tunnel, which increases the total blockage area of the tunnel and thus the mean drag force. Also, the sharp tips of the pyramids might cause the flow to separate at a prescribed point which is higher than for a smooth tunnel. This would increase the wake width which leads to a higher pressure gradient and a higher mean drag force.

In figure 4.9, the measured forces on the tunnels with varying roughness heights are shown. There is not much difference in mean drag force between the smooth tunnel and the tunnel with small roughness. This could be explained by noting two things that counteract each other. Firstly, the roughness fixes the separation point at the apex of one of the pyramids and thereby increasing the wake width and the mean drag force. Secondly, the presence of roughness decreases the critical Reynolds number and the flow could be already in the transcritical flow regime, which has a lower mean drag force. These two phenomena could balance each other out and lead to similar drag coefficients as the parametric smooth tunnel.

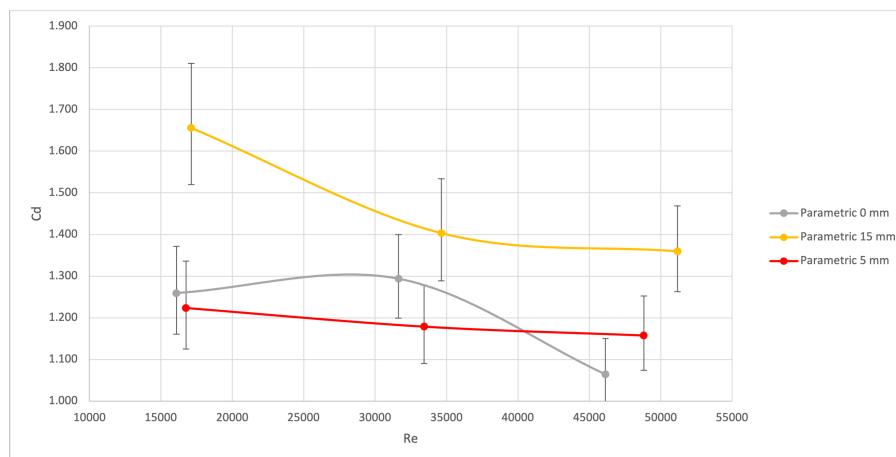


Figure 4.8: Drag coefficient for each roughness height in current conditions

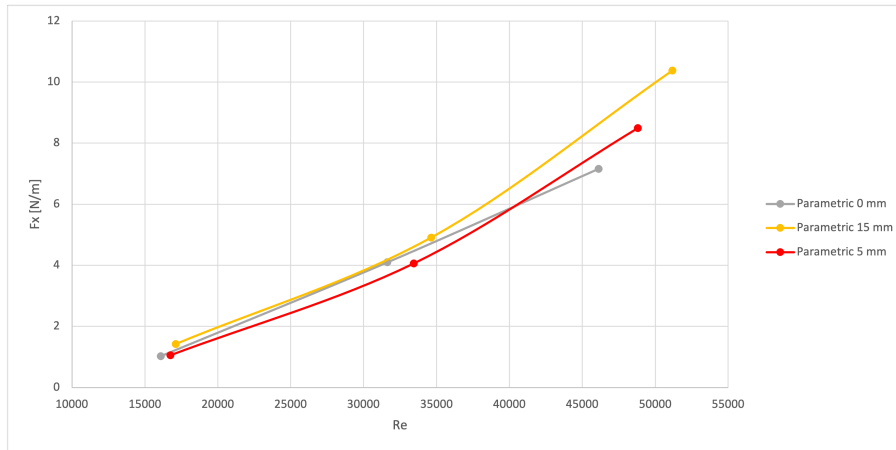


Figure 4.9: Measured horizontal force for varying roughness heights in current conditions

Influence of Coverage Percentage

The parametric-shaped tunnels with the different coverage percentages of 100%, 50%, and 0% are compared to investigate the influence of coverage percentage. In figure 4.10, the results are shown. The tunnel with a 100% coverage ratio has higher drag coefficients than the other two tunnels. However, there is not much difference between the smooth tunnel and the tunnel with a 50% coverage ratio after including the error bars. Again, the parametric smooth point at $Re = 32.000$ is the exception. When looking at the forces in 4.11, there is not much difference between the 0% and 50% coverage tunnels.

The mean drag force on the 50% coverage tunnel was expected to have a higher drag coefficient than the smooth tunnel, caused by its increased equivalent diameter. An explanation for why this is not the case could be the staggered design of the tunnel. As shown in figure 3.2b, in the direction of the flow there is a pathway between the pyramids for the flow to pass through. This makes it easier to circumvent the highest parts of the pyramids, which makes the tunnel act more like the 0% tunnel than the 100% tunnel.

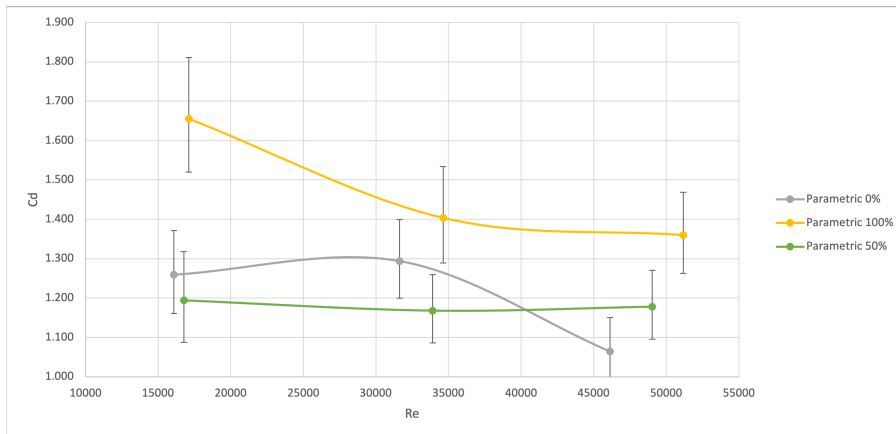


Figure 4.10: Drag coefficient for each coverage percentage in current conditions

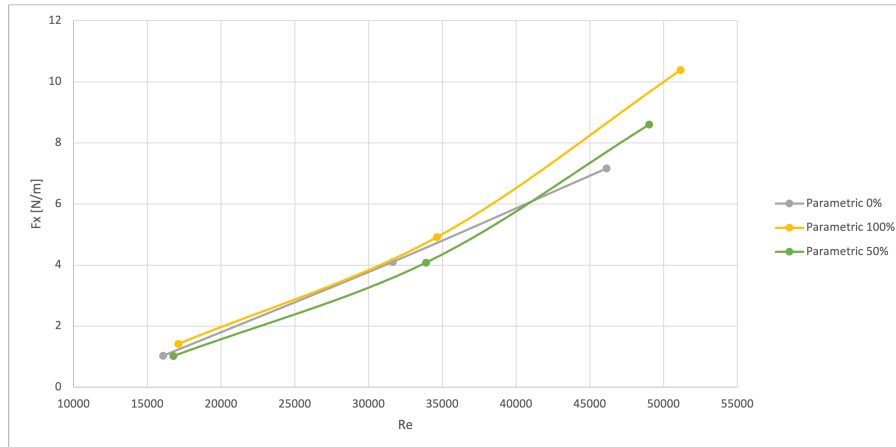


Figure 4.11: Measured horizontal force for varying coverage percentages in current conditions

4.1.4 Lift Coefficient

The lift coefficients of all tunnels are shown in figure 4.12. The expected lift coefficients for a circular smooth tunnel are between 0.4 and 0.7 for these Reynolds ranges, as shown in figure 2.6. The lift forces of the circular smooth tunnel in this experiment are lower but within a reasonable range of the expected values. However, the other tunnels all have much lower lift coefficients averaging around a value of 0.1. The low results can be explained by using the correlation length of the vortex-shedding cells.

In (Sumer and Fredsoe, 2006) it is explained that vortex-shedding takes place in vortex-shedding cells that span along the cylinder. This is not a uniform process and the vortex-shedding cells do not necessarily shed their cells in phase with each other along the span of the tunnel. In the Reynolds range of this experiment, the correlation length of a smooth cylinder is expected to be around 2 to 3 times the tunnel diameter, this means that there can be multiple cells present along the cylinder. Since the cells can be out of phase, the total force per unit length acting on the cylinder can be lower than the force per unit length inside a cell, since vortex-shedding is not happening over the entire length of the cylinder. In this experiment, the total vertical force per unit length on the tunnel is measured, and therefore, the lift coefficients are lower than expected.

The reason the circular rough and all parametric-shaped tunnels have even lower lift coefficients could be that the addition of roughness or the parametric shape distorts the vortex-shedding cells even more. If the vortex-shedding cells are more out of phase with each other along the span of the tunnel, or there are more cells present along the cylinder, the total measured force per unit length will become even lower compared to the force per unit length inside a cell. This is confirmed by figure 4.13, where it can be seen that the vertical force of the circular smooth tunnel shows a much more pronounced vortex-shedding pattern than the other tunnels.

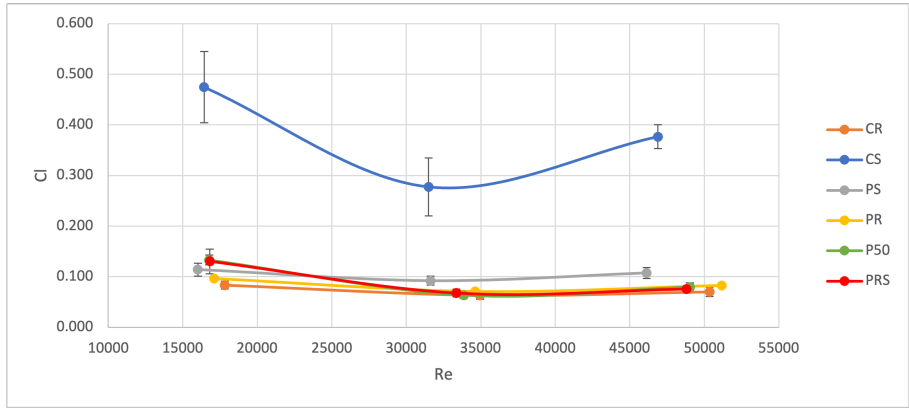


Figure 4.12: Lift coefficient of a circular smooth tunnel in current conditions

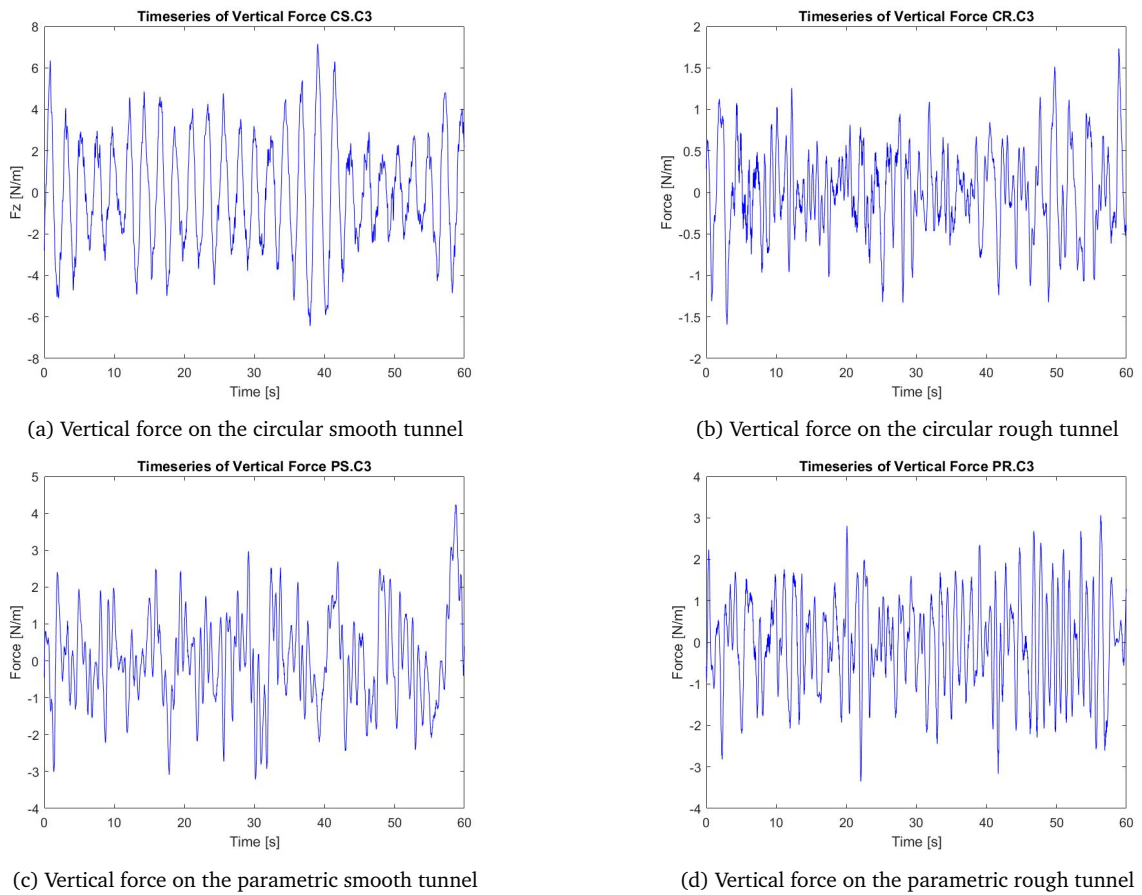


Figure 4.13: Measured vertical forces on the tunnels in current conditions

4.1.5 Strouhal Number

In this section, the Strouhal numbers of the tunnels are discussed. However, the results showed some discrepancies when compared to theoretical knowledge and to results from other studies. First, the results of the smooth tunnels are discussed, followed by a discussion on why the results differ from literature. An extensive analysis of the Strouhal results can be found in Appendix E.

Figure 4.14 shows the Strouhal numbers for both smooth tunnels under different current velocities. The error bars have been added to indicate the uncertainties in determining the correct vortex-shedding frequencies as explained in Chapter 3. In figure 2.3, it can be seen that the theoretical Strouhal number for a circular cylinder is approximately 0.2 for the tested range of Reynolds numbers. The CS results show a Strouhal number of 0.235 - 0.24. This can be explained using the high blockage ratio, where the flow velocities around the tunnel are higher than the measured velocities by the EMS. In the paper by (Roshko, 1960), it is said that the same correction formula that was used for the drag coefficient correction, can be used to correct the Strouhal number. This formula is shown in equation 4.2. Filling in this formula leads to a corrected Strouhal number for the circular smooth tunnel of 0.2 - 0.204.

$$\frac{St}{St'} = 1 - \frac{1}{2}St' \left(\frac{D_{eq}}{h} \right) - 2.5 \left(\frac{D_{eq}}{h} \right)^2 \quad (4.2)$$

Where:

- St = Corrected value of the Strouhal number [-]
- St' = Derived value of the Strouhal number [-]
- D_{eq} = Equivalent diameter [m]
- h = Water depth [m]

The streamlined shape of the parametric-shaped tunnel causes a decreased wake width, this would result in a higher Strouhal number for the parametric-shaped tunnel compared to the circular one. However, the opposite is found in the results. Additionally, adding roughness to a tunnel increases the diameter of the tunnel, and therefore the wake width. This would lower the Strouhal numbers of the rough tunnels, as was similarly found in the papers by (Marty et al., 2021) and (Sun et al., 2020) as mentioned in Chapter 2. Again, the opposite is found to be true in the results shown in Appendix E.

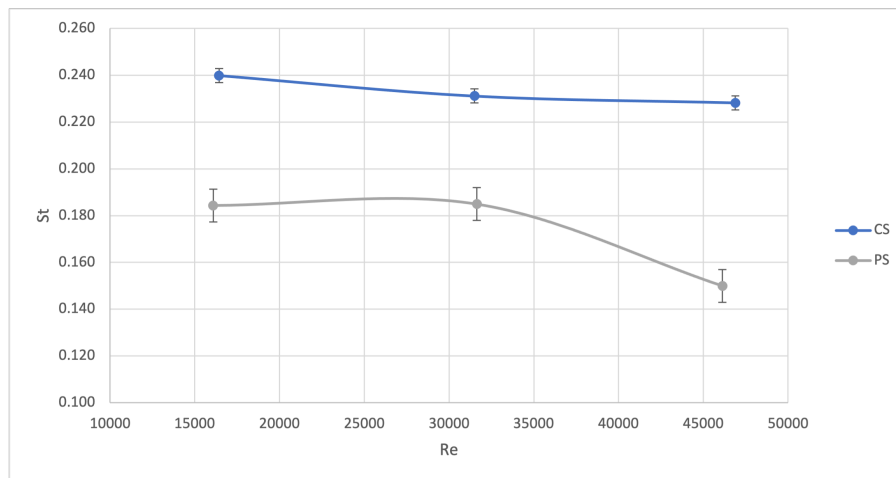


Figure 4.14: Strouhal number for each velocity in current conditions

Differences in Strouhal Number

The cause of the differences in Strouhal numbers can be explained by looking at the amplitude spectra of the tunnels. As mentioned in Chapter 3, there were difficulties in determining the correct vortex-shedding frequencies from the amplitude spectra. To check the found results, the signals were cut into five overlapping parts and the amplitude spectrum of each part was determined. The spectra of these five parts were then averaged to obtain a more smooth amplitude spectrum, and the results are shown in figure 4.15.

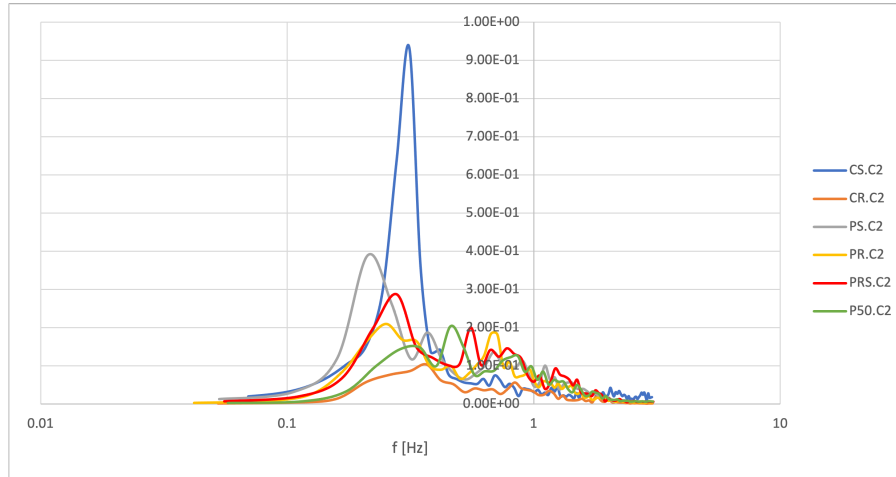


Figure 4.15: Comparison of the amplitude spectra with a current of 0.2 m/s

Only the circular smooth and the parametric smooth tunnels show a clear peak in their amplitude spectrum. The other tunnels all have peaks at multiple frequencies, and in general, show a much more chaotic spectrum where it is unclear what the dominant frequency is. Apparently, the addition of roughness disturbs the vortex-shedding process and leads to vortex-shedding with irregular frequencies and amplitudes.

To find an explanation for the lower Strouhal number of the parametric smooth tunnel, the video images of the wakes of both smooth tunnels were analyzed. Screenshots of the images are shown in Appendix F. These images showed a regular vortex-shedding process for the circular smooth tunnel, where the observed vortex-shedding period agreed with the inverse of the found frequency in the amplitude spectrum.

For the parametric smooth tunnel, the vortex-shedding was more unclear, and it was difficult to determine an accurate period. This agrees with the amplitude spectrum of the parametric smooth tunnel, which contains peaks at multiple frequencies. Smaller and larger vortices preceded each other and sometimes a reverse flow was observed. No clear explanation was found from the video images for the lower frequency of the parametric-shaped tunnel. The issue could possibly be solved by changing the definition of the Strouhal number to a more universal one. In the paper by (Adachi, 1997), different definitions for a universal Strouhal number were tested and it was concluded that the definition provided by (Bearman, 1967), which uses the size of the wake vortex street, gave the most uniform results.

4.2 Wave Tests

In this section, the results of the wave tests are presented. First, the observations from the experiment will be covered, and then the influence of the tunnel shape and the roughness parameters on the drag and inertia coefficients are discussed. These force coefficients are calculated using both the max/min method and the least squares method. The results of both methods matched well and resulted in almost equal force coefficients. The results of both methods are shown in Appendix G. Since the results are similar, only the least square method results are shown in this section, as that is the most advanced method.

As explained in Chapter 3, the sensitivity to the time shift is expressed in the error bars that are shown in the drag coefficient results. For the inertia coefficients, the error bars represent the maximum error between the time shift error and the standard deviation between the separate tests.

4.2.1 Experiment Observations

Typical Signals

In figure 4.16, a typical signal of the wave gauge, the EMS, and the load cell is presented. All signals are filtered using the methods described in Chapter 3. These signals show that at first, the water is at rest and there is no force acting on the tunnel. Then the waves start developing until they have reached their input wave height and period. After a few full waves have reached the tunnel, the first waves are reflected back from the end of the flume and also reach the tunnel again. When this happens an increase in wave height is observed and the wave generator is turned off, causing a rapid decrease in all signals.

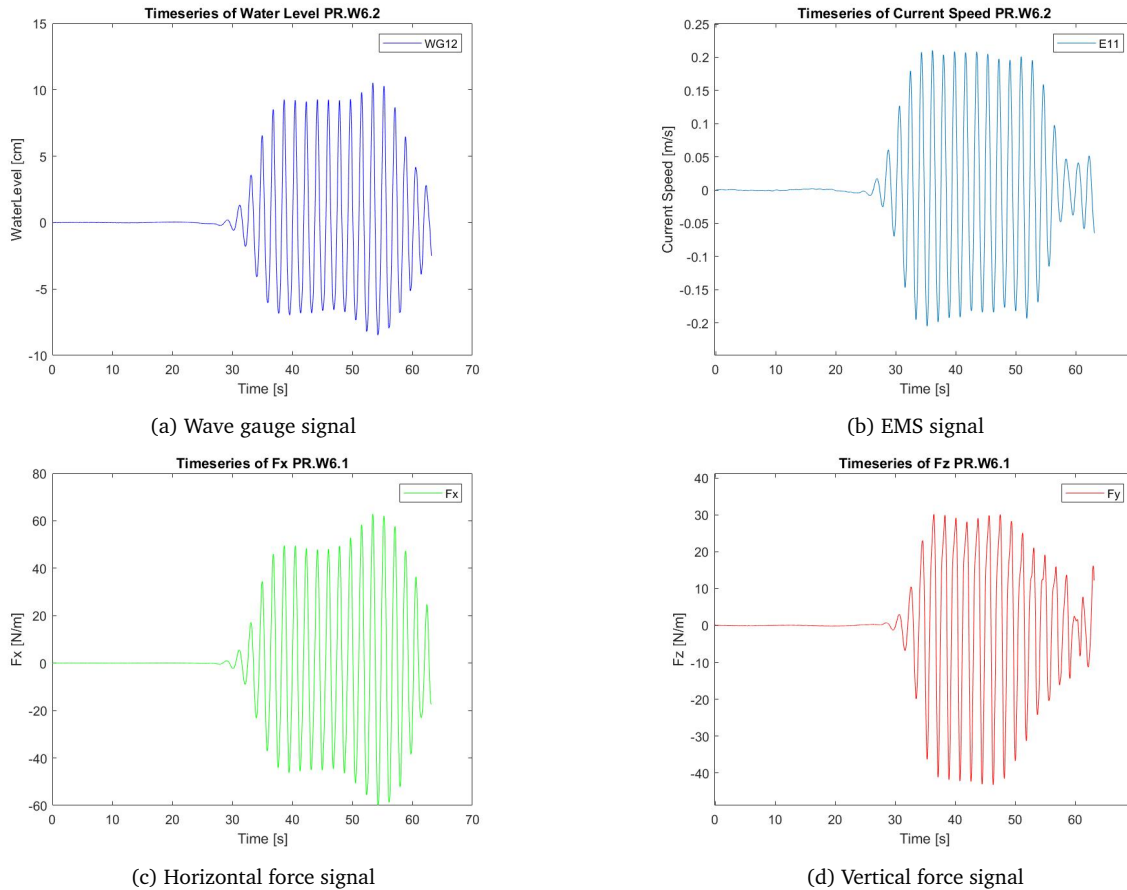


Figure 4.16: Typical signals for the wave tests

Velocity Signal Errors

When analyzing the results, it was noticed that the measured orbital velocities were much lower than their expected theoretical values, which in turn led to lower orbital accelerations. The theoretical values were calculated using the measured wave heights and periods, and Stokes' second-order wave theory. The lower orbital velocities were present in all wave cases, as illustrated by figure 4.17, where the measured and theoretical horizontal velocities can be seen of the smallest and largest wave condition. For the smallest wave, the velocity went down from 0.049 m/s to 0.041 m/s, a decrease of 16.3%, and for the largest wave, the velocity went down from 0.26 m/s to 0.2 m/s, a decrease of 23.1%. A decrease this large can not be explained by boundary condition effects, and the effect the boundary conditions would have on the generated waves is already included by using the measured wave heights and periods to calculate the theoretical orbital velocity.

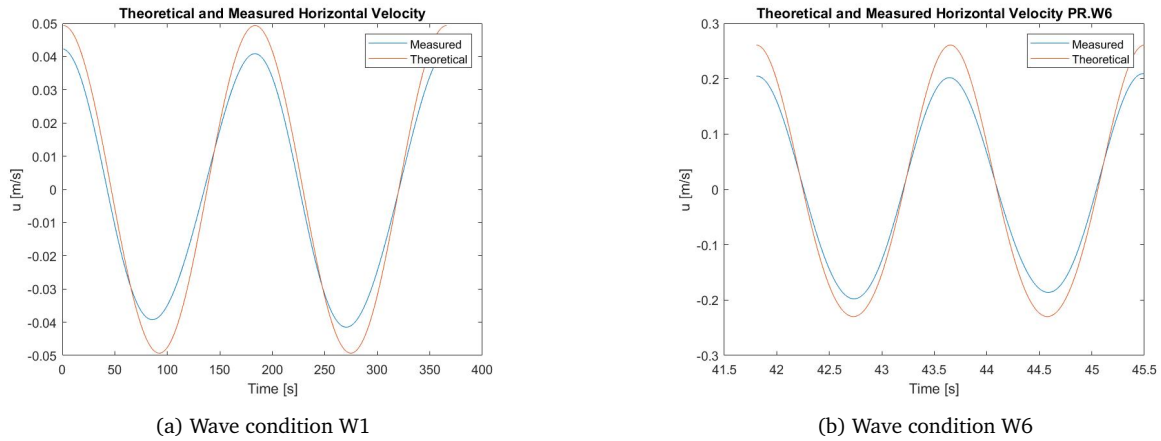


Figure 4.17: Measured and theoretical horizontal orbital velocities

Figure 4.18 shows that filtering the signal was not the cause of the decrease, the measured velocity increased to 0.213 m/s without filtering, which still corresponds with a decrease of 18.1%. The cause of the decrease remains unclear. Possible factors are an error in the calibration formula, insufficient accuracy of the EMS, or damping effects from the waves reflected from the tunnel. However, using lower velocities and accelerations will lead to an increase in the calculated force coefficients. Therefore, it has been decided to use the theoretical values of the orbital velocities in the force coefficient calculations.

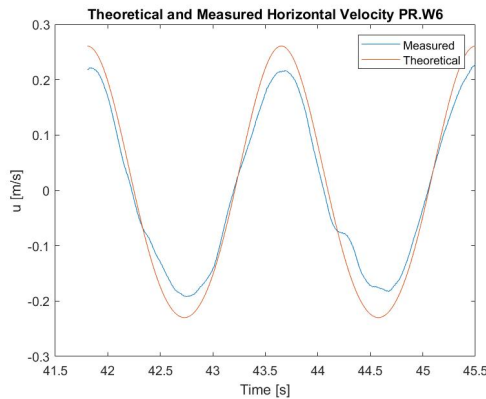


Figure 4.18: Unfiltered measured and theoretical orbital velocities

Inertia Dominance

Due to the low KC numbers considered for this experiment, the drag force only has a small contribution to the total force. In figure 4.19, the horizontal force components of the parametric rough tunnels are shown for a small wave (W1) and a large wave (W6), at the calculated time shift, and at the time shift point + 0.1 s. Figure 4.19a shows that for a large wave, the total force mainly consists of the inertia force and that the drag force component is determined by the starting value of the total force. The starting value itself relies completely on the time shift of the force signal, and a shift of 0.1 seconds can significantly change the value of the drag coefficient. Figure 4.19b shows this time shift increase of 0.1 s. The drag coefficient is lowered from 3.24 to 1.55, and the inertia coefficient is increased from 1.39 to 1.44

Results of the parametric rough tunnel with a small wave are shown in figure 4.19c. The time shift led to a much higher starting value of the measured force which caused an increase in drag coefficient and a decrease in inertia coefficient. When increasing the time shift by 0.1 s, the force components look like figure 4.19d. With this time shift, the drag coefficient is lowered from 69.6 to 39.1, and the inertia

coefficient is increased from 1.25 to 1.54. This illustrates that the drag coefficient is very sensitive to the time shift for all wave cases, and the inertia coefficient is mainly sensitive to the time shift for the lower wave cases, explaining why the error bars shown in the next sections are much larger for the smaller wave cases. The sensitivity of the drag coefficient and its small contribution to the total force makes the drag coefficient results not the most relevant for engineering practice, but they do give some insight into how the roughness parameters and the tunnel shape influence the drag force.

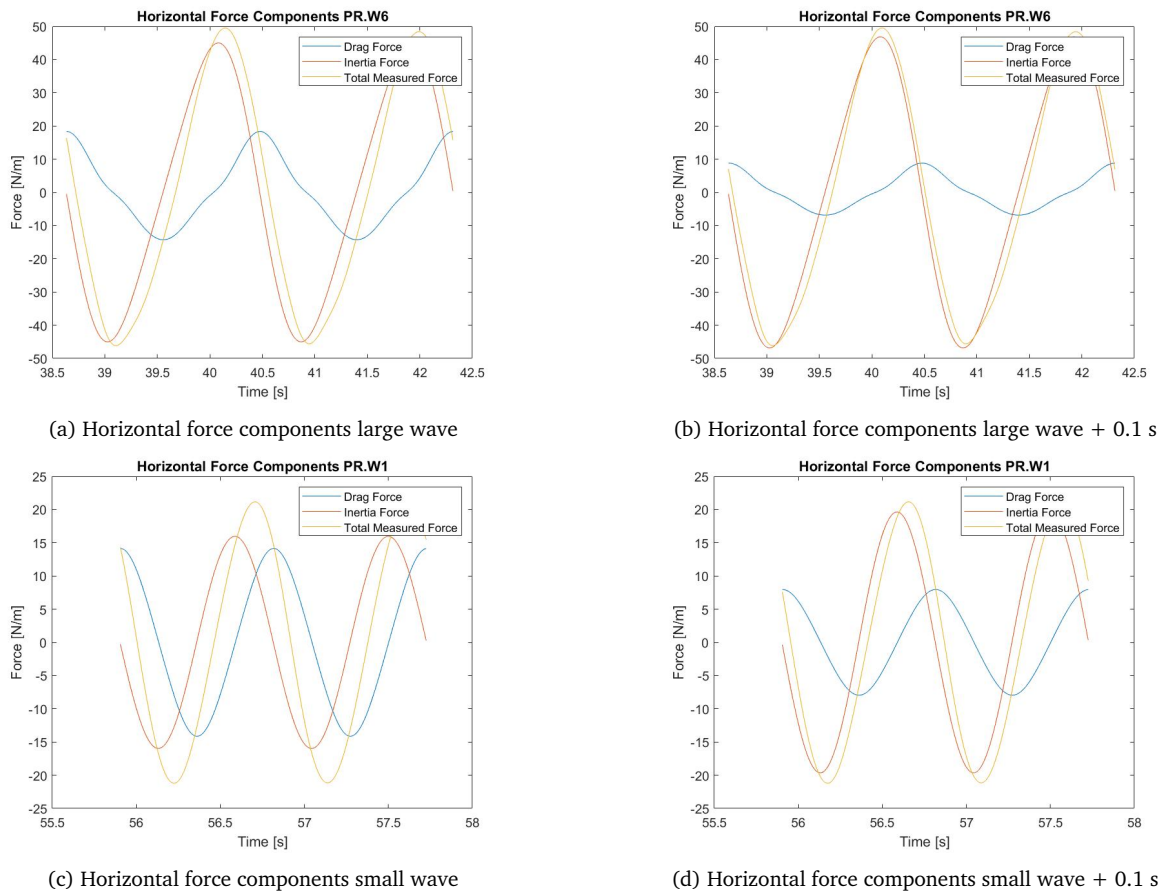
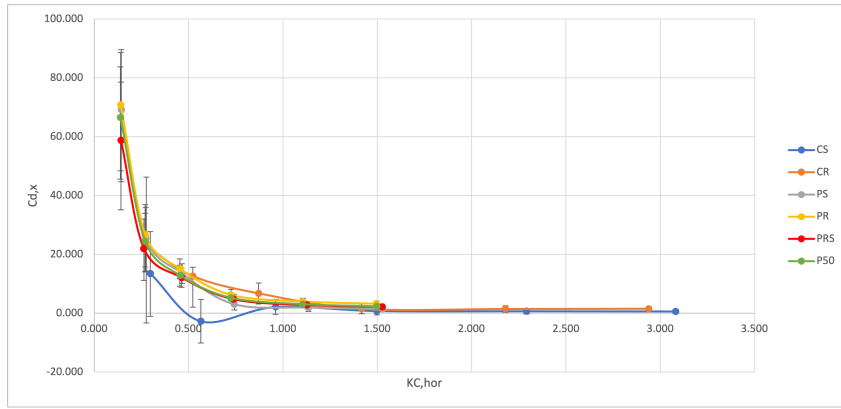
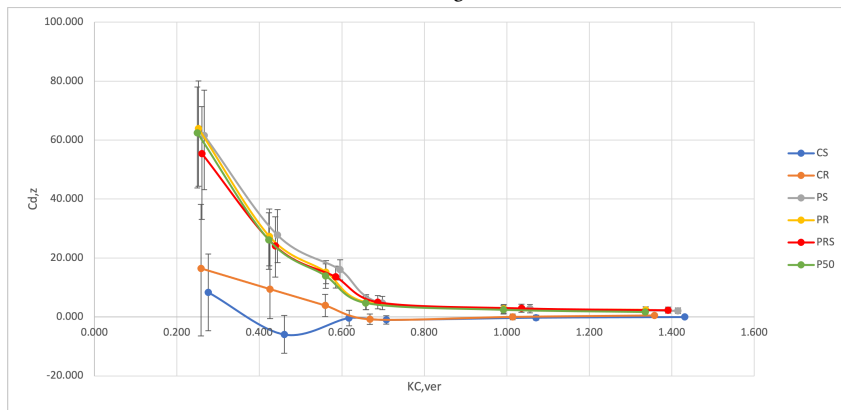


Figure 4.19: Horizontal force components of a small and large wave

Figure 4.20 shows the horizontal and vertical drag coefficient results, along with their error bars. Because of the low KC numbers, the horizontal drag coefficients of the first three wave conditions are too large. This distorts the vertical scale and makes it difficult to analyze the results. To make the graphs more readable, the first three wave conditions are removed when analyzing the drag coefficients in the coming paragraphs.



(a) Horizontal drag coefficients



(b) Vertical drag coefficients

Figure 4.20: Drag coefficients in wave conditions

4.2.2 Influence of the Tunnel Shape

Horizontal Inertia Coefficient

Figure 4.21 shows the horizontal inertia coefficients for both tunnel shapes, where the smooth and the large roughness case are included. The difference in horizontal KC numbers between the tunnel shapes comes from the larger horizontal diameter of the parametric-shaped tunnels, this increases the denominator in equation 3.4, lowering the KC numbers of the parametric-shaped tunnels. Figure 2.9 shows that according to literature, the value of the inertia coefficient is expected to be 2 throughout the entire KC range used in this experiment. This matches well with the found results and thereby provides confidence that the results are physically realistic.

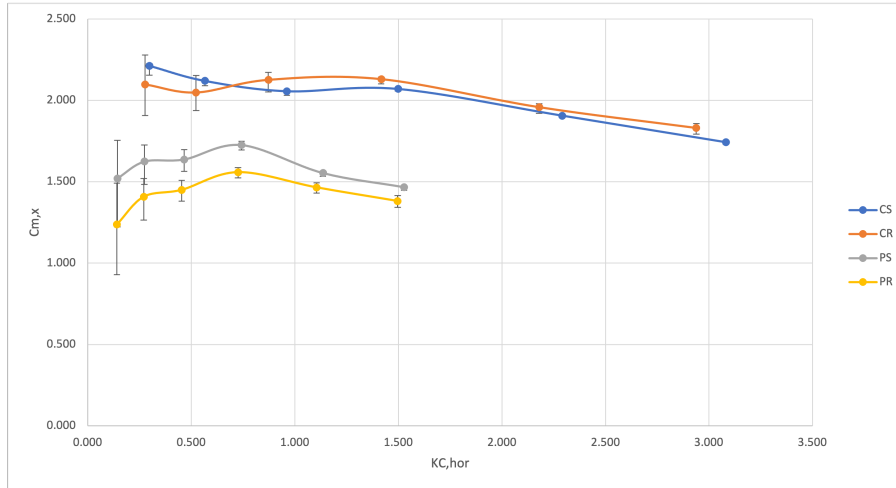


Figure 4.21: Horizontal inertia coefficient for varying tunnel shapes in wave conditions

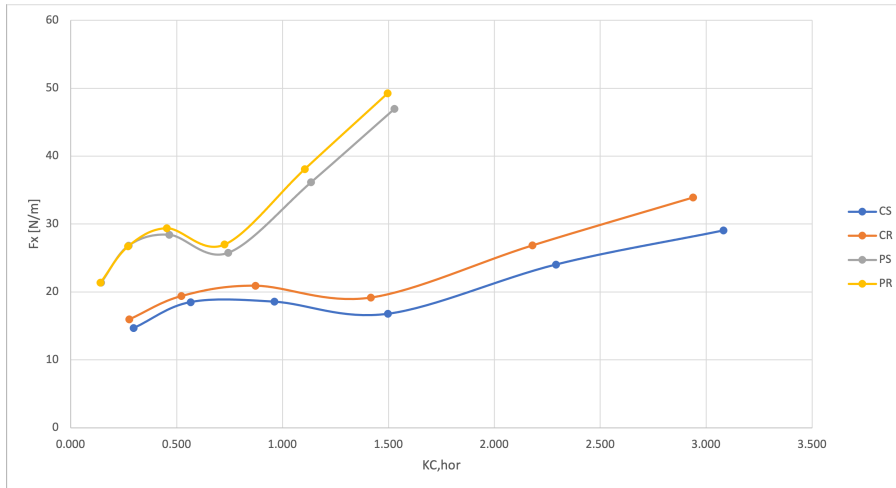


Figure 4.22: Measured horizontal force for varying tunnel shapes in wave conditions

Figure 4.21 clearly shows a lower inertia coefficient for the parametric-shaped tunnels, and a slight decrease in inertia coefficient is observed for increasing KC numbers. However, when looking at the measured forces in figure 4.22, the parametric-shaped tunnels experience a larger total force than the circular ones. These opposing statements can be understood by taking two factors into account, the differences in displaced water volume and the cross-sectional area between the two tunnel shapes.

The inertia force, as explained in section 2.4.1, is a force that is caused by a fluid mass that is attached to the tunnel and accelerates. When the tunnel has a larger displaced water volume, this accelerating fluid mass increases as well. Since the fluid accelerations for the circular and the parametric-shaped tunnels are almost equal, a larger fluid mass leads to a larger inertia force on the tunnel, explaining why the inertia force on the parametric-shaped tunnels is larger. In the least squares method formulas used to determine the inertia coefficient, the coefficient is multiplied by the cross-sectional area of the tunnel, meaning that a higher cross-sectional area would need a lower inertia coefficient to reach the measured force since almost equal fluid accelerations were used. This is the reason that for similar forces, the parametric-shaped tunnels would have lower inertia coefficients.

Combining the explanations from the previous paragraph would mean that the difference in measured force between the circular and parametric-shaped tunnels must be smaller than their difference in cross-sectional area. The circular and parametric rough tunnels in wave case W6 were taken as an example to

verify this statement. The cross-sectional area of the circular rough tunnel equals 55% of the parametric rough tunnel's area. The measured maximum horizontal force on the circular rough tunnel is 68.6% of that of the parametric rough tunnel. The difference in measured force is smaller than the difference in cross-sectional areas, which explains the lower inertia coefficients for the parametric-shaped tunnels while experiencing larger forces.

When looking at figure 4.21, there is a difference observed in how the circular and the parametric-shaped tunnels react to the addition of roughness. Contrary to the parametric-shaped tunnel, the circular rough tunnel does not have smaller inertia coefficients compared to the smooth tunnel. The same example of the W6 case is used to find the reason for this difference.

The cross-sectional area of the circular smooth tunnel equals 87.6% of the circular rough area, and the maximum measured force on the circular smooth tunnel equals 85.7% of that on the circular rough tunnel. The cross-sectional area of the parametric smooth tunnel equals 91% of the parametric rough area, and the maximum measured force on the parametric smooth tunnel equals 95.7% of that on the parametric rough tunnel. The increase in horizontal inertia force on the parametric-shaped tunnels is smaller than that for the circular-shaped tunnels when adding roughness to the tunnel. An explanation for this difference could be that the higher number of roughness elements present on the parametric-shaped tunnel, leads to a higher decrease in inertia force.

Vertical Inertia Coefficient

Contrary to the horizontal inertia coefficients, the vertical ones are smaller for the circular-shaped tunnels than for the parametric-shaped tunnels, as shown in figure 4.23, despite the differences in cross-sectional area as mentioned in the previous section. The cause is found by looking at the measured forces shown in figure 4.24 and using the circular and parametric rough tunnels as an example. The total measured vertical force on the circular rough tunnel has a maximum of 10 N/m for the largest wave condition, while the parametric rough tunnel has a maximum of 41.8 N/m. This large difference has two reasons, one being the larger displaced water volume mentioned in the horizontal inertia coefficient section, and the other reason being the larger blockage area the fluid encounters for the parametric-shaped tunnels. The horizontal diameter of the parametric-shaped tunnels is approximately twice as large compared to that of the circular-shaped tunnels. So when the motion of the fluid is directed vertically, the blockage area is also twice as large for the parametric-shaped tunnel, leading to a higher vertical inertia force. The increase in force is now higher than the decrease in cross-sectional area, resulting in higher vertical inertia coefficients for the parametric-shaped tunnels.

The dip in vertical force that can be seen from the second to the fourth wave condition can be explained by looking at the measured wave heights and periods in Appendix C. The vertical orbital velocities and accelerations depend on the wave periods and wave heights, where a larger wave period decreases the vertical acceleration and a larger wave height increases both the vertical velocity and acceleration. The first wave condition had a smaller wave height than the second condition. Therefore, there is an increase in force found between the first and second points. From there, the height remained equal but the period increased, decreasing the acceleration and thus the force. From the fourth wave condition, the period remained constant and the height increased, causing a linear increase in vertical force.

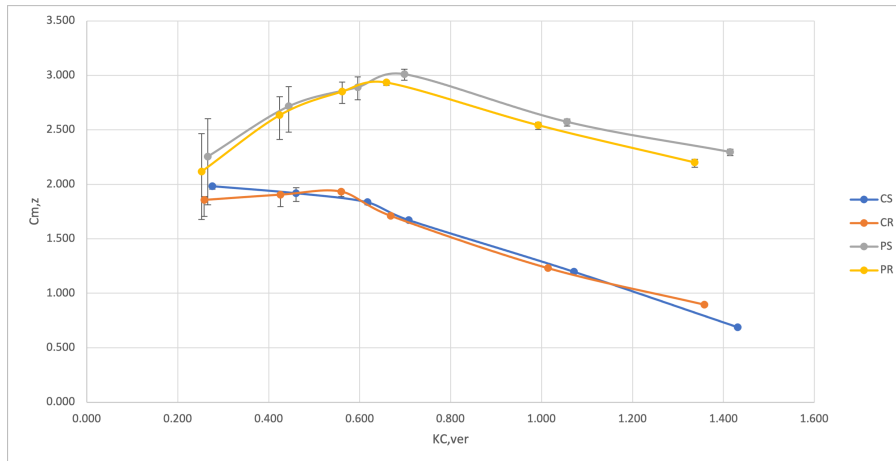


Figure 4.23: Vertical inertia coefficient for varying tunnel shapes in wave conditions

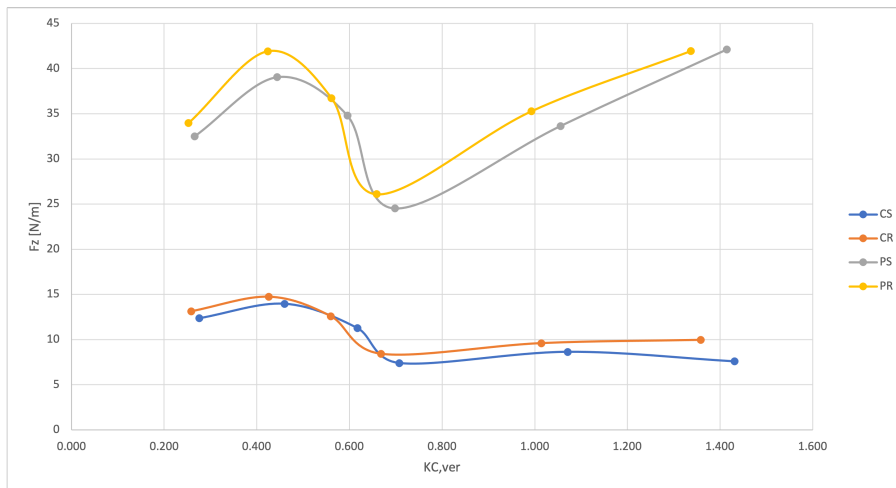


Figure 4.24: Measured vertical force for varying tunnel shapes in wave conditions

Horizontal Drag Coefficient

Horizontal drag coefficients for the wave tests follow the same theory as the ones from the current tests. Just like the drag coefficients in current conditions, the horizontal drag coefficients under waves are larger for a larger roughness height. However, the parametric-shaped tunnel now has larger horizontal drag coefficients than the circular-shaped tunnel, as seen in figure 4.25. This is explained by noting that in the KC range of this experiment, the skin friction will have a larger contribution to the total drag force. The parametric-shaped tunnels have larger surface areas and more roughness elements than the circular-shaped tunnels, and therefore the larger skin friction contribution has more effects on the parametric-shaped tunnels.

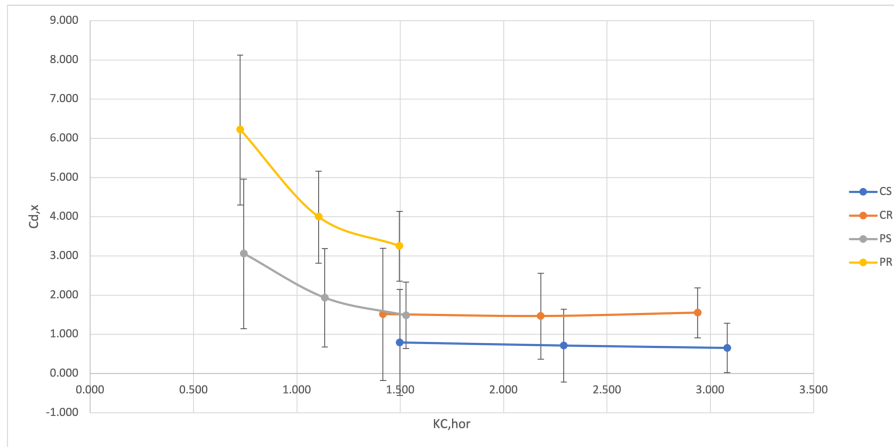


Figure 4.25: Horizontal drag coefficient for varying tunnel shapes in wave conditions

Vertical Drag Coefficient

In figure 4.26, the vertical drag coefficients for the parametric and circular smooth and rough cases are shown. Similar to the horizontal drag coefficient results, the parametric-shaped tunnels have larger vertical drag coefficients than the circular-shaped tunnels. This time, however, it was expected since the blockage area that the vertical flow encounters is much larger due to the larger horizontal diameter of the parametric shape. The vertical drag force of the circular-shaped tunnels takes a negative value at a number of points, this must be an error since it is physically impossible to have negative force coefficients. The error likely stems from the time shift because the KC value is low enough to make the vertical drag force contribution almost zero and if the time shift is slightly off, it could cross the zero mark and become negative.

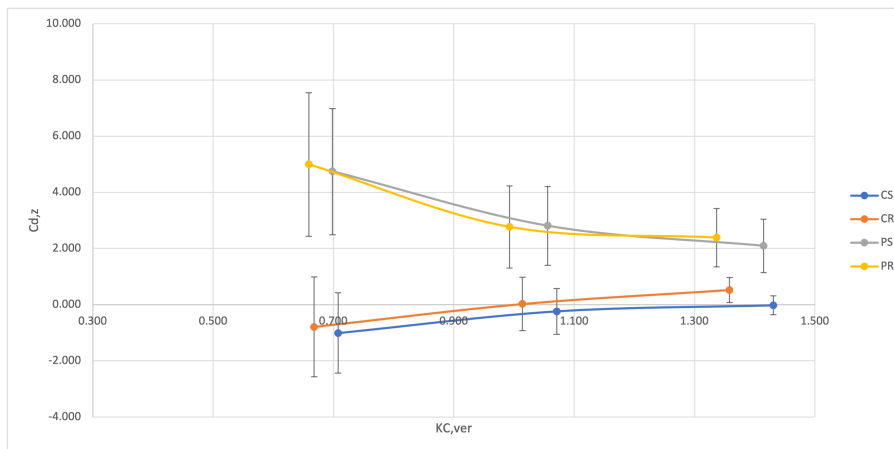


Figure 4.26: Vertical drag coefficient for varying tunnel shapes in wave conditions

4.2.3 Influence of the Roughness Height

Horizontal Inertia Coefficient

In figure 4.27, the influence of roughness height on the parametric-shaped tunnel is presented. The figure shows that the presence of roughness decreases the inertia coefficient. However, there was no clear influence of roughness height observed, since the small and large roughness cases share equal inertia coefficients in most cases. In figure 4.28, it can be seen that the force on the tunnel with a large roughness height is highest, the small roughness height tunnel experiences the lowest force, and the smooth case is equal to the large roughness case for small KC numbers, and equal to the small roughness case for larger

KC numbers.

Surface roughness increases the drag force on the tunnel by increasing its equivalent diameter, but decreases the inertia force by slowing down the flow around the tunnel, and this decrease in velocity is larger for a higher number of roughness elements. There is a balance between this increase and decrease in force, where the large roughness causes a higher increase in drag force than the decrease in inertia force, and the small roughness causes a higher decrease in inertia force than an increase in drag force.

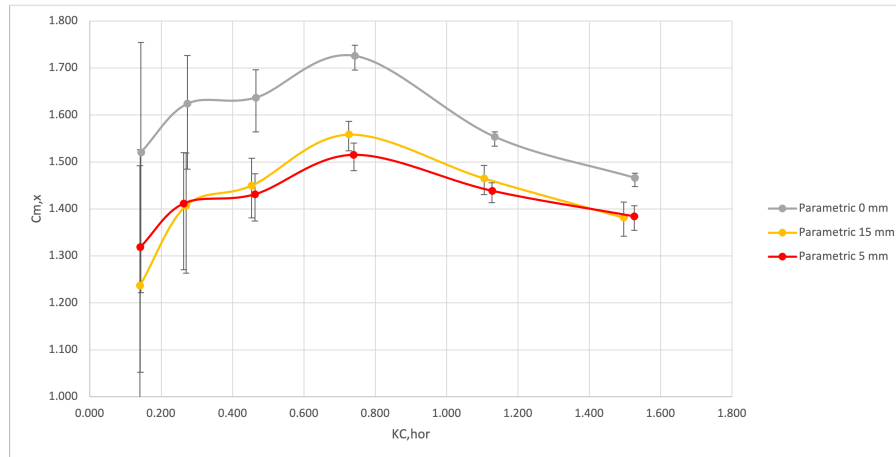


Figure 4.27: Horizontal inertia coefficient for varying roughness heights in wave conditions

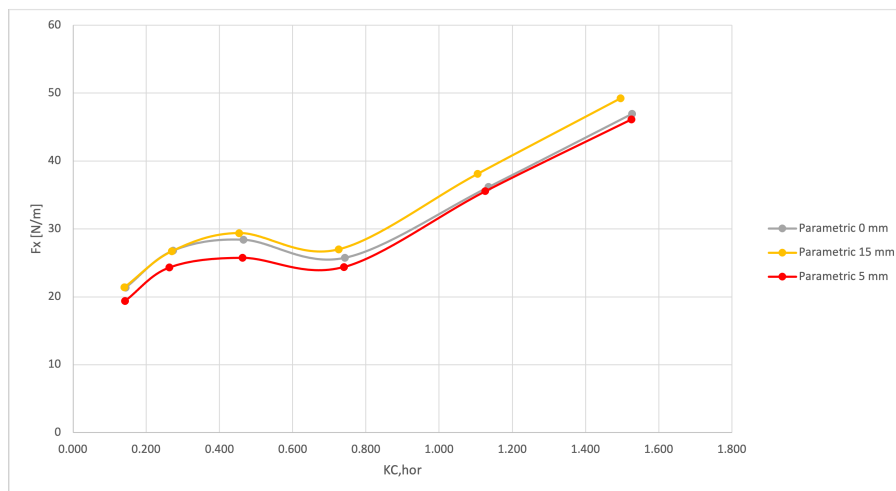


Figure 4.28: Measured horizontal force for varying roughness heights in wave conditions

Vertical Inertia Coefficient

Figure 4.29 shows the influence the roughness height has on the vertical inertia coefficient. For the largest two wave cases, a small decrease in inertia coefficients can be observed with increasing roughness height. This coincides with the last two wave cases having equal wave periods but increasing wave heights. Apparently, an increase in wavelength combined with changing roughness heights does not influence the vertical inertia coefficient much. An increase in wave height, however, does seem to lower the vertical inertia coefficient slightly when combined with increasing roughness height. The measured vertical forces shown in figure 4.30 show similar behavior to the horizontal forces. Where the large roughness increases the total force, but the small roughness shares similar forces with the smooth tunnel.

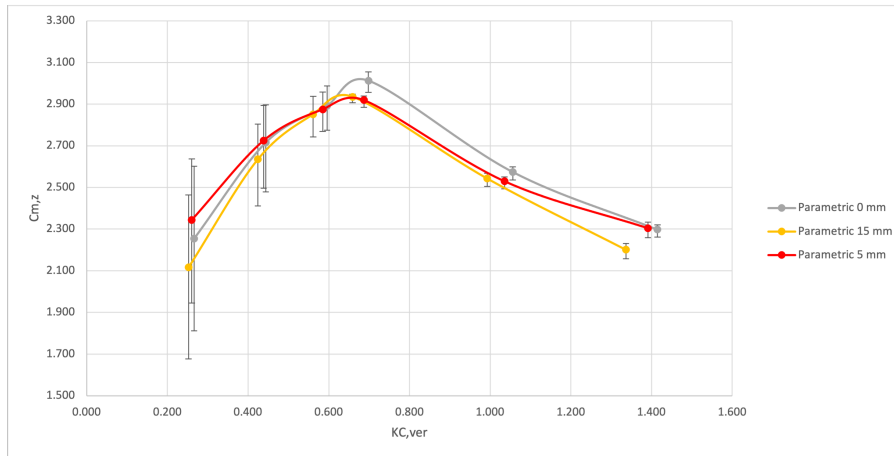


Figure 4.29: Vertical inertia coefficient for varying roughness heights in wave conditions

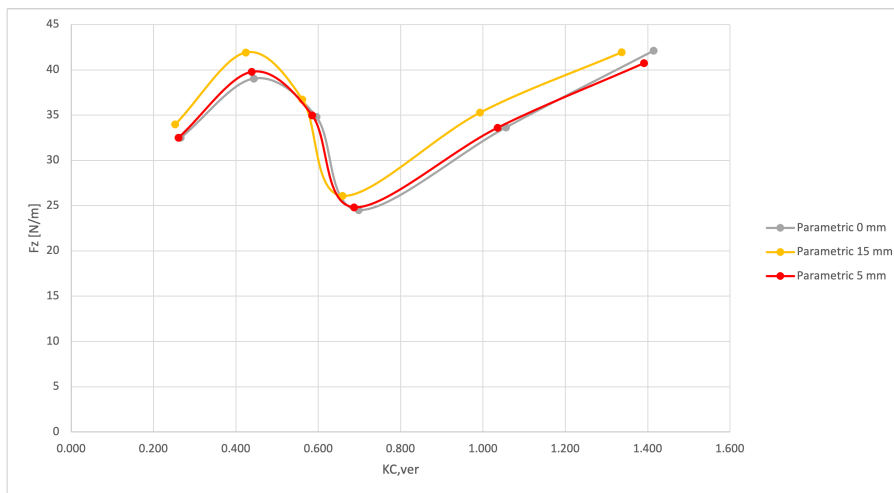


Figure 4.30: Measured vertical force for roughness heights in wave conditions

Horizontal Drag Coefficient

Similar to the current tests, increasing roughness height leads to higher drag coefficients, as shown in figure 4.31. As explained before, in this KC range the skin friction contributes a larger part to the total force, and the addition of roughness increases the surface area of the tunnel, which increases the effect of the higher friction contribution. The increase in skin friction combined with a larger equivalent diameter, explains the increase in drag coefficient with increasing roughness height.

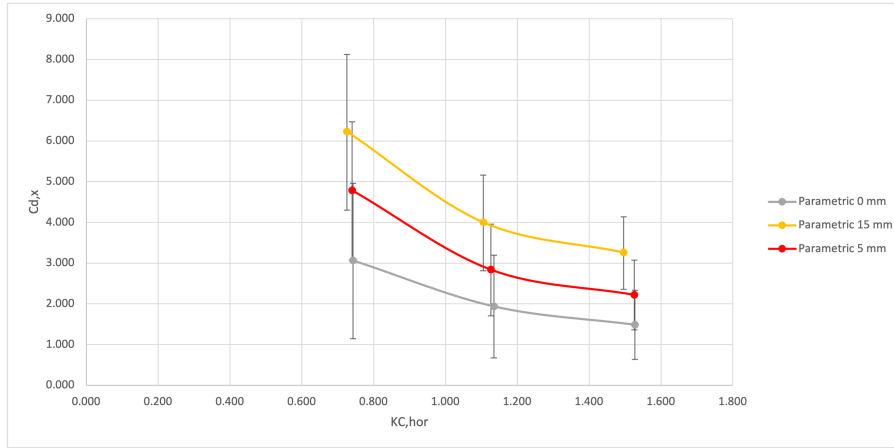


Figure 4.31: Horizontal drag coefficient for varying roughness heights in wave conditions

Vertical Drag Coefficient

In figure 4.32, the vertical drag coefficient results can be seen. From this figure, it is clear that there is no noticeable influence of the roughness height on the vertical drag coefficients, as all results fall within the error bar margins of the results of the other tunnels.

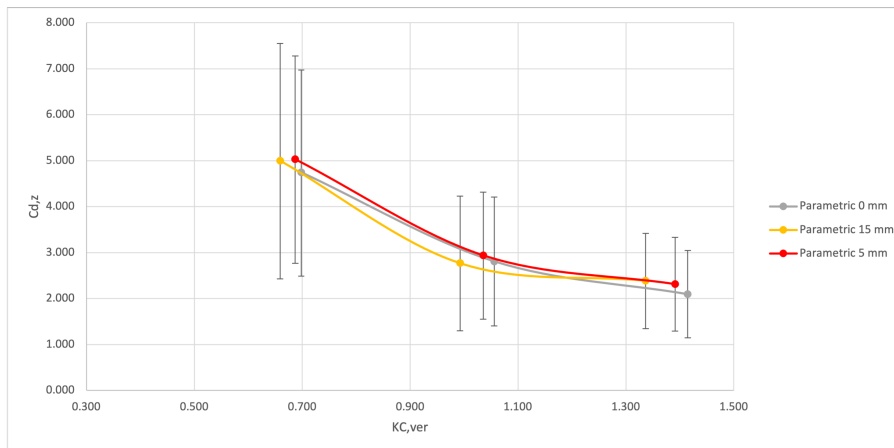


Figure 4.32: Vertical drag coefficient for varying roughness heights in wave conditions

4.2.4 Influence of the Coverage Percentage

Horizontal Inertia Coefficient

It was concluded in the previous section that the small and large roughness cases have similar coefficients. Figure 4.33 shows that the horizontal inertia coefficients decrease for increasing coverage percentages. The forces found in figure 4.34 show that 100% and 50% covered tunnels experience the same force. This leads to the conclusion that the percentage of surface area covered with roughness is less important than the roughness height, as the force of both the large roughness case and the 50% coverage case is higher than for the small roughness case. The differences between the coefficients come from the differences in cross-sectional area.

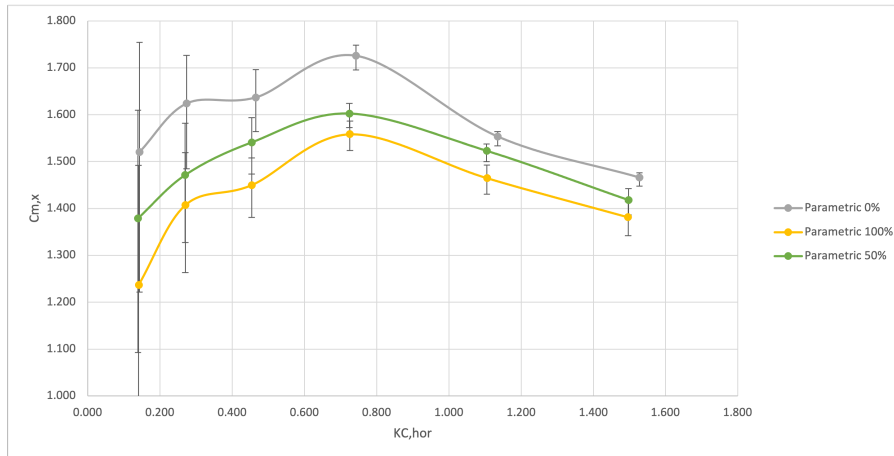


Figure 4.33: Horizontal inertia coefficient for varying coverage percentages in wave conditions

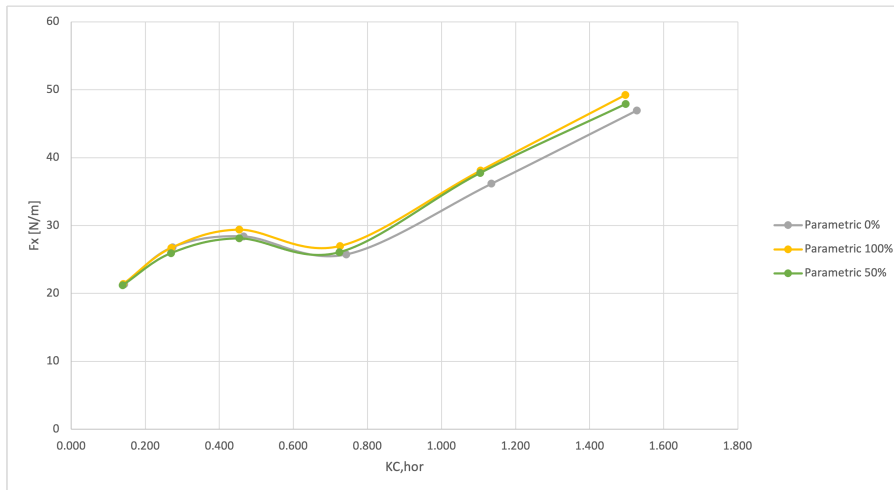


Figure 4.34: Measured horizontal force for varying coverage percentages in wave conditions

Vertical Inertia Coefficient

A similar result as found for the influence of roughness height on the vertical inertia coefficient is found for the influence of coverage percentage. Figure 4.35 shows a similar graph, where only the last wave case shows a slight decrease in the vertical inertia coefficient for increasing coverage percentage.

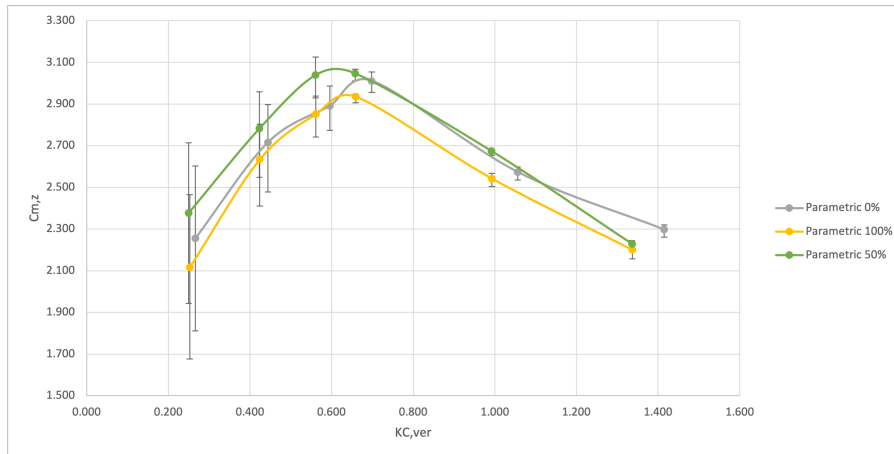


Figure 4.35: Vertical inertia coefficient for varying coverage percentages in wave conditions

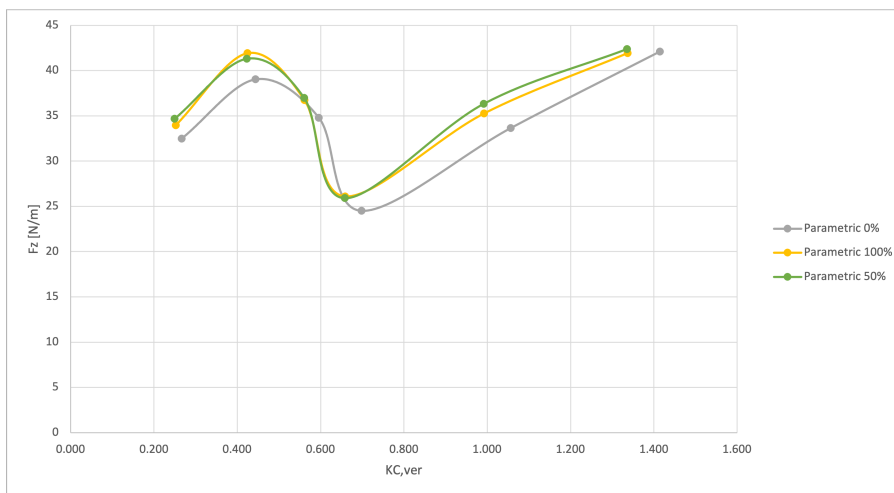


Figure 4.36: Measured vertical force for varying coverage percentages in wave conditions

Horizontal and Vertical Drag Coefficient

The influence of coverage percentages on the horizontal and vertical drag coefficients are combined in this paragraph, since they both show similar behavior to the results found in the influence of roughness height section, as shown in figure 4.37. There is not much difference between the drag coefficients of the 50% coverage tunnel and the small roughness tunnel, leading to the conclusion that coverage percentage and roughness height share an equal influence on the drag coefficients.

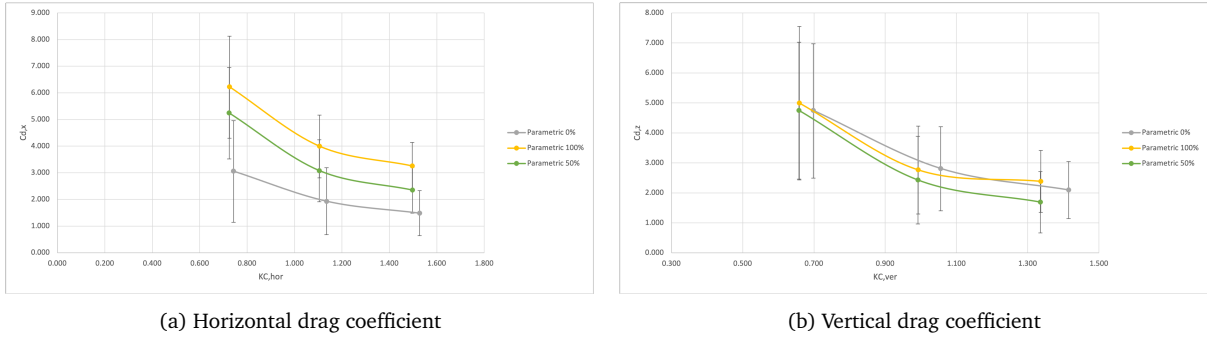


Figure 4.37: Horizontal and vertical drag coefficients for varying coverage percentages in wave conditions

4.3 Combined Tests

In this section, the results of the combined tests are covered. First, the observations from the experiment will be mentioned and then the drag and inertia coefficients are discussed. These coefficients are calculated using both the max/min method and the least squares method. However, only the least squares method results are shown, since the Max/Min method greatly overestimates the force coefficients, as shown in Appendix G. The Max/Min method makes use of the fact that when the orbital acceleration is at its maximum, the orbital velocity is zero and the force is fully made up of inertia force. However, in the combined conditions there is a constant drag force due to the steady current. Therefore, the Max/Min method does not work in combined conditions.

In literature, (Iwagaki and Asano, 1984) for example, force coefficients in combined conditions are plotted against a factor that relates the maximum orbital velocity from the waves to the total velocity that includes the current velocity, this factor is called U_w/U_t . When this factor tends to 0, it resembles the current-only condition and when this factor tends to 1, it resembles the wave-only condition. The vertical drag and inertia coefficients will also be plotted to this factor, even though the vertical velocity only consists of a wave part, the waves themselves are still influenced by the coexisting current.

4.3.1 Experiment Observations

Typical Signals

Figure 4.38 shows typical signals in the combined tests from the wave gauge, the EMS, and the load cell, where the signals have been filtered using the methods described in Chapter 3. For the larger waves, such as the ones presented in the figure, the signals are similar to the ones from the wave tests. The main difference is that in the first part of the signal, the water is not at rest. This is seen in the EMS signal where a velocity of around 0.2 m/s is measured, but also in the horizontal force signal where a constant horizontal force is present. If the unfiltered vertical force signals were used, oscillating lift forces would be observed in the first part of the signal, and once the waves arrive it would be more chaotic.

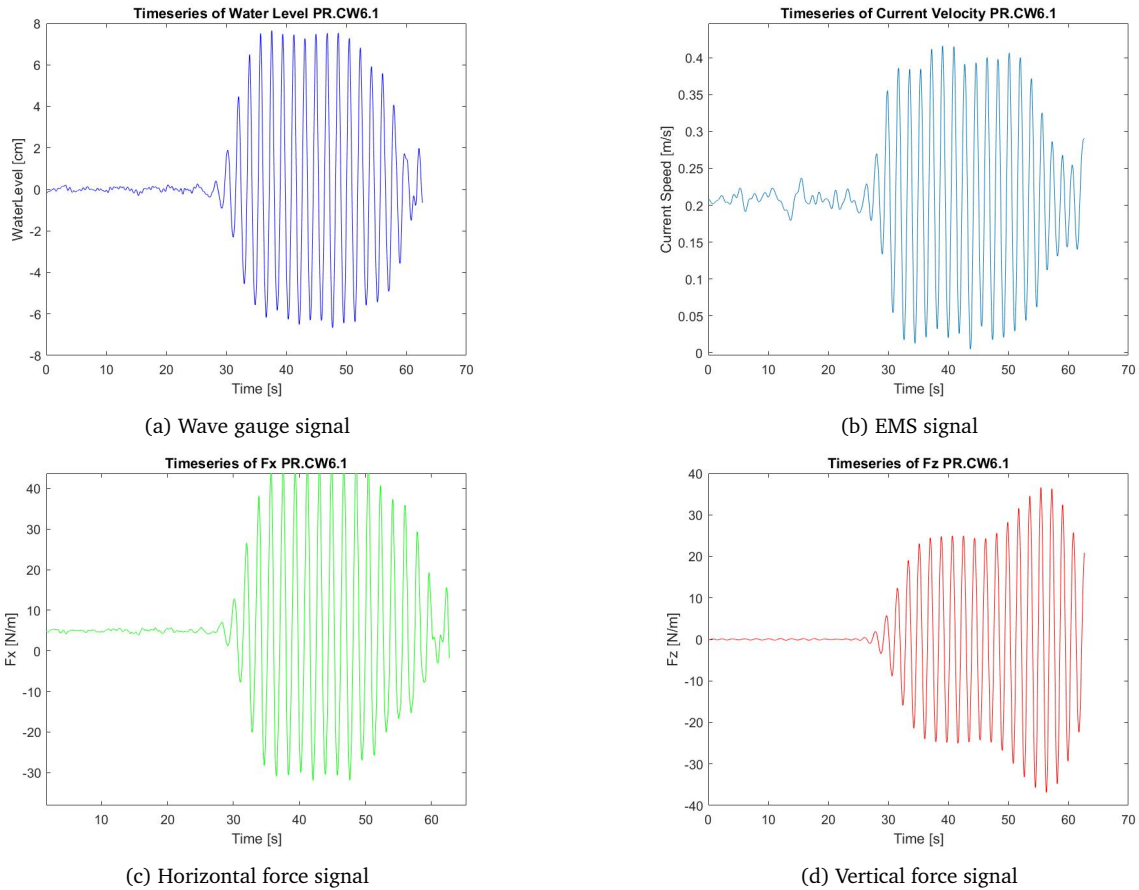


Figure 4.38: Typical signals for combined tests with large waves

Smaller generated waves show a higher current interference in their wave, velocity, and force signals. For the combined tests with the smallest waves, the CW1 tests, this was visibly noticeable as a transverse wave through the flume was observed. This could have had a significant influence on the measurements of the wave gauges and the EMS and the CW1 tests will therefore be removed from this chapter since the results can not be trusted. In figure 4.39, typical signals of the CW2 test are shown. Especially the wave gauge and EMS signals were more distorted by the coexisting current. Extra care was taken in choosing the two waves that were used in calculating the coefficients, and the variability within the signals is also the reason that the error bars of the combined results are bigger than those of the wave tests.

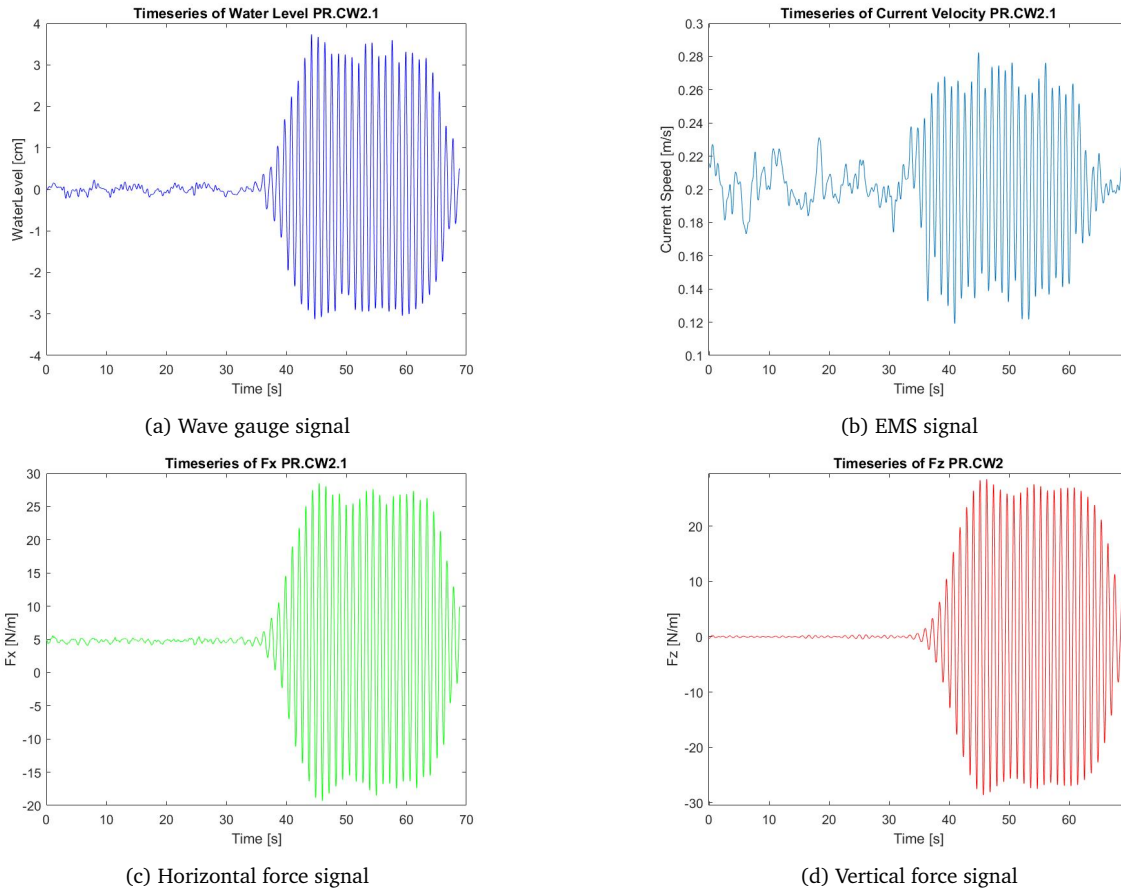


Figure 4.39: Typical signals for combined tests with small waves

Velocity Signal Errors and Inertia Dominance

For similar reasons as mentioned in Section 4.2, the measured orbital velocities in the combined tests are lower than for a theoretical Stokes wave. The measured wave heights and periods for each separate test were used to calculate these velocities, which means the decrease in wave height and length caused by the current is already included in the calculations, and still, the orbital velocities are too low. In the force coefficient calculations for the combined conditions, the theoretical orbital velocities were used as well, and the velocity signal was created by adding the measured mean current velocity to the theoretical velocity signal.

For the combined conditions, the horizontal results are not as inertia dominated as was the case for the wave conditions, because the added current velocity increases the KC number. For the vertical results, the KC number is still very low and the regime remains inertia dominated. The addition of the current only distorted the vertical velocity and acceleration signals, leading to a high variability in vertical drag coefficient results. Therefore, the results of the vertical drag coefficient are moved to Appendix H.

4.3.2 Influence of Tunnel Shape

Horizontal Inertia Coefficient

Figure 4.40 shows that the influence of the tunnel shape is much less pronounced in combined conditions compared to the wave test results. The smooth parametric-shaped tunnel and both circular-shaped tunnels have equal horizontal inertia coefficients when looking at the last three conditions. However, when roughness is added to the parametric-shaped tunnel, the inertia coefficient decreases, which was

also observed in the wave tests.

The forces in figure 4.41 show that the parametric-shaped tunnels show no increase in horizontal force when roughness is added to the tunnel. The roughness was expected to increase the drag force on the tunnel by increasing its equivalent diameter. This was not the case, indicating that the presence of surface roughness decreases the inertia force by slowing down the flow around the tunnel. But also that the current increases the KC and Reynolds numbers, which lowers the relative contribution of the skin friction, thereby changing the balance between the increase in drag force and the decrease in inertia force.

For the circular-shaped tunnels, however, there is an increase in horizontal force observed, when roughness is added to the tunnel. This could be explained by noting that the increase in equivalent diameter is equal between both tunnel shapes, but the parametric-shaped tunnels have much more roughness elements, leading to a larger decrease in flow velocity and thereby a larger decrease in inertia force. In the wave test results, there was an increase in horizontal force observed between the parametric smooth and rough tunnels. The fact that in combined conditions they experience equal forces, indicates that the addition of a current somehow lowers the added mass or its acceleration.

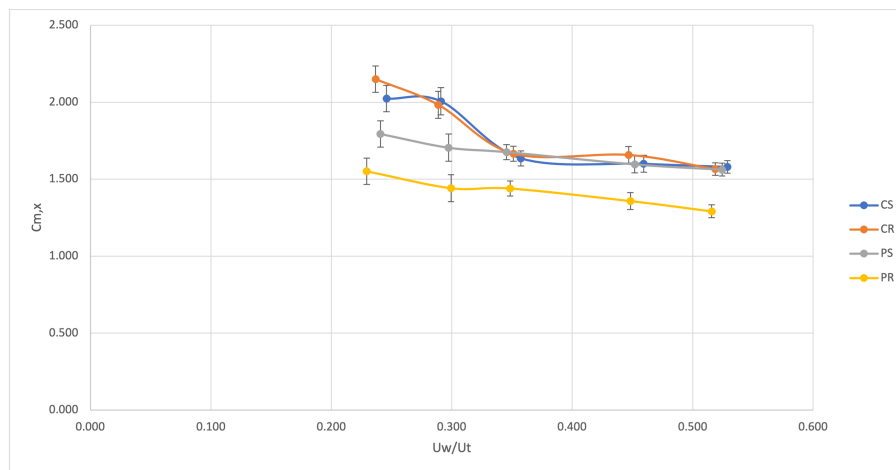


Figure 4.40: Horizontal inertia coefficients for varying tunnel shapes in combined conditions

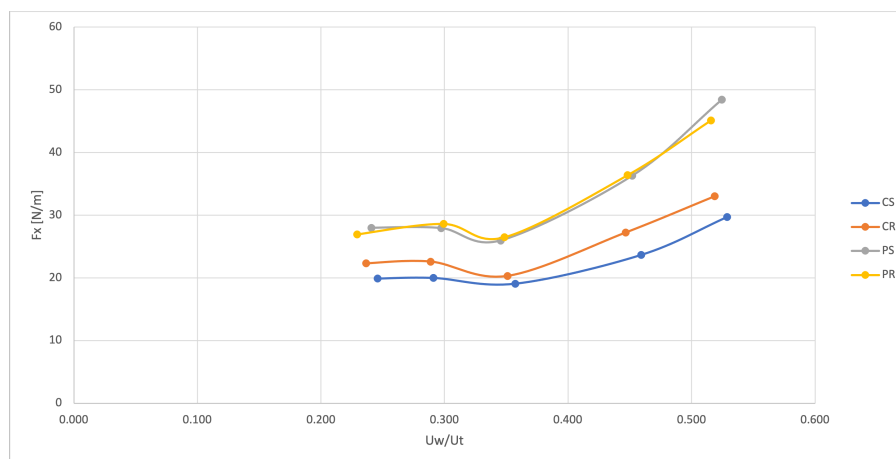


Figure 4.41: Measured horizontal forces for varying tunnel shapes in combined conditions

Vertical Inertia Coefficient

Similar to the wave test results, figure 4.42 shows that the parametric-shaped tunnels have larger vertical inertia coefficients. The explanation used in the wave test section, which includes the larger blockage area and the larger displaced water volume, still holds. The addition of a current that flows in the horizontal direction only has a small effect on the vertical coefficients. The forces in figure 4.43 show the same behavior as the forces from the wave tests.

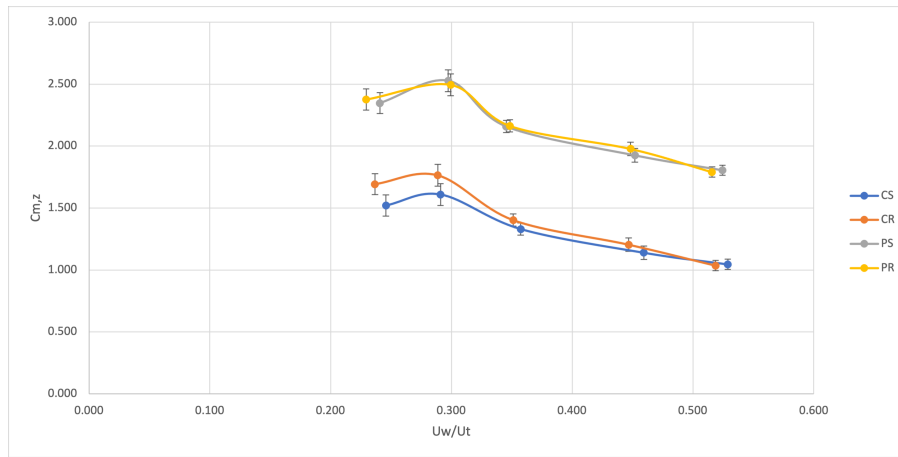


Figure 4.42: Vertical inertia coefficients for varying tunnel shapes in combined conditions

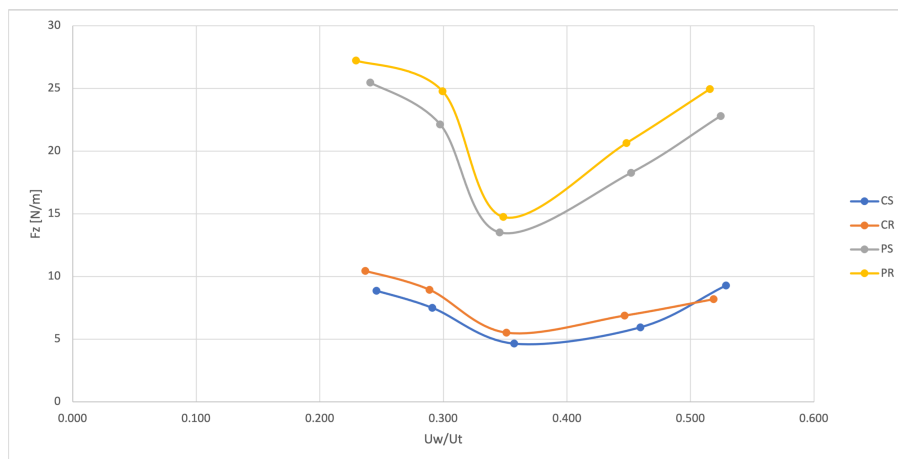


Figure 4.43: Measured vertical forces for varying tunnel shapes in combined conditions

Horizontal Drag Coefficient

In figure 4.44, the horizontal drag coefficients are presented. There is no influence of the shape of the tunnel observed in the graph since both smooth tunnels share equal coefficients, and while the parametric rough tunnel has larger horizontal drag coefficients in some of the cases; it still overlaps with the error bars from the circular rough tunnel. The equivalent diameter is the most important parameter for the drag coefficient. The circular and parametric rough tunnels share an equal increase in equivalent diameter, which explains why they have similar values for their drag coefficients. The advantage of the streamlined shape of the parametric-shaped tunnel on the drag coefficient seems to be reduced in the combined conditions.

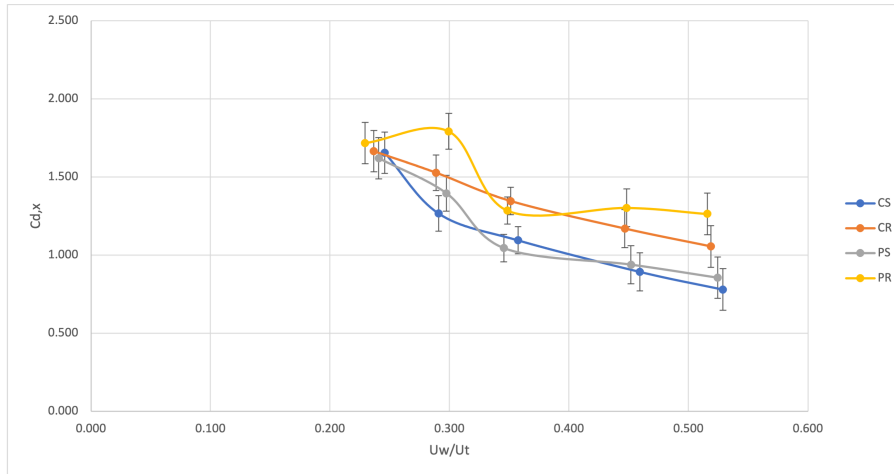


Figure 4.44: Horizontal drag coefficients for varying tunnel shapes in combined conditions

4.3.3 Influence of Roughness Height

Horizontal Inertia Coefficient

The results presented in figure 4.45 show that the presence of roughness decreases the inertia coefficients, as it does in the wave test results as well. There is no difference between the coefficients of the small and large roughness cases. However, the forces in figure 4.46 show that the tunnel with small roughness experiences a smaller force than the large roughness case. This can in part be explained by the larger increase in equivalent diameter for the large roughness case, causing a larger increase in drag force. It could also mean that the higher number of roughness elements in the small roughness case, causes a larger decrease in inertia force by decreasing the flow velocity. The smooth tunnel has the highest force for the last combined case, indicating that the decrease in inertia force caused by the presence of roughness, is larger than the increase in drag force.

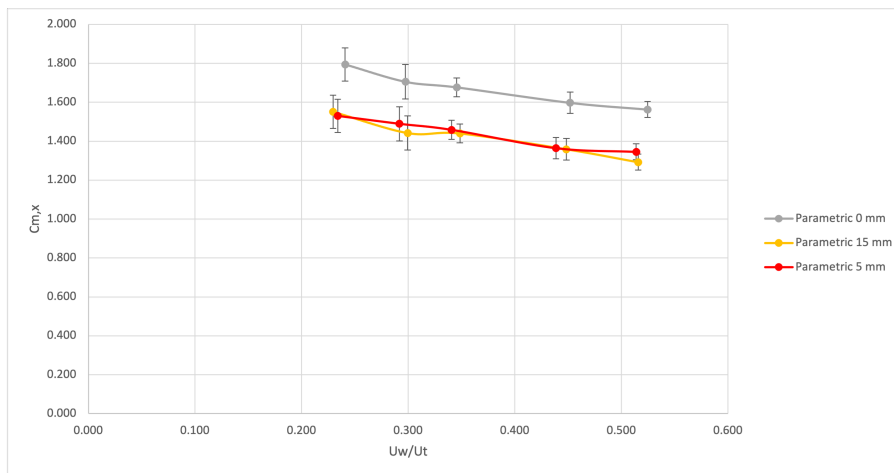


Figure 4.45: Horizontal inertia coefficients for varying roughness heights in combined conditions

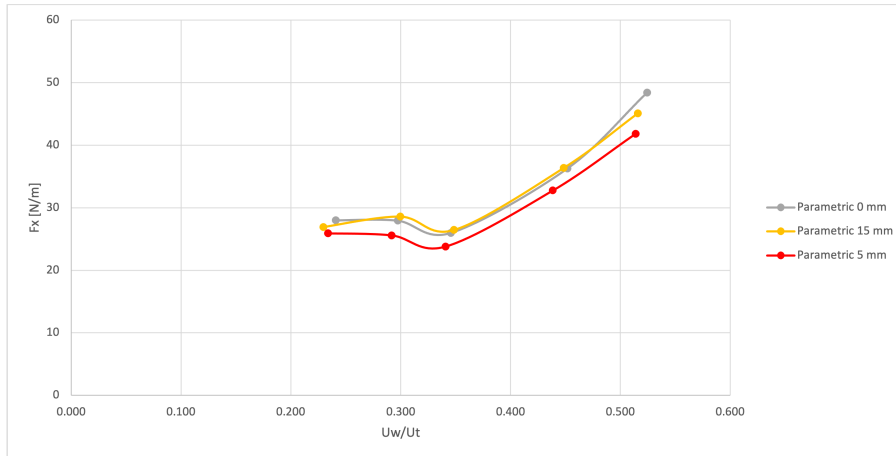


Figure 4.46: Measured horizontal forces for varying roughness heights in combined conditions

Vertical Inertia Coefficient

For the vertical inertia coefficient, there is no influence of the roughness height found when analyzing figure 4.47. All three roughness heights have the same vertical inertia coefficients. Since the current only acts in the horizontal direction, it was expected that similar results would be found compared to the wave tests. The forces in figure 4.48 show that the small and large roughness height cases share equal vertical forces. Again, there is a balance between the increase in drag force when the roughness height increases and the decrease in inertia force when the number of roughness elements increases.

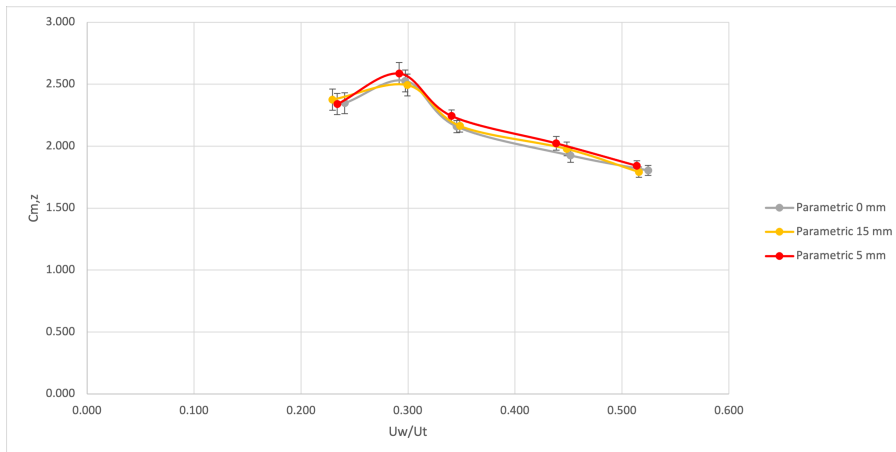


Figure 4.47: Vertical inertia coefficients for varying roughness heights in combined conditions

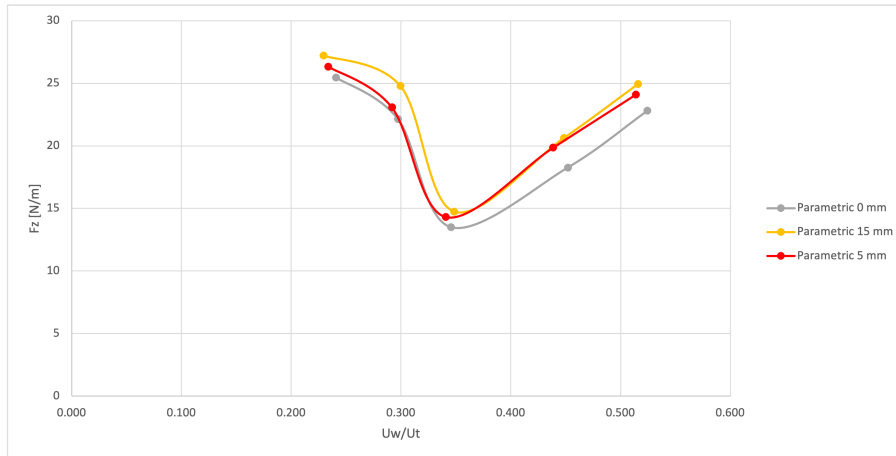


Figure 4.48: Measured vertical forces for varying roughness heights in combined conditions

Horizontal Drag Coefficient

Figure 4.49 shows the horizontal drag coefficient results for varying roughness heights. The tunnel with large roughness has higher drag coefficients compared to the smooth and small roughness cases. This can be explained by the higher equivalent diameter of the tunnel leading to a larger wake, and the roughness elements adding more surface area to the tunnel. The small roughness tunnel has a similar, and sometimes even lower, drag coefficient compared to the smooth case. However, they fall within the range of each other's error bars.

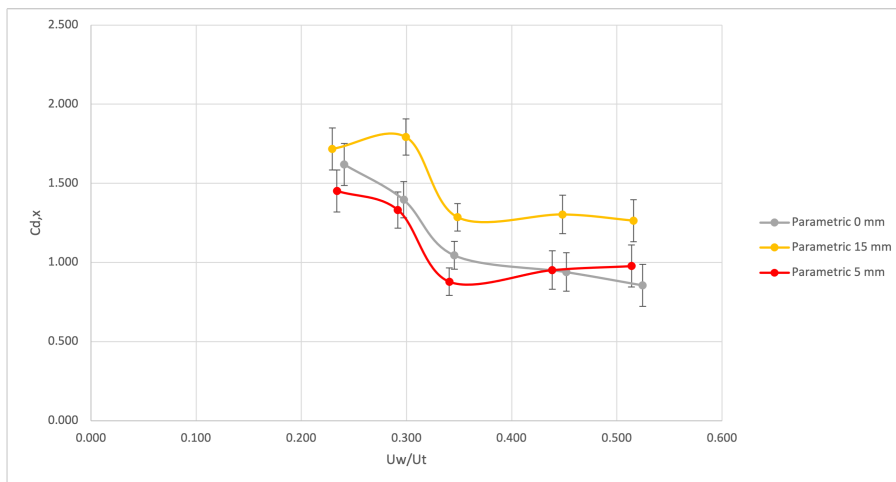


Figure 4.49: Horizontal drag coefficients for varying roughness heights in combined conditions

4.3.4 Influence of Coverage Percentage

Horizontal Inertia Coefficient

Similar to the results for the influence of roughness height, figures 4.50 and 4.51 show that while the inertia coefficients of the 100% and 50% coverage tunnels are close, the force on the 50% coverage tunnel is lower. The 100% coverage tunnel has the largest equivalent diameter, leading to a larger drag force, and apparently, the decrease in inertia force that the higher number of elements on this tunnel causes is lower than the increase in drag force.

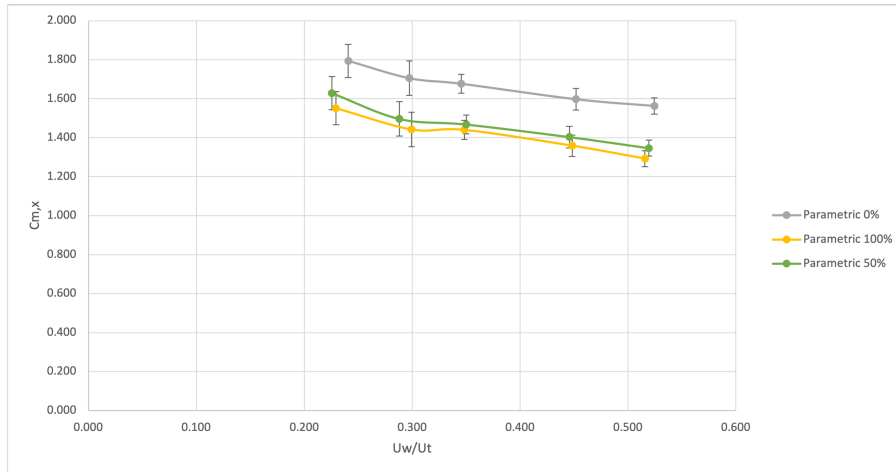


Figure 4.50: Horizontal inertia coefficients for varying coverage percentages in combined conditions

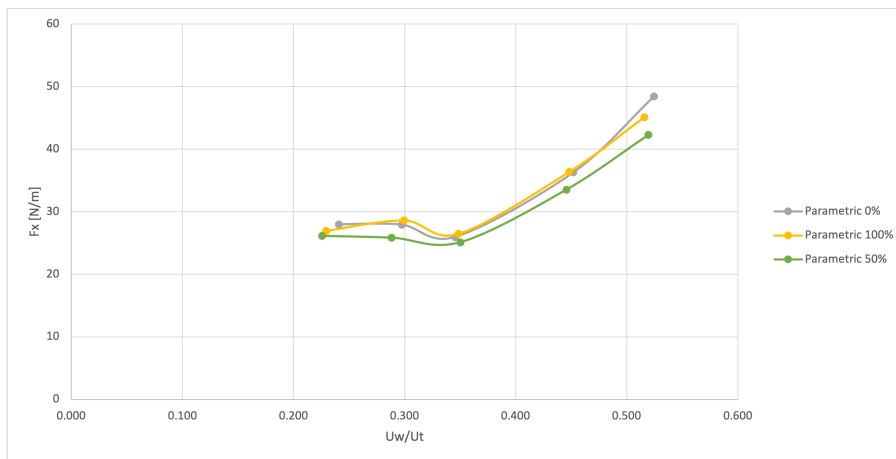


Figure 4.51: Measured horizontal forces for varying coverage percentages in combined conditions

Vertical Inertia Coefficient

Figures 4.52 and 4.53 show similar behavior to the influence of roughness height graphs. All three coverage percentage tunnels have equal inertia coefficients, while the vertical force on the 50% and 100% tunnels is equally larger. The increase in equivalent diameter and number of elements is in balance again.

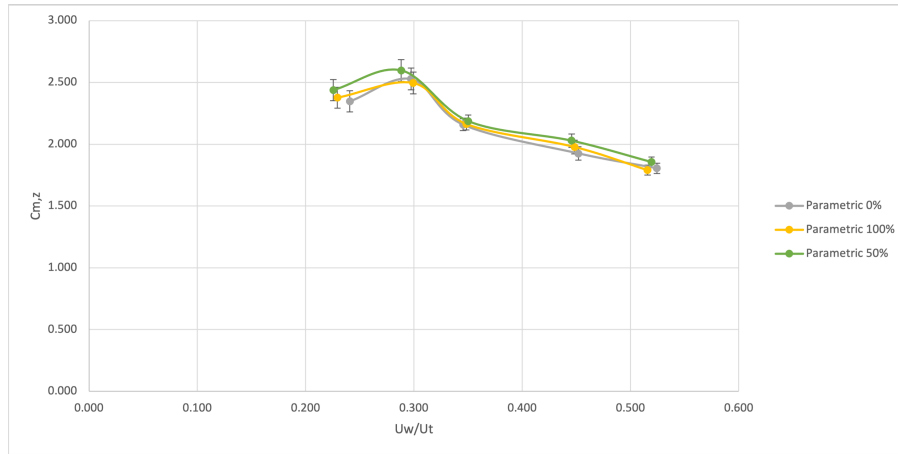


Figure 4.52: Vertical inertia coefficients for varying coverage percentages in combined conditions

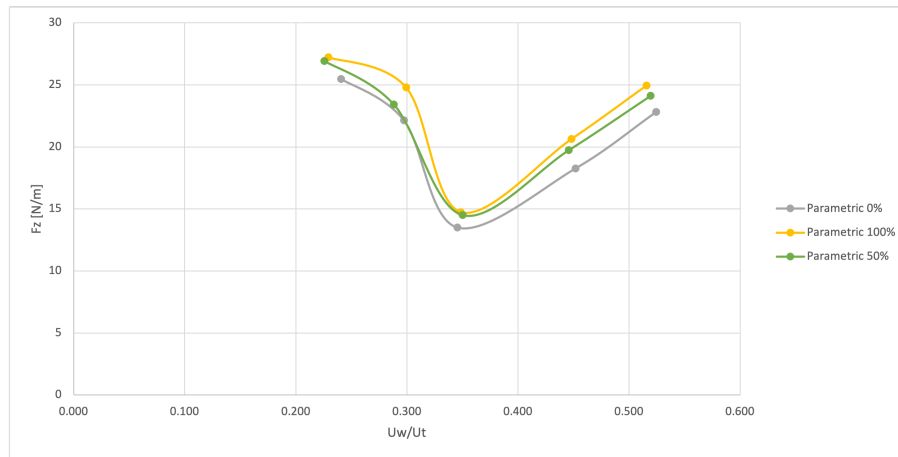


Figure 4.53: Measured vertical forces for varying coverage percentages in combined conditions

Horizontal Drag Coefficient

Similar to the current only results, the horizontal drag coefficients of the 0% and 50% covered tunnels are equal, as shown in figure 4.54. The 100% coverage tunnel shows a clear increase in drag coefficient, caused by the increase in equivalent diameter and surface area. Compared to the wave conditions, the increased equivalent diameter causes a higher increase in drag force for the combined conditions. This can be explained by noting that the addition of the current increases the KC and Reynolds numbers, thereby decreasing the relative contribution of the skin friction and increasing the importance of the equivalent diameter.

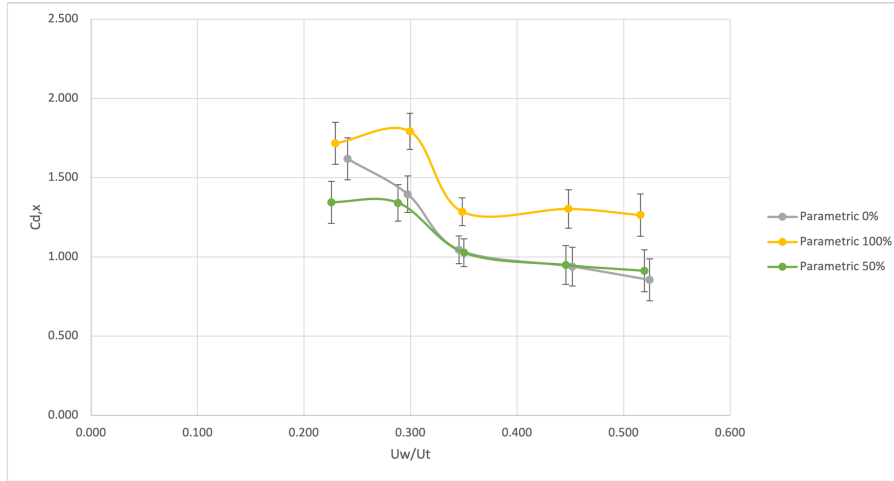


Figure 4.54: Horizontal drag coefficients for varying coverage percentages in combined conditions

4.4 Force Prediction

In this section, the force coefficients found in this thesis are used to propose fitted force coefficients. These can be used to predict the forces on a submerged floating tunnel with different shapes, roughness heights, and coverage percentages. The proposed coefficients are valid for the tested range of KC numbers and for similar blockage ratios. For the wave results, the horizontal KC numbers range from 0.15 to 1.5 for the parametric-shaped tunnels, and from 0.3 to 3 for the circular-shaped tunnels. The vertical KC numbers range from 0.25 to 1.4 for both tunnels. For the combined results, the factor Uw/Ut ranges from 0.22 to 0.52. All blockage ratios are between 22.3% and 24.5%. Coefficients from engineering codes are used to predict the forces as well, and the results are compared to the measured forces to find the accuracy of each set of coefficients. First, coefficients from engineering codes are discussed, followed by the newly found coefficients. Finally, the results of the force prediction using the Morison equation are presented.

4.4.1 Force Coefficients from Engineering Codes

Force coefficients from the API (API, 2014) and DNV (DNV, 2010) codes are used to predict the force on the tunnels. For wave conditions, this is achieved by providing drag and inertia coefficients and using them in the Morison equation. For the drag coefficient, both codes use a steady flow drag coefficient named C_{Ds} that has separate values for rough and smooth cylinders, and combine it with a wake amplification factor that is a function of the KC number. For the inertia coefficients, both codes state that there is no difference in the inertia coefficient for smooth and rough cylinders, as long as KC is smaller than 12.

For current conditions, the drag coefficients are equal to the steady flow drag conditions. For combined wave and current conditions, the same coefficients as for the wave conditions are used. The only difference is the KC number, which is now calculated by adding the current velocity to the maximum orbital velocity and using that value in the KC formula. In the following paragraphs, the coefficients of both codes are discussed.

DNV Code

According to (DNV, 2010), the drag coefficient can be determined by using the following formula:

$$C_D = C_{DS,DNV} \cdot \psi(KC) \quad (4.3)$$

Where:

$$\begin{aligned}
C_D &= \text{Drag coefficient [-]} \\
C_{DS,DNV} &= \text{Steady flow drag coefficient from (DNV, 2010) [-]} \\
\psi(K_C) &= \text{Wake amplification factor as a function of } KC \text{ [-]}
\end{aligned}$$

The wake amplification factor, ψ , can be calculated using the equations 4.4 and 4.5, and the steady flow drag coefficients are given in 4.6.

$$\psi(K_C) = \begin{cases} C_\pi + 0.10(K_C - 12) & 2 \leq K_C < 12 \\ C_\pi - 1.00 & 0.75 \leq K_C < 2 \\ C_\pi - 1.00 - 2.00(K_C - 0.75) & K_C \leq 0.75 \end{cases} \quad (4.4)$$

$$C_\pi = 1.50 - 0.024 \cdot (12/C_{DS} - 10) \quad (4.5)$$

$$C_{DS,DNV} = \begin{cases} 0.65 & \text{(smooth)} \\ 1.05 & \text{(rough)} \end{cases} \quad (4.6)$$

The inertia coefficient is defined as $C_M = C_A + 1$, where C_A is the added mass coefficient. For $KC < 3$, the added mass coefficient has a constant value of 1. For $KC > 3$, the inertia coefficient is determined using equation 4.7.

$$C_A = \max \left\{ \begin{array}{l} 1.0 - 0.044(K_C - 3) \\ 0.6 - (C_{DS} - 0.65) \end{array} \right\} \quad (4.7)$$

API Code

In (API, 2014), the following steady flow drag coefficients are provided:

$$C_{DS,API} = \begin{cases} 0.6 & \text{(smooth)} \\ 1.1 & \text{(rough)} \end{cases} \quad (4.8)$$

The drag coefficient can be determined using the wake amplification factor relations shown in the graphs from figure 4.55, where $K = KC$.

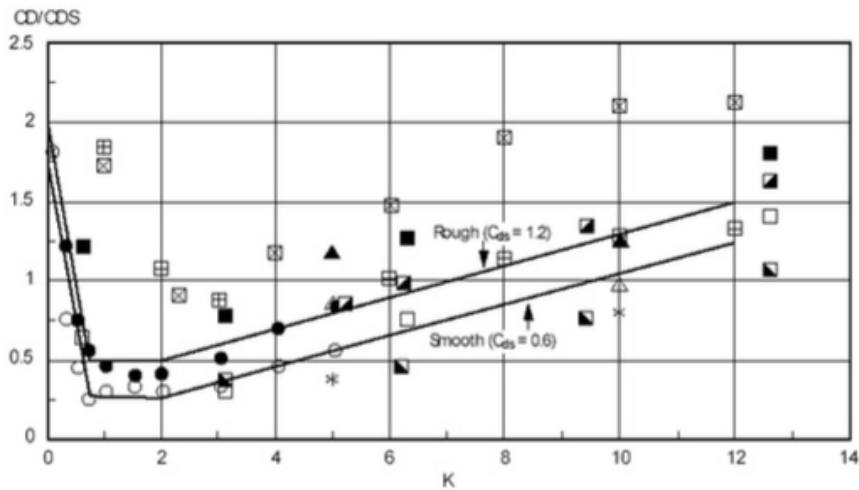


Figure 4.55: Wake amplification factor for drag coefficients (API, 2014)

The inertia coefficient can be determined using the relations shown in the graphs from figure 4.56, where $K = KC$.

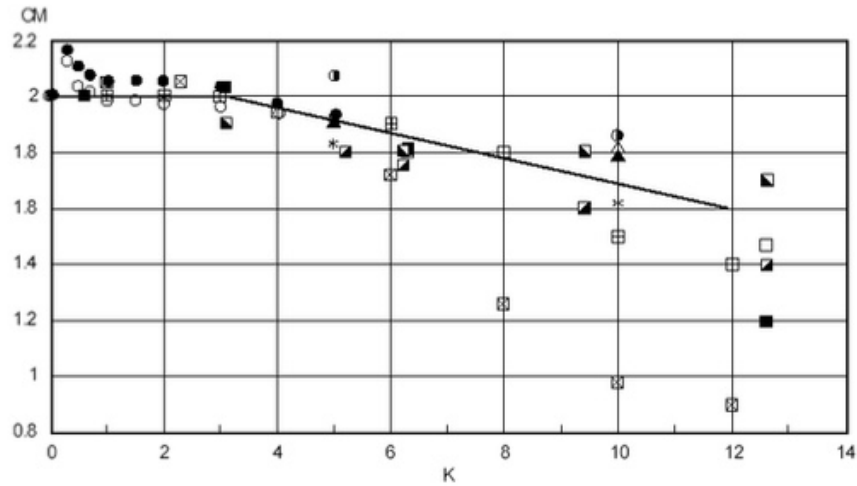


Figure 4.56: Inertia coefficient as a function of KC (API, 2014)

4.4.2 Fitted Force Coefficients

As shown in the previous section, force coefficients in engineering codes are proposed with different expressions for different segments of KC numbers. The same method is used to fit the force coefficients for the tested range of KC numbers, and the coefficients that are presented in this section are only valid in this range and offer no information outside of it. The fitted force coefficients were found by drawing trend lines through the scatter plots of the found results. Separate coefficients were determined for the current tests, wave tests, and combined tests. In the paragraphs below, the method of finding the fitted coefficients is described per condition.

Current Coefficients

From the current test results, only the drag coefficients are covered in this chapter, since the lift coefficient results proved to be too low. As explained in section 4.1, the downwards trend that was found in the drag coefficients and shown in figure 4.5, is not there in results from other studies. Therefore, a constant value was chosen as the fitted drag coefficient for each separate tunnel. The average value of the drag coefficients for the three different current velocities was rounded and used as the constant value. Because of the large error bars and the scatter in the results, the drag coefficients are proposed along with a 10% range to account for this variability. In table 4.1, the fitted drag coefficients in current conditions are presented.

Tunnel	C_d
CS	$1.7 \pm 10\%$
CR	$1.7 \pm 10\%$
PS	$1.2 \pm 10\%$
PR	$1.5 \pm 10\%$
PRS	$1.2 \pm 10\%$
PR50	$1.2 \pm 10\%$

Table 4.1: Fitted drag coefficients in current conditions

Wave and Combined Coefficients

The fitted drag and inertia coefficients were determined by drawing trend lines through the coefficient curves. For each curve, the best-fitting trend line was chosen. If all coefficients were close and their error bars overlapped, one trend line was determined by drawing it for all the values of each of the test cases. An example is shown in figure 4.57, where the parametric-shaped tunnels in wave conditions

share similar vertical inertia coefficients, and a second-order polynomial trend line was drawn through all the data points. If there were significant differences, multiple coefficients were determined either per tunnel shape or per roughness case. In Appendix I, a detailed explanation of the determination of all fitted coefficients can be found. The found expressions cannot be used outside of the tested range of KC numbers, because that would quickly lead to unrealistic coefficients. For the drag coefficients, the current results can be used as an indication of the drag coefficient at high KC numbers, since current-only conditions are equivalent to an infinite KC number. For the inertia coefficients, more tests need to be conducted at higher KC numbers to determine the coefficient expressions outside the tested segment of KC.

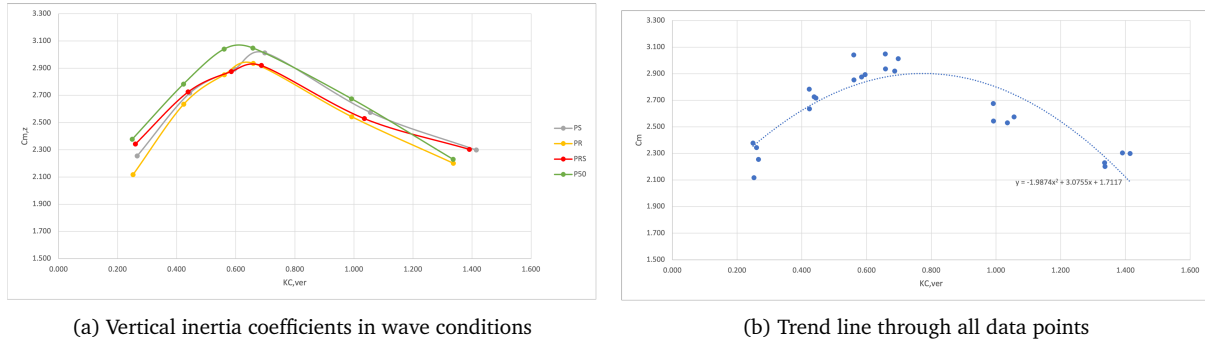


Figure 4.57: Vertical inertia coefficients of the parametric-shaped tunnels and their combined trend line

Fitted Coefficient Results

In tables 4.2 and 4.3, the results of fitting the force coefficients are summarized for the wave conditions and combined conditions, respectively. Here it can be seen that the vertical drag coefficients of the circular tunnels are zero in wave conditions, an explanation for this is offered in Appendix I.

	Cd_x	Cm_x	Cd_z	Cm_z
CS	$3.9 KC_x^{-1.4}$	$-0.125 KC_x + 2.2$	0	$-1.1 KC_z + 2.38$
CR	$3.9 KC_x^{-1.4}$	$-0.125 KC_x + 2.2$	0	$-1.1 KC_z + 2.38$
PS	$3.9 KC_x^{-1.4}$	$-0.37 KC_x^2 + 0.54 KC_x + 1.48$	$3.37 KC_z^{-2.171}$	$-1.99 KC_z^2 + 3.1 KC_z + 1.7$
PR	$3.9 KC_x^{-1.4}$	$-0.39 KC_x^2 + 0.67 KC_x + 1.25$	$3.37 KC_z^{-2.171}$	$-1.99 KC_z^2 + 3.1 KC_z + 1.7$
PRS	$3.9 KC_x^{-1.4}$	$-0.39 KC_x^2 + 0.67 KC_x + 1.25$	$3.37 KC_z^{-2.171}$	$-1.99 KC_z^2 + 3.1 KC_z + 1.7$
PR50	$3.9 KC_x^{-1.4}$	$-0.39 KC_x^2 + 0.67 KC_x + 1.25$	$3.37 KC_z^{-2.171}$	$-1.99 KC_z^2 + 3.1 KC_z + 1.7$

Table 4.2: Fitted force coefficients for all tunnels in wave conditions

	Cd_x	Cm_x	Cd_z	Cm_z
CS	$-2.52 Uw/Ut + 2.18$	$-1.85 Uw/Ut + 2.48$	$0.125 Uw/Ut^{-1.63}$	$-2.3 Uw/Ut + 2.23$
CR	$-2.52 Uw/Ut + 2.18$	$-1.85 Uw/Ut + 2.48$	$0.125 Uw/Ut^{-1.63}$	$-2.3 Uw/Ut + 2.23$
PS	$-1.94 Uw/Ut + 1.93$	$-0.78 Uw/Ut + 1.96$	$0.155 Uw/Ut^{-2.25}$	$-2.3 Uw/Ut + 3.04$
PR	$-1.94 Uw/Ut + 1.93$	$-0.81 Uw/Ut + 1.74$	$0.155 Uw/Ut^{-2.25}$	$-2.3 Uw/Ut + 3.04$
PRS	$-1.94 Uw/Ut + 1.93$	$-0.81 Uw/Ut + 1.74$	$0.155 Uw/Ut^{-2.25}$	$-2.3 Uw/Ut + 3.04$
PR50	$-1.94 Uw/Ut + 1.93$	$-0.81 Uw/Ut + 1.74$	$0.155 Uw/Ut^{-2.25}$	$-2.3 Uw/Ut + 3.04$

Table 4.3: Fitted force coefficients for all tunnels in combined conditions

4.4.3 Force Prediction Results

Using the API and DNV coefficients and the newly fitted coefficients, labeled as NC, the forces on the tunnels are predicted. The maxima of the predicted forces are compared with the measured forces to

check the prediction accuracy of each coefficient. For the wave and combined results, the measured force is determined by taking the mean value of the maxima of the selected waves that were used to determine the coefficients. For the current results, the predicted forces are compared to the mean drag forces. The error is calculated by taking the ratio of predicted force over measured force. A negative error indicates an underestimation of the force, a positive error indicates an overestimation. In the following paragraphs, the force prediction results are presented and discussed, along with their errors compared to the measured forces. It must be noted that the fitted coefficients are determined from a scattered data set and that the found coefficients should be applied with a margin of error. The margin of error needs to be determined by conducting more tests and comparing the results to the forces predicted by using the fitted coefficients.

Current Results

The (API, 2014) and (DNV, 2010) codes do not contain a correction factor for the increased velocity caused by the high blockage ratio of a cylinder. Therefore, an underestimation of the drag force on the circular-shaped tunnels is expected. Additionally, the proposed coefficients in the codes are for circular cylinders, and no shape factor that corresponds to the parametric shape of the tunnels is offered. Force prediction using the API and DNV coefficients indeed underestimates the mean drag forces on a circular smooth tunnel by more than 60%, as shown in table 4.4. The forces on a circular rough tunnel are underestimated by at least 33% for both codes, as can be seen in table 4.5.

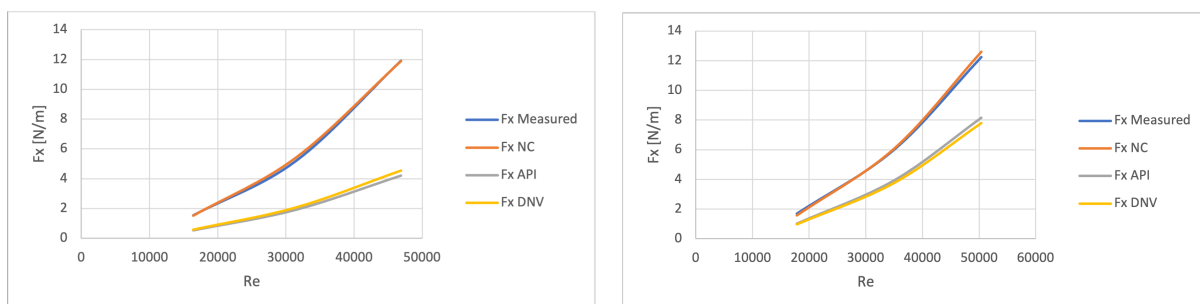
	Error NC	Error API	Error DNV
CS.C1	-1.95%	-65.58%	-62.34%
CS.C2	4.24%	-63.20%	-60.12%
CS.C3	-0.25%	-64.77%	-61.83%

Table 4.4: Force prediction errors for the circular smooth tunnel in current conditions

	Error NC	Error API	Error DNV
CR.C1	-6.51%	-39.64%	-42.60%
CR.C2	1.34%	-34.39%	-37.40%
CR.C3	3.02%	-33.33%	-36.36%

Table 4.5: Force prediction errors for the circular rough tunnel in current conditions

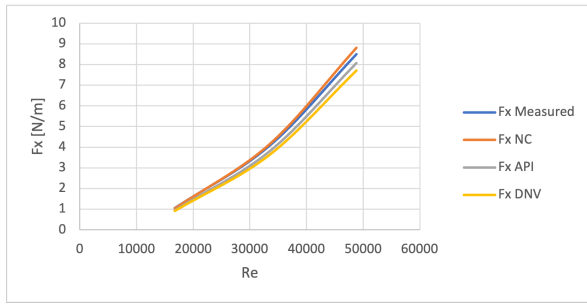
In figure 4.58, the predicted drag forces are compared to the measured horizontal force for both circular-shaped tunnels. These figures show the large underestimation for the circular smooth tunnel and the smaller underestimation for the circular rough tunnel. The coefficients from the codes predict the forces on the parametric-shaped tunnels much better, as shown in figure 4.59. This is not as surprising as it sounds, since the parametric shape lowers the drag coefficients, which negates the increase in drag coefficients caused by the high blockage ratio. In Appendix J, the errors of each coefficient for the parametric-shaped tunnels can be found.



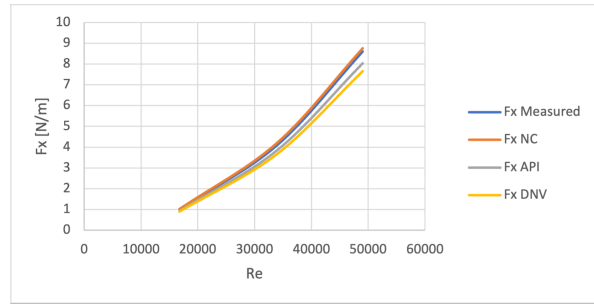
(a) Predicted forces on the circular smooth tunnel

(b) Predicted forces on the circular rough tunnel

Figure 4.58: Mean drag force prediction on the circular-shaped tunnels in current conditions



(a) Predicted forces on the parametric small roughness tunnel

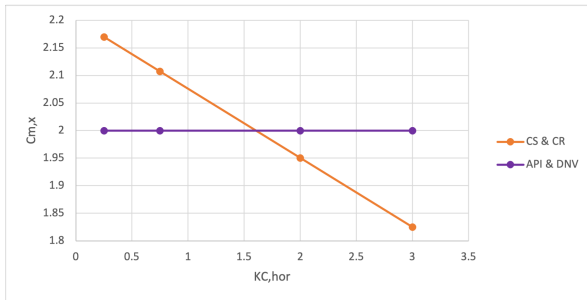


(b) Predicted forces on the parametric 50% coverage tunnel

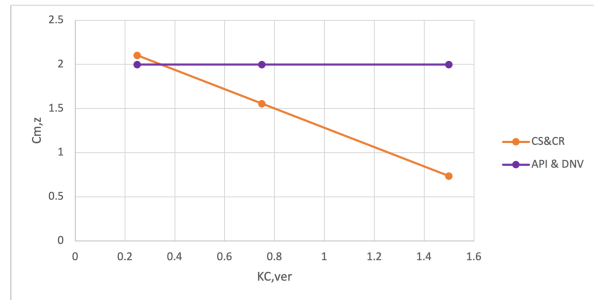
Figure 4.59: Mean drag force prediction on two parametric-shaped tunnels in current conditions

Wave Results

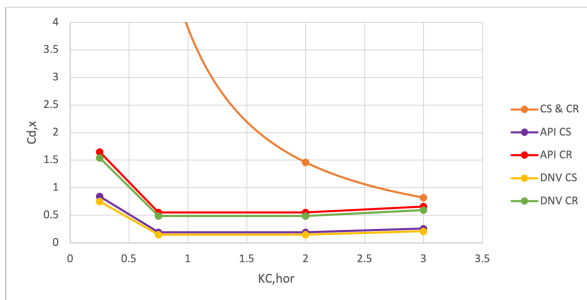
In figure 4.60, the coefficients from API and DNV codes are compared to the fitted coefficients found in this thesis. Only the circular-shaped tunnels are compared to the codes since no shape influence factor that matches the parametric-shaped tunnel is provided. The vertical coefficients follow the same equations as the horizontal ones, as the API and DNV codes base their coefficients for wave forces on vertical cylinders and no information is provided on horizontal cylinders.



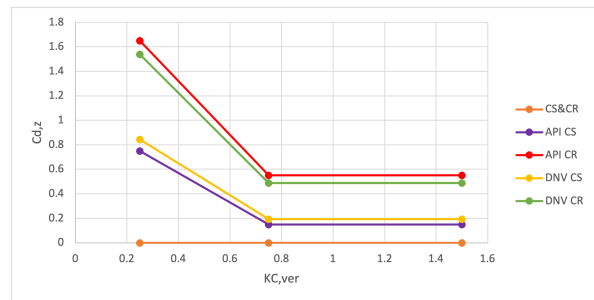
(a) Horizontal inertia coefficients



(b) Vertical inertia coefficients



(c) Horizontal drag coefficients



(d) Vertical drag coefficients

Figure 4.60: Fitted force coefficients compared to code for circular-shaped tunnels in wave conditions

In tables 4.6 and 4.7, the force prediction errors of each of the coefficients are shown for the circular smooth and the circular rough tunnel, respectively. For both the horizontal and vertical force, coefficients from the API and DNV codes compare negatively to the NC coefficients. The errors are much larger for the vertical direction, but this was expected since horizontal cylinders are not covered in the codes so there are no specific vertical coefficients proposed.

	Error NC	Error API	Error DNV
CS.W1	-1.70%	-11.11%	-11.09%
CS.W2	-2.70%	-9.57%	-9.54%
CS.W3	-0.43%	-5.06%	-5.07%
CS.W4	-1.61%	-2.98%	-2.98%
CS.W5	-1.41%	2.16%	2.19%
CS.W6	4.30%	14.05%	14.12%

	Error NC	Error API	Error DNV
CS.W1	-5.26%	-1.46%	-1.49%
CS.W2	-5.44%	-1.58%	-1.59%
CS.W3	-4.97%	4.44%	4.47%
CS.W4	-0.68%	16.35%	16.35%
CS.W5	-7.87%	55.56%	55.51%
CS.W6	-7.92%	146.31%	146.35%

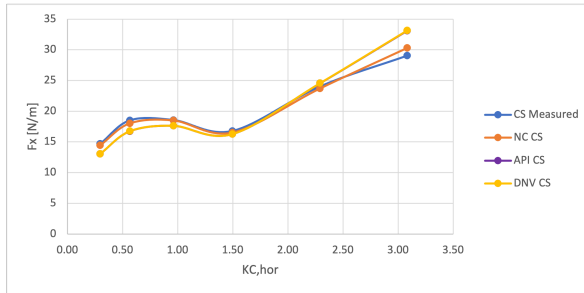
Table 4.6: Horizontal (left) and vertical (right) force prediction errors for the circular smooth tunnel in wave conditions

	Error NC	Error API	Error DNV
CR.W1	-0.19%	-11.58%	-11.57%
CR.W2	1.34%	-7.01%	-7.03%
CR.W3	-4.01%	-9.22%	-9.23%
CR.W4	-6.31%	-8.34%	-8.34%
CR.W5	-3.39%	-0.78%	-0.84%
CR.W6	-1.83%	6.34%	6.22%

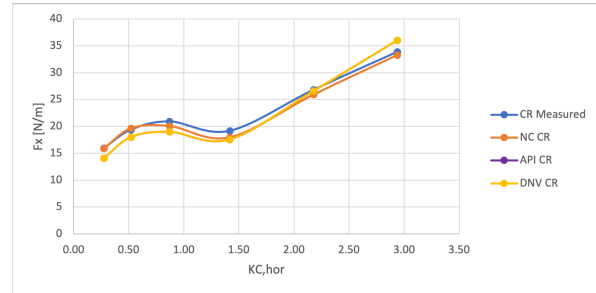
	Error NC	Error API	Error DNV
CR.W1	-3.96%	0.46%	0.42%
CR.W2	-2.85%	0.54%	0.53%
CR.W3	-6.75%	0.79%	0.77%
CR.W4	-3.09%	10.45%	10.43%
CR.W5	-2.60%	51.67%	51.6%
CR.W6	-16.27%	103.31%	103.22%

Table 4.7: Horizontal (left) and vertical (right) force prediction errors for the circular rough tunnel in wave conditions

In figure 4.61, the predicted horizontal forces are compared to the measured horizontal force for both the circular smooth and the circular rough tunnel. The API and DNV results overlap because of their almost equal coefficients. The figure shows that while the API and DNV codes provide an accurate prediction of the horizontal force, it is not as accurate as the new coefficients. There is a larger underestimation of the force for the lower KC values, and a larger overestimation for the higher KC values.



(a) Horizontal forces on the circular smooth tunnel



(b) Horizontal forces on the circular rough tunnel

Figure 4.61: Comparison between measured and predicted horizontal forces on the circular-shaped tunnels in wave conditions

There are several factors that negatively influence the accuracy of the force predictions using code coefficients. The absence of blockage influence and the lack of consideration of horizontal cylinders are already mentioned. Additionally, the definition of the cylinder diameter is different in this thesis, as an equivalent diameter is used. The diameter influences the coefficients and the dimensionless parameters such as the KC number, which possibly leads to different results. Also, the codes provide coefficients for the post-critical flow regime. In the experiments, the flow was still in the sub-critical regime, which might also explain some of the differences. These factors need to be included in engineering codes to provide reasonable force predictions.

The errors for the parametric-shaped tunnel force predictions can be found in Appendix J. There it is shown that the new coefficients have a prediction error below 10% for all tunnels in both the horizontal

and vertical forces. The API and DNV have a prediction error between 10% and 40%, this shows the need for new guidelines concerning the parametric-shaped tunnel if it is to be constructed.

Combined Results

In order to determine the coefficients from the codes, the KC numbers needed to be calculated for the combined conditions by adding the current velocity to the maximum orbital velocity. It was then determined to which U_w/U_t values the new KC numbers correspond. In figure 4.62, the coefficients from API and DNV codes are compared to the fitted coefficients found in this thesis. Figure 4.62a shows that the horizontal inertia coefficients from the codes do have a downward trend, but the angle is much smaller. The horizontal drag coefficients presented in figure 4.62c show that the trend of the coefficients from the codes is directed upward, contrary to the fitted coefficients that have a downward trend. Surprising is the fact that the vertical drag coefficients from the codes match the fitted coefficients well, even though they were not derived for horizontal cylinders.

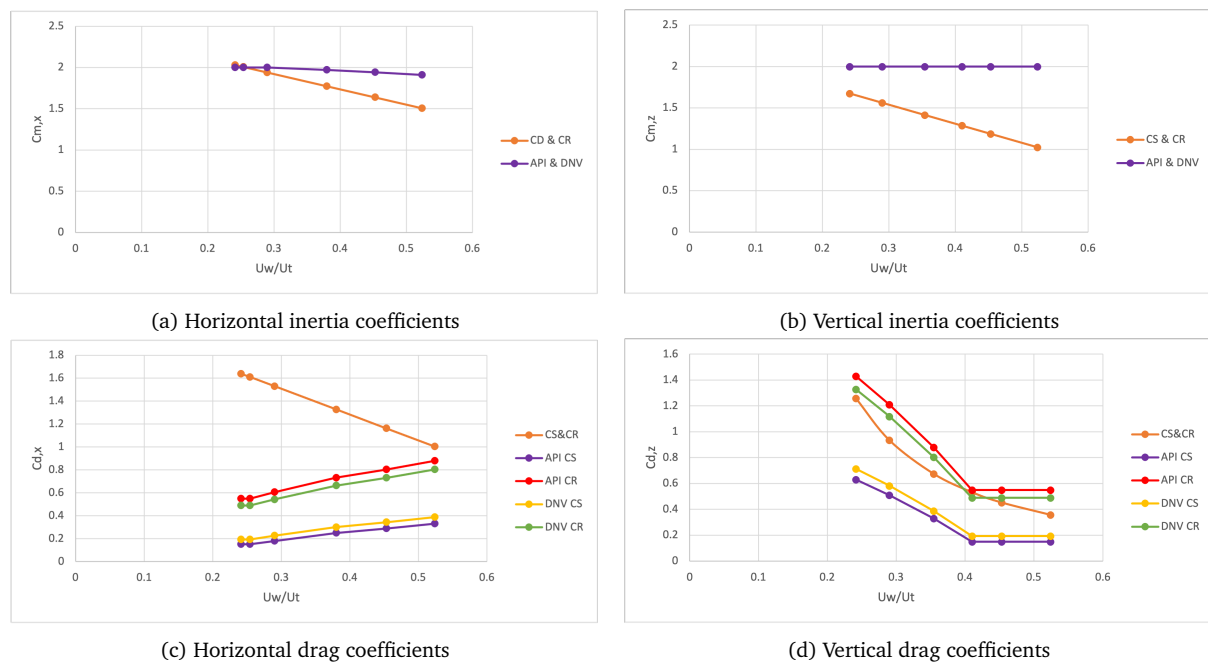


Figure 4.62: Fitted force coefficients compared to code for circular-shaped tunnels in combined conditions

In tables 4.8 and 4.9, the force prediction errors of each of the coefficients are shown for the circular smooth and the circular rough tunnel, respectively. Similar to the wave test results, the API and DNV codes underestimate the horizontal forces on the circular-shaped tunnels. Only for the highest U_w/U_t case, the force is predicted well by the code coefficients. At this point, the underestimation of the drag coefficient is compensated for by an overestimation of the inertia coefficient. The vertical forces are significantly overestimated when using the API coefficients. This is caused by a large overestimation of the inertia coefficient.

	Error NC	Error API	Error DNV
CS.CW2	-4.18%	-29.40%	-28.71%
CS.CW3	-5.36%	-25.21%	-24.45%
CS.CW4	-5.62%	-22.47%	-21.52%
CS.CW5	-6.09%	-8.07%	-7.07%
CS.CW6	-12.89%	-4.17%	-3.14%

	Error NC	Error API	Error DNV
CS.CW2	5.64%	25.34%	25.34%
CS.CW3	-1.07%	27.36%	27.36%
CS.CW4	13.58%	59.43%	59.45%
CS.CW5	15.49%	93.85%	93.85%
CS.CW6	-13.69%	68.77%	68.77%

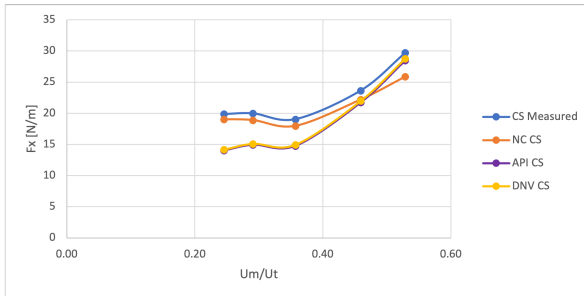
Table 4.8: Horizontal (left) and vertical (right) force prediction errors for the circular smooth tunnel in combined conditions

	Error NC	Error API	Error DNV
CR.CW2	-5.96%	-25.48%	-26.50%
CR.CW3	-7.61%	-21.29%	-22.39%
CR.CW4	-2.17%	-11.03%	-12.55%
CR.CW5	-6.10%	-3.49%	-4.93%
CR.CW6	-13.39%	4.39%	2.82%

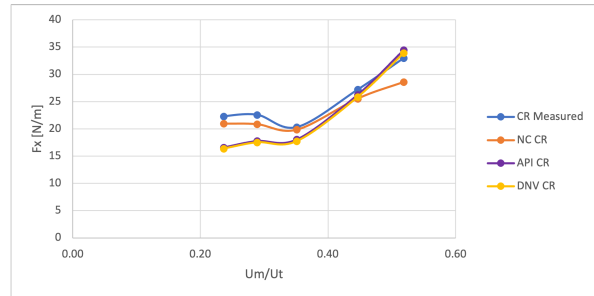
	Error NC	Error API	Error DNV
CR.CW2	-2.30%	15.53%	15.41%
CR.CW3	-9.06%	16.67%	16.50%
CR.CW4	4.91%	46.88%	46.63%
CR.CW5	9.75%	82.20%	82.02%
CR.CW6	7.82%	108.39%	108.12%

Table 4.9: Horizontal (left) and vertical (right) force prediction errors for the circular rough tunnel in combined conditions

In figure 4.63, the predicted horizontal forces are compared to the measured horizontal force for both the circular smooth and the circular rough tunnel. The API and DNV codes compensate their low drag coefficients with high inertia coefficients, and even overestimate the horizontal force on the circular rough tunnel at the highest U_w/U_t value. Similar reasons as mentioned for the wave test results are used to explain the large errors in the code-predicted forces. Not factoring in the increased velocity due to the high blockage ratio, having different definitions for the cylinder diameter, and not having separate equations for horizontal cylinders are the main issues that need to be resolved, if reasonable force predictions for SFTs are to be made. Similar to the wave test results, the errors of the force prediction for parametric-shaped tunnels in combined conditions can be found in Appendix J. There it is shown that the new coefficients can predict the forces within a 15% error margin, which is much more accurate than the code coefficients are able to.



(a) Forces on the circular smooth tunnel



(b) Forces on the circular rough tunnel

Figure 4.63: Comparison between measured and predicted forces on the circular-shaped tunnels in combined conditions

Now that all the relevant data of this research has been defined and analyzed, and is proven to have sufficient accuracy to provide physically realistic results, a discussion will follow on its possible limitations. These limitations originate from the chosen methodology, the data processing, and the assumptions that were made during this research. The next chapter will cover all these points to provide insight into how they might have had an influence on the found results.

Chapter 5

Discussion

In this chapter, a discussion about the methodology of this research, its limitations, and the assumptions made in the process can be found, where their possible errors and their influence on the found results are covered.

5.1 Definitions

For this research, various parameters had to be defined, and their definition was not always consistent with other research papers. The way some of these parameters were defined, could greatly influence the obtained results. In this section, those parameters are discussed.

5.1.1 Equivalent Diameter

The definition of the equivalent diameter influences the calculations of all drag coefficients. For this thesis, it was defined as the diameter of a tunnel with a blockage area equal to that of the used tunnel while including roughness. In literature, it is either defined as the smooth diameter, the rough diameter, or the author's own definition of an equivalent diameter, as seen in the paper by (Marty et al., 2021). As it is not known what the correct definition is, this can lead to different coefficients for similar experiments.

5.1.2 Cross-Sectional Area

Inertia coefficients are influenced by the definition of cross-sectional area, where a larger area leads to lower inertia coefficients. In this thesis, every roughness element is included in the total area. It is also possible to use the smooth cross-sectional area for all cases, which would remove the difference in cross-sectional area increase between different tunnel shapes. This was explained in 4.2, where the relative increase in cross-sectional area was larger for the circular-shaped tunnels than for the parametric-shaped tunnels.

5.1.3 Non-Dimensional Numbers

There are multiple definitions of the non-dimensional numbers used in this thesis, which include the Keulegan-Carpenter number, the U_w/U_t parameter, the Strouhal number, and the Reynolds number. A horizontal and vertical KC number was defined to include the effect of the horizontal diameter of the parametric-shaped tunnel, and the U_w/U_t parameter was used to show the ratio between orbital velocity and total velocity. In section 4.1, it was mentioned that a more universal definition of the Strouhal number could be adopted. All the mentioned non-dimensional numbers also depend on the definition of the equivalent diameter. Using different definitions of these numbers could lead to incorrect interpretations of the results.

5.2 Errors in the Velocity Signals

The velocity signals have two possible error sources, measurement inaccuracies, and data processing. Both of these sources are discussed in this section since most of the data processing issues originate from the way that the EMS measured the velocity. There were two main issues with the velocity signals measured by the EMS, it only measured velocity in the horizontal direction, and the velocity signal had a much smaller amplitude than was expected from using Stokes' second-order wave theory. For the current tests, these issues did not have to be solved in order to obtain usable results.

For the waves and combined conditions, the fact that only the horizontal velocity was measured has been dealt with by using a scaled value of the theoretical vertical orbital velocity, as was explained in Chapter 3. Later this scaling factor was removed when it was found that the velocity amplitude was too low, and both the horizontal and vertical theoretical orbital velocity signals were used. Whether the vertical velocity signal looks like the theoretical signal is unknown, and any boundary effects on the shape of the actual signal compared to a perfect Stokes wave were neglected in this research.

The wave period and wave height were measured for each test, and those values were used in the Stokes equations. Therefore, the damping that the boundary conditions of the flume had on the generated waves was already included in the theoretical signals. But as mentioned in the previous paragraph, there could be other effects that would lead to a more damped signal with a lower velocity, and these effects have been neglected by using the theoretical wave signals. This method was chosen because the measured amplitude of the orbital velocity was up to 25% lower in some wave cases, and since Stokes' theory is a method proven to be accurate, it was decided to trust Stokes' results over the measured EMS signals.

In the combined conditions, the wave height was decreased compared to the input wave height by the addition of the current, as can be seen in Appendix C. These lowered wave heights were used in the Stokes equations and the results together with the mean current velocity were used in the Morison equation. The waves became distorted by the current because of the inflow conditions, where the current first enters the flume in a small reservoir directly below the panel of the wave generator. This caused a very turbulent flow that disturbed the generated waves. The wave heights and period were measured for every separate test, but due to the current, these values had a lot of variability between them. This led to differences in wave heights between some of the tests, especially for the smaller waves, which in turn led to differences in the theoretical velocity signals. This could have a significant influence on the found results.

5.3 Time Shift Calculation Errors

In section 4.2, it was shown that the effect of the time shift is large when it comes to the drag coefficients, but it was also significant for determining the inertia coefficients. There are several factors that could negatively influence the time shift calculations, the determined wave celerity, the distance between the wave gauges and their distance to the tunnel, the motion of the tunnel, and the definition of the location where to measure the time shift.

The wave celerity and the distance between the equipment have been covered in Chapter 3, and their influence was included in the calculation of the error bars. However, the motion of the tunnel and the definition of the location for the time shift calculation have not been mentioned so far. In most literature, the time is shifted to the center of the tunnel, either by shifting the time to that location or by measuring the velocity at that exact location by installing a partition in the flume and measuring the undisturbed flow velocity. The location of the tunnel changes slightly by the observed motion of the tunnel, this motion was relatively small and was therefore assumed to not have a significant influence on the results.

In this research, it was chosen to determine the time shift to the front of the tunnel, as the tunnel 'feels' the wave first at that location. When using the center of the tunnel, the wave has already interacted with the tunnel and the load cell will have picked that interaction up. The Morison equation used the

undisturbed velocity, which can be measured at the center of the cylinder in a separate partition, but this does not mean that the force signal should be from that same location as it will start at the moment the front of the wave reaches the flume.

Because the waves used for this experiment were small compared to the tunnel dimensions, leading to a low range of KC numbers. Because of these low values, the flow is heavily inertia dominated. This means that especially the drag coefficients are very sensitive to the time shift, while the inertia coefficients have a lower, but still significant, sensitivity to the time shift. Errors in the time shift calculation by the factors mentioned in the previous paragraphs, lead to large errors in the calculated force coefficients, as indicated by the error bars shown in sections 4.2 and 4.3.

5.4 Influence of the High Blockage Ratio

5.4.1 Current Conditions

As explained in section 4.1, the high blockage factor of the tunnel compared to the water depth leads to an overestimation of the drag coefficient. This is caused by an underestimation of the flow velocity around the tunnel. The effect of the blockage ratio was corrected by using a correction formula that was used in (Roshko, 1960). In this paper, the researchers themselves mention that it is a crude method and not completely reliable, as it does not take the effect of changes in wake structures into account. However, this is most important in Reynolds ranges where the drag coefficient changes rapidly with changing Reynolds numbers, and this is not the case in this research.

The correction formula is formulated for circular cylinders without surface roughness. How the parametric shape and the addition of surface roughness will influence this correction, remains unclear. New tests will need to be conducted with a lower blockage ratio to determine what its effect on the forces and coefficients is.

5.4.2 Wave and Combined Conditions

The effect that the blockage ratio has in wave or combined conditions is currently unknown. For the drag force and coefficient, it is likely that the effect is similar to the current conditions since the drag force in wave and combined conditions follows the same theory as for current conditions. It can therefore be assumed that the drag coefficients found in wave and combined conditions are overestimated. However, since the KC numbers are small, this overestimation is smaller for the wave conditions than it was for the current conditions. The drag coefficients found for the combined conditions will share equal overestimations with the current results.

The influence of the high blockage ratio on the inertia forces remains unclear, whether it will change the hydrodynamic-mass attached to the tunnels, or the acceleration of this fluid mass, needs to be investigated more.

5.5 Measurement Inaccuracies

All measurements are prone to small inaccuracies, and while it was attempted to keep these inaccuracies as small as possible, they can combine to decrease the accuracy of the results. In this section, the most important measurement inaccuracies are provided. The accuracy of the EMS, its inability to measure vertical velocities, and the possible errors with the conversion formula were already discussed at length throughout this thesis and summarized in section 5.2.

5.5.1 Equipment

The sensitivity of all equipment depends on the chosen sampling frequency. After it was found that the frequency of 50Hz was too low for the circular smooth tunnel, it was increased to 200Hz for the rest of

the tests. The accuracy of all time shift and wave period calculations is equal to the chosen sampling frequency. The possible inaccuracies of the measurement equipment are discussed in the following paragraphs.

Load Cell

The load cell has an accuracy of 0.5N, and for the forces measured in the smallest current conditions, this can be up to 50% of the measured force. While calibrating the load cell increases the accuracy, there could possibly be some incorrect results found. Furthermore, the offset of the load cell had to be manually put to 0. When during the experiments the cable to the load cell was slightly adjusted, this offset could change. The cable was locked in place after this was observed, and during the experiments, it was often checked whether this had occurred. However, it could still have had some influence on the found results.

Wave Gauge

The signal from each wave gauge was calibrated in order to find a conversion formula, these conversion formulas have an accuracy of 1 to 2 mm since the water level had to be observed visually. Long waves could still have been present in the flume, and this could have had an effect on the measured wave heights

5.5.2 Signal Filtering

As discussed in Chapters 3 and 4, the filtering of the signals has some influences on its amplitude and phase. All filtered signals were checked to make sure the filtering did not alter the signals too much, but some small changes were accepted that could influence the final results slightly.

5.5.3 Tunnels

Due to the shrinkage of the epoxy, the horizontal and vertical tunnel diameters were slightly smaller than the input diameters used to create the molds of the tunnel slices. The tunnel diameters were measured after it was constructed, but the diameters of different slices could vary slightly. Therefore, tunnel diameter could have a small variation along the tunnel, and its measurement accuracy is 1 to 2 mm, which could affect the calculated coefficients. The cross-sectional area that was used in the calculations was determined using an approximation of the epoxy shrinkage. The cross-sectional area of the input dimensions was decreased by this approximated shrinkage factor. Furthermore, some tunnels experienced leakages that could affect the results. However, some experiments were re-tested when the small amount of water was drained from the tunnel, and no significant changes were found.

5.6 Conclusion

All possible measurement inaccuracies and other errors mentioned in this chapter have been monitored during the experiments and while performing the data processing. The inaccuracies or errors that could not be prevented, have been included in the results in the form of error bars. Therefore, it can be stated with confidence that the total error is finite and that the conclusions drawn from the results are within the bandwidth of the error margins.

Chapter 6

Conclusions and Recommendations

In this chapter, the important conclusions of this research are summarized by presenting answers to the research questions. Finally, recommendations for improving this research and future research topics are given.

6.1 Answers to the Research Questions

1. What is the influence of an optimized tunnel shape and multiple roughness parameters on the hydrodynamic properties of a submerged floating tunnel, when exposed to different environmental parameters?

Current Conditions

As expected, an increase in current velocity leads to an increase in mean drag force. The parametric shape decreases the mean drag force acting on the tunnel when exposed to currents. For the lower Reynolds number, the differences are small, but they become more pronounced when the current velocity and therefore the Reynolds number increase.

A larger roughness height causes a higher drag force by increasing the width of the wake of the tunnel. However, when the roughness is small, this effect becomes much less clear and is only observed for the largest Reynolds numbers used in this experiment. For the first two current conditions, the small roughness height does not seem to influence the mean drag force on the tunnel. The tunnel with roughness with a 50% coverage ratio has similar drag coefficients compared to the small roughness case, where it only leads to a higher mean drag force for the largest Reynolds number.

It has to be noted that the found drag coefficients are overestimated significantly, due to the influence of the high blockage ratio. Apart from the circular smooth tunnel results, the coefficients could not be corrected for this high blockage ratio, since there is no correction formula available that includes different tunnel shapes or surface roughness effects. Furthermore, the lift coefficients and the Strouhal numbers provided results that need further research, as explained in section 4.1. The lift coefficients, however, could provide an indication of the amplitude of the varying peak force on a tunnel segment, which is useful information when the tunnel is constructed in separate segments.

Wave Conditions

The force on a submerged floating tunnel when exposed to regular waves consists of two force contributions, a drag force, and an inertia force. It is concluded that in the studied KC range of $0 < KC < 3$, the parametric shape increases both the horizontal drag force and the horizontal inertia force. The low KC numbers lead to a larger contribution of skin friction, which combined with the larger surface area of the parametric-shaped tunnel, results in a higher drag force. The larger displaced water volume of the

parametric-shaped tunnels is the cause of the increased inertia force, as it increases the hydrodynamic-mass surrounding the tunnel. If a much larger KC value would be considered, the drag force could be reduced by the parametric shape, and at a certain point, this decrease in drag force might be larger than the increase in inertia force, leading to a lower horizontal force acting on the parametric-shaped tunnel. This agrees with the current test results, as the current-only condition corresponds to an infinite KC number and it does lead to lower horizontal forces on the parametric-shaped tunnels.

The horizontal forces on the parametric-shaped tunnel are higher than those on the circular-shaped tunnel when the vertical diameter of the tunnel is equal. However, one of the benefits of the parametric shape is that a lower vertical diameter is needed in order to achieve the same clearance height, and lowering the vertical diameter will decrease the forces acting on the tunnel. The parametric shape also experiences much larger vertical forces, due to its larger horizontal diameter. However, the most common foundation methods for a submerged floating tunnel provide more stiffness in the vertical direction, which means that this will not be an important issue when constructing an SFT.

When surface roughness is added to the tunnels, both the drag and the inertia force are affected. At small KC numbers, the drag force is increased by the added surface area the roughness provides. When the KC numbers increase, the relative contribution of the friction force decreases. At this point, the increase in equivalent diameter caused by the roughness becomes more important. The inertia force, however, is decreased by the presence of roughness. The flow around the tunnel is slower between the roughness elements, which decreases the inertia force acting on the tunnel. A balance is observed between roughness height and the number of roughness elements. A larger roughness height increases the surface area and the equivalent diameter but includes fewer roughness elements, which slows down the flow. A similar observation is made for the coverage percentage, where a lower coverage percentage leads to a lower equivalent diameter, but also a lower number of elements, therefore resulting in equal forces on the tunnel.

Combined Conditions

For the combined conditions, similar results to the wave conditions were found in the vertical direction. The current flows in the horizontal direction, and mainly affects the vertical forces by decreasing the wave height compared to the input wave parameters. However, in the horizontal direction, the results showed some differences compared to the wave test results. These differences are not observed in the influence of the tunnel shape on the horizontal forces acting on the tunnels, as the parametric-shaped tunnels again experience larger forces compared to the circular ones. The differences are illustrated by the fact that there is no difference in horizontal force found between the parametric rough and parametric smooth tunnel.

The two force contributions, the drag and inertia force, are kept in balance. The mean drag force has an increased form drag contribution caused by the larger equivalent diameter of the rough tunnels, and a decreased skin friction contribution caused by the larger KC and Reynolds numbers due to the added current. Similar to the wave-only condition, the inertia force is decreased by the presence of roughness, as the roughness elements have spaces in between them containing slow-moving fluid, which slows down the fluid around the tunnel and therefore the inertia force. Following the theory described in Chapter 2, it was expected that the larger equivalent diameter combined with the addition of a current would lead to larger horizontal forces, caused by the increased form drag. That this is not the case indicates that the increase in form drag is compensated by a decrease in skin friction and a decrease in inertia force. For the circular tunnels, there is an increase in horizontal force observed when surface roughness is added to the tunnel. This leads to the conclusion that the balance between the increase in drag force and the decrease in inertia force is shifted towards the side of the drag force, which can be explained by the smaller number of roughness elements present on the circular-shaped tunnels. A smaller number of roughness elements leads to a smaller decrease in inertia force, and therefore an increase in horizontal force on the circular rough tunnel compared to the circular smooth tunnel.

The influence of the roughness height is seen in the fact that the tunnel with a 5 mm roughness height experiences lower forces than the smooth tunnel and the tunnel with a 15 mm roughness height. This can

be explained by using the same balancing processes as mentioned above, an increase in form drag and a decrease in inertia force. For the combined conditions, the parametric smooth tunnel experiences a small increase in horizontal force while both parametric rough tunnels experience a decrease in horizontal force. This leads to the conclusion that the increase in form drag is smaller than the decrease in inertia force for the parametric rough tunnels in combined conditions.

2. How accurately can the hydraulic forces on parametric and circular-shaped tunnels be predicted using the Morison equation, and how does the prediction accuracy of standard coefficients found in engineering codes compare to the coefficients found in this research?

When using coefficients that are provided by the engineering codes (API, 2014) and (DNV, 2010), a very low force prediction accuracy is achieved. Predicting the mean drag force caused by a steady current leads to a force underestimation of 30% to 60% when using the API or DNV coefficients. This can be explained by noting that the increase in velocity around the tunnel, caused by the high blockage ratio, is not included in both codes.

In wave conditions, the API and the DNV coefficients are almost equal, and therefore, have equal force prediction accuracy. The API has slightly higher smooth steady flow drag coefficients and slightly lower rough steady flow drag coefficients. Both inertia coefficients have a constant value of 2 for $0 < KC < 3$ and follow a downward trend for $3 < KC < 12$. Both codes underestimate the horizontal inertia coefficient in wave conditions for $0 < KC < 1.5$ and overestimate it for $1.5 < KC < 3$. In the inertia-dominated range of KC numbers, an overestimation of the inertia coefficients will lead to an overestimation of the force, which is what was found in the force prediction errors as well, as the force is underestimated for the smallest KC numbers and overestimated for the largest. In the vertical direction, both codes overestimate the inertia coefficient. Both predict a constant value in the tested KC range, while the experiment results show a rapid decrease for increasing KC numbers, this leads to a large overestimation of the vertical force.

In combined conditions, both the horizontal and vertical inertia coefficients are overestimated by the codes, and both codes also underestimate the slope of the linear decrease in the inertia coefficient. However, the addition of a steady current decreases the inertia dominance and thereby increases the contribution of the drag coefficient. The horizontal drag coefficient is found to have a downward trend for increasing U_w/U_t and KC numbers, while the codes provide an upwards trend. The vertical drag coefficient is accurately predicted by the rough drag coefficients of both codes, but their horizontal drag coefficients show an inverse trend compared to the experiment results. The large underestimation of the drag coefficient combined with a small overestimation of the inertia coefficient leads to an underestimation of the horizontal force acting on the tunnel.

New fitted force coefficients were determined from the results of the current, wave, and combined tests. For the circular-shaped tunnels in wave and combined conditions, only one set of fitted force coefficients was used as the found coefficients did not vary much between the two tunnels. For the parametric-shaped tunnels, one fitted coefficient was defined for all three rough tunnels, and a separate fitted coefficient was defined for the smooth tunnel. These coefficients are only valid in the tested range of KC numbers, outside of this range they offer no information on the expected values of the force coefficients. Using the newly found coefficients for circular-shaped tunnels improves the prediction accuracy significantly compared to the code coefficients. For the current-only condition, an error below 7% was found, compared to an error of 30% - 60% using the code coefficients. For the wave-only condition, the horizontal force is predicted with an error below 7%, and the vertical force with an error up to 16%. The code coefficients lead to errors of up to 15% for the horizontal force, and errors of up to 146% for the vertical force. For the parametric-shaped tunnels, the fitted coefficients lead to a maximum prediction error of 10%, while the code coefficients have a prediction error that ranges from 10% to 40%.

In conclusion, the current engineering codes do not provide force coefficients that can be used in the design of submerged floating tunnels. The influence of their large blockage ratio, their low KC values, their

horizontal orientation, and possibly their varying shape, is not included in the provided coefficients. The newly found fitted coefficients have a much higher prediction accuracy compared to the coefficients from the API and DNV codes. It has to be noted that the fitted coefficients are only valid in the tested range of Reynolds and KC numbers, and therefore, further research is necessary to improve the engineering standards so that they provide force coefficients that can be used in the future design of an SFT.

6.2 Recommendations

In this section, several recommendations are formulated to improve the conducted experiments for future studies. First, by recommending changes to the set-up and the methodology, followed by more detailed recommendations to improve the accuracy of the results. Afterwards, suggestions on future research topics are given.

6.2.1 Improving the Experiments

Changes to the Set-Up

There are multiple facets where the set-up of the experiment can be improved. The inflow of the current should be more smooth, as the current interferes too much with the generated waves. The equipment used for the velocity measurements should have a sufficient range and accuracy, and its results should be validated before the start of the experiments. Additionally, the equipment should be able to measure vertical and horizontal velocities, as this will allow for the use of the measured velocity signals, instead of the theoretical ones.

The size of the flume that was used is the cause of most limitations concerning the wave height and wavelength. The water depth must be large enough to not increase the blockage ratio any further, and the wave height must be low enough to make sure that no spilling occurs. Together, the combination of the water depth and the wave height must be sufficient so that the waves are not influenced by the bottom boundary condition. If a deeper flume is used, the blockage ratio can be decreased by increasing the water depth and the wave height can be increased without the waves 'feeling' the bottom of the flume. A longer flume would allow for larger wavelengths to be tested, as the wavelength must be much smaller than the length of the flume to make sure several waves fit into the flume. Otherwise, the waves are reflected toward the tunnel before accurate measurements can be made.

The force measurements were proven to be relatively accurate, as shown in Appendix D. However, the method of measuring the horizontal forces can be improved. There was a large distance between the load cell and the tunnel, leaving it vulnerable to inaccuracies caused by the small motions of the tunnel. If the tunnel is suspended on both sides, instead of in the middle, more stiffness is provided. Two load cells can then be attached to the two suspensions, and the forces can be measured even more accurately. The vertical force measurements should be obtained with a different method as well. As discussed in section 4.1, the current method measures the lift force integrated over the length of the tunnel. Preferable would be to measure the vertical force using strips along the tunnel in the flow direction. This way, the vertical force within a vortex-shedding cell can be determined.

Changes to the Methodology

The methodology of the experiments can be improved upon by making a few changes. If more combinations of wave heights and wave periods were tested, the influence of the wavelength, the wave height, and the KC number on the obtained force coefficients could become more clear. The definition of the Strouhal number should be changed to the universal Strouhal number defined by (Bearman, 1967). This definition uses the size of the wake vortex street, which leads to more uniform results when surface roughness is added to a cylinder.

As mentioned in Chapter 4, the force coefficients are very sensitive to the calculation of the time shift. In the next paragraph, a more detailed recommendation is given on how to deal with this high sensitivity.

High Sensitivity to the Time Shift

The issue of high sensitivity to the calculated time shift can be solved in two different ways, either by eliminating the need for a time shift or by decreasing the sensitivity to it. The need for a time shift of the signals can be eliminated by measuring everything at the same location. This can be achieved by separating the flume into two partitions, and by installing a thin screen that does not interfere with the flow. The measuring equipment can be installed in one partition, and the tunnel will be installed in the other partition. One has to determine at which location to measure, at the center of the tunnel, or at the leading edge where the flow first interacts with the tunnel.

The sensitivity to the time shift can be decreased by increasing the KC numbers of the tunnel, and there are several options that can be used to achieve this. Either a smaller tunnel needs to be fabricated, which would increase the size of the waves relative to the tunnel, or the wave height and length need to be increased, which would serve a similar purpose. Possible issues with decreasing the size of the tunnel that need to be considered are the size of the roughness itself, and the low force that will be acting on the tunnels. The size of the roughness needs to be large enough to still consider the tunnel hydraulically rough, and the force on the tunnel will be smaller, so the equipment used must be much more sensitive to accurately measure the differences. Furthermore, a smaller tunnel will lead to lower Reynolds numbers, which will also influence the results.

When increasing the wave height and length, a larger flume is needed. If the length of the flume is too short compared to the wavelength, not enough waves will fit into the flume and they will be quickly distorted by reflection. If the water depth is too shallow compared to the wave height, either spilling will occur or there will be boundary effects where the bottom will be felt by the wave. The issue of a large blockage ratio can be solved by the previous solutions as well; if the tunnel size is decreased or the flume size is increased, the blockage ratio will go down.

6.2.2 Future Research

Recommendations on future research topics related to the submerged floating tunnel are summarized below:

- The influence of the blockage ratio needs to be further investigated, since its effect on the wave and combined conditions is currently unknown. This can be achieved by testing similar tunnels in different water depths, thereby changing the blockage ratio. However, the effects that the different depths have on the submergence depth of the tunnel, and the velocities and accelerations it experiences, need to be carefully accounted for.
- More research is necessary on the influence of the equivalent diameter and the cross-sectional area, and how they are defined, as they share a significant influence on the found coefficients. It remains unclear what the correct definition is, and it would be beneficial to know which definitions would result in the most uniform coefficients that can be provided in engineering codes. This could prevent having to provide multiple coefficients for different roughness heights and coverage percentages.
- In the KC range used in this experiment, the decrease in drag force caused by the parametric shape, was much smaller than the increase in inertia force due to the shape. It would be interesting to investigate at which KC values, the decrease in drag force would be larger than the increase in inertia force, for waves and combined conditions.
- The influence of other roughness parameters needs to be investigated in combination with a submerged floating tunnel, along with more realistically shaped and sized roughness distributions. While the pyramid-shaped roughness gives an indication of the influence of different roughness parameters, real marine fouling shows many different distributions, skewness, colonization, and multiple roughness heights combined. The effects this would have on an SFT and on the parametric shape, need further research.

- For this research, only regular waves were tested. In future research, the influence of irregular waves on the parametric-shaped tunnel needs to be investigated. Force coefficients for different wave spectra can then be derived.
- To more accurately see what happens with the flow surrounding the tunnels, particle image velocimetry measurements can be made to measure the flow field and analyze the details of flow separation and boundary layers.

Bibliography

- Adachi, T. (1997). Effects of surface roughness on the universal strouhal number over the wide reynolds number range. *Journal of Wind Engineering and Industrial Aerodynamics*.
- Airy, G. (1845). On tides and waves. *Encyclopaedia Metropolitana*, 5.
- Ameryoun, H., Schoefs, F., Barillé, L., and Thomas, Y. (2019). Stochastic modeling of forces on jacket-type offshore structures colonized by marine growth. *Journal of Marine Science and Engineering*, 7(158).
- API (2014). Recommended practice 2a-wsd: Planning, designing, and constructing fixed offshore platforms — working stress design.
- Bai, J., Ma, N., and Gu, X. (2017). Study of interaction between wave-current and the horizontal cylinder located near the free surface. *Applied Ocean Research*, 67.
- Bearman, P. (1967). On vortex street wakes. *J, Fluid Mech.*, 28.
- Chaplin, J. (1988). Loading on a cylinder in uniform oscillatory flow: Part ii - elliptical orbital flow. *Applied Ocean Research*, 10.
- Cook, G. and Simiu, E. (1989). Hydrodynamic forces on vertical cylinders and the lighthill correction. *Ocean Engineering*, 16(4):355–372.
- Demirel, Y., Uzun, D., Zhang, Y., Fang, H.-C., Day, A., and Turan, O. (2017). Effect of barnacle fouling on ship resistance and powering. *Biofouling*, 33(10):819–834.
- DNV (2010). Recommended practice dnv-rp-c205: Environmental conditions and environmental loads.
- Drost, L. C. (2019). The submerged floating tunnel, an experimental study on the hydrodynamics and kinematics of a submerged rectangular cylinder in a wave-current environment. Master's thesis, Delft University of Technology.
- Faggiano, B., Landolfo, R., and Mazzolani, F. M. (2005). The sft: An innovative solution for waterway strait crossings. *IABSE Symposium Report*, 90.
- Hemel, M. J. (2019). Submerged floating tunnel, the dynamic response due to fluid structure interaction. Master's thesis, Delft University of Technology.
- Henry, P.-Y., Nedrebø, E. L., and Myrhaug, D. (2016). Visualisation of the effect of different types of marine growth on cylinders' wake structure in low re steady flows. *Ocean Engineering*, 115:182–188.
- Holthuijsen, L. (2007). *Waves in Oceanic and Coastal Waters*. Cambridge University Press.
- Indridason, B., Rupakhety, R., Remseth, S., and Sigbjornsson, R. (2014). Earthquake-induced response of submerged floating tunnels with tension leg anchorage.
- Iwagaki, Y. and Asano, T. (1984). Hydrodynamic forces on a circular cylinder due to combined wave and current loading. *Coastal Engineering*.
- Karlsson, J., Ytreberg, E., and Eklund, B. (2009). Toxicity of anti-fouling paints for use on ships and leisure boats to non-target organisms representing three trophic levels. *Environmental Pollution*, 158.

- Legendre, A. M. (1805). Nouvelles methodes pour la determination des orbites des cometes.
- LeMehaute, B. (1976). *An Introduction to Hydrodynamics and Water Waves*. Springer Science Business Media.
- Mai, T. (2019). Estimation of drag and inertia coefficients for a tripod support structure of offshore wind turbine. *International Conference on Asian and Pacific Coasts*.
- Mansard, E. and Funke, E. (1980). The measurement of incident and reflected spectra using a least squares method. *Int. Conf. on Coastal Engineering*.
- Marty, A., Berhault, C., Damblans, G., Facq, J., Gaurier, B., Germain, G., Soulard, T., and Schoefs, F. (2021). Experimental study of hard marine growth effect on the hydrodynamical behaviour of a submarine cable. *Applied Ocean Research*, 114.
- Morison, J., Johnson, J., and Schaaf, S. (1950). The force exerted by surface waves on piles. *Journal of Petroleum Technology*.
- Ostlid, H. (2010). When is sft competitive? *Procedia Engineering*, 4.
- Roshko, A. (1960). Experiments on the flow past a cylinder at very high reynolds number. *Journal of Fluid Mechanics*, 10(3).
- Salta, M., Chambers, L., Wharton, J., Wood, R., Briand, J.-F., Blanche, Y., and Stokes, K. (2009). Marine fouling organisms and their use in antifouling bioassays.
- Sarakinos, S. and Busse, A. (2019). *Recent Advances in CFD for Wind and Tidal Offshore Turbines*, chapter An Algorithm for the Generation of Biofouled Surfaces for Applications in Marine Hydrodynamics. Springer.
- Schoefs, F. and Ameryoun, H. (2013). Probabilistic modeling of the bio-colonization effects on hydrodynamic forces with several combinations of sea-state condition: a study on jacket-platforms in the gulf of guinea. *ASME 2013 32nd International Conference on Ocean, Offshore and Arctic Engineering*.
- Schoefs, F., O'Byrne, M., Pakrashi, V., Ghosh, B., Oumouni, M., Soulard, T., and Reynaud, M. (2021). Fractal dimension as an effective feature for characterizing hard marine growth roughness from underwater image processing in controlled and uncontrolled image environments. *Journal of Marine Science and Engineering*, 9(12).
- Song, S., Ravenna, R., Dai, S., Muscat-Fenech, C., Tani, G., Demirel, Y., Atlar, M., Day, S., and Incecik, A. (2021). Experimental investigation on the effect of heterogeneous hull roughness on ship resistance. *Ocean Engineering*, 223.
- Stokes, G. (1847). On the theory of oscillatory waves.
- Sumer, B. M. and Fredsoe, J. (2006). *Hydrodynamics around cylindrical structures*. World Scientific.
- Sun, C., Zhou, T., an, H., Zhu, H., and Cheng, L. (2020). Effect of surface roughness heights on circular cylinder wakes. *22nd Australasian Fluid Mechanics Conference*.
- Sundar, V. (2016). *Ocean Wave Mechanics: Applications in Marine Structures*. John Wiley Sons Ltd.
- Theophanatos, A. and Wolfram, J. (1989). Hydradynamic loading on macro-roughened cylinders of various aspect ratios. *Journal of Offshore Mechanics and Arctic Engineering*, 111.
- Uzun, D., Zhang, Y., Demirel, Y., and Turan, O. (2017). Experimental determination of added resistance of barnacle fouling on ships by using 3d printed barnacles. *5th International Conference on Advanced Model Measurement Technology for The Maritime Industry*.
- Venugopal, V., Varyani, K., and Westlake, P. (2008). Drag and inertia coefficients for horizontally submerged rectangular cylinders in waves and currents. *Institution of Mechanical Engineers, Part M: Journal of Engineering for the Maritime Environment*.

- West, G. and Apelt, C. (1982). The effects of tunnel blockage and aspect ratio on the mean flow past a circular cylinder with reynolds numbers between 10^4 and 10^5 . *Journal of Fluid Mechanics*, 114:361–377.
- Won, D., Seo, J., Kim, S., and Park, W.-S. (2019). Hydrodynamic behavior of submerged floating tunnels with suspension cables and towers under irregular waves. *Applied Sciences*, 9.
- Zeinoddini, M., Bakhtiari, A., Ehteshami, M., and Seif, M. (2016). Towards an understanding of the marine fouling effects on viv of circular cylinders: Response of cylinders with regular pyramidal roughness. *Applied Ocean Research*, 59.
- Zou, P., Bricker, J., and Uijttewaal, W. (2020). Optimization of submerged floating tunnel cross section based on parametric bezier curves and hybrid backpropagation - genetic algorithm. *Marine Structures*, 74.

Appendix A

Linear Wave Theory

The following assumptions are necessary to apply linear wave theory:

- Fluid density is constant
- Fluid is incompressible
- Fluid has no viscosity
- Fluid is irrotational
- Bed is rigid and impermeable
- Only acting force is the gravitation force, other forces like the Coriolis force, friction force, surface tension, and wind stress are negligible.

Linear wave theory makes use of two balance equations, the mass balance, and the momentum balance. By assuming irrotationality, a velocity potential function, ϕ , can be introduced. The mass balance can be rewritten using the velocity potential, resulting in the Laplace equation (A.1). The momentum balance can be rewritten to the Bernoulli equation (A.2). The velocity potential is formulated as seen in equation A.3.

$$\frac{\partial^2 \phi}{\partial x^2} + \frac{\partial^2 \phi}{\partial y^2} + \frac{\partial^2 \phi}{\partial z^2} = 0 \quad (\text{A.1})$$

$$\frac{\partial \phi}{\partial t} + \frac{1}{2} |\nabla \phi|^2 + \frac{p}{\rho} + gz = 0 \quad (\text{A.2})$$

$$\phi = \hat{\phi}(z) \cos(\omega t - kx) \quad (\text{A.3})$$

Where:

$$\hat{\phi}(z) = \frac{\omega a \cosh[k(d+z)]}{k \sinh(kd)} \quad (\text{A.4})$$

The boundary conditions are that at the water surface, particles may not leave the surface, at the bottom the particles may not penetrate the bed, and the pressure at the water surface is zero. The Laplace and Bernoulli equations are the equations of motion and together with the boundary conditions, they form the governing equations. These equations can be linearized if the wave height is small compared to the wavelength and the water depth. The linearized system of equations has one analytical solution, a propagating harmonic wave in the following form:

$$\eta(x, t) = a \sin(\omega t - kx) \quad (\text{A.5})$$

The velocity potential is defined in such a way that the following equations always hold:

$$u_x = \frac{\partial \phi}{\partial x} \quad (\text{A.6})$$

$$u_z = \frac{\partial \phi}{\partial z} \quad (\text{A.7})$$

This leads to the following equations for the orbital particle velocities (Holthuijsen, 2007):

$$u_x = \hat{u}_x(z) \sin(\omega t - kx) \quad (\text{A.8})$$

$$u_z = \hat{u}_z(z) \cos(\omega t - kx) \quad (\text{A.9})$$

With:

$$\hat{u}_x(z) = \omega a \frac{\cosh[k(d+z)]}{\sinh(kd)} \quad (\text{A.10})$$

$$\hat{u}_z(z) = \omega a \frac{\sinh[k(d+z)]}{\sinh(kd)} \quad (\text{A.11})$$

Where:

u_x	=	Horizontal particle velocity [m/s]
u_z	=	Vertical particle velocity [m/s]
\hat{u}_x	=	Amplitude of the horizontal particle velocity [m/s]
\hat{u}_z	=	Amplitude of the vertical particle velocity [m/s]
z	=	Depth of the water particle [m]
ω	=	Radial frequency [rad/s]
k	=	Wave number [rad/m]
a	=	Wave amplitude [m]
d	=	Water depth [m]

From the boundary condition that states that the surface pressure is zero, the dispersion relation can be formulated. It can be written in two forms, equations A.12 and A.13. The dispersion relation links the wave period to the wavelength and has to be solved iteratively. The formula for the phase velocity of the wave can be seen in equation A.14. Combining equations A.13 and A.14, the phase velocity can be written in the form seen in equation A.15 (Holthuijsen, 2007):

$$\omega^2 = gk \tanh(kd) \quad (\text{A.12})$$

$$L = \frac{gT^2}{2\pi} \tanh\left(\frac{2\pi d}{L}\right) \quad (\text{A.13})$$

$$c = \frac{L}{T} = \frac{\omega}{k} \quad (\text{A.14})$$

$$c = \frac{g}{\omega} \tanh(kd) = \sqrt{\frac{g}{k} \tanh(kd)} \quad (\text{A.15})$$

Where:

c	=	Phase velocity [m/s]
L	=	wavelength [m]
T	=	Wave period [s]
ω	=	Radial frequency [rad/s]
k	=	Wave number [rad/m]
d	=	Water depth [m]

Appendix B

Calibration Results

In this appendix, the results of the calibration tests of the wave gauges and load cell are shown.

B.1 Wave Gauges

The wave gauges were calibrated by filling the flume to a reference level, 0.7 m in this case, and writing down the voltage that each gauge measures. Then the flume is emptied and filled to different water levels, and the change in voltage is denoted. This gave the results presented below, all the graphs show a straight line which led to the conclusion that the calibration was accurate.

Water level [m]:	Difference [m]:	G18 [V]	G22 [V]	G21 [V]	G12 [V]	G15 [V]	G7 [V]
0.667	-0.031	-1.27	-1.27	-1.27	-1.54	-1.51	-1.52
0.683	-0.015	-0.6	-0.61	-0.61	-0.74	-0.73	-0.73
0.694	-0.004	-0.12	-0.16	-0.14	-0.19	-0.2	-0.2
0.698	0	0.01	0.01	0.02	-0.01	-0.01	0
0.716	0.018	0.75	0.7	0.71	0.84	0.8	0.82
0.722	0.024	1.01	0.95	0.97	1.15	1.09	1.12
0.733	0.035	1.47	1.4	1.42	1.69	1.62	1.65
0.75	0.052	2.17	2.09	2.1	2.51	2.42	2.46
0.757	0.059	2.45	2.37	2.38	2.85	2.74	2.79

Table B.1: Wave gauge calibration results

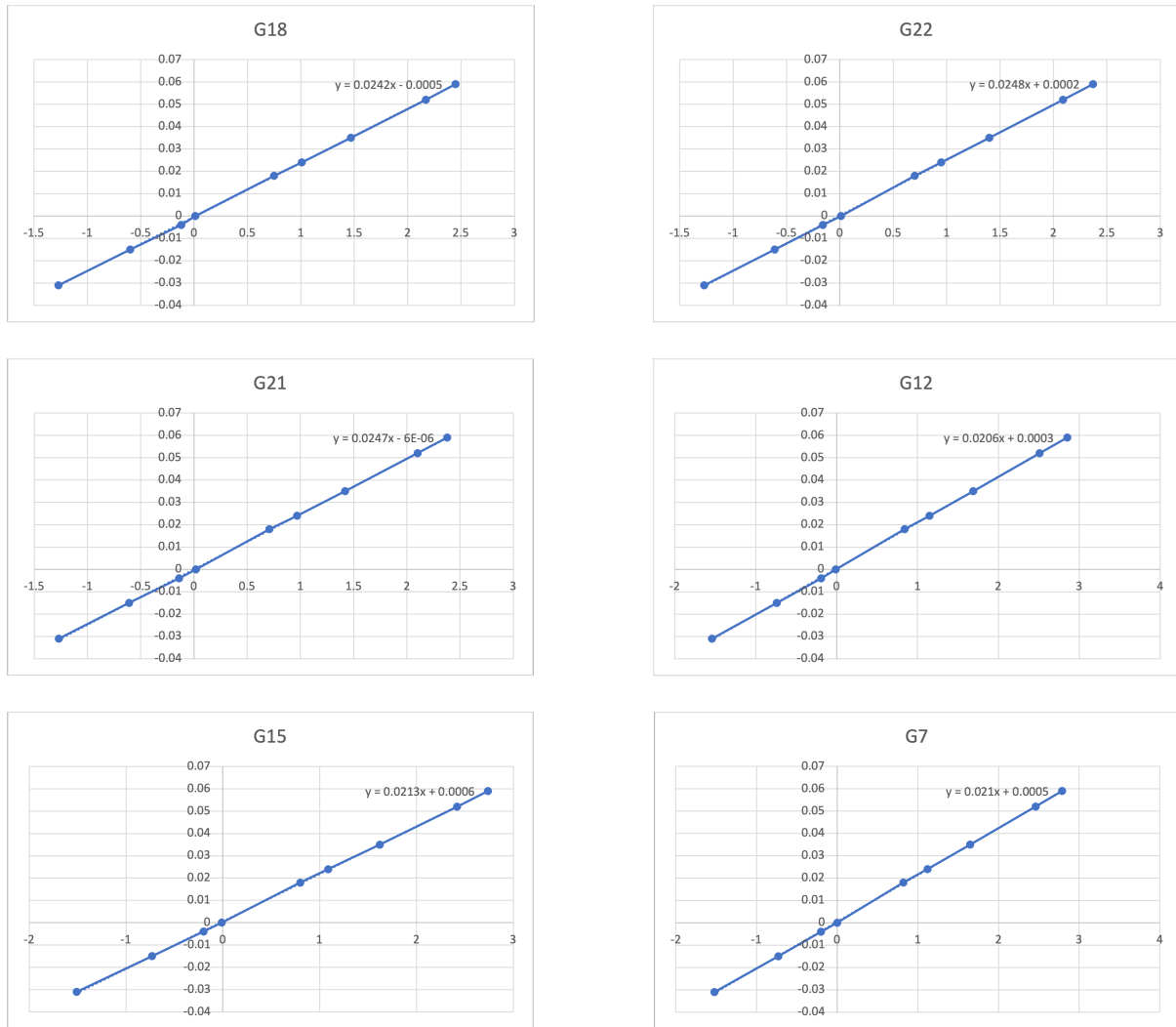


Figure B.1: Calibration results of all six wave gauges

B.2 Load Cell

The vertical direction of the load cell was calibrated by noting the measured voltage at rest, and then attaching different weights to the load cell and noting the change in voltage. For the horizontal direction, the same method was used but the load cell was rotated 90°. The results are shown below, the graphs show a straight line which led to the conclusion that the calibration was accurate.

At rest [V]:	Added weight [g]	Voltage measured [V]:	Difference [V]:	Added [N]:
0.01	68	0.08	0.07	0.66708
	243	0.25	0.24	2.38383
	407	0.41	0.4	3.99267
	619	0.62	0.61	6.07239
	1023	1.02	1.01	10.03563
	1857	1.84	1.83	18.21717
	2562	2.53	2.52	25.13322
	3647	3.6	3.59	35.77707
	4885	4.82	4.81	47.92185
	5804	5.73	5.72	56.93724
	6786	6.7	6.69	66.57066
	7909	7.8	7.79	77.58729
	8543	8.43	8.42	83.80683
	9493	9.36	9.35	93.12633

Table B.2: Results of load cell calibration in vertical direction

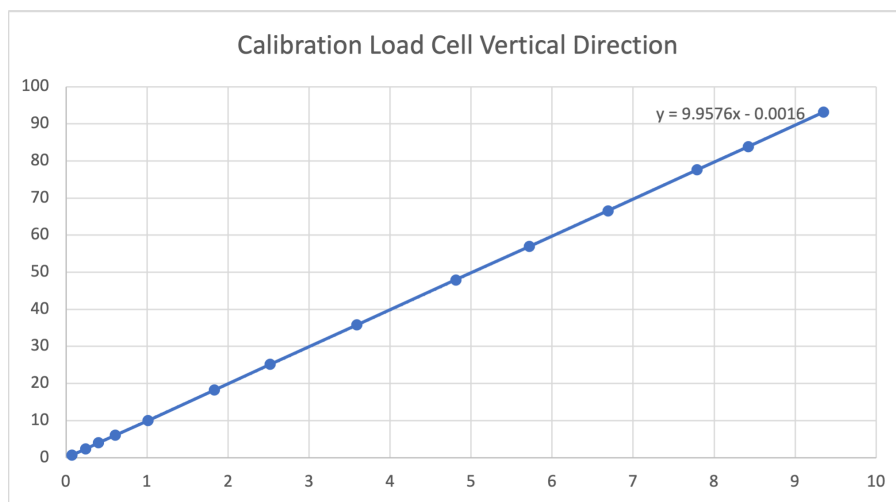


Figure B.2: Load cell calibration results vertical direction

At rest [V]:	Added weight [g]	Voltage Measured [V]:	Difference [V]:	Added [N]
-0.28	68	-0.34	0.06	0.66708
	238	-0.5	0.22	2.33478
	647	-0.89	0.61	6.34707
Extra [g]:	851	-1.09	0.81	8.34831
470	1321	-1.54	1.26	12.95901
645	1966	-2.16	1.88	19.28646
859	2825	-2.98	2.7	27.71325
653	3478	-3.61	3.33	34.11918
691	4169	-4.28	4	40.89789
574	4743	-4.83	4.55	46.52883
796	5539	-5.59	5.31	54.33759
1114	6653	-6.66	6.38	65.26593
901	7554	-7.52	7.24	74.10474
1001	8555	-8.48	8.2	83.92455
1134	9689	-9.57	9.29	95.04909

Table B.3: Results of load cell calibration in horizontal direction

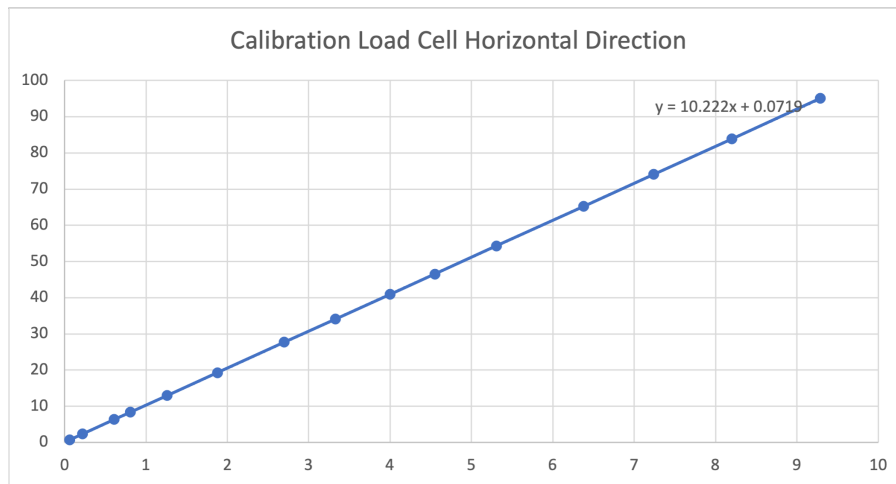


Figure B.3: Load cell calibration results horizontal direction

Appendix C

Results of Wave Heights and Periods per test

In this appendix, the calculated wave heights and wave periods for each test are presented in the tables below, along with their standard deviation.

C.1 Wave Tests

W1	T [s]	std(T)	H [m]	std(H)
CS	0.9200	0.0026	0.075446	0.0037
CR	0.9145	0.0026	0.076477	0.0260
PS	0.9162	0.0035	0.074446	0.0204
PR	0.9147	0.0032	0.074908	0.0165
PR50	0.9148	0.0005	0.074132	0.0229
PRS	0.9158	0.0025	0.074288	0.0209

Table C.1: Wave characteristics for W1 tests

W2	T [s]	std(T)	H [m]	std(H)
CS	1.1208	0.0022	0.079095	0.0126
CR	1.1203	0.0018	0.078020	0.0315
PS	1.1194	0.0008	0.077388	0.0078
PR	1.1193	0.0009	0.078146	0.0844
PR50	1.1203	0.0009	0.077841	0.0065
PRS	1.1188	0.0010	0.077975	0.0200

Table C.2: Wave characteristics for W2 tests

W3	T [s]	std(T)	H [m]	std(H)
CS	1.4114	0.0028	0.080595	0.0233
CR	1.4132	0.0022	0.077771	0.0177
PS	1.4123	0.0016	0.078702	0.0098
PR	1.4122	0.0000	0.078394	0.0080
PR50	1.4140	0.0009	0.078231	0.0177
PRS	1.4127	0.0012	0.078749	0.0068

Table C.3: Wave characteristics for W3 tests

W4	T [s]	std(T)	H [m]	std(H)
CS	1.8413	0.0029	7.9939	0.0056
CR	1.8442	0.0028	8.0395	0.0148
PS	1.8443	0.0030	7.9836	0.0325
PR	1.8446	0.0015	7.9639	0.0168
PR50	1.8439	0.0023	7.9527	0.0154
PRS	1.8438	0.0010	8.0055	0.0272

Table C.4: Wave characteristics for W4 tests

W5	T [s]	std(T)	H [m]	std(H)
CS	1.8435	0.0023	0.0120176	0.0090
CR	1.8510	0.0030	0.0121090	0.0208
PS	1.8463	0.0014	0.0119937	0.0736
PR	1.8481	0.0007	0.0119119	0.0260
PR50	1.8481	0.0033	0.0119034	0.0299
PRS	1.8461	0.0016	0.0119859	0.0404

Table C.5: Wave characteristics for W5 tests

W6	T [s]	std(T)	H [m]	std(H)
CS	1.8435	0.0020	0.0159290	0.0413
CR	1.8512	0.0050	0.0160796	0.0690
PS	1.8433	0.0020	0.0159471	0.0245
PR	1.8458	0.0019	0.0159175	0.0169
PR50	1.8482	0.0059	0.0158963	0.0213
PRS	1.8485	0.0068	0.0159569	0.0462

Table C.6: Wave characteristics for W6 tests

C.2 Combined Tests

CW1	T [s]	std(T)	H [m]	std(H)
CS	0.933	0.0126	0.0547	0.00545
CR	0.928	0.0106	0.0589	0.00000
PS	0.918	0.0106	0.0625	0.00431
PR	0.928	0.0035	0.0581	0.00042
PR50	0.928	0.0071	0.0505	0.01407
PRS	0.920	0.0247	0.0529	0.00028

CW2	T [s]	std(T)	H [m]	std(H)
CS	1.123	0.0150	0.0643	0.00026
CR	1.120	0.0035	0.0631	0.00226
PS	1.123	0.0035	0.0640	0.00127
PR	1.125	0.0035	0.0607	0.00191
PR50	1.111	0.0018	0.0632	0.00028
PRS	1.118	0.0177	0.0642	0.00290

CW3	T [s]	std(T)	H [m]	std(H)
CS	1.405	0.0058	0.0640	0.00079
CR	1.408	0.0000	0.0630	0.00170
PS	1.408	0.0141	0.0649	0.00085
PR	1.404	0.0018	0.0652	0.00035
PR50	1.406	0.0053	0.0648	0.00007
PRS	1.419	0.0018	0.0639	0.00021

CW4	T [s]	std(T)	H [m]	std(H)
CS	1.845	0.0058	0.0699	0.00068
CR	1.840	0.0141	0.0692	0.00000
PS	1.845	0.0106	0.0689	0.00078
PR	1.838	0.0106	0.0696	0.00134
PR50	1.841	0.0018	0.0696	0.00085
PRS	1.833	0.0106	0.0697	0.00064

CW5	T [s]	std(T)	H [m]	std(H)
CS	1.840	0.0082	0.1048	0.00090
CR	1.836	0.0018	0.1029	0.00085
PS	1.835	0.0071	0.1040	0.00078
PR	1.836	0.0053	0.1042	0.00120
PR50	1.843	0.0071	0.1034	0.00057
PRS	1.834	0.0018	0.1042	0.00057

CW6	T [s]	std(T)	H [m]	std(H)
CS	1.848	0.0096	0.1379	0.00035
CR	1.843	0.0035	0.1381	0.00028
PS	1.853	0.0141	0.1374	0.00141
PR	1.838	0.0071	0.1367	0.00042
PR50	1.849	0.0018	0.1368	0.00332
PRS	1.853	0.0000	0.1357	0.00042

CW7	T [s]	std(T)	H [m]	std(H)
CS	1.843	0.0058	0.1328	0.00093
CR	1.833	0.0035	0.1253	0.00537
PS	1.833	0.0071	0.1342	0.00021
PR	1.855	0.0035	0.1331	0.00396
PR50	1.845	0.0177	0.1301	0.00042
PRS	1.838	0.0106	0.1291	0.00318

Appendix D

Load Cell Test

To make sure the load cell worked properly, some force tests were conducted. A calibrated spring that shows with which force is being pulled was attached to the tunnel using a stiff metal wire. With the tunnel at rest, five different loads will be manually applied to the tunnel using the spring. In figures [D.1](#), [D.2](#), and [D.3](#), the results of these tests are shown.

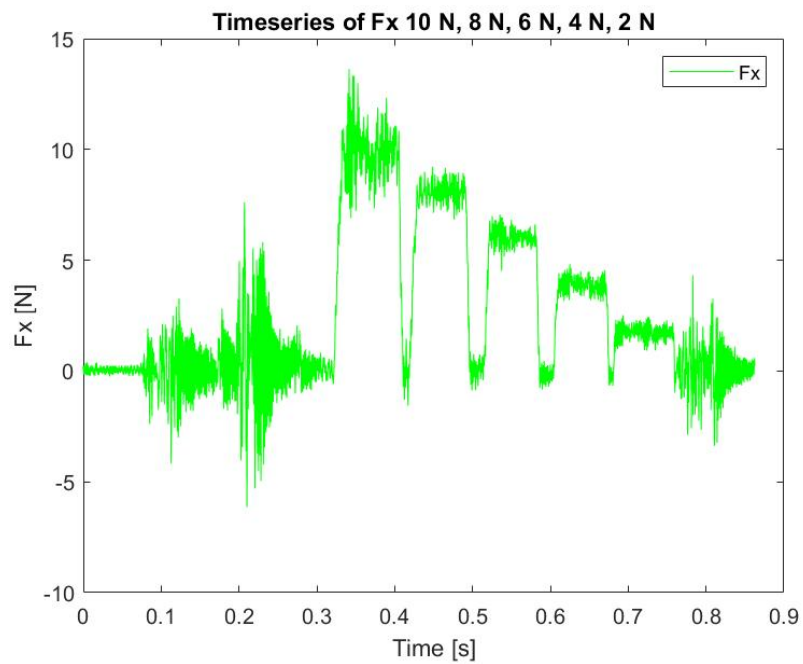


Figure D.1: Load Cell Test in x-direction, all loads

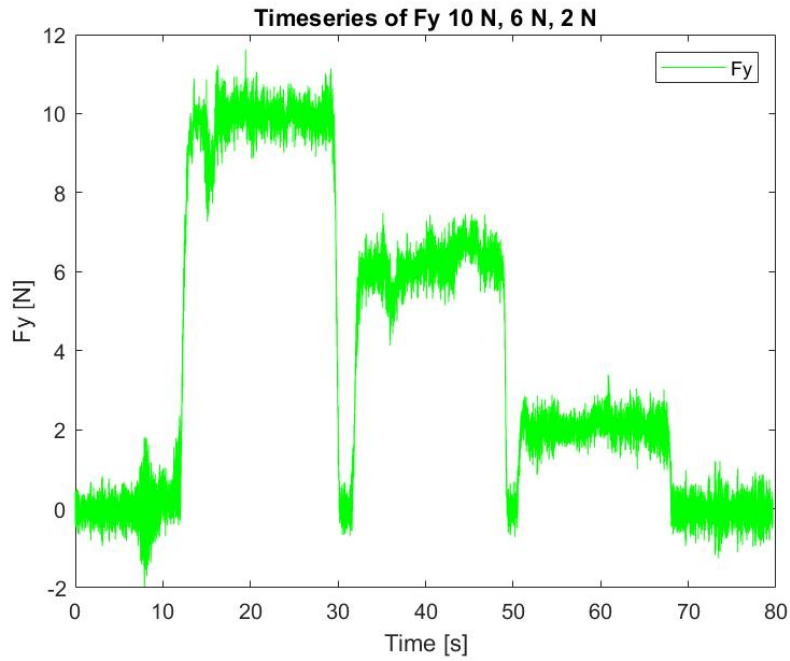


Figure D.2: Load Cell Test in y-direction, 10 N, 6 N, 2 N

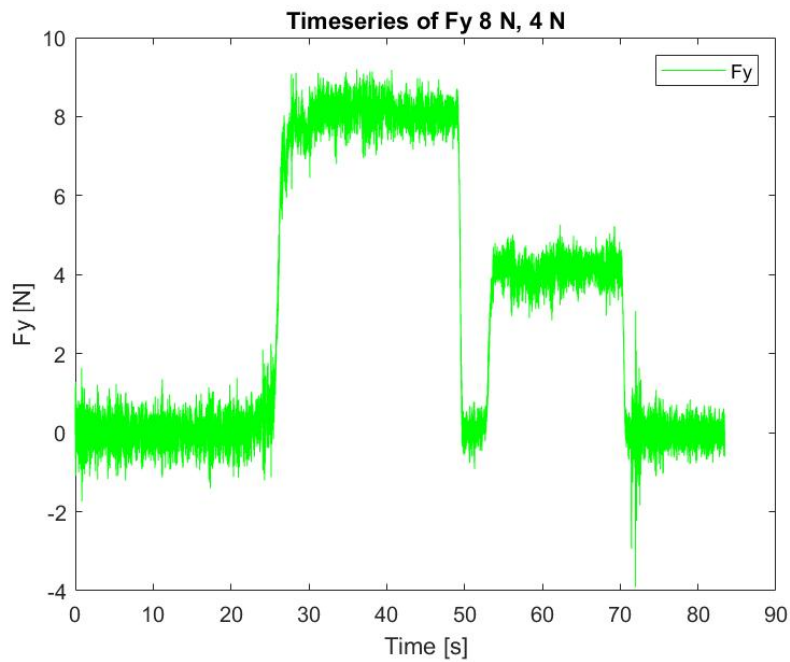


Figure D.3: Load Cell Test in y-direction, 8 N, 4 N

In tables [D.1](#) and [D.2](#), the average force over the pulling duration compared to the applied force can be found. This table shows that the load cell is accurate and that there are no errors occurring in the measurements themselves. The small differences are easily explained by the fact that there was not a perfect constant load applied since it was done manually. This also explains the larger difference for the smallest loads, as it was more difficult to keep the spring at 2 N because there was almost no tension in the spring, so it became more unstable.

F_{Applied} [N]	F_{Measured} [N]	ΔF [N]
10.00	9.94	-0.06
8.00	8.08	0.08
6.00	6.05	0.05
4.00	3.89	-0.11
2.00	1.75	-0.25

Table D.1: Results of the Load Cell Tests in x-direction

F_{Applied} [N]	F_{Measured} [N]	ΔF [N]
10.00	9.97	-0.03
8.00	8.08	0.08
6.00	6.21	0.21
4.00	4.08	0.08
2.00	2.08	0.08

Table D.2: Results of the Load Cell Tests in y-direction

Appendix E

Strouhal Results

In the following paragraphs, the influence of the current velocity, the tunnel shape, the roughness height and the coverage percentage on the Strouhal number will be presented and discussed.

Influence of Current Velocity

Figure E.1 shows the Strouhal numbers for each tunnel under different current velocities. The error bars have been added to indicate the uncertainties in determining the correct vortex shedding frequencies as explained in Chapter 3. In general, the Strouhal number shows a slight downward trend with increasing current velocity. In figure 2.3, it can be seen that the expected Strouhal number for a circular cylinder is approximately 0.2. The CS results show a Strouhal number of 0.235 - 0.24. This can be explained using the high blockage ratio, where the flow velocities around the tunnel are higher than the measured velocities by the EMS. Using the increased flow velocity in equation 2.2 would lead to a lower Strouhal number.

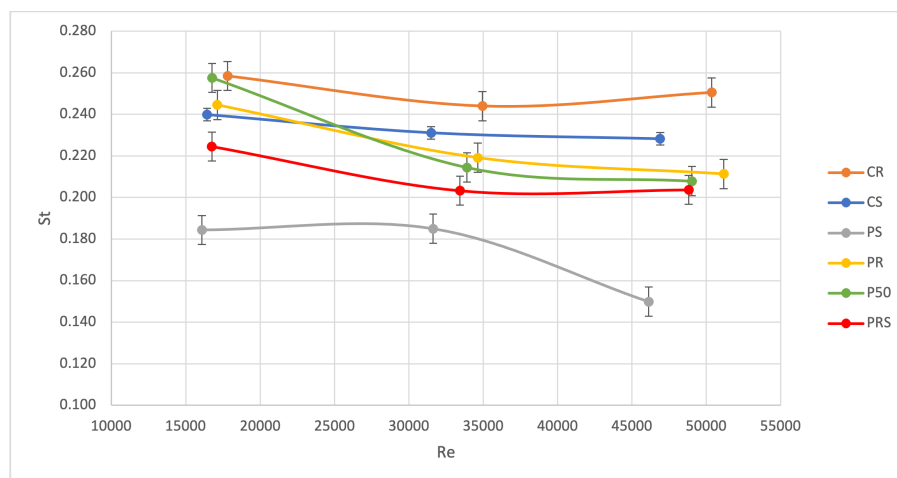


Figure E.1: Strouhal number for each current velocity

Influence of Tunnel Shape

In figure E.2, the influence of the shape of the tunnel is shown. It was expected that the parametric-shaped tunnel would have a higher Strouhal number than the circular-shaped tunnel. Since, similar to the explanation for a lower drag coefficient due to tunnel shape, the parametric tunnels have a smaller wake width due to their streamlined shape, which makes it easier for the vortices to interact. However, the parametric-shaped tunnels have lower Strouhal numbers than the circular-shaped tunnels, as can be seen in figure E.2.

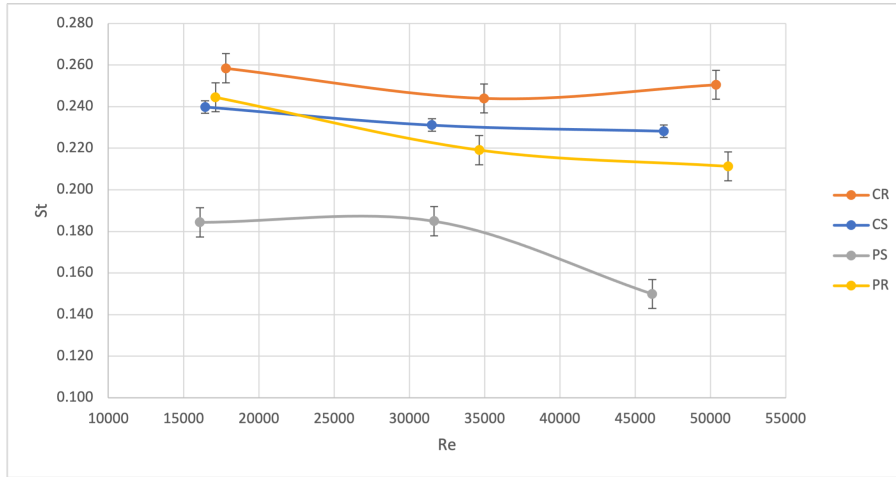


Figure E.2: Strouhal number for each tunnel shape

Influence of Roughness Height

In figure E.3, the influence of the roughness height can be seen. It shows that an increase in roughness height leads to an increased Strouhal number. This can be explained by assuming the roughness makes the boundary layer transition to turbulent much quicker, which allows the flow to stay attached to the tunnel longer. This moves the separation point downstream and creates a smaller wake width where it is easier for the vortices to interact and they do so at a higher frequency and therefore a higher Strouhal number. The roughness height also increases the equivalent diameter of the tunnels, which increases the Strouhal number as well as it is calculated using the equivalent diameters. However, in the papers from (Marty et al., 2021) and (Sun et al., 2020) mentioned in Chapter 2, it was concluded that adding roughness decreases the Strouhal number because the separation point was moved upstream.

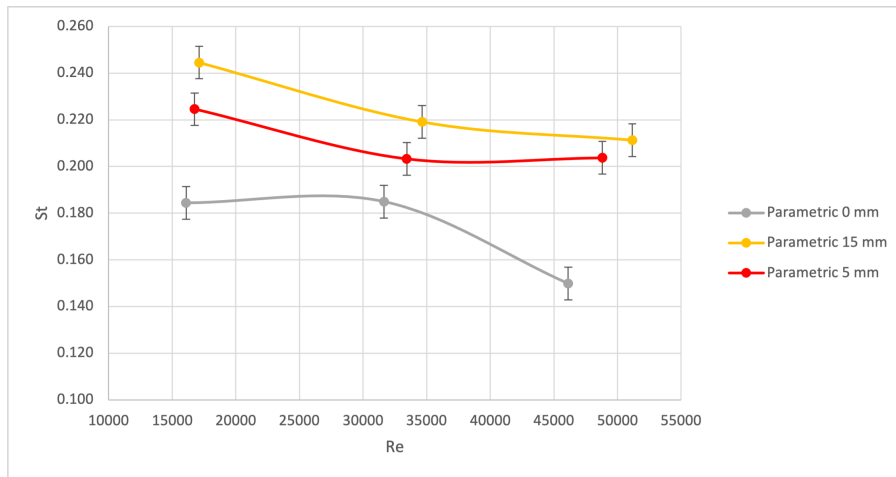


Figure E.3: Strouhal number for each roughness height

Influence of Coverage Percentage

The influence of the coverage percentage is shown in figure E.4. There is no significant difference between the tunnels with a 100% and a 50% coverage ratio, as they both have a similar increase in Strouhal number compared to the smooth tunnel. This leads to the conclusion that the height of the roughness is a much more important parameter than the coverage percentage when it comes to the vortex shedding frequency.

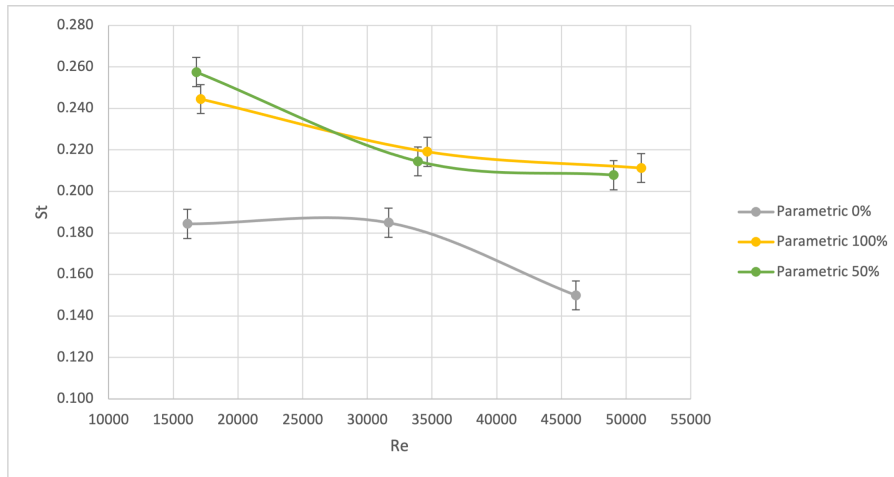


Figure E.4: Strouhal number for each coverage percentage

Appendix F

Video Images of the Wake Structure

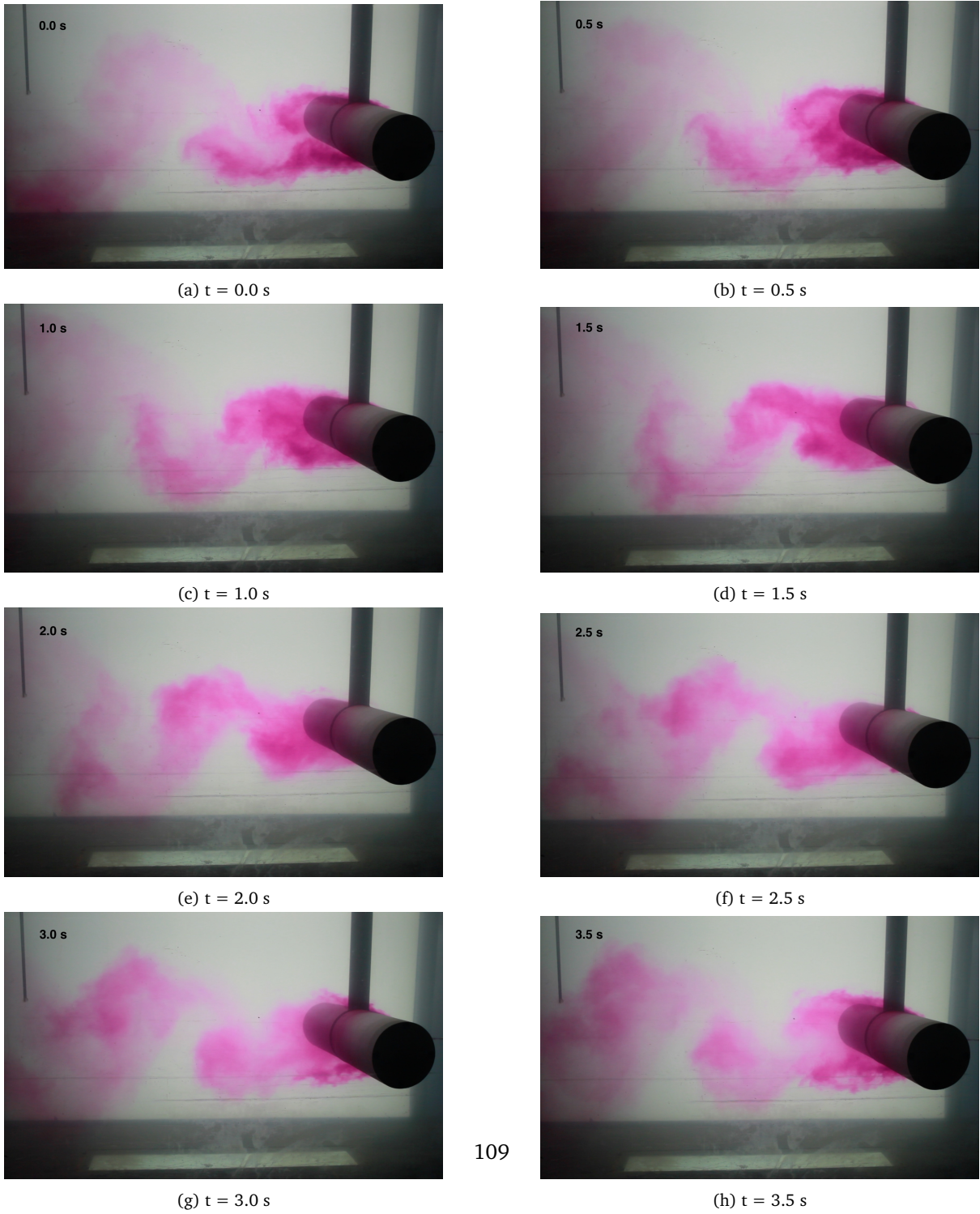


Figure F.1: Evolution of the wake of a circular smooth tunnel



(a) $t = 0.0$ s



(b) $t = 0.5$ s



(c) $t = 1.0$ s



(d) $t = 1.5$ s



(e) $t = 2.0$ s



(f) $t = 2.5$ s



(g) $t = 3.0$ s



(h) $t = 3.5$ s

Figure F.2: Evolution of the wake of a parametric smooth tunnel

Appendix G

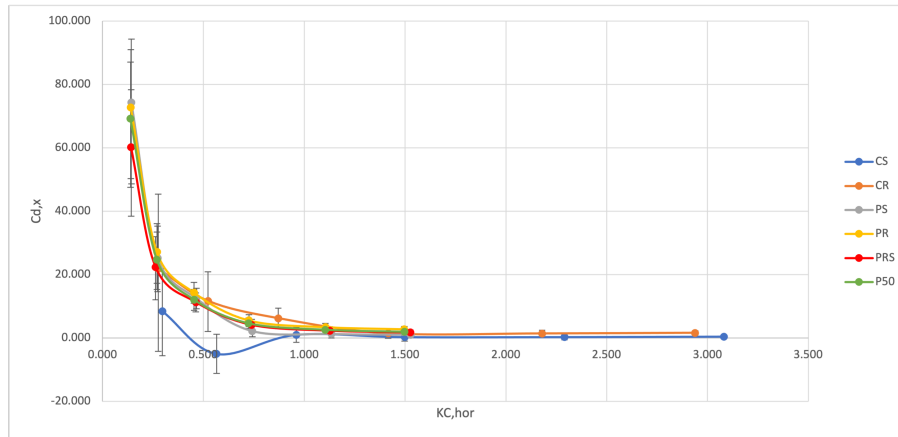
Difference between Max/Min Method and Least Squares Method

In this Appendix, the differences between the Max/Min method and the least squares method are presented.

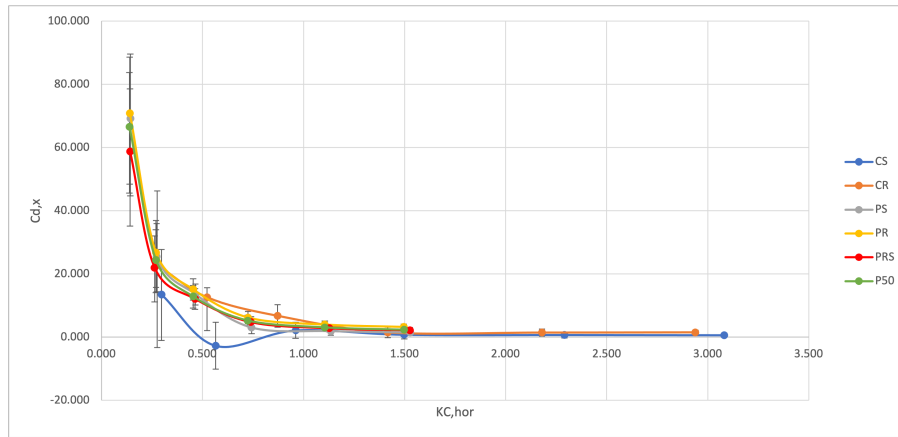
G.1 Waves

In this section, a comparison is shown between the Max/Min method force coefficients and the least squares method force coefficients in wave conditions. The graphs show that both methods result in practically equal force coefficients, providing extra confidence in the found results.

G.1.1 Horizontal Drag

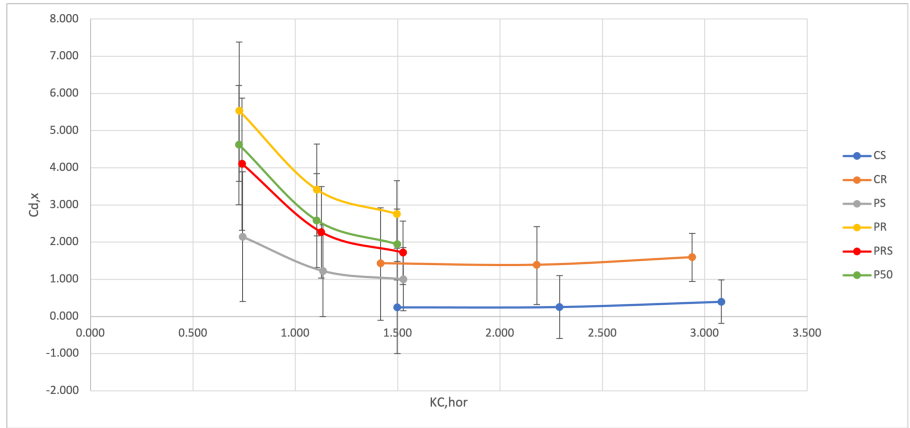


(a) Horizontal drag coefficients, max/min method

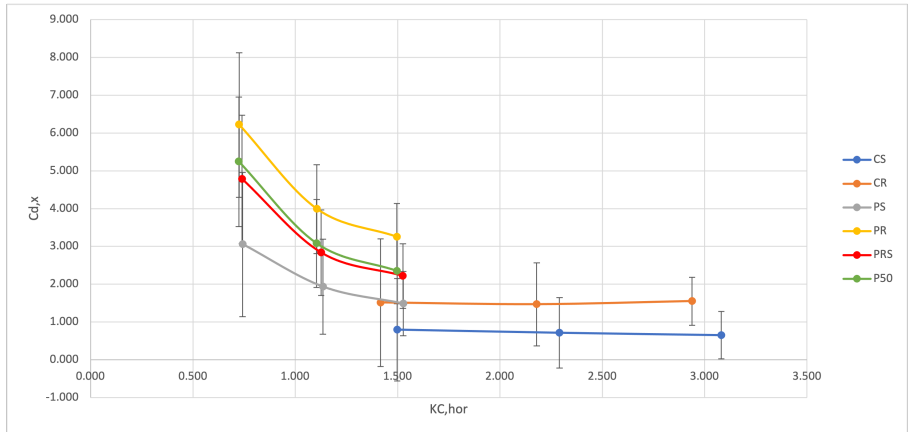


(b) Horizontal drag coefficients, least squares method

Figure G.1: Horizontal drag coefficients under waves



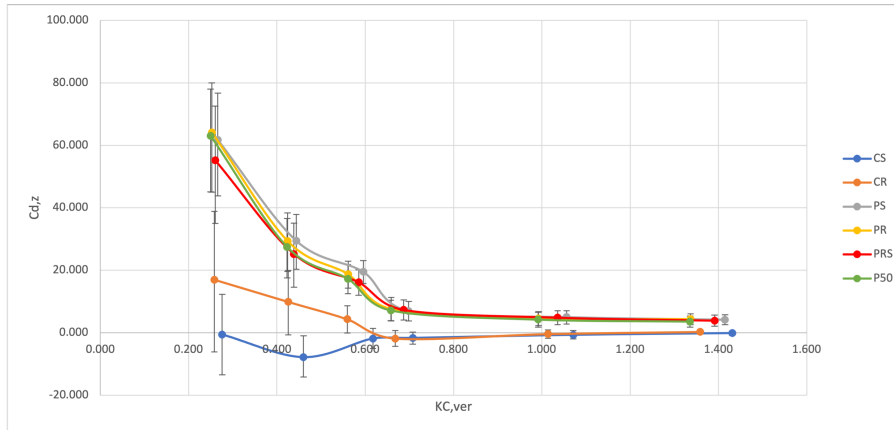
(a) Horizontal drag coefficients, max/min method



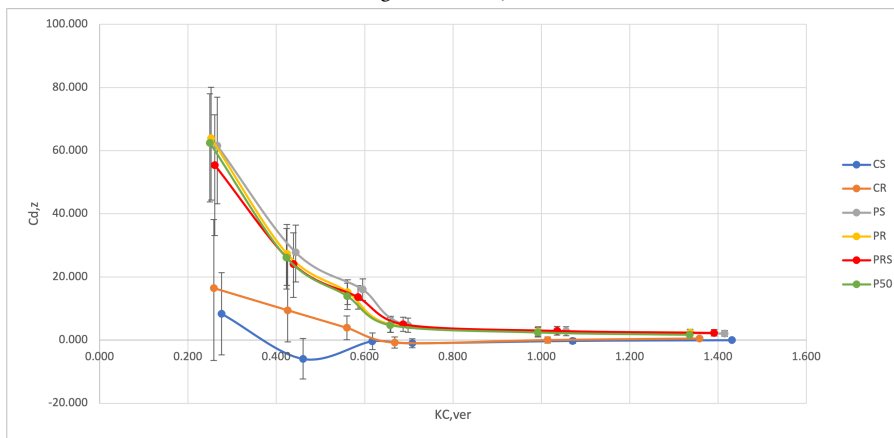
(b) Horizontal drag coefficients, least squares Method

Figure G.2: Horizontal drag coefficients under waves

G.1.2 Vertical Drag

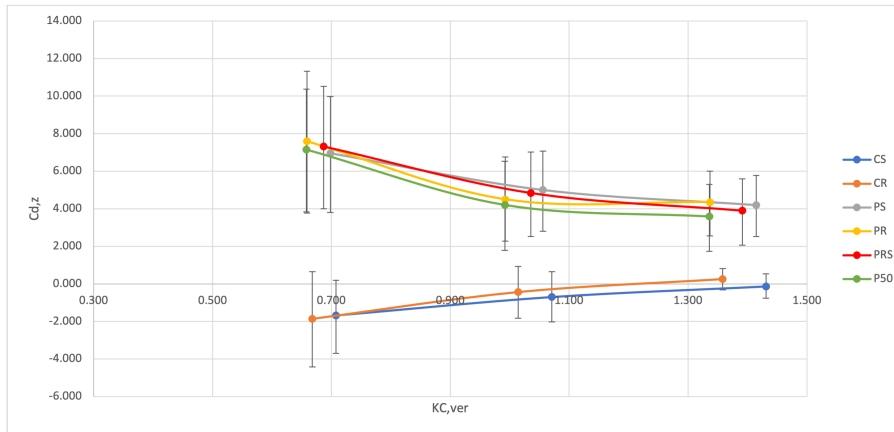


(a) Vertical drag coefficients, max/min method

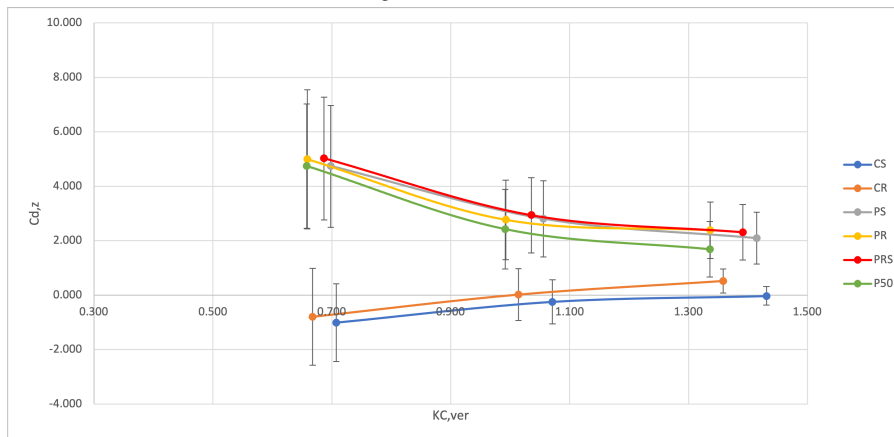


(b) Vertical drag coefficients, least squares method

Figure G.3: Vertical drag coefficients under waves



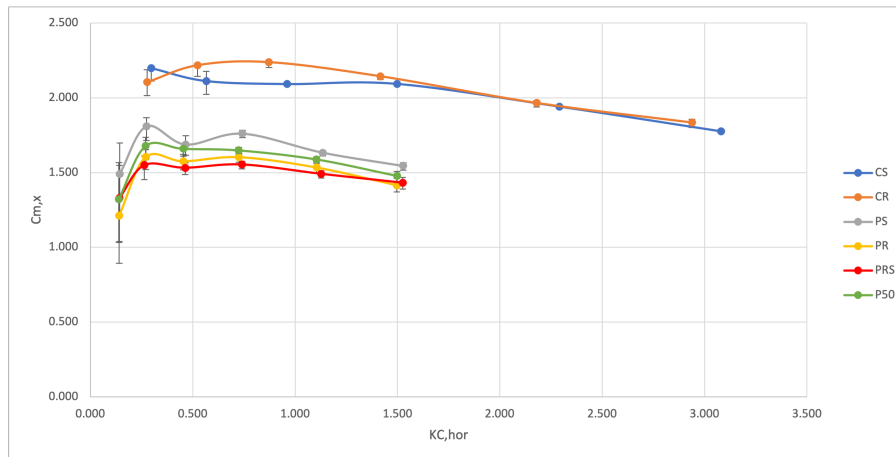
(a) Vertical drag coefficients, max/min method



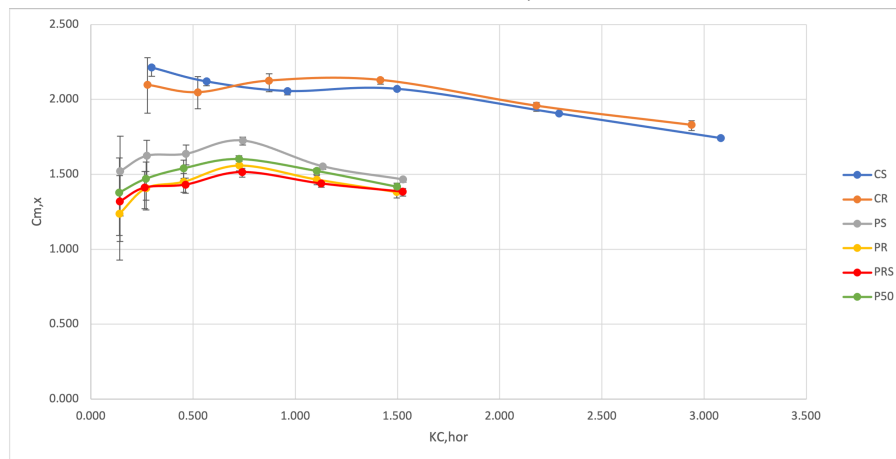
(b) Vertical drag coefficients, least squares method

Figure G.4: Vertical drag coefficients under waves

G.1.3 Horizontal Inertia



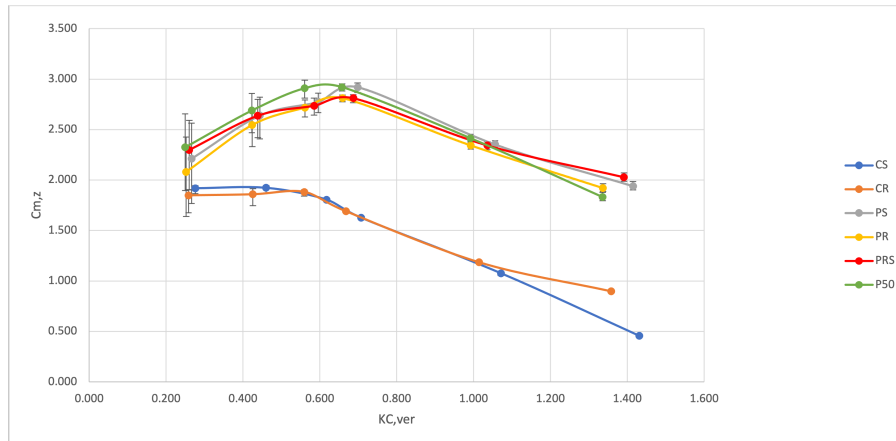
(a) Horizontal inertia coefficients, max/min method



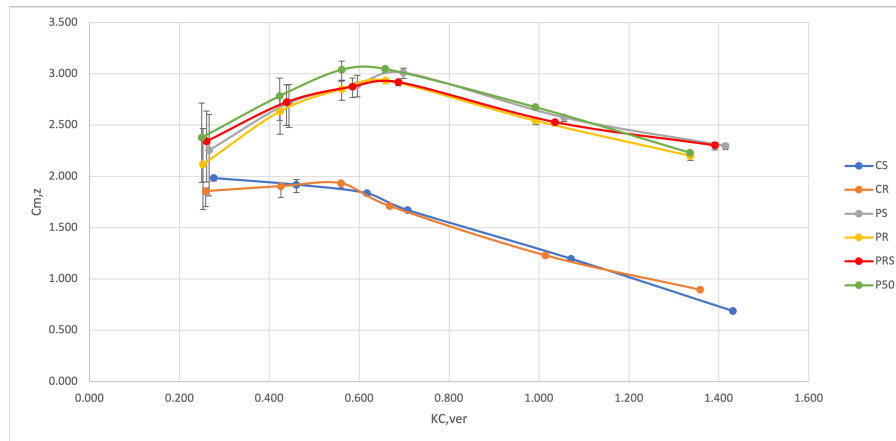
(b) Horizontal inertia coefficients, least squares method

Figure G.5: Horizontal inertia coefficients under waves

G.1.4 Vertical Inertia



(a) Vertical inertia coefficients, max/min method



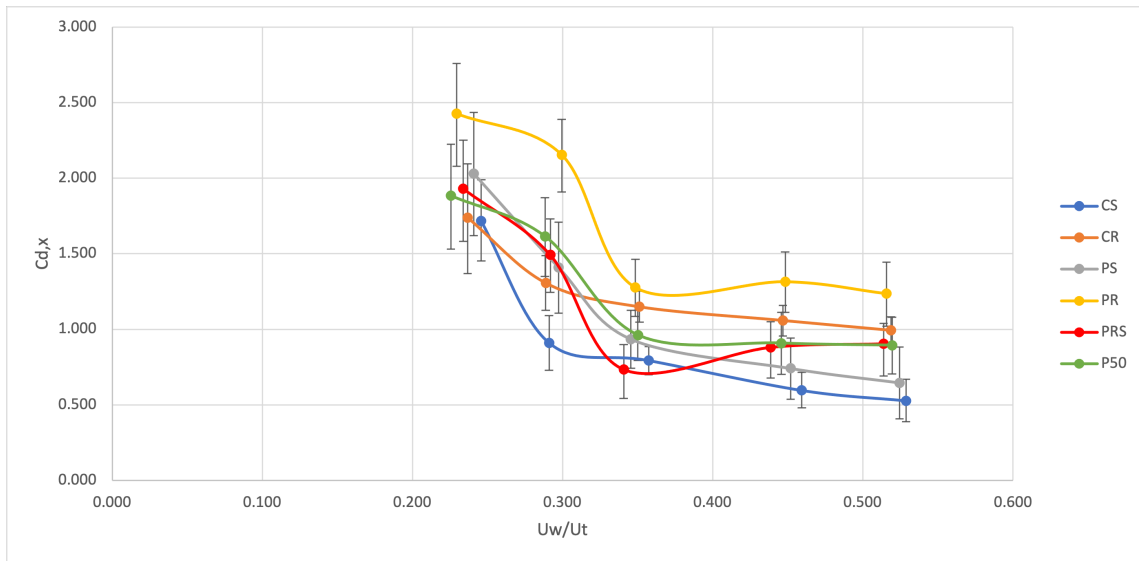
(b) Vertical inertia coefficients, least squares method

Figure G.6: Vertical inertia coefficients under waves

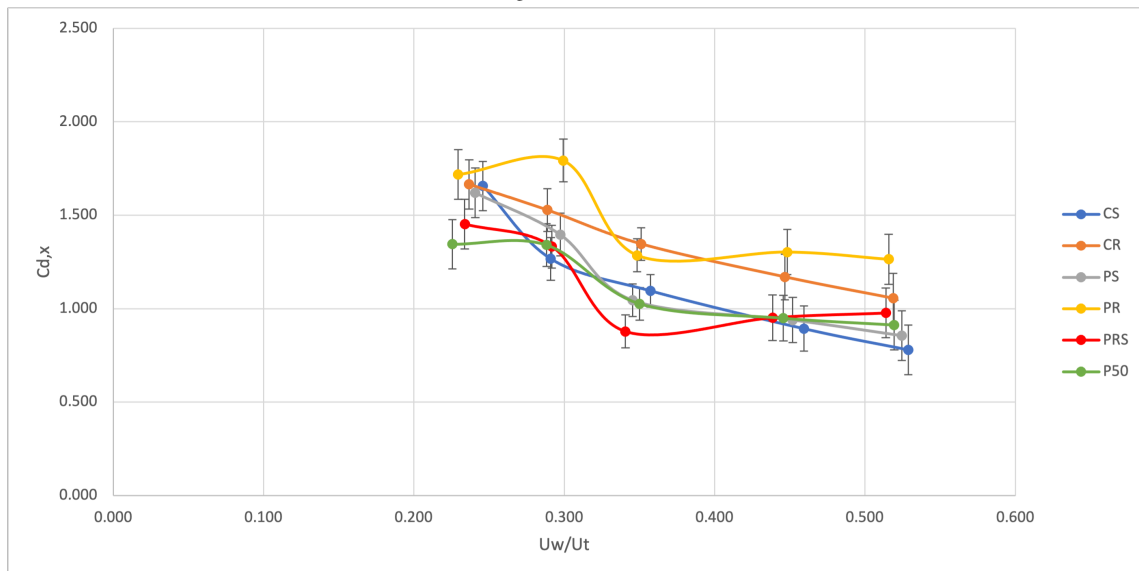
G.2 Combined

In this section, the combined condition results of the force coefficients calculated with the Max/Min method and the least squares method are compared. It is shown that the Max/Min method overestimates the force coefficients for combined conditions.

G.2.1 Horizontal Drag



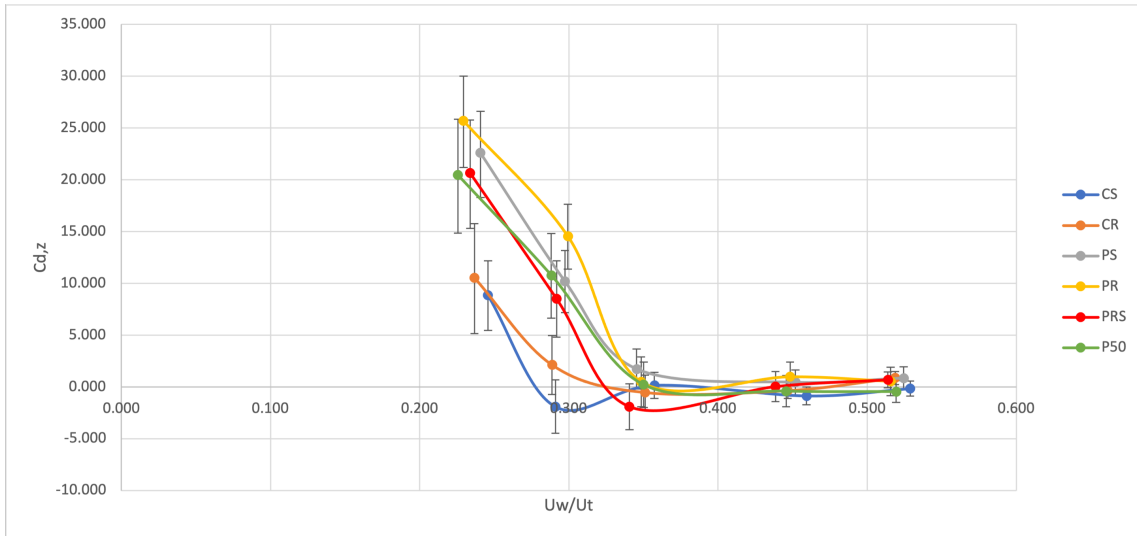
(a) Horizontal drag coefficients, max/min method



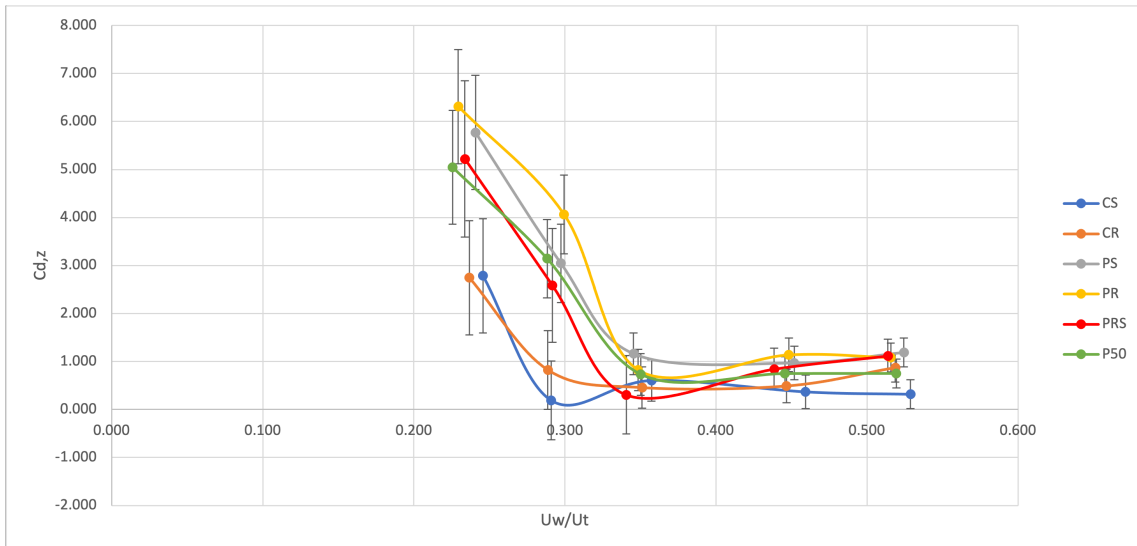
(b) Horizontal drag coefficients, least squares method

Figure G.7: Horizontal drag coefficients

G.2.2 Vertical Drag



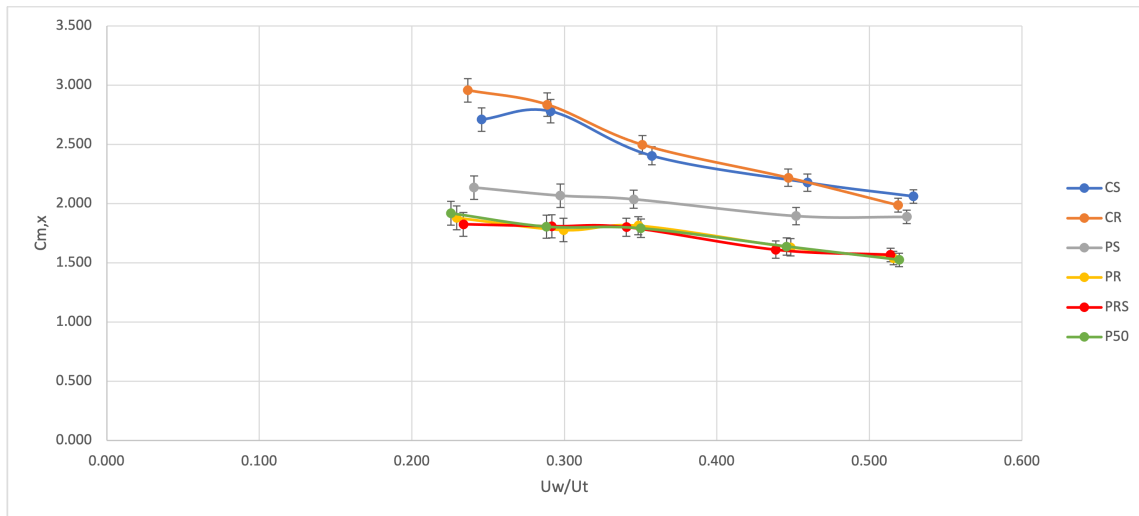
(a) Vertical drag coefficients, max/min method



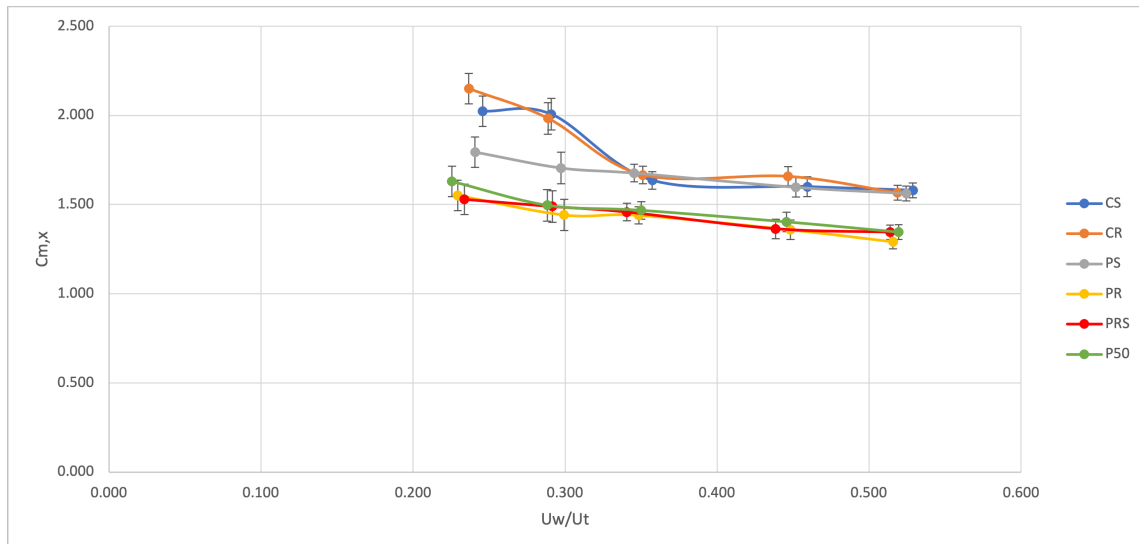
(b) Vertical drag coefficients, least squares method

Figure G.8: Vertical drag coefficients

G.2.3 Horizontal Inertia



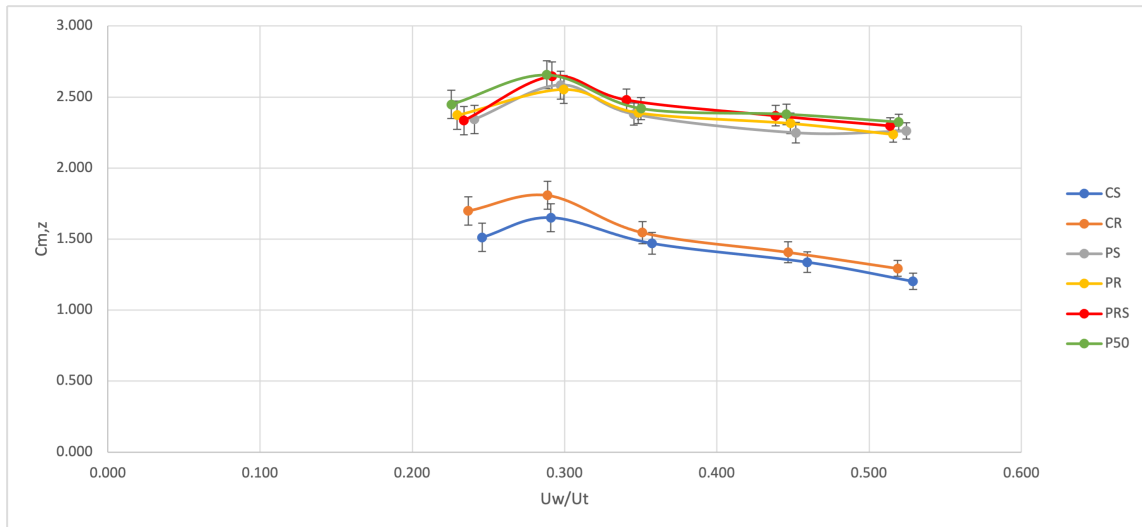
(a) Horizontal inertia coefficients, max/min method



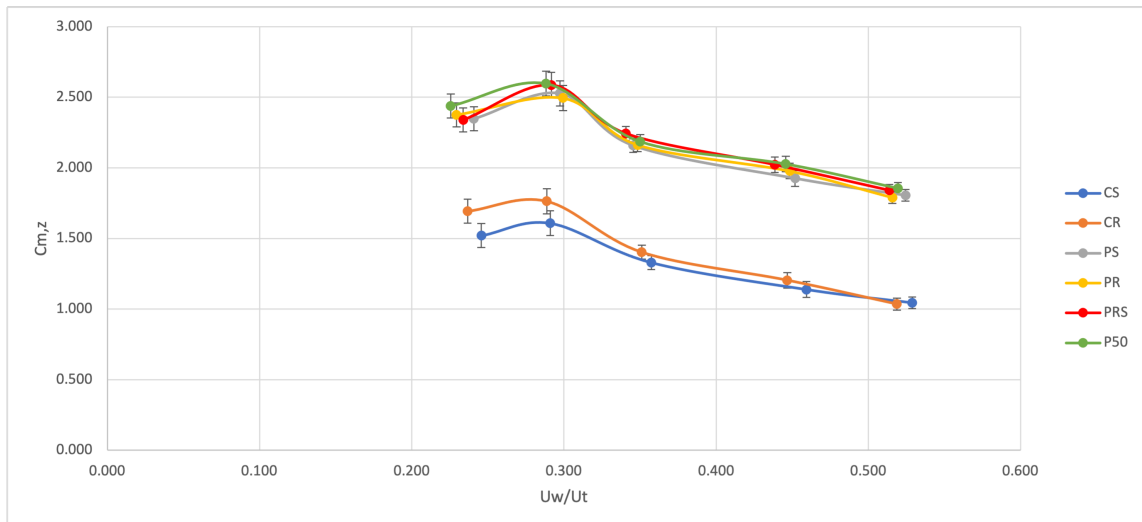
(b) Horizontal inertia coefficients, least squares method

Figure G.9: Horizontal inertia coefficients

G.2.4 Vertical Inertia



(a) Vertical inertia coefficients, max/min method



(b) Vertical inertia coefficients, least squares method

Figure G.10: Vertical inertia coefficients

Appendix H

Combined Conditions Results

H.1 Influence of Tunnel Shape

H.1.1 Vertical Drag Coefficient

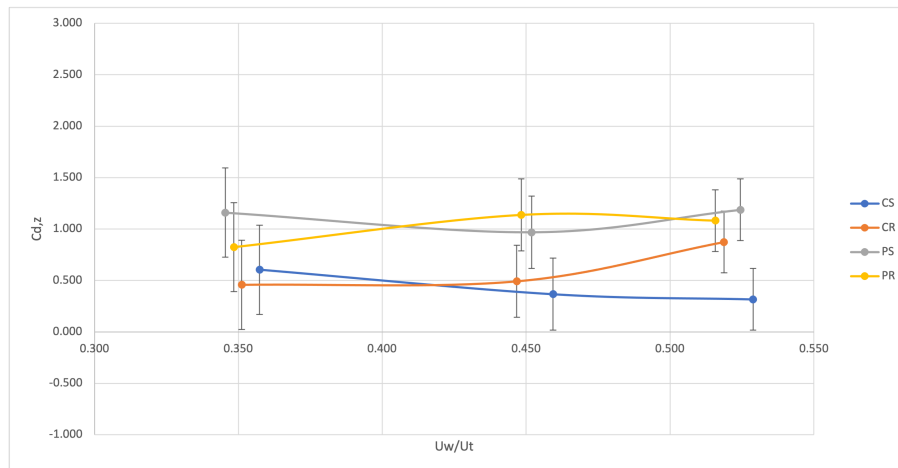


Figure H.1: Vertical drag coefficients for varying tunnel shapes

H.2 Influence of Roughness Height

H.2.1 Vertical Drag Coefficient

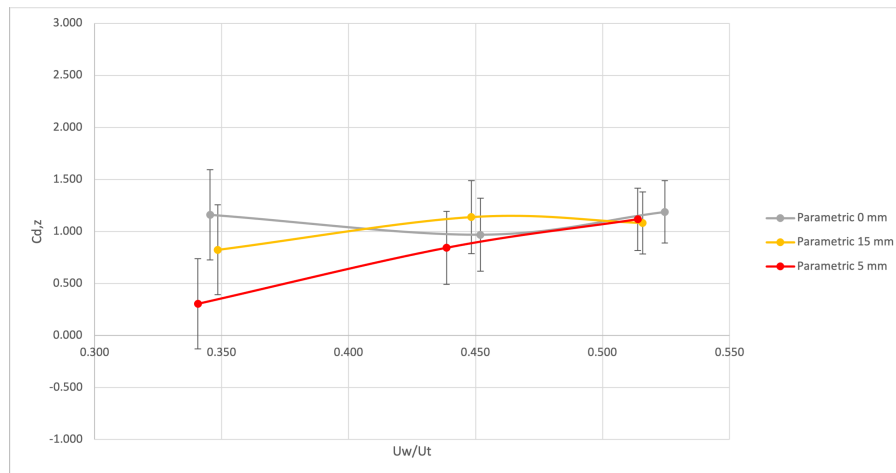


Figure H.2: Vertical drag coefficients for varying roughness heights

H.3 Influence of Coverage Percentage

H.3.1 Vertical Drag Coefficient

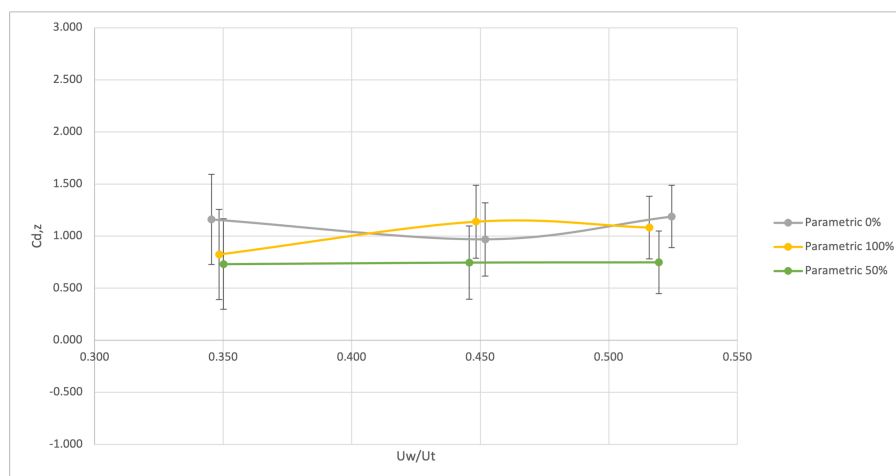


Figure H.3: Vertical drag coefficients for varying coverage percentages

Appendix I

Fitted Coefficients

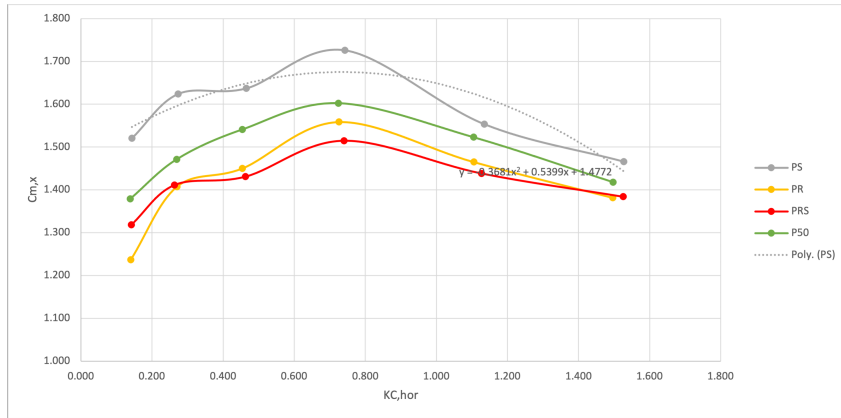
In this Appendix, the method of fitting the force coefficients for wave conditions and combined conditions is described. The fitted coefficients are only valid in the tested range of KC numbers. For other segments of KC numbers, new tests need to be conducted to determine their force coefficient expressions. First, the wave results are discussed, and then the combined results.

I.1 Wave Results

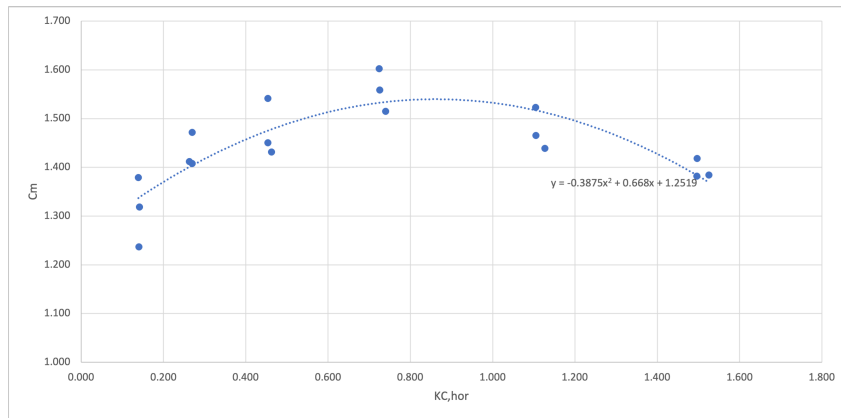
I.1.1 Horizontal Inertia Coefficient

Parametric Tunnel

All three rough parametric tunnels share similar horizontal inertia coefficients. Therefore, a second-order polynomial trend line is used to determine the fitted coefficient, as seen in figure [I.1b](#). The parametric smooth tunnel has a higher horizontal inertia coefficient and received its own fitted coefficient, shown in figure [I.1a](#).



(a) Horizontal inertia coefficient results

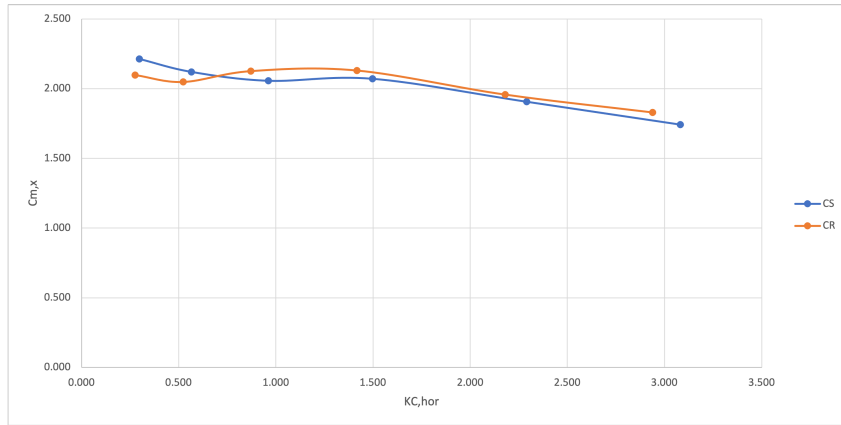


(b) Fitted coefficient for the parametric rough tunnels

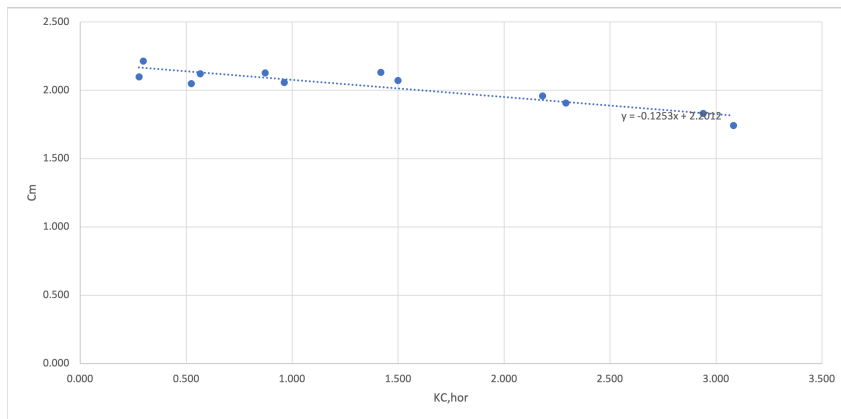
Figure I.1: Fitted horizontal inertia coefficients for the parametric tunnels in wave conditions

Circular Tunnel

Both the rough and smooth circular tunnels share similar horizontal inertia coefficients, where a downward trend is observed, as shown in figure I.2a. Figure I.2b shows the linear trend line that is used for the fitted coefficients.



(a) Horizontal inertia coefficient results



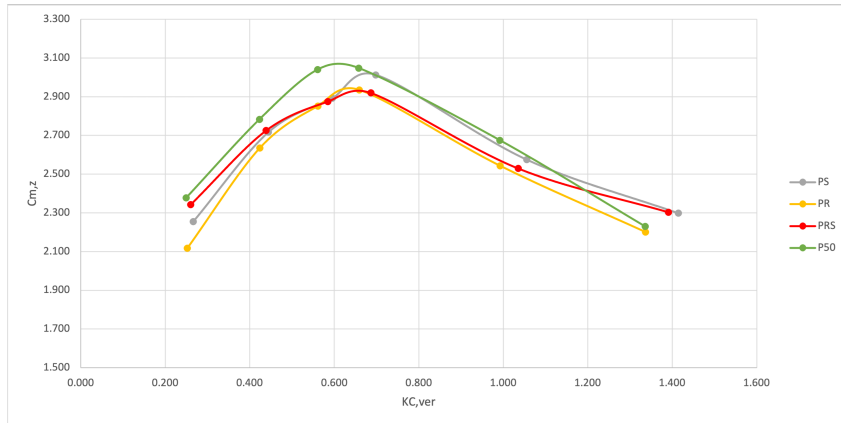
(b) Fitted coefficients for the circular tunnels

Figure I.2: Fitted horizontal inertia coefficients for the circular tunnels in wave conditions

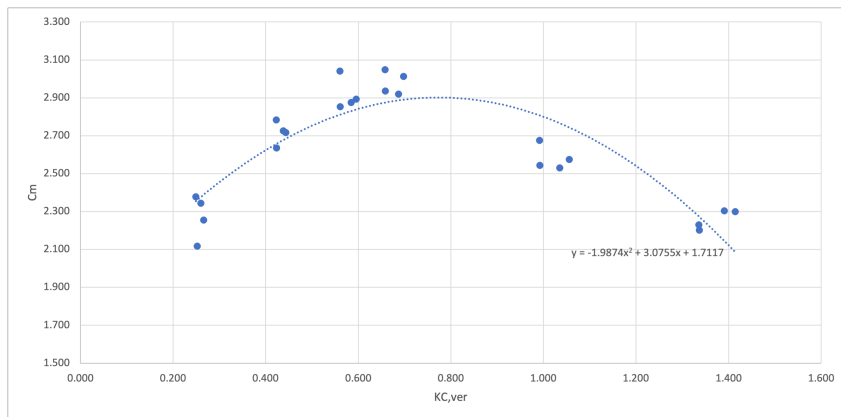
I.1.2 Vertical Inertia Coefficient

Parametric Tunnels

All parametric tunnels share similar vertical inertia coefficients, and a second-order polynomial trend line is used to determine the fitted coefficients. In figure I.3, both the coefficient results for the parametric tunnel and the trend line can be seen.



(a) Vertical inertia coefficient results

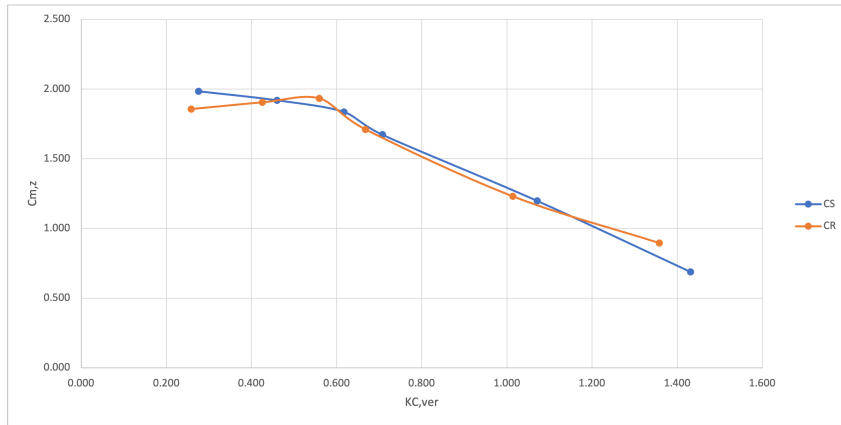


(b) Fitted coefficients for the parametric tunnels

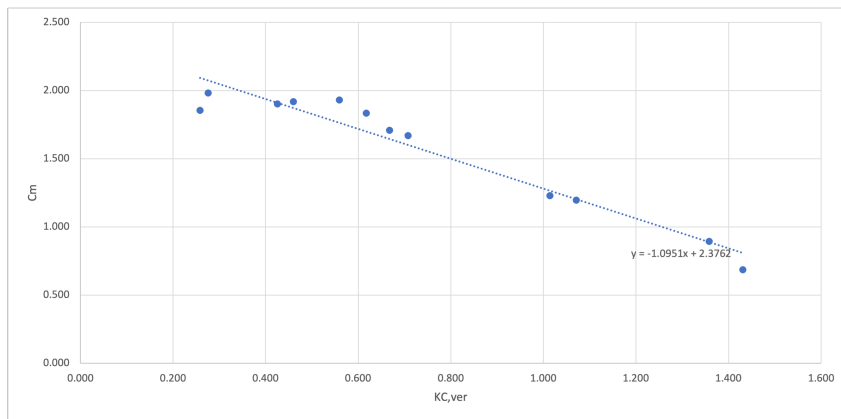
Figure I.3: Fitted vertical inertia coefficients for the parametric tunnels in wave conditions

Circular Tunnels

There is not much difference between the vertical inertia coefficients of the rough and smooth circular tunnels. Their fitted coefficients are described by a linear trend line through their results, shown in figure I.4.



(a) Vertical inertia coefficient results

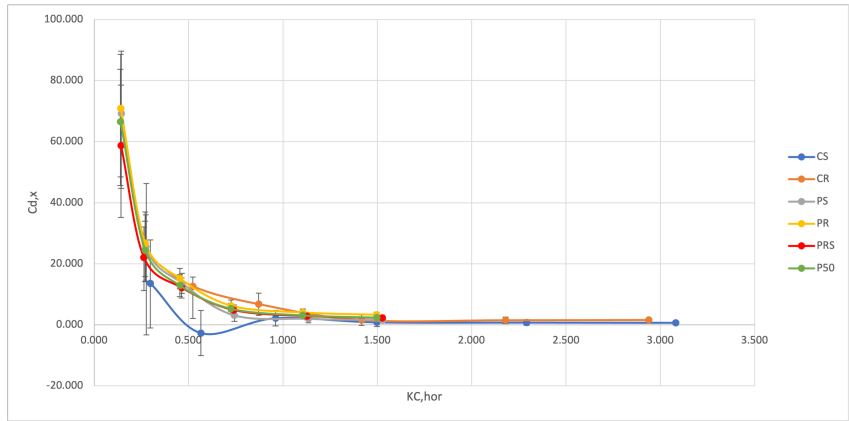


(b) Fitted coefficients for the circular tunnels

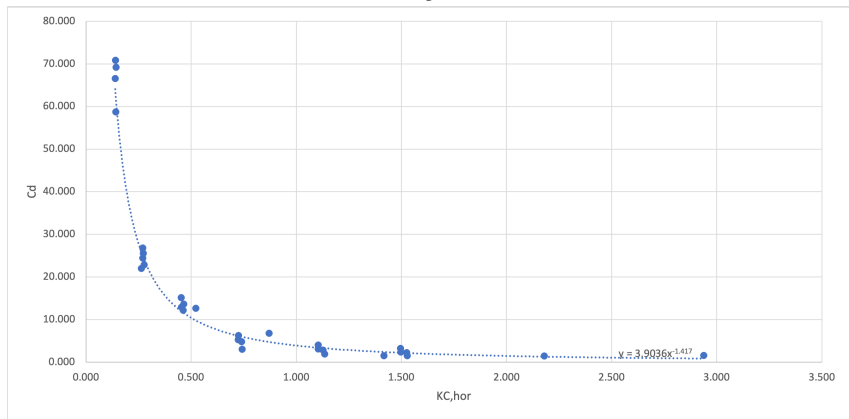
Figure I.4: Fitted vertical inertia coefficients for the circular tunnels in wave conditions

I.1.3 Horizontal Drag Coefficient

The error bars of the horizontal drag coefficients of all tunnels overlap, with the exception of the circular smooth results, as shown in figure I.5a. However, a negative drag coefficient is not realistic, and therefore, all tunnels will share the same fitted horizontal drag coefficients, described by the trend line shown in figure I.5b.



(a) Horizontal drag coefficient results



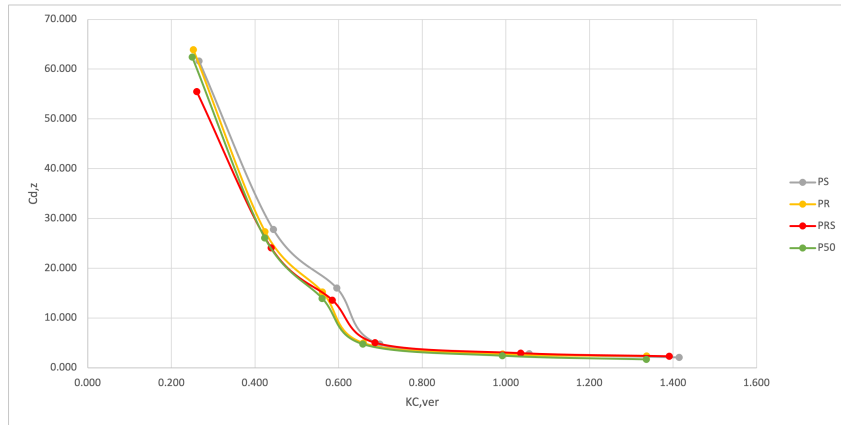
(b) Fitted coefficients for all tunnels

Figure I.5: Fitted horizontal drag coefficients for all tunnels in wave conditions

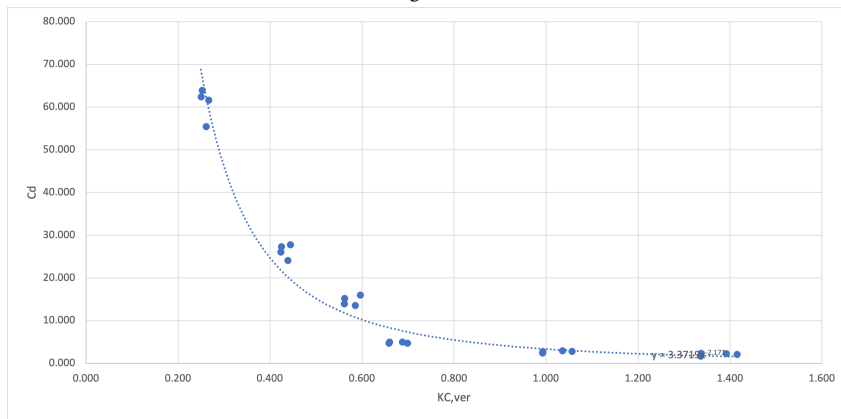
I.1.4 Vertical Drag Coefficient

Parametric Tunnels

Similar to their vertical inertia coefficients, the vertical drag coefficients of the parametric tunnels are close to each other, as shown in figure I.6a. They are described using the trend line shown in figure I.6b.



(a) Vertical drag coefficient results



(b) Fitted coefficients for the parametric tunnels

Figure I.6: Fitted vertical drag coefficients for the parametric tunnels in wave conditions

Circular Tunnels

The vertical drag coefficients of the circular tunnels are shown in figure I.7. Here it can be seen that besides for the smallest KC numbers, the vertical drag coefficients approach zero. Since the drag force contribution becomes smaller for decreasing KC numbers, it was decided to use no vertical drag coefficients for the circular tunnels, and propose a fitted coefficient of 0.

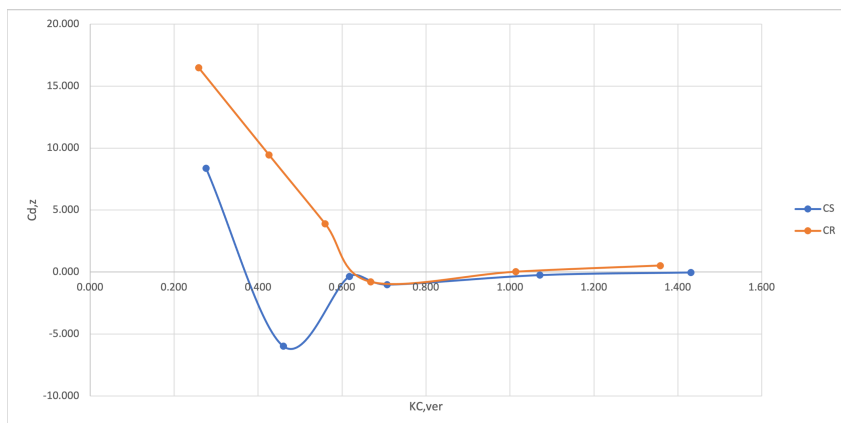


Figure I.7: Vertical drag coefficients for the circular tunnels in wave conditions

I.1.5 Summary of all Coefficients

In table I.1, the proposed fitted force coefficients for submerged floating tunnels in wave conditions are presented.

	Cd_x	Cm_x	Cd_z	Cm_z
CS	$3.9 KC_x^{-1.4}$	$-0.125 KC_x + 2.2$	0	$-1.1 KC_z + 2.38$
CR	$3.9 KC_x^{-1.4}$	$-0.125 KC_x + 2.2$	0	$-1.1 KC_z + 2.38$
PS	$3.9 KC_x^{-1.4}$	$-0.37 KC_x^2 + 0.54 KC_x + 1.48$	$3.37 KC_z^{-2.171}$	$-1.99 KC_z^2 + 3.1 KC_z + 1.7$
PR	$3.9 KC_x^{-1.4}$	$-0.39 KC_x^2 + 0.67 KC_x + 1.25$	$3.37 KC_z^{-2.171}$	$-1.99 KC_z^2 + 3.1 KC_z + 1.7$
PRS	$3.9 KC_x^{-1.4}$	$-0.39 KC_x^2 + 0.67 KC_x + 1.25$	$3.37 KC_z^{-2.171}$	$-1.99 KC_z^2 + 3.1 KC_z + 1.7$
PR50	$3.9 KC_x^{-1.4}$	$-0.39 KC_x^2 + 0.67 KC_x + 1.25$	$3.37 KC_z^{-2.171}$	$-1.99 KC_z^2 + 3.1 KC_z + 1.7$

Table I.1: Fitted force coefficients for all tunnels in wave conditions

I.2 Combined Results

I.2.1 Horizontal Inertia Coefficient

The horizontal inertia coefficient results of the combined tests are shown in figure I.8. Here it can be seen that the three rough parametric tunnels share similar coefficients, which can be described by a linear downward trend as shown in figure I.9a. The parametric smooth tunnel has a separate linear downward trend, as shown in figure I.8. The fitted coefficients of the circular tunnels are described by the linear trend line shown in figure I.9b.

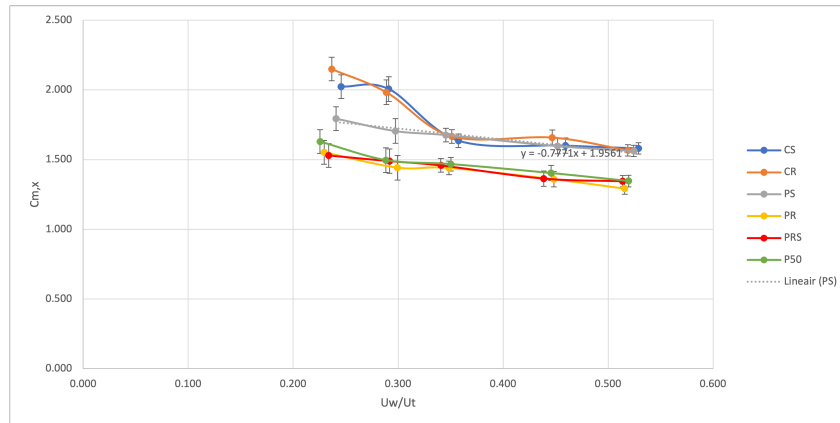
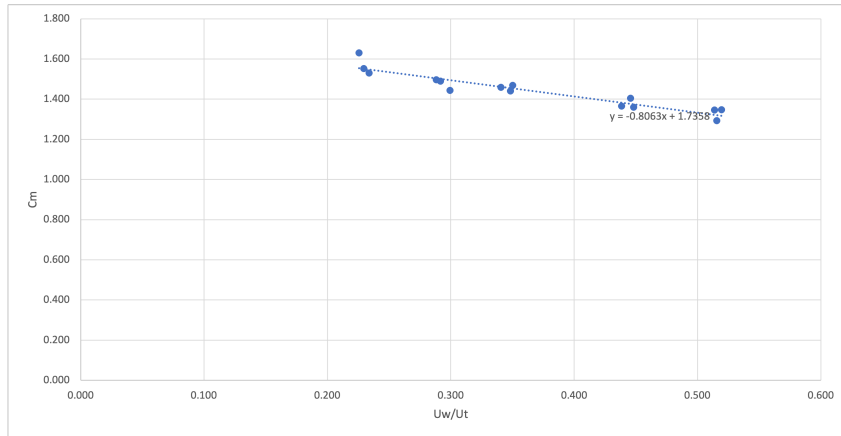
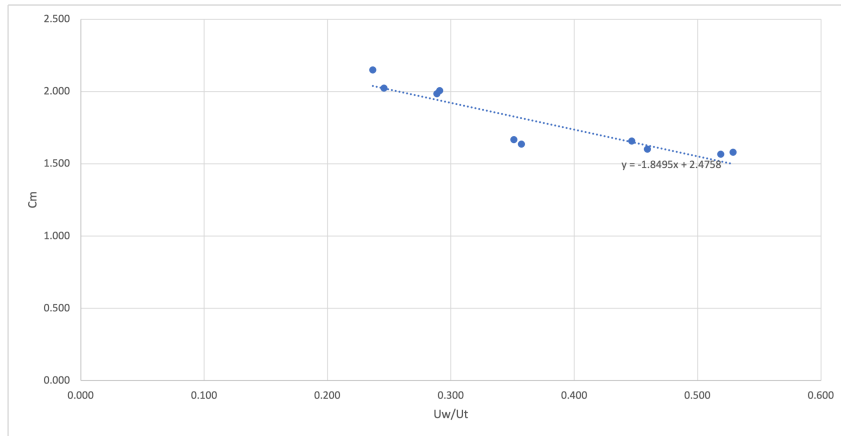


Figure I.8: Horizontal inertia coefficients for the combined tests



(a) Fitted coefficients for the parametric rough tunnels



(b) Fitted coefficients for the circular tunnels

Figure I.9: Fitted horizontal inertia coefficients for all tunnels in combined conditions

I.2.2 Vertical Inertia Coefficient

The vertical inertia coefficient results in combined conditions are shown in figure I.10. The fitted vertical inertia coefficients of the parametric and circular tunnels are both described by linear downward trends, as shown in figures I.11a and I.11b, respectively.

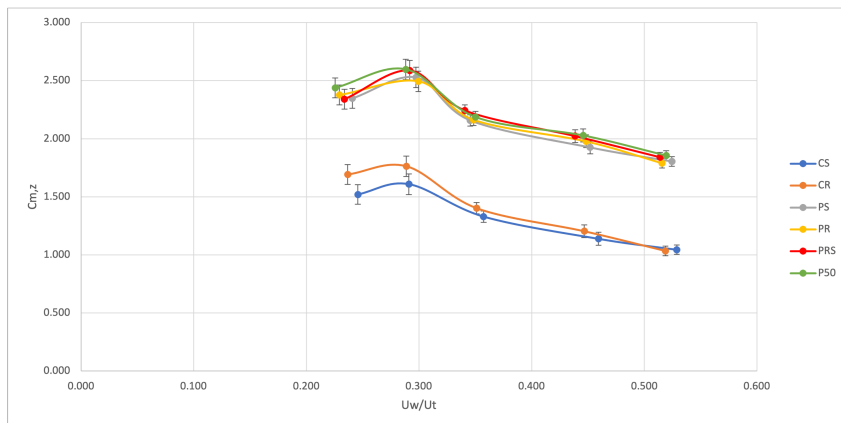
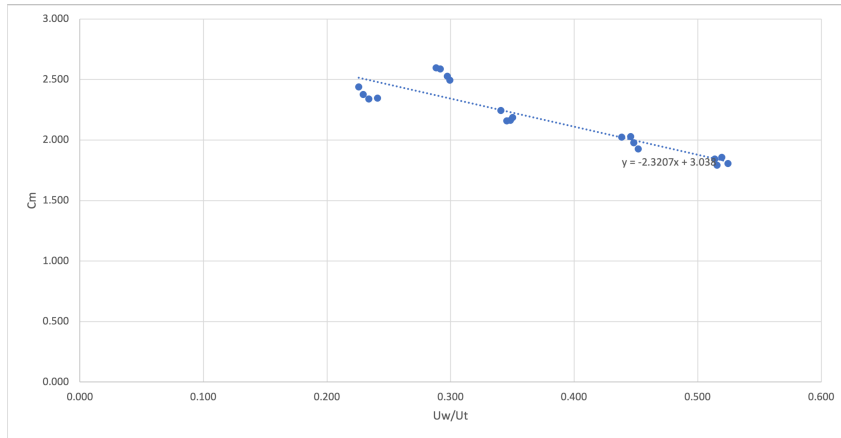
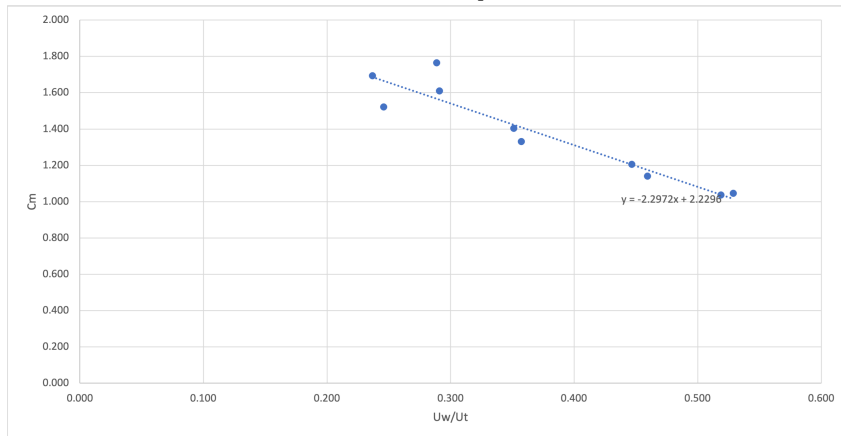


Figure I.10: Vertical inertia coefficients for the combined tests



(a) Fitted coefficients for the parametric tunnels



(b) Fitted coefficients for the circular tunnels

Figure I.11: Fitted vertical inertia coefficients for all tunnels in combined conditions

I.2.3 Horizontal Drag Coefficient

The horizontal drag coefficient results in combined conditions are shown in figure I.12. Since no clear relation was observed between the drag coefficient and the roughness height, the coverage percentage, and the number of roughness elements, all parametric tunnels will share equal fitted coefficients. The circular tunnels have coefficients that are close in value when considering the error bars. Therefore, they will share equal fitted coefficients as well. The fitted coefficients for the parametric tunnels are shown in figure I.13a, and the fitted coefficients for the circular tunnels are shown in figure I.13b.

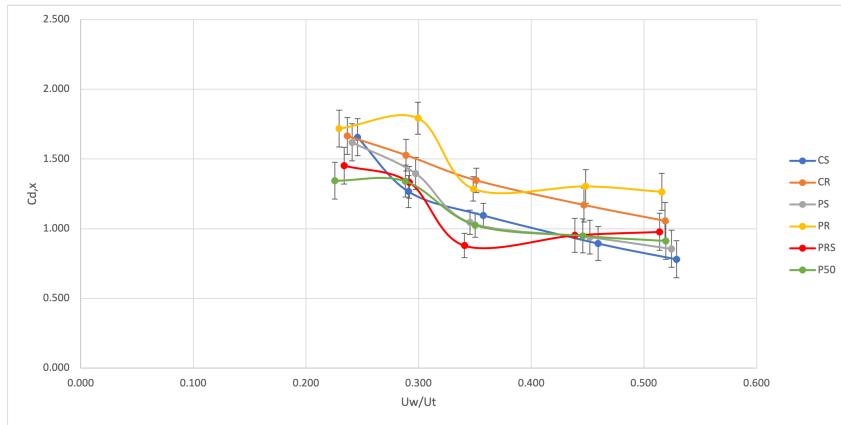
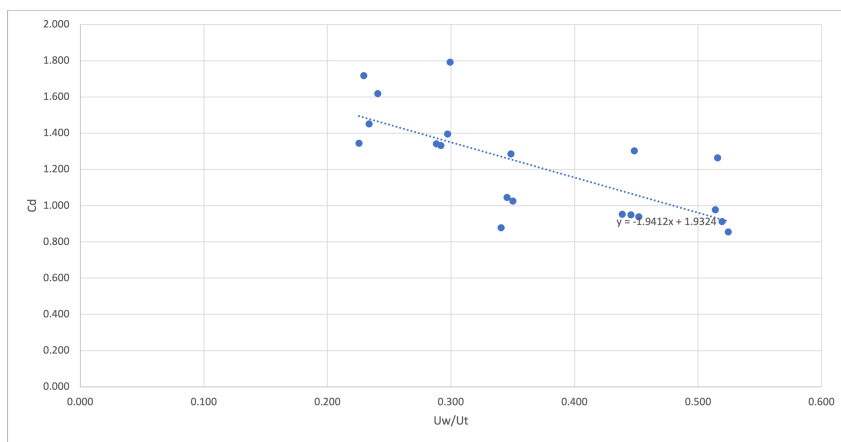
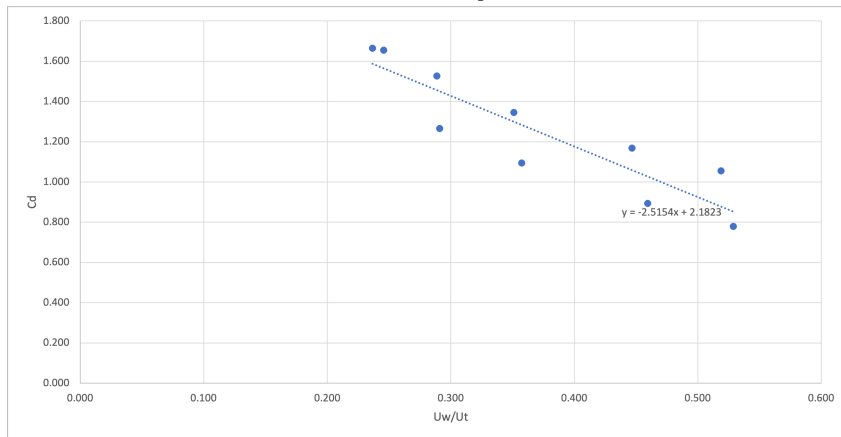


Figure I.12: Horizontal drag coefficients for the combined tests



(a) Fitted coefficients for the parametric tunnels



(b) Fitted coefficients for the circular tunnels

Figure I.13: Fitted horizontal drag coefficients for all tunnels in combined conditions

I.2.4 Vertical Drag Coefficient

The vertical drag coefficient results in combined conditions are shown in figure I.14. The fitted vertical inertia coefficients of the parametric and circular tunnels are both described by a downward power trend line, as shown in figures I.15a and I.15b, respectively.

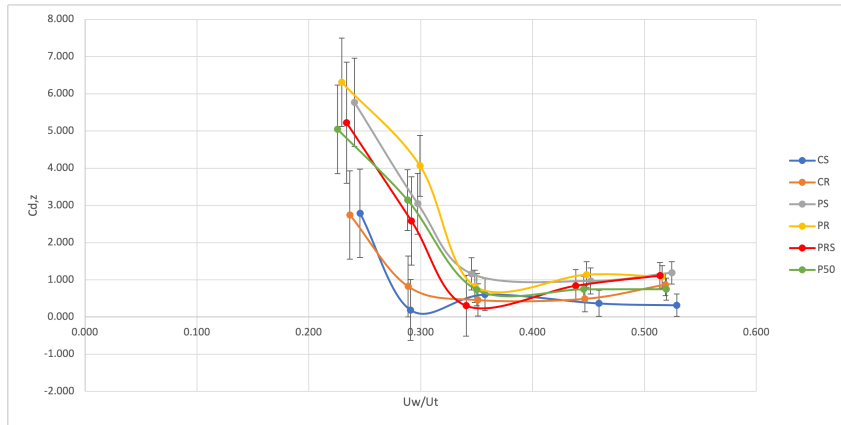
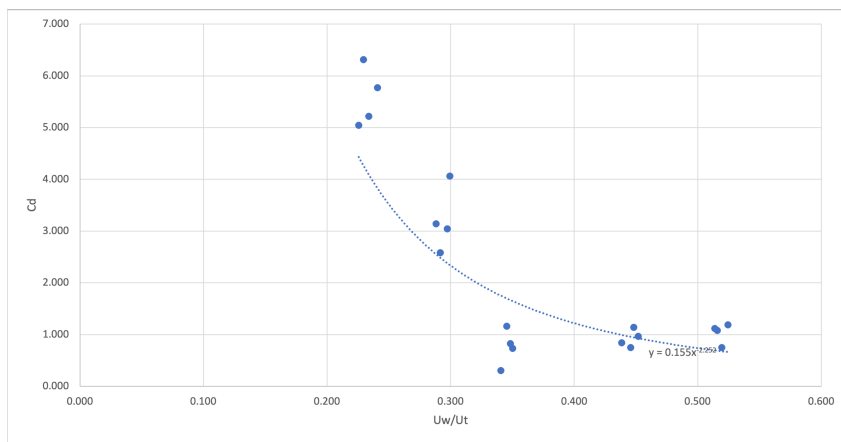
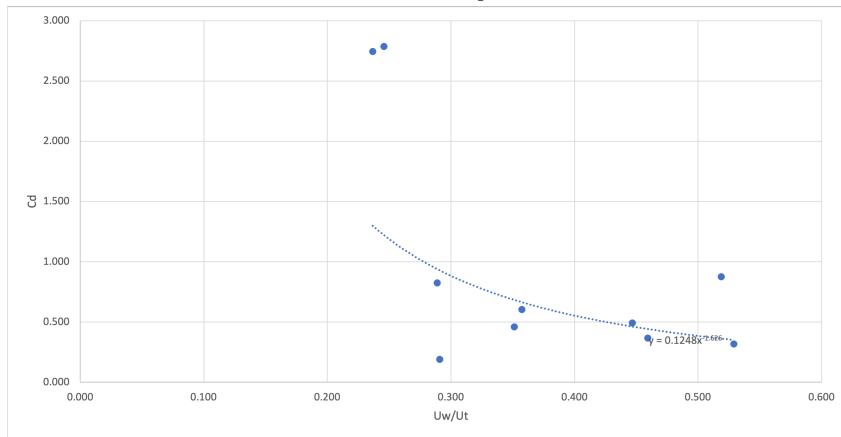


Figure I.14: Vertical drag coefficients for the combined tests



(a) Fitted coefficients for the parametric tunnels



(b) Fitted coefficients for the circular tunnels

Figure I.15: Fitted vertical drag coefficients for all tunnels in combined conditions

I.2.5 Summary of all Coefficients

In table I.2, the proposed fitted force coefficients for submerged floating tunnels in wave conditions are presented.

	Cd_x	Cm_x	Cd_z	Cm_z
CS	$-2.52 U_w/U_t + 2.18$	$-1.85 U_w/U_t + 2.48$	$0.125 U_w/U_t^{-1.63}$	$-2.3 U_w/U_t + 2.23$
CR	$-2.52 U_w/U_t + 2.18$	$-1.85 U_w/U_t + 2.48$	$0.125 U_w/U_t^{-1.63}$	$-2.3 U_w/U_t + 2.23$
PS	$-1.94 U_w/U_t + 1.93$	$-0.78 U_w/U_t + 1.96$	$0.155 U_w/U_t^{-2.25}$	$-2.3 U_w/U_t + 3.04$
PR	$-1.94 U_w/U_t + 1.93$	$-0.81 U_w/U_t + 1.74$	$0.155 U_w/U_t^{-2.25}$	$-2.3 U_w/U_t + 3.04$
PRS	$-1.94 U_w/U_t + 1.93$	$-0.81 U_w/U_t + 1.74$	$0.155 U_w/U_t^{-2.25}$	$-2.3 U_w/U_t + 3.04$
PR50	$-1.94 U_w/U_t + 1.93$	$-0.81 U_w/U_t + 1.74$	$0.155 U_w/U_t^{-2.25}$	$-2.3 U_w/U_t + 3.04$

Table I.2: Fitted force coefficients for all tunnels in combined conditions

Appendix J

Force Prediction Accuracy and Comparison

In this Appendix, the force prediction errors of the different force coefficients for the parametric tunnels are presented.

J.1 Current Results

	Error NC	Error API	Error DNV
PS.C1	-4.85%	-52.43%	-48.54%
PS.C2	-7.32%	-53.66%	-49.76%
PS.C3	12.85%	-43.58%	-38.83%

Table J.1: Force prediction errors PS in current conditions

	Error NC	Error API	Error DNV
PR.C1	-11.27%	-35.21%	-38.03%
PR.C2	6.92%	-21.59%	-25.25%
PR.C3	10.31%	-19.17%	-22.83%

Table J.2: Force prediction errors PR in current conditions

	Error NC	Error API	Error DNV
PRS.C1	-1.89%	-10.38%	-14.15%
PRS.C2	1.72%	-6.65%	-11.08%
PRS.C3	3.65%	-4.95%	-9.31%

Table J.3: Force prediction errors PRS in current conditions

	Error NC	Error API	Error DNV
PR50.C1	0.00%	-7.84%	-11.76%
PR50.C2	2.70%	-5.88%	-10.29%
PR50.C3	1.74%	-6.63%	-10.93%

Table J.4: Force prediction errors PR50 in current conditions

J.2 Wave Results

	Error NC	Error API	Error DNV
PS.W1	-1.17%	9.37%	9.35%
PS.W2	-4.29%	11.22%	11.23%
PS.W3	-5.53%	10.52%	10.54%
PS.W4	-3.26%	12.70%	12.73%
PS.W5	0.47%	21.34%	21.37%
PS.W6	-6.69%	25.95%	25.98%

	Error NC	Error API	Error DNV
PS.W1	-0.86%	-32.90%	-32.91%
PS.W2	-5.40%	-37.24%	-37.26%
PS.W3	-6.72%	-39.74%	-39.75%
PS.W4	-2.73%	-37.33%	-37.32%
PS.W5	-6.51%	-28.54%	-28.53%
PS.W6	-8.81%	-20.64%	-20.63%

Table J.5: Horizontal (left) and vertical (right) force prediction errors for the parametric smooth tunnel

	Error NC	Error API	Error DNV
PR.W1	-2.06%	20.02%	20.04%
PR.W2	-5.28%	22.80%	22.78%
PR.W3	-9.42%	17.52%	17.50%
PR.W4	-6.82%	18.35%	18.34%
PR.W5	-1.42%	26.85%	26.81%
PR.W6	-6.01%	32.39%	32.35%

	Error NC	Error API	Error DNV
PR.W1	8.16%	-29.45%	-29.44%
PR.W2	-6.18%	-35.76%	-35.76%
PR.W3	-5.61%	-37.22%	-37.22%
PR.W4	-0.23%	-35.22%	-35.22%
PR.W5	8.00%	-24.98%	-25.00%
PR.W6	1.36%	-12.21%	-12.25%

Table J.6: Horizontal (left) and vertical (right) force prediction errors for the parametric rough tunnel

	Error NC	Error API	Error DNV
PRS.W1	2.17%	25.19%	25.18%
PRS.W2	-1.56%	27.44%	27.45%
PRS.W3	-2.10%	26.82%	26.80%
PRS.W4	-2.54%	23.70%	23.67%
PRS.W5	-0.37%	28.47%	28.44%
PRS.W6	-5.88%	33.64%	33.57%

	Error NC	Error API	Error DNV
PRS.W1	5.78%	-30.34%	-30.34%
PRS.W2	-6.51%	-36.02%	-36.04%
PRS.W3	-6.21%	-37.67%	-37.69%
PRS.W4	-1.01%	-35.63%	-35.65%
PRS.W5	5.60%	-25.60%	-25.61%
PRS.W6	-6.46%	-14.61%	-14.64%

Table J.7: Horizontal (left) and vertical (right) force prediction errors for the parametric small roughness tunnel

	Error NC	Error API	Error DNV
PR50.W1	-4.19%	15.50%	15.48%
PR50.W2	-6.05%	20.66%	20.67%
PR50.W3	-9.18%	17.32%	17.31%
PR50.W4	-7.75%	16.91%	16.90%
PR50.W5	-4.80%	22.28%	22.25%
PR50.W6	-7.52%	30.05%	29.99%

	Error NC	Error API	Error DNV
PR50.W1	3.12%	-34.01%	-34.01%
PR50.W2	-8.38%	-37.74%	-37.75%
PR50.W3	-10.00%	-40.47%	-40.48%
PR50.W4	-3.51%	-37.71%	-37.71%
PR50.W5	0.36%	-30.44%	-30.47%
PR50.W6	-4.08%	-17.04%	-17.09%

Table J.8: Horizontal (left) and vertical (right) force prediction errors for the parametric 50% coverage tunnel

J.3 Combined Results

	Error NC	Error API	Error DNV		Error NC	Error API	Error DNV
PS.CW2	-5.22%	-11.87%	-11.36%	PS.CW2	1.88%	-22.11%	-22.07%
PS.CW3	-2.97%	-6.37%	-5.84%	PS.CW3	-5.56%	-22.72%	-22.67%
PS.CW4	0.85%	-0.88%	-0.26%	PS.CW4	12.51%	-2.03%	-1.97%
PS.CW5	-2.56%	6.41%	6.91%	PS.CW5	14.34%	12.81%	12.83%
PS.CW6	-9.15%	5.87%	6.33%	PS.CW6	13.46%	22.91%	22.95%

Table J.9: Horizontal (left) and vertical (right) force prediction errors for the parametric smooth tunnel in combined conditions

	Error NC	Error API	Error DNV		Error NC	Error API	Error DNV
PR.CW2	-3.16%	6.03%	5.19%	PR.CW2	4.41%	-19.33%	-19.43%
PR.CW3	-7.27%	5.74%	4.93%	PR.CW3	-7.46%	-23.43%	-23.56%
PR.CW4	-3.33%	12.99%	12.03%	PR.CW4	13.23%	-0.24%	-0.44%
PR.CW5	-6.43%	21.84%	21.03%	PR.CW5	11.34%	10.28%	10.16%
PR.CW6	-7.10%	30.05%	29.24%	PR.CW6	14.19%	24.26%	24.08%

Table J.10: Horizontal (left) and vertical (right) force prediction errors for the parametric rough tunnel in combined conditions

	Error NC	Error API	Error DNV		Error NC	Error API	Error DNV
PRS.CW2	-3.13%	4.68%	3.80%	PRS.CW2	3.42%	-21.14%	-21.25%
PRS.CW3	-0.23%	12.23%	11.31%	PRS.CW3	-4.94%	-22.25%	-22.38%
PRS.CW4	3.62%	19.39%	18.32%	PRS.CW4	11.38%	-2.97%	-3.17%
PRS.CW5	-0.27%	28.44%	27.52%	PRS.CW5	10.37%	8.35%	8.22%
PRS.CW6	-4.04%	33.03%	32.16%	PRS.CW6	12.78%	21.63%	21.44%

Table J.11: Horizontal (left) and vertical (right) force prediction errors for the parametric small roughness tunnel in combined conditions

	Error NC	Error API	ErrorDNV		Error NC	Error API	ErrorDNV
PR50.CW2	-2.79%	4.98%	2.92%	PR50.CW2	1.89%	-22.02%	-22.98%
PR50.CW3	0.00%	12.41%	10.23%	PR50.CW3	-5.59%	-22.51%	-23.51%
PR50.CW4	-0.72%	14.33%	12.01%	PR50.CW4	10.83%	-3.02%	-4.37%
PR50.CW5	-1.49%	26.82%	24.56%	PR50.CW5	12.01%	10.23%	8.93%
PR50.CW6	-3.95%	33.12%	30.81%	PR50.CW6	13.60%	22.87%	21.39%

Table J.12: Horizontal (left) and vertical (right) force prediction errors for the parametric 50% coverage tunnel in combined conditions